Femtosecond Wavevector Overtone Spectroscopy of Anharmonic Lattice Dynamics in Ferroelectric Crystals

by

Ciaran Joseph Brennan

M.S. Physics, University of Illinois, 1986
B.S. Physics, University of Notre Dame, 1984

Submitted to the Department of Chemistry in partial fulfillment of the requirements for the degree of

DOCTOR OF PHILOSOPHY

at the

MASSACHUSETTS INSTITUTE OF TECHNOLOGY

June 1997

Signature of Author _____
Department of Chemistry
May 12, 1997

Certified by _____
Keith A. Nelson
Thesis Supervisor

Accepted by _____
Dietmar Seyferth
Chairman, Departmental Committee on Graduate Students

This doctoral thesis has been examined by a committee of the Department of Chemistry as follows:

Professor Moungi G. Bawendi _____
Chairman

Professor Keith A. Nelson _____
Thesis Supervisor

Professor Robert W. Field _____

Femtosecond Wavevector Overtone Spectroscopy of Anharmonic Lattice Dynamics in Ferroelectric Crystals

Ciaran Joseph Brennan

Submitted to the Department of Chemistry on May 12, 1997 in partial fulfillment of the requirements for the degree of Doctor of Philosophy in Chemistry

ABSTRACT

Impulse Stimulated Raman Scattering (ISRS) is a useful technique for characterizing the soft optic modes that are responsible for the polar distortion in ferroelectric crystals. ISRS provides an impulse force to the selected mode at a specific wavevector, and the subsequent oscillations and damping of the mode can be observed. Previous researchers have used this technique to measure the wavevector-dependent frequency and damping of optic phonons and phonon-polaritons in a variety of ferroelectric crystals.

The recent development of powerful amplified Ti:sapphire femtosecond lasers opens the possibility that the impulse force applied to the ferroelectric soft mode is so large that the resultant ionic excursions will sample the anharmonic portions of the potential energy surface for the soft mode. This would, in principle, allow the experimental measurement of the potential energy surface by carefully characterizing the anharmonic content of the ISRS signals. This information would give insight into the causal mechanism for the phenomenon of ferroelectricity.

Measurements of anharmonic phonon-polaritons in ferroelectric crystals have been performed using Wavevector Overtone Spectroscopy (WOS), a refinement of the impulsive stimulated Raman scattering (ISRS) technique. Numerical simulations suggest that harmonics of the polariton wavevector, rather than harmonics of the polariton frequency, are the key signatures of lattice anharmonicity in a time resolved grating experiment. The predicted

signals at the wavevector overtones were observed up to the 5th order in $LiTaO_3$, providing strong evidence of anharmonicity of the phonon-polariton response. Further evidence for anharmonicity comes from ISRS measurements at the fundamental wavevector and measurements of diffraction efficiency. The ISRS data shows non-sinusoidal response with a rich overtone spectrum, while the diffraction efficiency measurements reveal ionic displacements of about 1% of the ferroelectric distortion.

These measurements provide a confirmation of the anharmonicity in the large-amplitude phonon-polariton response created by the intense light field of the amplified femtosecond laser. It is possible to extract a potential energy surface for the phonon-polariton from the anharmonic coefficients when measured over a range of experimental wavevectors.

Thesis Supervisor: Dr. Keith A. Nelson
Title: Professor of Chemistry

Acknowledgments:

I would like to express my gratitude for my family, whose support and encouragement has been invaluable to my academic success: my parents, Drs. Joseph and Sheilah Brennan, who instilled in me a love of learning and the value of perseverance, and who have provided love and assistance from afar; my wife Kathryn, who provided endless love and support during the past five years, brought home the bacon, and bore two wonderful sons; and my parents-in-law, Ted and Mary Hatch, who provided encouragement, great holiday meals, and baby-sitting too!

I would like to thank my advisor, Keith Nelson. Keith is a model of scientific enthusiasm, optimism and creativity, and is also a genuinely nice person. I appreciate the freedom I have had to pursue science while working in Keith's group.

I greatly appreciate the financial support I have received from The Charles Stark Draper Laboratory, who underwrote my education at MIT through the Draper Fellowship program. I would like to thank my former boss and Draper Fellow sponsor Tony Marques for his support, patience and understanding.

A special mention goes to Dr. Jianping Zhou. Without his expertise in building ultrafast lasers none of my experiments would have been successful. In addition, Jianping is an exemplar of hard work, patience, politeness, price negotiation, and "The Force" - that remarkable ability to make recalcitrant lasers work.

I have been fortunate in having some wonderfully intelligent peers to discuss ideas with and to learn from. Tom Dougherty, Gary Wiederrecht, Lisa Dhar, Marc Wefers, Tim Crimmins and Richard Koehl are fellow femtosecond ferroelectric spectroscopists, and many of the ideas presented here have been developed and refined in conversations with these individuals. I have also learned things of value from all the other Nelson group members that I have worked with: Andy, Matt, Weining, Laura, John, John, Yang, Dutch, Dora,

Greg, Jun, Yasuo, Hitoshi, Alex, Tanya, Randy, Ariya, Toshi, Saturo, Yusaku, OV, and Takashi. Special thanks go to Dora Paolucci and her significant other Anand Mehta for being good friends and occasional babysitters.

Finally, I wish to recognize two of my science teachers from my school days: Patrick Miller, my high school physics teacher, and Paul Pedersen, my 8th grade chemistry teacher. I remember these gentlemen as exceptional teachers, and I think the value of good teachers cannot be overstated. I thank them for encouraging my interest in the sciences.

Dedication

To my wife Kathryn and my sons Ian and Nathaniel.

Table of Contents

Chapter 1:
Introduction

The goal of this research is to develop techniques to induce large amplitude vibrations in crystal lattices, and to learn about the shape of the potential energy surfaces related to those vibrations by observing nonlinearities in the lattice oscillations. In particular, I will be discussing the generation of phonon-polariton oscillations in ferroelectric crystals. The experimental techniques that I will present are variations of the Impulsive Stimulated Scattering (ISS) method[1-4].

1.1. Ferroelectric crystals

Ferroelectric crystals have a stable electrical polarization in the absence of an applied field. They are named in analogy to ferromagnetic materials; ferroelectrics exhibit a permanent polarization in a manner similar to the permanent magnetism of ferromagnetic materials, and they have a P-E hysteresis curve that resembles the B-H curve of ferromagnetic materials. They do not generally contain iron.

The bistable nature of the lattice polarization leads to a double well potential energy curve along the polarization axis. Figure 1.1 shows the result of an ab-initio energy calculation[5]. This is a frozen-phonon calculation at T=0. This means that the total energy is calculated for various configurations of the lattice in which all the ions are moved to specific fixed positions that

represent a stationary displacement along the normal-mode phonon coordinates.

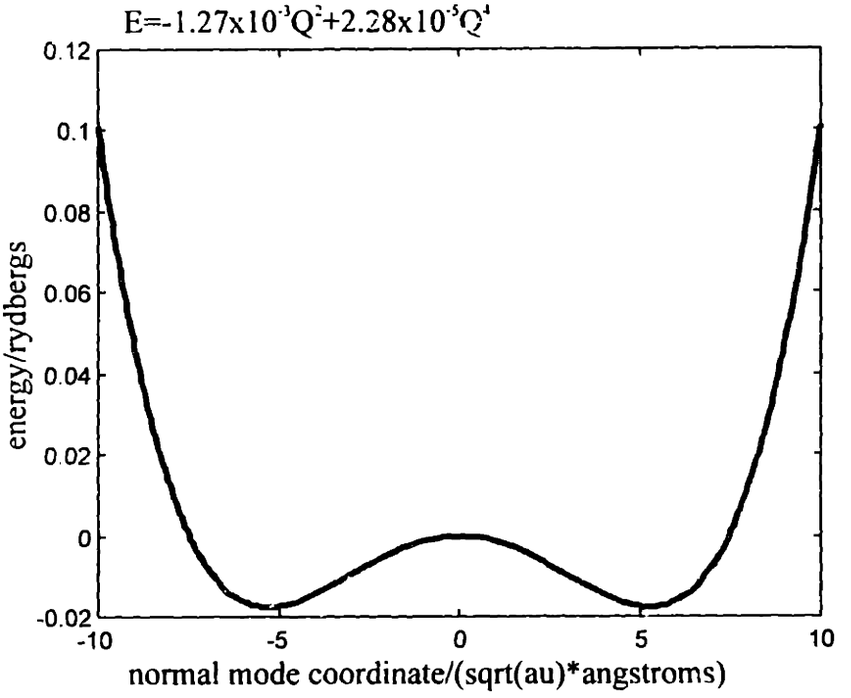

Figure 1.1 The potential energy along the soft-mode axis for $LiTaO_3$.

The polarization of most ferroelectrics is said to occur along the soft-mode coordinates. Above the Curie temperature the ferroelectric crystal becomes symmetric and loses its polarization. As the temperature is cooled towards the critical temperature, the frequency of one transverse polar optic mode (the soft mode) decreases dramatically and approaches zero. At the phase transition the crystal becomes permanently distorted along the direction of this phonon mode. Since it is a polar mode, the ferroelectric exhibits a net electric dipole as a result of the lattice distortion.

The soft mode and the potential energy surface that govern its dynamics are intrinsically linked to the basic mechanism that drives ferroelectricity. The exact mechanism for ferroelectricity is still somewhat controversial. The most recent theories come from ab-initio calculations, which show that partial covalencies between the ions in the lattice play an intrinsic role in stabilizing the ferroelectric state. The lattice experiences long-range dipole-dipole interactions which favor the polarized state, and inter-ion repulsive forces that favor the centro-symmetric state. The partial covalent interactions reduce the inter-ion repulsion in the distorted ferroelectric configuration, and thereby stabilize the long-range ordering dipole forces[6].

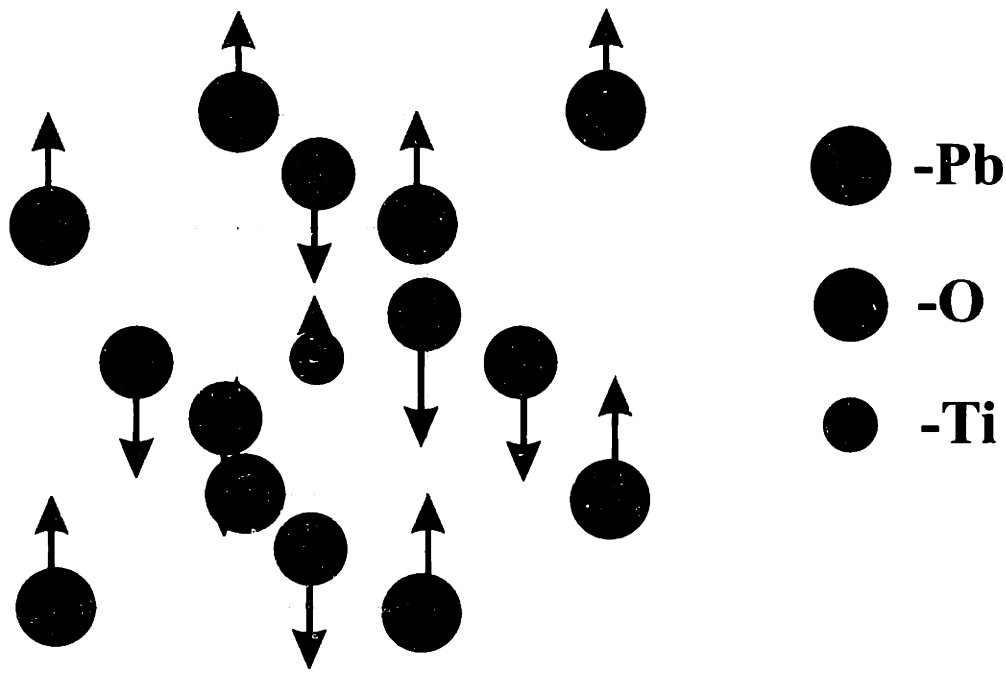

Figure 1.2 The A1 mode of lead titanate. The ferroelectric polarization is a permanent distortion along this mode. There are six degenerate directions for this mode - along both directions of the three crystal axes.

Figure 1.2 displays the ferroelectric distortion for the perovskite ferroelectric lead titanate ($PbTiO_3$). The polarization results from a net shift of the negative oxygen sublattice against the positive cation sublattices. This mode has A_1 symmetry. The partial covalencies occur between the titanium atom and the oxygen atoms along the displacement axis, which reduces the repulsive forces between the ions and allows the cations to move closer to the anions. The lead ions also are highly polarizable and interact with the surrounding oxygen atoms[7]. Note that the distortion shown is along one of 6 degenerate directions (up, down, left, right, in, out). The lattice can become polarized along any of these directions.

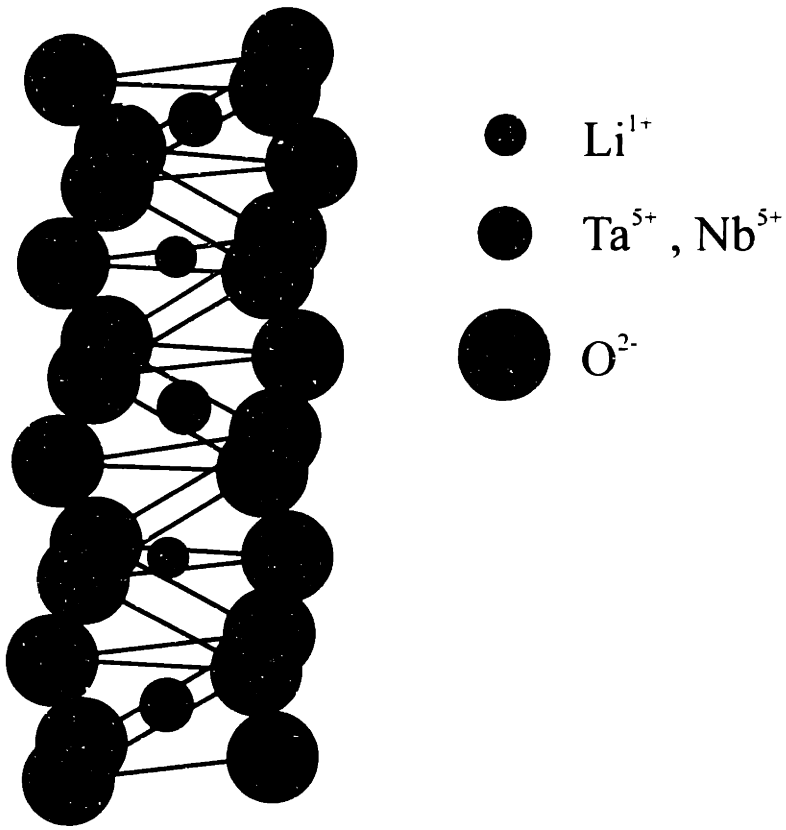

Figure 1.3 The crystal structure for lithium tantalate and lithium niobate. These crystals have a 10 atom unit cell. These are uniaxial ferroelectrics with a single polar axis.

The ferroelectric crystal used for most of the work described in this thesis is lithium tantalate ($LiTaO_3$). This material was chosen as a sample because it produces a very strong ISS signal and is readily available in high quality from commercial sources. The unit cell structure of $LiTaO_3$ is shown in Figure 1.3. It has a more complicated 10-atom unit cell compared to the 5-atom unit cell of $PbTiO_3$. The mechanism for the ferroelectric distortion for $LiTaO_3$ is similar to $PbTiO_3$[5].

1.2. The ISS experiment

The ISS experiment is a four-beam transient grating experiment. Two coherent pump pulses are overlapped in the sample. The time duration of the pump pulses is short compared to the period of the material excitation that they will create, so the light acts as an impulsive force on the material excitation. The two beams interfere with each other to produce a grating with a fringe spacing determined by the angle of intersection θ between them. As the material excitation evolves in time, it produces a time-dependent grating with the same periodicity as the pump grating. If the material excitation interacts with light in any distinctive manner, such as by modulating the index of refraction or by changing the absorption at some frequency, it can be monitored by diffracting a third beam - the probe beam - from the dynamic grating produced by the material excitation. The probe beam is introduced at the Bragg angle for the grating, so the diffracted beam is created in a phase-coherent manner. The fourth beam - the diffracted

beam - is then sent to a detector. The ISS experiment is shown schematically in Figure 1.4.

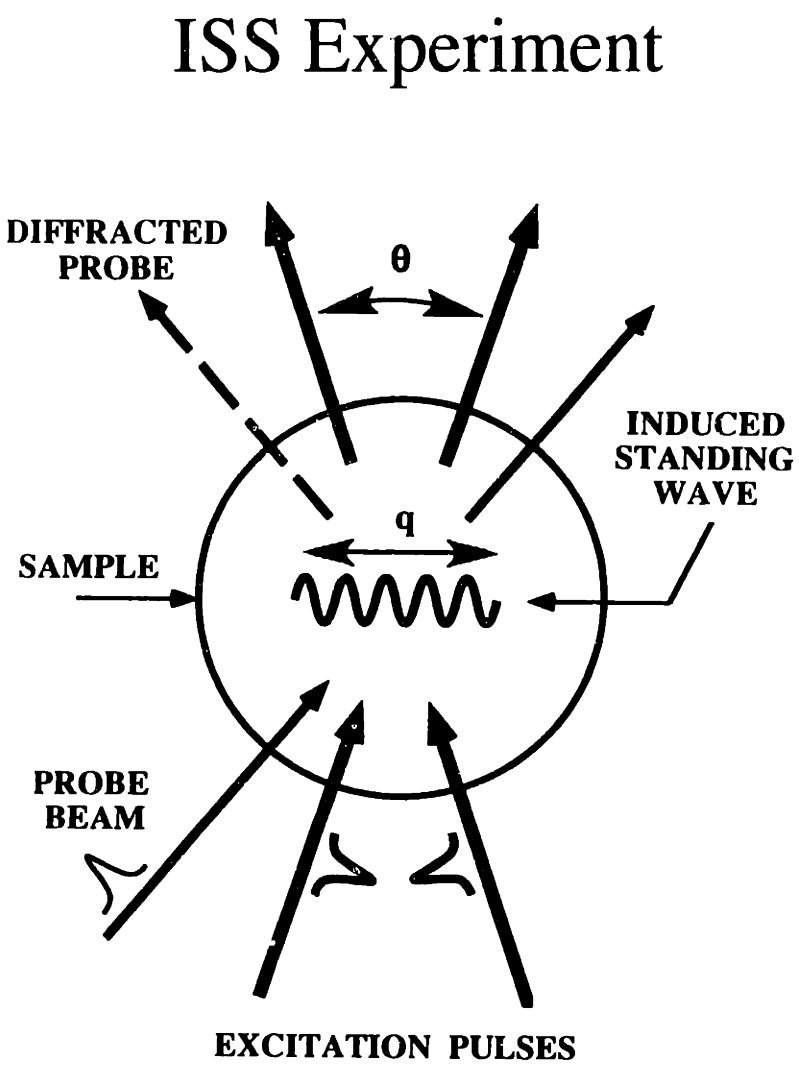

Figure 1.4 Configuration of ISS experiment. The ISS experiment is a four-beam transient grating experiment. The wavevector of the excitation is governed by the angle between the pump pulses. The signal consists of light diffracted from the grating created by the material excitation.

In the case of ferroelectric crystals, the driving force is the Impulsive Stimulated Raman Scattering (ISRS) mechanism. ISRS produces a force on

the transverse optic phonons in the material and causes them to oscillate. These phonons are the material excitations that are observed. The phonon displacements modulate the index of refraction of the crystal to produce a phase grating. The oscillations of the phonons are observed by varying the time delay between the pump and the probe pulses. Each value of the probe pulse delay samples a specific time in the material response after the pump pulses. By this method the entire impulse response of the phonon mode can be determined. Figure 1.5 shows a sample of ISRS data for $LiTaO_3$.

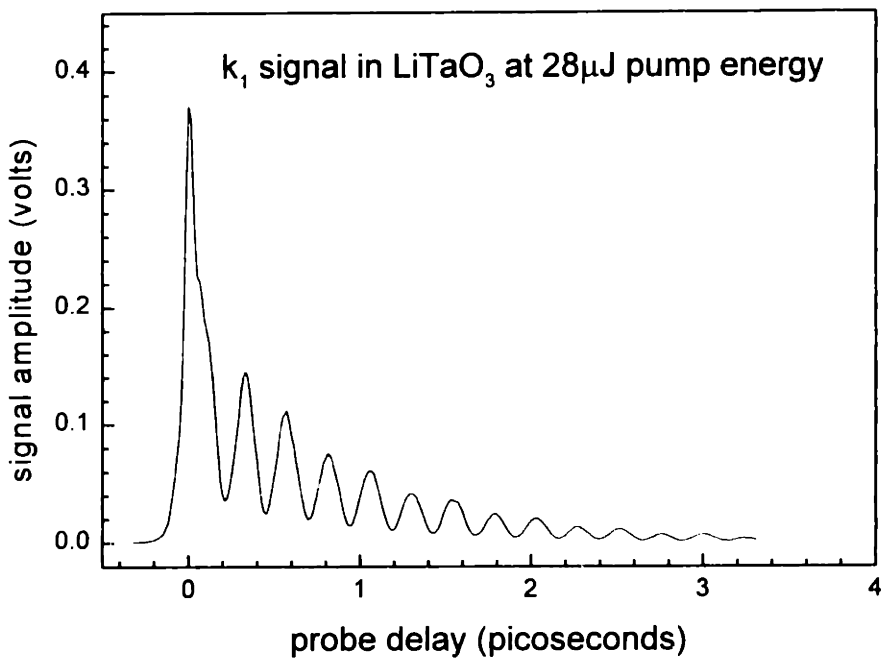

Figure 1.5 ISRS data for $LiTaO_3$ at k = 2700 cm^{-1}.

The ferroelectric crystals lack a center of symmetry in the polar state. As a result, the phonon modes that are driven by the ISRS force are also IR active. As they oscillate, they generate a far-IR electromagnetic wave in the THz (10^{12} Hz) frequency region. This E-M wave couples strongly to the phonon

mode in the region where the wavevectors and frequencies of the E-M wave and the phonon are commensurate. The coupled E-M wave/phonon response is called a phonon-polariton. Most of the ISRS data taken on ferroelectrics is in the phonon-polariton region. This region is marked by strong dispersion of the measured signal, i.e. the frequency changes strongly with the phonon wavelength. The phonon wavelength in the ISRS experiment can be controlled via the angle of intersection between the excitation beams. The experimental technique is to adjust the beam angles and to observe the frequency of the polariton that results.

1.3. Wavevector Overtone Spectroscopy

ISRS experiments in the linear regime measure only the frequency and damping of the phonon or phonon-polariton mode as a function of wavevector. The peak displacements induced by the laser are very small - on the order of 10^{-6} to 10^{-4} Å. The recently invented amplified Ti:sapphire lasers provide much greater power (1.45 μJ/pulse at 1KHz) and very short pulses (<30 fs). These improvements allow us to create displacements on the order of 10^{-2} Å. At these displacements we may be able to observe anharmonic behavior. The oscillations of a phonon mode may become anharmonic due to anharmonicity in the potential energy surface, for example. In the case of phonon-polaritons, either the ionic restoring force or the electronic polarization may change in a nonlinear manner with the lattice displacement. We would gain valuable information about the chemical

bonding and the electronic structure in the crystal lattice if we could measure such nonlinearities.

Anharmonicity in the polariton response would be expected to produce harmonics of the fundamental frequency. However, even with our improved lasers the lattice displacements we produce are still fairly small and the amount of anharmonicity in the material response is also likely to be small. The dynamic range and signal-to-noise quality of the experiment may be inadequate to measure the anharmonic components in the presence of strong fundamental signal. In addition, there is more than one type of possible nonlinearity in the material, and there is more than one way that some nonlinearities can influence the observed signal. These points suggest that the standard ISRS technique is a limited tool for characterizing lattice anharmonicity.

One of the principal ideas of this thesis is that lattice anharmonicity will also produce harmonics in the polariton wavevector, i.e. harmonics of the spatial profile of the polariton. Furthermore, these spatial harmonics or overtones can be observed by diffraction, and may provide a more sensitive and more distinctive signature of lattice anharmonicity. I call this Wavevector Overtone Spectroscopy (WOS).

The generation of spatial overtones of a phonon or phonon-polariton is illustrated in Figure 1.6. The pump beams produce a sinusoidal interference

grating, which produces a sinusoidal impulse force in the sample. The spatial distribution of the momentum in the phonon mode is initially sinusoidal. However, as the oscillation evolves on a anharmonic potential energy surface, the sine wave becomes distorted, i.e. anharmonic. The anharmonic response is a direct manifestation of the anharmonic potential. The lattice displacements modulate the index of refraction in the material through the linear electro-optic coefficient, resulting in an anharmonic diffraction grating.

The observation of the anharmonic diffraction grating using the WOS technique is depicted in Figure 1.7. The anharmonic grating consists of the fundamental wavevector plus a series of integer multiples of the grating. These are the wavevector overtones. They are observed by introducing the probe beam at the Bragg angle for the selected overtone. The probe beam will not be correctly phase matched for the fundamental or the other overtones, so the diffracted light will be due primarily to the selected overtone component of the grating. (The fundamental wavevector as well as other overtones may contribute to the signal via higher-order diffraction, which is strongly suppressed in a thick grating). The time response of the signal associated with the wavevector overtones provides a signature of the lattice anharmonicity.

One principal advantage of the WOS technique is that the strong signal at the fundamental is strongly attenuated in the overtone signals, so the experiment

will be more sensitive than the standard ISRS measurement to small nonlinearities. In addition, lattice anharmonicity in a ferroelectric can result in the generation of polaritons at frequencies other than the harmonics of the fundamental frequency. These new polaritons will have wavevectors that are overtones of the fundamental wavevector. Polaritons with these characteristics are a signature of specific types of lattice anharmonicity. Therefore the WOS technique can provide a more sensitive and more distinctive measurement of lattice anharmonicity than the standard ISRS experiment.

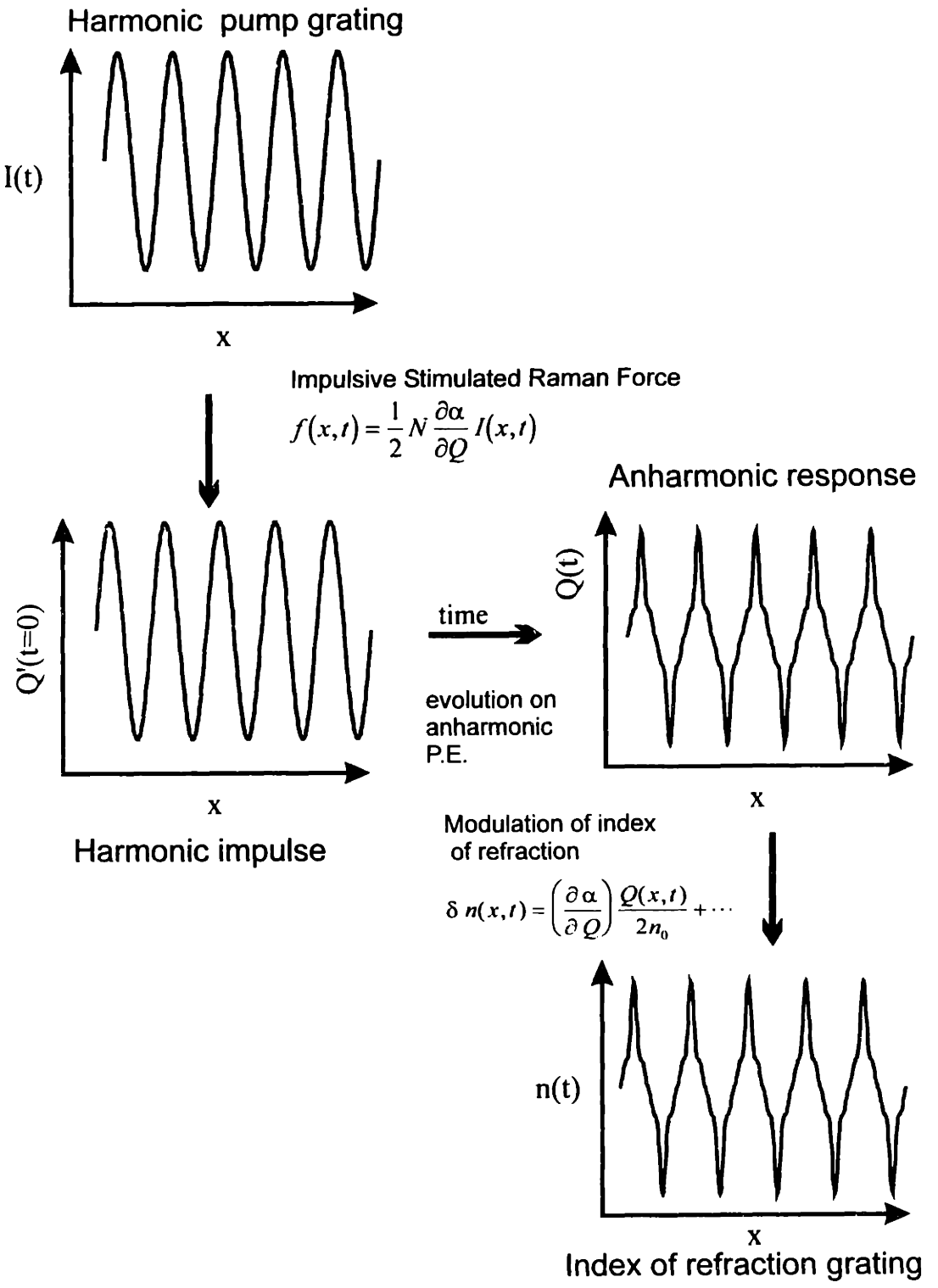

Figure 1.6 Schematic of generation of anharmonic index of refraction grating due to anharmonic lattice oscillations.

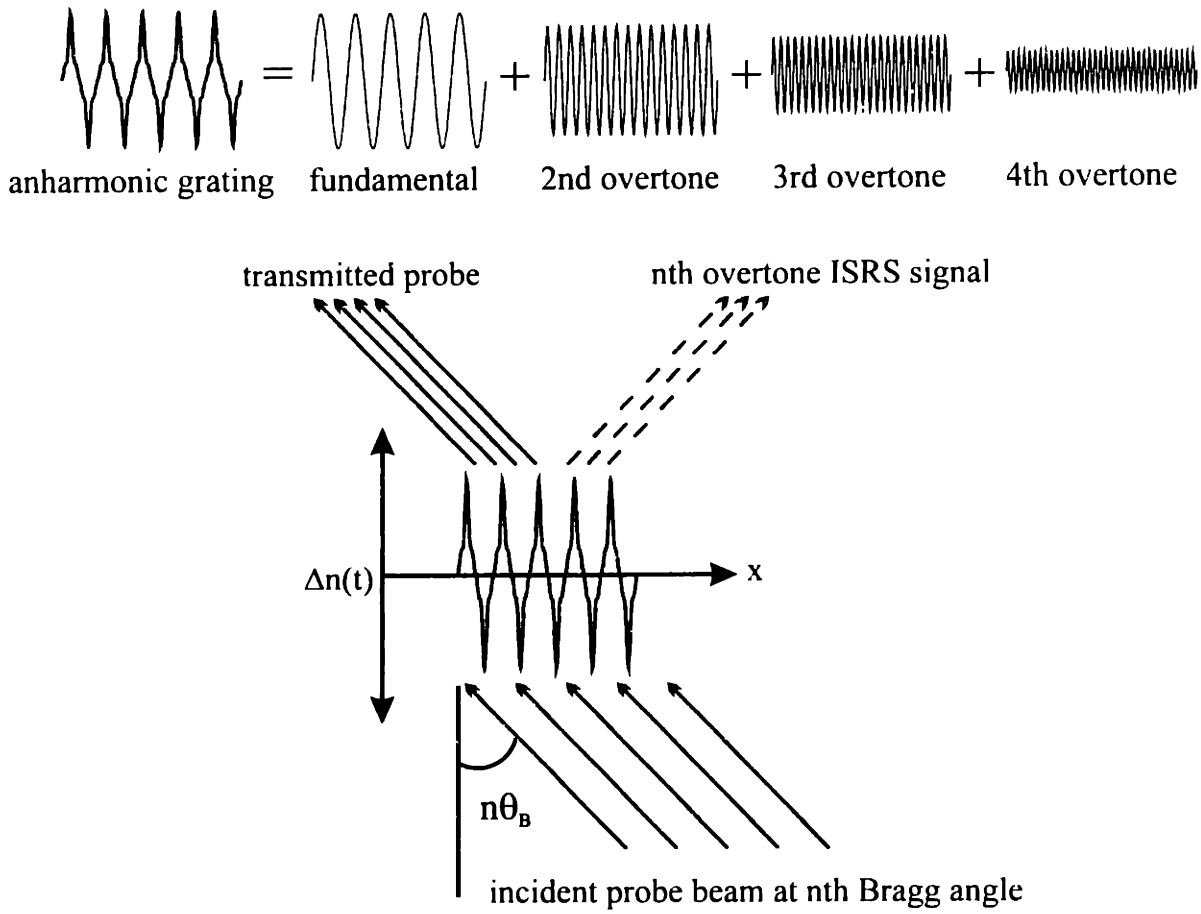

Figure 1.7 Wavevector overtone spectroscopy (WOS) is performed by diffracting the probe light from the spatial overtones resulting from anharmonicity of the material excitation grating.

1.4. References

1. Yan, Y.-X., J. Edward B. Gamble, and K.A. Nelson, *Impulsive stimulated scattering: General importance in femtosecond laser pulse interactions with matter, and spectroscopic applications.* J. Chem. Phys., 1985. **83**(11): p. 5391-5399.
2. Yan, Y.-X. and K.A. Nelson. *Impulsive stimulated Raman, Brillouin, and Rayleigh scattering: Comprehensive theory and comparison between time-domain and frequency-domain light scattering spectroscopies.* in *International Conference on Lasers '86.* 1986: STS Press, McClean.

3. Yan, Y.-x. and K.A. Nelson, *Impulsive stimulated light scattering. I. General theory.* J. Chem. Phys., 1987. **87**(11): p. 6240-6256.
4. Yan, Y.-x. and K.A. Nelson, *Impulsive stimulated light scattering. II. Comparison to frequency-domain light-scattering spectroscopy.* J. Chem. Phys., 1987. **87**(11): p. 6257-6265.
5. Inbar, I. and R.E. Cohen, *Comparison of the electronic structures and energetics of ferroelectric LiNbO/sub 3/ and LiTaO/sub 3/.* Phys. Rev. B, 1996. **53**(3): p. 1193-1204.
6. Cohen, R.E., *Origin of ferroelectricity in perovskite oxides.* Nature, 1992. **358**: p. 136-138.
7. Cohen, R.E. and H. Krakauer, *Electronic Structure Studies of the Differences in Behavior of BaTiOsub 3 and PbTiOsub 3.* Ferroelectrics, 1992. **136**: p. 65-84.

Chapter 2:
Theory of Phonon-Polaritons Generated by ISRS

2.1. Introduction

The basic physical theory of phonon-polaritons in ferroelectrics has been understood for many years [1,2]. More recently, the generation and measurement of polaritons in femtosecond transient grating experiments has been studied by members of the Nelson research group, as well as by other researchers around the world [3-12]. However, I found that the theoretical understanding of polaritons in ISRS experiments was incomplete, and some of what had been published was incorrect. I have worked to provide a more complete theoretical description of the ISRS polariton experiment in the linear regime, and have worked in particular on the following issues:

1. The ISRS driving force has been considered a distinct phenomenon from the second-order optical nonlinearity in ferroelectrics, and previous authors have differed over which one is the principal driving force of polaritons in ferroelectrics in a transient grating experiment. I show that the ISRS phenomenon is not distinct from the second-order optical nonlinearity in ferroelectrics. In fact the Raman susceptibility is a significant component of the second order optical nonlinearity, and is the dominant driving force for the polariton in many ferroelectrics.
2. The wavevector of the polariton has been assumed to be equal to the wavevector of the grating. I show that the wavevector of the polariton is often substantially different from that of the grating, and derive the

relationship between the two from a conservation argument. This has important consequences for the correct interpretation of experimental data.

3. I derive the phase matching condition between the polariton response and the transient grating to show that the polariton response is coherent and phase matched to the grating.
4. As a consequence of the previous points, I show that a substantial portion of the upper branch of the polariton cannot be observed by a transient grating experiment. The regions that can be observed will have marked differences between the wavevectors of the grating and the polariton.
5. The Raman differential polarizability can be derived from diffraction efficiency measurements in a transient grating experiment. However, there are certain errors in the existing formulas for calculating the differential polarizability from phonon grating diffraction measurements. In addition, the derivation of the differential polarizability for the phonon-polariton grating had not been addressed. I derive a new expression for the differential polarizability for both the phonon and phonon-polariton cases.
6. A detailed treatment of high-order diffraction from a phase grating requires the use of coupled-wave theory. I present a simple extension of this theory to treat diffraction from a grating with spatial harmonics.

I have worked to clarify and correct some of these theoretical issues. A correct theoretical description of these points is necessary to design an

experiment to produce large-amplitude ionic motion and to interpret the data. This chapter contains a summary of the theory of ferroelectric polaritons, with particular attention paid to those issues that I have worked on.

2.2. The transient grating

This section discusses the characteristics of the interference grating produced by the two pump beams.

2.2.1 Scaling pump pulses

The first thing to do is to convert the input spatial dimensions and time duration given in full-width half-maximum (FWHM) values and convert them to a Gaussian form. We assume that the intensity profile is Gaussian, i.e. $I(x) \propto \exp\left[-x^2/\sigma^2\right]$. We find the Gaussian width parameter σ from the FWHM value:

$$\sigma = \frac{FWHM}{2\sqrt{-\log(1/2)}} = 0.60 * FWHM \tag{2.1}$$

Properly normalized, the pulse is written as

$$I(x,z,t) = I_0 \pi^{-\frac{3}{2}} \frac{1}{\sigma_x \sigma_z \sigma_t} e^{-\left(\frac{x-x_0}{\sigma_x}\right)^2} e^{-\left(\frac{z-z_0}{\sigma_z}\right)^2} e^{-\left(\frac{t-t_0}{\sigma_t}\right)^2} \tag{2.2}$$

σ_x, σ_z and σ_t are the Gaussian parameters for the horizontal, vertical and temporal dimensions of the pulse, calculated from Eq. (2.1), and x_0, z_0, and t_0 are the center values of the Gaussians. The y direction is along the direction

of travel - the depth - and the profile in this direction can be specified either by σ_y or σ_t.

The electric field strength can be calculated from the intensity using the following relation[13]:

$$E(x,y,t) = \sqrt{\frac{I(x,y,t)}{n\epsilon_0 c}} \tag{2.3}$$

where n is the index of refraction in the material, ϵ_0 is the permittivity of free space, and c is the speed of light in the vacuum. Since all the beams are vertically polarized in this work I am not using tensors to describe the fields and intensities of the beams.

2.2.2 Propagation of pump pulses

I assume that the two pump beams are perfectly overlapped at the face of the crystal. The pump beams define the grating in the horizontal direction. The force exerted by the pump beams on phonon normal mode displacement Q at any point specified by (x,y,t) is found by determining the intensity of each beam at that point based on its spatial and temporal profile, calculating the interference between the two beams based on the specified grating wavevector k_g, then calculating the ISRS force. I_1 is the beam traveling from left to right, while I_2 travels right to left. The beams are at angles of $\pm\theta/2$ with respect to the bisector and travel at speed $c' = c/\sqrt{\varepsilon_\infty}$. The intensity of the two beams is:

$$I_1(x,y,t) = I_0 \exp\left[-\left(\frac{x - x_0 - y\tan\frac{\theta}{2}}{\sigma_x}\right)^2\right]\exp\left[-\left(\frac{t - t_0 - \frac{1}{c'}\left(y\cos\frac{\theta}{2} + (x - x_0)\sin\frac{\theta}{2}\right)}{\sigma_t}\right)^2\right] \quad (2.4)$$

$$I_2(x,y,t) = I_0 \exp\left[-\left(\frac{x - x_0 + y\tan\frac{\theta}{2}}{\sigma_x}\right)^2\right]\exp\left[-\left(\frac{t - t_0 - \frac{1}{c'}\left(y\cos\frac{\theta}{2} - (x - x_0)\sin\frac{\theta}{2}\right)}{\sigma_t}\right)^2\right] \quad (2.5)$$

Eqns. (2.4) and (2.5) give the intensity at any given point $\{x, y, t\}$ based on the propagation of the Gaussian pump pulse. The center of the pulse is incident on the front face of the crystal at $\{x = x_0, y = 0, t = t_0\}$. (The front of the crystal corresponds to y=0). Since most of the calculations are done in the plane of incidence, we can ignore the profile in the z direction and simply treat the pulse as a 2-D object that has been integrated over the z direction.

2.2.3 The interference grating

The intensity at each point resulting from the interference of the two beams is given by:

$$I(x,y,t) = I_1(x,y,t) + I_2(x,y,t) + 2\cos\left(k_g(x - x_0)\right)\sqrt{I_1(x,y,t)I_2(x,y,t)} \quad (2.6)$$

k_g is the wavevector of the grating. Figure 2.1 shows a plot of the intensity plotted along the x-axis.

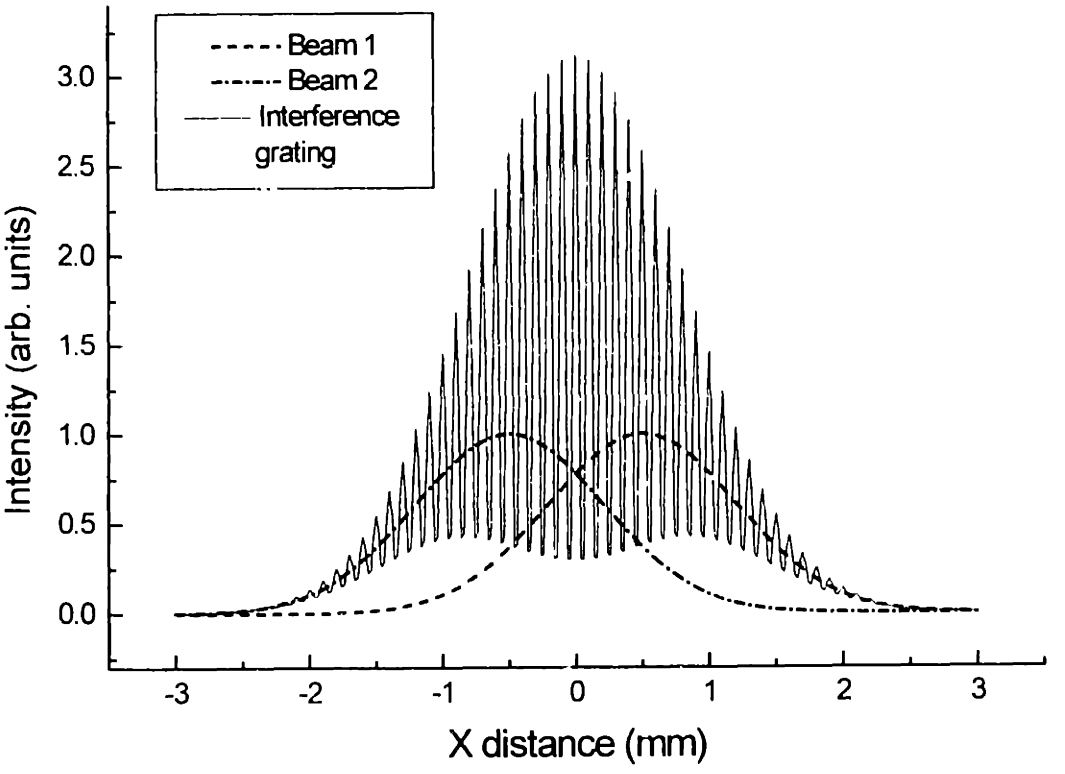

Figure 2.1 The interference grating created between two beams of Gaussian spatial profile. The centers of the two beams are offset by ±0.5 mm. This leads to incomplete constructive and destructive interference of the two beams and a non-Gaussian profile for the interference grating peak-to-peak amplitude.

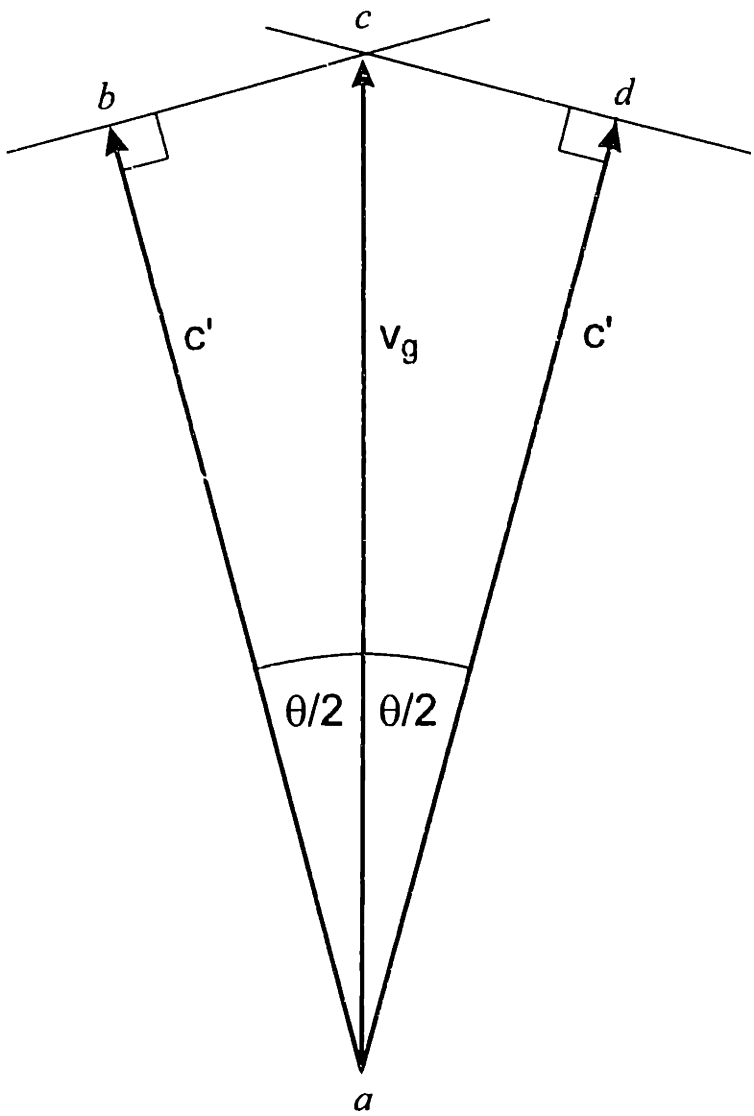

Figure 2.2 Vector diagram to calculate the phase velocity of the interference grating in the material. The phase velocity v_g is greater than the speed of light in the material c'.

2.2.4 The forward phase velocity of the grating

The phase velocity of the grating is represented in Figure 2.2. Line segments $\overline{bc}$ and $\overline{dc}$ represent the phase fronts of the two forward moving pump beams. The group velocity of the pump beams equals the speed of light in the sample c', as represented by vectors $\overline{ab}$ and $\overline{ad}$. The grating formed

from the intersection of these two phase fronts has phase velocity v_g given by vector $\overline{ac}$:

$$v_g = \frac{c'}{\cos(\theta/2)} \tag{2.7}$$

The phase velocity of the grating is always greater than the speed of light in the material.

2.2.5 Limitations on wavevector selectivity

The pump pulses have a duration of a few tens of femtoseconds. This means that their spatial depth in the forward direction may be 10 microns or less in the sample. The pulses have been described as "pancakes", much wider in the horizontal direction than in depth. As a result, the spatial overlap of the two pump beams is often limited by the pulse duration rather than how tightly the beams are focused in the horizontal direction. The overlap of the two beams is shown in Figure 2.3. From the geometry we can deduce the following relation for the number of interference fringes n_f we may expect to produce:

$$n_f = \frac{w \cdot k_g}{2\pi} = \frac{2L}{\lambda} = \frac{2\tau c'}{\lambda} \tag{2.8}$$

where λ is the pump beam wavelength, τ is the pulse duration, L is the spatial depth of the pulse, and w is the width of the overlap region.

For 30 fs pulses of 800 nm light in $LiTaO_3$, which has an index of refraction of 2.3, we will get a grating with about 22 fringes. This places a limit on the selectivity of the grating in wavevector space. To estimate the linewidth of the excitation grating in k-space, we can consider a wave with wavelength λ_g such that $\left(n_f \pm 1/2\right)\lambda_g = w$, that is, you can fit n_f plus or minus a half wavelength into the grating overlap region. If this wave is in phase with the grating on the left side, it will be exactly out of phase at the right side. Therefore the interaction of the wave with the grating on the left side will be fully canceled by the right side. The FWHM linewidth of the grating should be given by approximately half this amount of phase shift, i.e. a quarter wave: $\lambda_{g\pm} = w/\left(n_f \pm 1/4\right)$. From this we can derive the range of wavevectors in this linewidth:

$$\frac{\Delta k_g}{k_g} \approx \pm \frac{\lambda}{4\tau c'} \tag{2.9}$$

For the example above, this gives a FWHM uncertainty of about 5% to the determination of the grating wavevector. This makes sense, because if we have N fringes in the grating, we expect a range of wavevectors of 1/N, which is consistent with Eqs. (2.8) and (2.9). Clearly we no longer have extremely precise control of the wavevector with pulses this short.

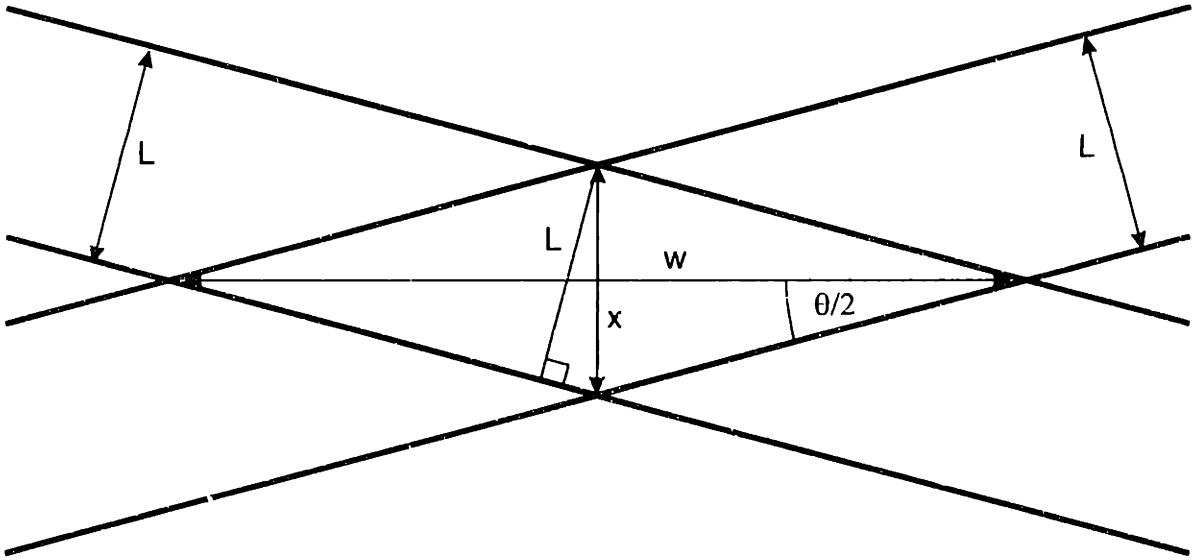

Figure 2.3 Diagram for calculating the number of interference fringes that will be produced by the overlap of two pump beams with length in the direction of travel of L.

2.3. The ISRS driving force

There has been some disagreement in the literature on impulsive time-resolved studies of polaritons in ferroelectrics on the nature of the impulsive driving force. The phenomena that have been discussed as the driving forces include non-linear frequency mixing[4], optical rectification[14], inverse electro-optic effect[15], and impulsive stimulated Raman scattering (ISRS)[6, 7, 16]. I show that ISRS is a $\chi^{(2)}$ process when regarded solely as a polariton driving mechanism. Furthermore, using a standard classical nonlinear optic model I show that the ISRS mechanism is in fact identical to the $\chi^{(2)}$ term that has been identified as the dominant source of optical rectification and nonlinear mixing in ferroelectrics.

2.3.1 The nature of the driving force in ferroelectrics

The phenomena that have been discussed as the driving forces for phonon-polaritons in ferroelectrics include non-linear frequency mixing, optical rectification, inverse electro-optic effect, and impulsive stimulated Raman scattering (ISRS). The first three mechanisms are due to $\chi^{(2)}$ nonlinearities, and sometimes have been regarded as fundamentally different in nature from ISRS, a $\chi^{(3)}$ process. In fact, when ISRS is considered only as a polariton driving mechanism it can be regarded as a $\chi^{(2)}$ process. (The complete ISRS process including light scattering from the polariton is a $\chi^{(3)}$ process because the polariton produces the light scattering via the first order polarizability). ISRS is actually one component of the generalized nonlinear optic response, which includes both electronic and ionic terms. We see below that the ISRS polariton driving mechanism is readily derived from a standard classical second order non-linear optic model. Furthermore, it is in fact identical to the optical rectification term identified by Kaminow and Johnston[17], and Auston and Nuss[14] as the dominant polariton generation mechanism in $LiTaO_3$ and similar materials.

I believe that the controversy is due to confused terminology. In many materials $\chi^{(2)}$ nonlinearities arise from purely electronic nonlinearities which may be strong even if the Raman cross sections are small. Some authors appear to refer to only the electronic effects when discussing nonlinear mixing or inverse electro-optic effect. However, the general

nonlinear optic model includes a term involving purely electronic susceptibility, another term involving purely ionic susceptibility, and several terms that couple electronic and ionic susceptibilities. In the ferroelectric crystals the dominant $\chi^{(2)}$ term combines the second order electronic susceptibility with the first order ionic susceptibility. Therefore, $\chi^{(2)}$ mechanisms in ferroelectric materials must be understood to involve substantial ionic contributions and are not purely electronic effects. In addition, the ISRS driving mechanism should be referred to with the understanding that it is one component of the generalized nonlinear optic model and is in fact identical with one of the $\chi^{(2)}$ terms. In this viewpoint ISRS and the various $\chi^{(2)}$ mechanisms are all adequately described in the generalized nonlinear optic model.

2.3.2 The general nonlinear optic model

The following nonlinear optic model is taken from Auston and Nuss, who use it to describe the electro-optic generation of polaritons through optical rectification. It follows the original treatment of Raman scattering from polariton modes by Barker and Loudon[2]. We show that the differential polarizability that is the key element of ISRS can be simply derived from this model. The ISRS force is also obtained directly from the model by taking the derivative of the energy of the electric field.

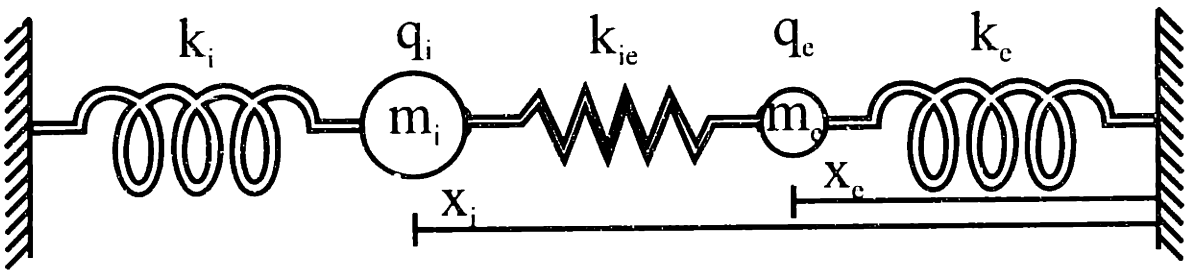

Figure 2.4 Ball and spring model for the general nonlinear optic model. The nonlinear spring k_{ie} couples the ionic and electronic oscillators.

The model consists of two ball and spring harmonic oscillators coupled by a nonlinear spring, as shown in Figure 2.4. The equations for this motion for this system are:

$$m_i\ddot{x}_i + k_i x_i = k_{ie}(x_i - x_e)^2 + q_i E \tag{2.10}$$

$$m_e\ddot{x}_e + k_e x_e = k_{ie}(x_i - x_e)^2 + q_e E \tag{2.11}$$

m is the mass, k is the spring constant, x is the displacement, q is the charge, E is the electric field, and the subscripts i and e denote the ionic and electronic subsystems. k_{ie} is the nonlinear force constant. These equations can be expressed in terms of macroscopic quantities using the following relations:

$$P_e = \epsilon_0 \chi_e E = N q_e x_e \tag{2.12}$$

$$P_i = \epsilon_0 \chi_i E = N q_i x_i \tag{2.13}$$

$$\omega_i = \left\{\frac{k_i}{m_i}\right\}^{1/2}; \quad \omega_e = \left\{\frac{k_e}{m_e}\right\}^{1/2} \tag{2.14}$$

$$\chi_i^s = \frac{Nq_i^2}{\epsilon_0 k_i}; \quad \chi_e^s = \frac{Nq_e^2}{\epsilon_0 k_e} \tag{2.15}$$

$$\chi_{iee}^s = \frac{Nk_{ie}q_i q_e^2}{\epsilon_0 k_i k_e^2}; \quad \text{etc.} \tag{2.16}$$

where P_i and P_e are the ionic and electronic contributions to the macroscopic polarization, χ_i^s, χ_e^s, and χ_{iee}^s are the static ($\omega = 0$) linear and nonlinear susceptibilities due to ionic and electronic effects, and N is the density of oscillators per unit volume. Using these relations the equations of motion can be written:

$$\ddot{P}_i + \omega_i^2 P_i = \omega_i^2 \epsilon_0 \left\{ \chi_i^s E + \frac{\chi_{iee}^s P_e^2}{\epsilon_0^2 \left[\chi_e^s\right]^2} + \ldots \right\} \tag{2.17}$$

$$\ddot{P}_e + \omega_e^2 P_e = \omega_e^2 \epsilon_0 \left\{ \chi_e^s E + \frac{\chi_{eee}^s P_e^2}{\epsilon_0^2 \left[\chi_e^s\right]^2} + \ldots \right\} \tag{2.18}$$

Auston and Nuss include a total of six of the χ_{xxx} terms covering all combinations of electronic and ionic susceptibilities. Only the two terms important for polariton generation are included here. The χ_{iee} term couples the second order in the electronic polarization to the ionic motion. Auston and Nuss state that this is the primary source of optical rectification. We will see that this term is equivalent to the ISRS driving force. The χ_{eee} term is a purely electronic term coupling the second order electronic polarization to the electronic oscillator. This term produces nonlinear frequency mixing and

also contributes to optical rectification, though in $LiTaO_3$ it is an order of magnitude smaller than the χ_{iee} component[17]. It is the χ_{eee} term that is generally associated with $\chi^{(2)}$ nonlinearities.

2.3.2.1 Derivation of differential polarizability

The differential polarizability, i.e. the derivative of the polarizability with respect to the ionic displacement, is the source of the stimulated Raman scattering process. Modes with nonzero differential polarizability coefficients are Raman active. We can derive the differential polarizability, and hence the ISRS driving mechanism, from the nonlinear optic model.

We start from the equation of motion for the electronic system (Eq. (2.11)). In a nonresonant Raman process, the frequency ω is far below the electronic resonance frequency ω_e. In this case, $m_e\ddot{x}_e << -k_e x_e$, and we can ignore the $m_e\ddot{x}_e$ term. This is because $m_e\ddot{x}_e = -m_e\omega^2 x_e << -m_e\omega_e^2 x_e = -k_e x_e$ for a periodic solution to the oscillator equation. We then solve for x_e in terms of x_i and E.

$$x_e = \frac{k_e + 2k_{ie}x_i \pm \sqrt{k_e^2 - 4Ek_{ie}q + 4k_e k_{ie}x_i}}{2k_{ie}} \tag{2.19}$$

The negative root in the above equation corresponds to the correct physical result. The electronic polarization is related to the electronic polarizability α by the following:

$$P_e = Nq_e x_e = \epsilon_0 N\alpha E \tag{2.20}$$

From Eqs. (2.20) and (2.19) we derive an expression for α:

$$\alpha = \frac{q_e}{\epsilon_0}\frac{\partial x_e}{\partial E} = \frac{-2k_e k_{ie} q_e^2}{\epsilon_0\left(k_e^2 - 4Ek_{ie}q + 4k_e k_{ie}x_i\right)^{3/2}} \tag{2.21}$$

The differential polarizability, i.e. the rate of change of the *electronic* polarizability with respect to the *ionic* displacement, is found by taking the derivative with respect to x_i:

$$\left.\frac{\partial\alpha}{\partial x_i}\right|_{x_i=0} = \frac{-2k_e k_{ie} q_e^2}{\epsilon_0\left(k_e^2 - 4Ek_{ie}q\right)^{3/2}} \approx \frac{-2k_{ie}q_e^2}{\epsilon_0 k_e^2} \tag{2.22}$$

where the approximation in the denominator holds for small values of nonlinearity. One may view the effective spring constant of the nonlinear coupling term to be $k_{ie}(x_i - x_e)$. The ionic displacement changes the effective spring constant on the electronic oscillator and thus modulates the electronic polarizability.

The ISRS driving force can be found using the standard classical expression:

$$F_{ISRS} = \frac{1}{2}\epsilon_0\frac{\partial\alpha}{\partial x_i}E^2 \approx \frac{-k_{ie}q_e^2}{k_e^2}E^2 \tag{2.23}$$

This proves that the nonlinear optic model includes the ISRS force as one of several possible responses. We can show that the ISRS force is equivalent to the optical rectification and frequency mixing driving mechanism derived by Auston and Nuss from this same model by relating the Raman differential

polarizability to the second order optical nonlinearity χ_{iee}. Using Eqs. (2.22) and (2.16) χ_{iee} can be expressed in terms of $\partial\alpha/\partial x$:

$$\chi_{iee} = -\frac{Nq_i}{2k_i}\frac{\partial\alpha}{\partial x_i} \tag{2.24}$$

This shows that the optical rectification effect discussed by Auston and Nuss is related to the ISRS force by a constant.

2.3.2.2 Derivation of ISRS

Stimulated Raman scattering is derived in a classical model directly from the energy in the electric field[18]. We use this method to derive the ISRS force from the nonlinear optic model, and show that it is equal to the force calculated using the differential polarizability. This confirms that the differential polarizability calculated above yields the correct ISRS driving force.

The energy in the electric field is:

$$W = \tfrac{1}{2}DE = \tfrac{1}{2}\left(\epsilon_0 E^2 + N(q_i x_i + q_e x_e)E\right) \tag{2.25}$$

W is the energy of the electric field and D is the electric displacement. We can ignore the x_i term in the energy because we are only interested in the optical frequency to which the ions are too massive to respond, so $x_i \sim 0$. We find the force by taking the derivative of the energy with respect to the low frequency ionic displacement:

$$F_{ISRS} = -\frac{1}{N}\frac{\partial W}{\partial x_i}\bigg|_{x_i=0} = -\frac{1}{2}q_e E\frac{\partial x_e}{\partial x_i}\bigg|_{x_i=0} \tag{2.26}$$

Substituting the expression for $x_e(x_i, E)$ in Eq (2.19) and taking the derivative, we get:

$$F_{ISRS} = -\frac{1}{2}q_e E\left[1 + \frac{k_e}{\sqrt{k_e - 4Ek_{ie}q}}\right] \tag{2.27}$$

We expand this expression in a Taylor series and retain the E^2 term, which is the ISRS driving force:

$$F_{ISRS} \approx -\frac{1}{2}q_e E\left[\frac{2k_{ie}q_e E}{k_e^2}\right] = \frac{-k_{ie}q_e^2}{k_e^2}E^2 \tag{2.28}$$

This expression is identical to the one derived in Eq (2.23) by computing the differential polarizability.

2.3.2.3 Deriving the differential polarizability from the electro-optic coefficient

The nonlinear susceptibility χ_{iee} can be related to the electro-optic coefficient r_{33} in the following manner[14]:

$$\chi_{iee} \approx -\frac{1}{4}\varepsilon_\infty^2 r_{33} \tag{2.29}$$

which is valid where the experimental evidence shows that for LiTaO3 and LiNbO3 that the purely electronic contributions are small[17]. Using Eqs. (2.22) and (2.16) χ_{iee} can be expressed in terms of $\partial\alpha/\partial x$:

$$\chi_{iee} = -\frac{Nq_i}{2k_i}\frac{\partial \alpha}{\partial x_i} \tag{2.30}$$

Therefore $\partial\alpha/\partial Q$ can be expressed in terms of r_{33}:

$$\frac{\partial \alpha}{\partial x_i} = \frac{k_i \varepsilon_\infty^2}{2Nq_i} r_{33} \tag{2.31}$$

This shows once again that the ISRS mechanism is the dominant nonlinear electro-optic effect in these materials.

2.3.3 Discussion of ISRS vs. electro-optic nonlinearity

As mentioned above, the literature on impulsive generation of polaritons in ferroelectrics contains confusion over the relationship between the second-order electro-optic nonlinearity and the ISRS impulsive driving force. We have shown above that ISRS force is one component of the general second-order nonlinear optic model.

2.3.3.1 ISRS as a chi(2) process

We must clarify our description of the ISRS polariton driving mechanism as a $\chi^{(2)}$ process. In its entirety, an ISRS light scattering experiment is a $\chi^{(3)}$ process. This involves the generation of the material response by the pump beams, and the subsequent scattering of a variably delayed probe beam from the material excitation. The total polarization in the ferroelectric created by impulsively driving the phonon displacement x is written as:

$$P_{tot} = \epsilon_0 \chi_e E + Nq_i x_i + \epsilon_0 N x_i \frac{\partial \alpha}{\partial x} E_3 \tag{2.32}$$

The first term involves the $\chi^{(1)}$ susceptibility, the second term involves the $\chi^{(2)}$ susceptibility through the generation of the phonon response x_i by the pump beams, and the third term introduces a $\chi^{(3)}$ susceptibility through the term $x_i \cdot \partial\alpha/\partial x_i$ which is acted upon by a third order in the electric field. It is this third term which produces the scattering of the probe pulse in a time-resolved transient grating experiment; the phonon displacement x_i modulates the permittivity through $\partial\alpha/\partial x_i$ and scatters the probe beam E_3.

The key point is that a Raman scattering process always involves a $\chi^{(3)}$ term, but in ferroelectric crystals it also involves a large $\chi^{(2)}$ term that dominates the excitation of the polaritons. A non-centrosymmetric ferroelectric crystal differs from a centrosymmetric crystal in that the Raman force produces a polarization directly by driving a polar mode, whereas this cannot happen in a centrosymmetric crystal. In a ferroelectric crystal the polar transverse optic modes driven by ISRS are both Raman and IR active. The displacement x_i contributes directly to the polarization via the second term, and indirectly vs. the third term in Eq. (2.32). In a centrosymmetric crystal, on the other hand, the Raman active modes cannot be IR active by symmetry considerations. Any x_i driven by a Raman effect is nonpolar and can not contribute to the polarization P_{tot}. The polarization produced by the Raman scattering results solely from the third term in Eq. (2.32) and is purely $\chi^{(3)}$. Therefore the polarization produced by the Raman scattering in

ferroelectrics is $\chi^{(2)}$ in terms of polariton generation and $\chi^{(3)}$ in terms of light scattering.

An additional distinction that should be made is that the second-order polarization in a ferroelectric crystal due to IR activity is at the THz polariton frequencies, not the much higher frequencies of the laser light. The scattering of the optical light is accomplished by the third-order polarization term, so the complete optical experiment is third-order in the polarization. However, the experiment would be a second-order experiment if the THz radiation were observed directly, which could be accomplished using photo-conductive antennas[19] or some other means.

2.3.3.2 Discussion of previous results

Dougherty et. al.[6] contrast the ISRS mechanism with the inverse electro-optic effect. They identify the inverse electro-optic effect with the purely electronic nonlinearity by which far-IR radiation is generated through mixing among the frequency components of the excitation pulses. This would correspond to the χ_{eee} term in Auston's notation. Dougherty et. al. assume that the polaritons in the Auston experiment are generated by this electronic nonlinearity. However, Auston and Nuss claim that χ_{iee}, not χ_{eee}, is the nonlinearity that dominates the driving force. We have shown that this is the same as the ISRS mechanism. Dougherty and Auston are actually in agreement as to the nature of the polariton driving mechanism; the disparity seems to be limited to confusion over the terminology.

Bakker et. al.[4, 20] state that excitation via ISRS is of minor importance in $LiTaO_3$ because the $\chi^{(2)}$ nonlinearity is large. However, we have shown that the relevant $\chi^{(2)}$ component is in fact identical to the ISRS driving process that produces the material excitation. Bakker et. al. do not recognize that the impulsive driving mechanism in ISRS is equivalent to the dominant $\chi^{(2)}$ nonlinearity in $LiTaO_3$ and similar ferroelectrics.

Etchepare et. al.[7] correctly attribute polariton generation in ferroelectrics to Raman activity. However, in another paper from the Etchepare group, Kien et. al[9]. assert that in the generation of a polariton the third order Raman susceptibility drives the phonon part, while the second order electronic polarizability drives the photon part via the electro-optic effect. This is not necessary, as the coupled equations of motion for the polariton may be effectively driven by either mechanism alone. In fact, the Raman and the electro-optic driving mechanisms differ in phase and may cancel each other under certain conditions[16].

An important early paper by Kaminow and Johnston[17] clearly shows that the Raman effect dominates the purely electronic response in the electro-optic response of $LiNbO_3$ and $LiTaO_3$. In addition, values are given for the Raman scattering efficiency, infrared oscillator strength, mode frequencies and linewidths of all the transverse and longitudinal optic modes. While this

paper does not deal directly with phonon-polaritons, its central relevance to this discussion is obvious.

2.3.4 Conclusions on the ISRS mechanism

I have demonstrated that ISRS may be considered a $\chi^{(2)}$ process for the generation of phonon-polaritons in ferroelectric crystals. Furthermore, ISRS is the dominant $\chi^{(2)}$ process in many ferroelectrics. I have shown that the various $\chi^{(2)}$ processes such as optical rectification and nonlinear frequency mixing that have been named as the driving mechanism for phonon-polaritons are in fact identical to the ISRS process. This insight should help resolve the apparent contradictions in the literature concerning the nature of phonon-polariton generation by ultrashort optical pulses.

2.4. Polariton equations of motion

I confine the discussion in this section to uniaxial ferroelectrics in which the polar phonon displacements **Q** (in general a vector quantity representing displacements along different lattice directions) and the electric polarization and electric field **P** and **E**, respectively, are parallel to the polar axis and can be treated hereafter as scalars. In addition I restrict the analysis to the transverse optic phonon mode whose natural frequency is ω_T.

2.4.1 Normal mode coordinates

The normal mode coordinate is related to the reduced mass displacement x by

$$Q = \sqrt{N\mu/2} \cdot x \tag{2.33}$$

where μ is the reduced mass, x is the reduced mass displacement, and N is the number density of oscillators. For a three component uni-axial system like $LiTaO_3$, the reduced mass is

$$\mu = \frac{m_1 m_2 m_3}{m_1 m_2 + m_1 m_3 + m_2 m_3} \tag{2.34}$$

The reduced mass displacement x can in turn be calculated from the displacements of the ionic components r_i as follows:

$$x = \sqrt{\frac{\sum m_i r_i^2}{\mu}} \tag{2.35}$$

Therefore the normal mode amplitude Q is given by:

$$Q = \sqrt{\frac{N\sum m_i r_i^2}{2}} \tag{2.36}$$

The equilibrium displacements for the ferroelectric distortion are generally known from x-ray and neutron diffraction data. For $LiTaO_3$, the displacements are given in Table 1.1.

Species	Displacement (nm)	Mass (au)	Charge (electrons)
Li_2	+0.043	13.9	+2
O_6	-0.017	95.9	-12
Ta_2	+0.0029	362	+10
normal mode	0.049	11.7	+6.5

Table 1.1 Displacement from normal structure of each of the ions and the corresponding normal mode displacement, mass, and charge.

Given these, we can calculate the equilibrium displacement for the reduced mass x_{eq}:

$$x_{eq} = \sqrt{\frac{\sum m_i r_i^2}{\mu}} \tag{2.37}$$

The value of x_{eq} for $LiTaO_3$ is 0.049 nm.

We will also need to know the effective charge q_{eff} associated with the reduced mass displacement x. The effective charge is defined so that the dipole moment calculated by the product of $x \cdot q_{eff}$ is equal to the dipole moment of the actual unit cell:

$$q_{eff} = \frac{1}{x_{eq}} \sum r_i q_i \tag{2.38}$$

where the r_i and q_i are the displacements and charges of each ionic species at the equilibrium position. These values are given in Table 1.1 for $LiTaO_3$. The effective charge for $LiTaO_3$ is 6.5 electron units.

2.4.2 *Equations of motion for ions*

The coupling between the phonon and electromagnetic modes to form mixed phonon-polaritons is described by the coupled equations of motion[1]:

$$\ddot{Q} = b_{11}Q - \Gamma\dot{Q} + b_{12}E + F' \tag{2.39}$$

$$P = b_{21}Q + b_{22}E \tag{2.40}$$

where Q is the normal mode coordinate, Γ is a phenomenological damping factor and F' represents an external driving force.

The force function in the normal mode coordinates is scaled as

$$F' = \sqrt{N/(2\mu)} \cdot F \tag{2.41}$$

where F is a force in standard units such as that exerted through ISRS.

Treating both the phonon and polarization modes in the linear response regime yields

$$b_{11} = -\omega_T^2 \tag{2.42}$$

$$b_{12} = b_{21} = \omega_T \sqrt{\epsilon_0(\varepsilon_0 - \varepsilon'_\infty)} \tag{2.43}$$

$$b_{22} = \epsilon_0(\varepsilon'_\infty - 1) \tag{2.44}$$

where ϵ_0 is the permittivity of free space, ε_0 is the low-frequency relative permittivity, ε'_∞ is the relative permittivity for IR frequencies above ω_T.

ε'_∞ may be larger than ε_∞, the permittivity in the visible light range, because there may be higher frequency polar modes that contribute to ε'_∞.

The derivations of the coupling constants in Eq. (2.42) to (2.44) is informative, so I will present it here. First we take the undriven form of Eq. (2.39):

$$\ddot{Q} = b_{11}Q - \Gamma\dot{Q} + b_{12}E \tag{2.45}$$

We assume a periodic plane wave solution $e^{i(kx-\omega t)}$ to get

$$-\omega^2 Q = b_{11}Q + i\omega\Gamma Q + b_{12}E \tag{2.46}$$

We now use the following relationships for susceptibility and relative permittivity in MKS units:

$$\begin{aligned} P &= \chi\epsilon_0 E \\ D &= (1+\chi)\epsilon_0 E = \epsilon_0\varepsilon_r E \end{aligned} \tag{2.47}$$

where χ is the susceptibility, D is the electric displacement, ϵ_0 is the permittivity of free space, and ε_r is the relative permittivity. Combining Eqns. (2.40), (2.46), and (2.47) gives

$$P = \left(b_{22} + \frac{b_{12}b_{21}}{-b_{11} - \omega^2 - i\omega\Gamma} \right) E = \chi\epsilon_0 E \tag{2.48}$$

Given that $\varepsilon_r = 1 + \chi$, the relative permittivity can be solved from Eq. (2.48) as

$$\varepsilon_r = \left(1 + \frac{b_{22}}{\epsilon_0}\right) + \frac{1}{\epsilon_0}\left(\frac{b_{12}b_{21}}{-b_{11} - \omega^2 - i\omega\Gamma}\right) \tag{2.49}$$

We compare this with the classical dielectric formula for the response of a singular damped oscillator (Böer, Eq. 11.37)[21]:

$$\varepsilon_r = \varepsilon_\infty + \frac{\omega_T^2(\varepsilon_0 - \varepsilon_\infty)}{\omega_T^2 - \omega^2 - i\omega\Gamma} \tag{2.50}$$

The coupling coefficients given in Eqns. (2.42) to (2.44) can now be obtained. It is clear from Eq. (2.46) that $b_{11} = \omega_T^2$, as this defines the motion of the harmonic oscillator even if E or $b_{12} = 0$. b_{22} can be found from Eqns. (2.49) and (2.50) by taking the limit $\omega \to \infty$. b_{12} and b_{21} can now be obtained from Eqns. (2.49) and (2.50) with the extra condition that $b_{12} = b_{21}$.

2.4.3 Equations of motion for electric field

The electric field obeys the wave equation for a polarizable medium, which can be derived directly from Maxwell's equations and Eq. (2.40) given the condition that $\nabla \cdot E = 0$. The derivation is straightforward but I will include it here for the sake of completeness, and also to avoid confusion over the many possible unit systems used in electromagnetics. The four Maxwell equations of motion are given below in MKSA units[13].

$$\nabla \cdot \mathbf{D} = \rho_f \tag{2.51}$$

$$\nabla \cdot \mathbf{B} = 0 \tag{2.52}$$

$$\nabla \times \mathbf{H} = \frac{\partial \mathbf{D}}{\partial t} + \mathbf{J}_f \tag{2.53}$$

$$\nabla \times \mathbf{E} = \frac{-\partial \mathbf{B}}{\partial t} \tag{2.54}$$

D is the electric displacement in coulombs/meter, **E** is the electric field in volts/meter, ϵ_0 is the permittivity of free space in farad/meter, **P** is the polarization in coulombs/meter, **B** is the magnetic induction in teslas, **H** is the magnetic field in amperes/meter, **M** is the magnetization in amperes/meter, μ_0 is the permeability of free space in henry/meter, ρ_f is the free charge density in coulombs/meter^3, and $\mathbf{J}_f$ is the free current density in amperes/meter^2. The relationships between the electric displacement, field and polarization are given by:

$$\mathbf{D} = \epsilon_0 \mathbf{E} + \mathbf{P} \tag{2.55}$$

The electric displacement includes the polarization of free space by the field plus any additional polarization of matter. Likewise, the relationships between the magnetic induction, field and magnetization are given by:

$$\mathbf{B} = \mu_0 (\mathbf{H} + \mathbf{M}) \tag{2.56}$$

The magnetic induction includes the magnetization of free space by the field plus any additional magnetization of matter.

We substitute Eqns. (2.55) and (2.56) in Eq. (2.53) and take the derivative with respect to time:

$$\frac{\partial}{\partial t}\frac{1}{\mu_0}(\nabla \times \mathbf{B}) = \epsilon_0 \frac{\partial^2 \mathbf{E}}{\partial t^2} + \sigma \frac{\partial \mathbf{E}}{\partial t} + \frac{\partial^2 \mathbf{P}}{\partial t^2} \tag{2.57}$$

The conductivity σ is defined by $\mathbf{J}/\mathbf{E}$. Wide-bandgap ferroelectric crystals are good insulators of very low conductivity. However, in the simulations that will be discussed in a later chapter I artificially add a conductivity gradient near the boundaries of the simulation grid to absorb the outgoing polariton waves. Away from the boundaries σ is zero.

Since spatial and temporal derivatives commute, we change the order of the derivatives and substitute Eq. (2.54) to get

$$\frac{1}{\mu_0}\left(\nabla \times \frac{\partial \mathbf{B}}{\partial t}\right) = \frac{1}{\mu_0}(-\nabla \times \nabla \times \mathbf{E}) = \frac{1}{\mu_0}\nabla^2 \mathbf{E} \tag{2.58}$$

This assumes that the condition that $\nabla \cdot E = 0$ is satisfied, which is true for the transverse waves that we are considering. Using Eq. (2.58) and (2.57) we get

$$\nabla^2 \mathbf{E} = \frac{1}{c^2}\frac{\partial^2 \mathbf{E}}{\partial^2 t} + \mu_0 \sigma \frac{\partial \mathbf{E}}{\partial t} + \mu_0 \frac{\partial^2 \mathbf{P}}{\partial^2 t} \tag{2.59}$$

where the speed of light $c = 1/\sqrt{\epsilon_0 \mu_0}$. We now substitute for $\mathbf{P}$ using Eq. (2.40) and (2.44) to get the final equation:

$$\nabla^2 \mathbf{E} = \frac{\varepsilon'_\infty}{c^2}\frac{\partial^2 \mathbf{E}}{\partial^2 t} + \mu_0 \sigma \frac{\partial \mathbf{E}}{\partial t} + \mu_0 b_{2i} \frac{\partial^2 \mathbf{Q}}{\partial^2 t} \tag{2.60}$$

2.4.4 Equations for coupling a relaxational mode to the polariton

Some ferroelectrics such as $LiTaO_3$ show a relaxational mode that is coupled to the polariton mode. We can simulate the exponential decay by a quantity Q_r' that has an instantaneous rate of change proportional to its magnitude. This relaxational mode is bilinearly coupled to the polariton equations of motion.

$$\ddot{Q} + \Gamma\dot{Q} + \omega^2 Q = b_{12}E + F' + B^{1r}Q_r' \tag{2.61}$$

$$B^{r1}Q - Q_r' = \tau\dot{Q}_r' \tag{2.62}$$

Eq. (2.61) shows the relaxational mode exerting a force on the polariton via the coupling term B^{1r}, while Eq. (2.62) shows the polariton mode driving the relaxational mode via B^{r1}. As we can see in Eq. (2.62) Q_r' will relax to the value $B^{r1}Q$ with a time constant of τ. For any given time the rate of change of Q_r' is proportional to the difference between its current value and the target value $B^{r1}Q$. The effect of the relaxational mode is to increase the damping on the phonon-polariton. The amount of damping introduced is frequency and wavevector dependent.

2.5. Polariton dispersion curves

The dispersion defines the relationship between ω and q_p for the polariton. The dispersion relation is simply

$$\epsilon_r = n^2 = \frac{c^2 k^2}{\omega^2} \tag{2.63}$$

We combine this with the expression for the damped oscillator, repeated here from Eq. (2.50):

$$\epsilon_r = \varepsilon_\infty + \frac{\omega_T^2(\varepsilon_0 - \varepsilon_\infty)}{\omega_T^2 - \omega^2 - i\omega\Gamma} \tag{2.64}$$

Combining Eq. (2.63) and (2.64) we get the following polynomial[6]:

$$\omega^4 \varepsilon'_\infty + \omega^3 i\Gamma \varepsilon'_\infty - \omega^2\left(c^2 q_p^2 + \omega_T^2 \varepsilon_0\right) - \omega i\Gamma c^2 q_p^2 + \omega_T^2 c^2 q_p^2 = 0 \tag{2.65}$$

Note that the dispersion relation in (2.65) is simply the combination of the dispersion definition and the classical model for the influence of a harmonic oscillator on the permittivity.

The dispersion curves for $LiTaO_3$ are shown in Figure 2.5. There is a complex conjugate pair of low frequency roots that describe the lower polariton branch, and a complex conjugate pair of high frequency roots that describe the upper polariton branch.[6] The real part of the root is the polariton frequency, while the imaginary part is the damping rate at that frequency. We are only concerned with the lower polariton branch, as the upper branch is too high in frequency to be observed with our current laboratory apparatus.*

---

* For example, the observable upper branch in $LiTaO_3$ is >18 THz (see Figure 2.9). The diffracted signal from the grating is squared, which doubles the observed frequency to

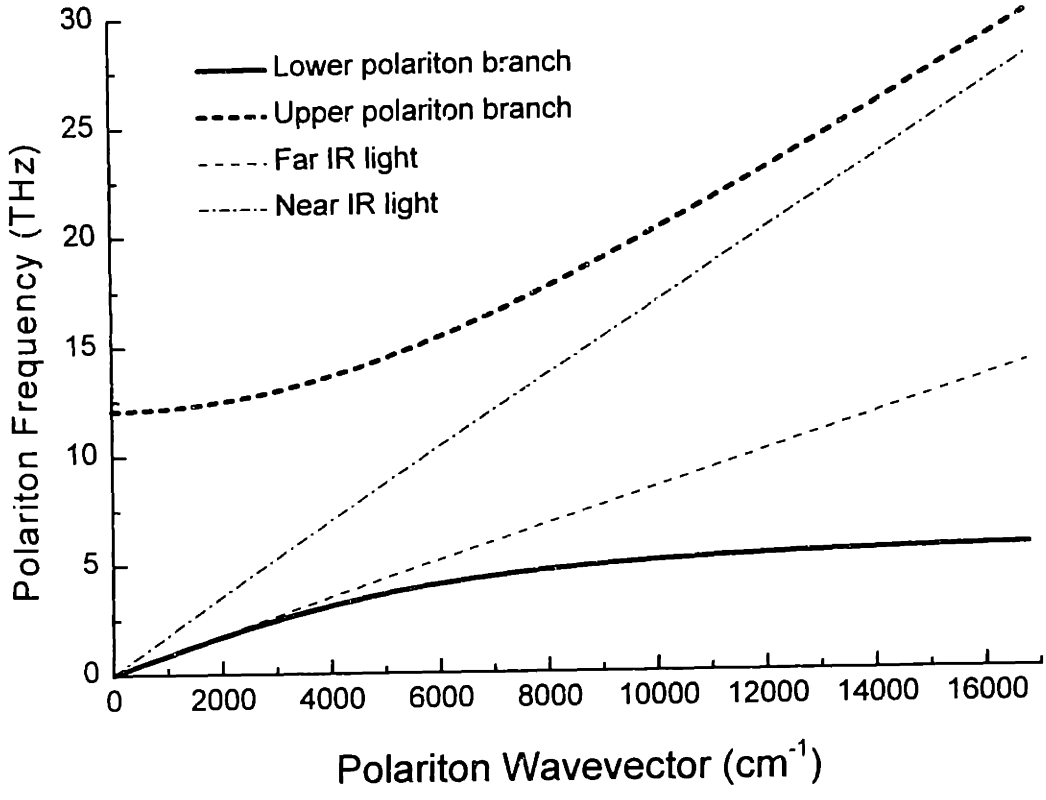

Figure 2.5 Dispersion curves for $LiTaO_3$.

Note that the dispersion curves described here relate the frequency of the polariton to the wavevector of the polariton. We will see in a subsequent section that the wavevector of the polariton may be different than the wavevector of the grating in an ISRS experiment.

>36 THz. The convolution factor for the probe pulse is $\exp(-\omega^2\tau^2/4)$, which results in an attenuation of the signal < 10^{-5} for a 30fs pulse. If heterodyne detection were used, the observed frequency would not be doubled, and the attenuation would only be 0.28. The conclusion is that heterodyne detection should be used to observe the upper polariton branch.

At small wavevectors, there is little coupling between the propagating electric field and the polar phonon (i.e. the harmonic oscillators). The lower branch acts very much like light, so the lower branch consists primarily of the propagating electric field. It has a nearly straight dispersion curve. The slope of this curve gives the group velocity, which is just the speed of light in the far IR for this material $c'' = c/\sqrt{\varepsilon_0}$. The upper branch acts like a pure phonon mode at small wavevectors, with a frequency of the longitudinal optic mode and little propagating field. (This *is not* the longitudinal mode. The motion of the mode is still transverse. At $k = 0$ the electric field does not propagate for this branch. Furthermore, because of the phase shift associated with the harmonic oscillator resonance at ω_T, the electric field is out of phase with the ionic motion. The electric field acts as a depolarizing field; i.e. it opposes the displacement of the ions, which adds to the restoring force and raises the frequency of the mode. The same thing happens in the case of the longitudinal mode, because the longitudinal electric field does not propagate either. So the $k = 0$ transverse mode of the upper branch has the same frequency as the longitudinal branch because both are coupled to a non-propagating field which opposes the ionic motion.)

In the limit of large wavevectors, the upper branch becomes light-like, while the lower branch becomes phonon-like. The upper branch becomes primarily a traveling electromagnetic wave with a velocity equal to the speed of near-IR light $c' = c/\sqrt{\varepsilon'_\infty}$. The lower branch becomes decoupled from the

propagating electromagnetic wave and oscillates with the transverse optic mode frequency ω_T. The lower branch is decoupled because the harmonic oscillator has a phase shift approaching 90° at resonance, so its motion becomes orthogonal to the coupling to the electric field.

The intermediate range between the two limits is the polariton regime. The phonon and the electromagnetic field are strongly coupled in both branches, and they oscillate and propagate together. This combined response is called the phonon-polariton.

2.6. Polariton generation, propagation and phase matching in a transient grating experiment

The generation of phonon-polaritons in ferroelectrics by ultra-short pulses of laser light and their subsequent propagation and dispersion have been extensively studied by transient grating and pump-probe experiments. However, there are several important points that have been overlooked or are in error in a number of these previous works. The polariton wavevector is not normal to the laser beam axis in a transient grating experiment as is often presumed, but instead has a forward component that may be a substantial fraction of the polariton total wavevector. As a result, the polariton wavevector is different than the wavevector of interference grating that produced it. This can produce significant errors in the interpretation of polariton dispersion measurements. The relative angles and magnitudes of the grating and polariton wavevectors are derived and may be used to

correctly interpret dispersion measurements obtained in transient grating experiments.

2.6.1 Deriving the polariton wavevector in a grating experiment

It has often been assumed in the previous literature on the subject that the polariton generated by the excitation grating in a time-resolved transient grating experiment has a wavevector that is equal to the wavevector of the grating, and that the polariton field consists of two plane waves that propagate in the direction perpendicular to the bisector of the two pump pulses[4, 6, 9, 11, 12, 20, 22-24]. In some other papers the correct magnitude of the wavevector of the polariton is derived, but it is assumed that the direction of propagation is essentially perpendicular to the axis of the pump beams[7, 16, 25]. I show that the polaritons in some materials such as $LiTaO_3$ have a forward component that is a substantial fraction of the perpendicular wavevector component, and that in the upper branch the polariton may propagate entirely in the forward direction. As a result, the polaritons have a wavevector differing in both magnitude and direction from the excitation wavevector. This result is demonstrated both by considering conservation of energy and momentum in the scattering process as well as considering the phase-matching conditions of coherent generation of the polariton field by the moving excitation grating. Significant errors in the interpretation of experimental data can result from overlooking this difference in the wavevectors.

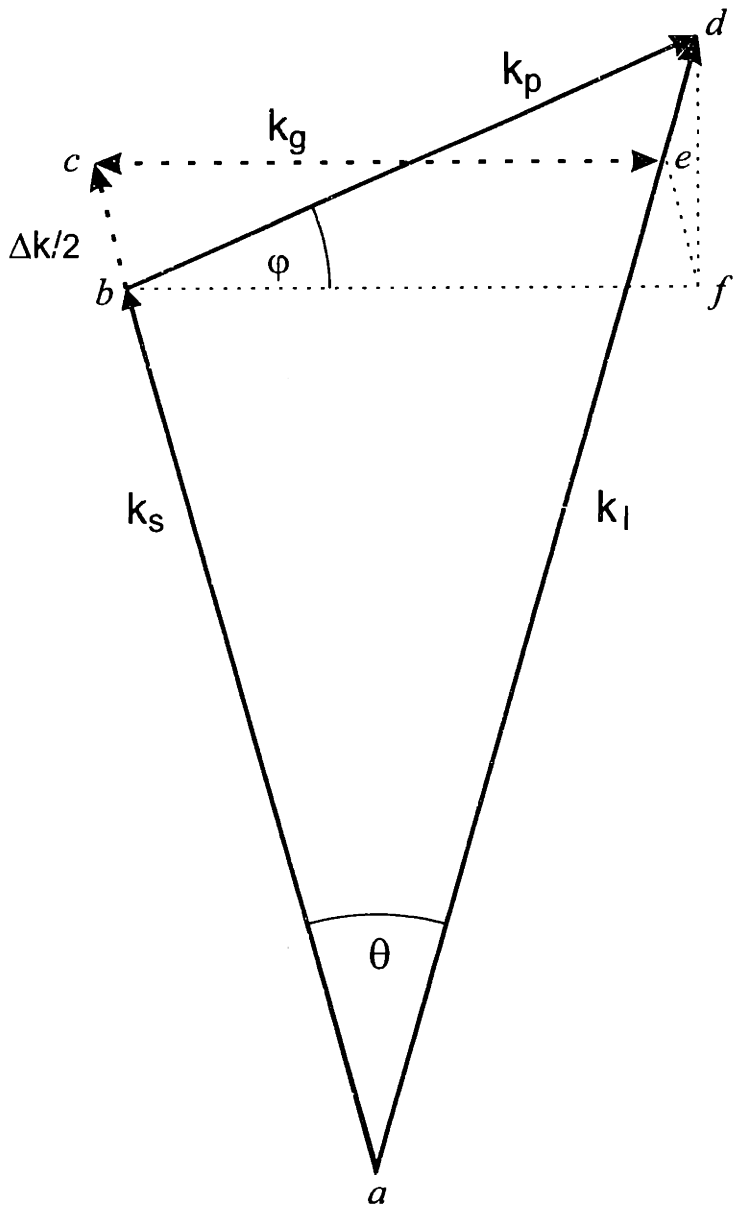

Figure 2.6 Vector diagram for momentum conservation in Raman scattering between laser beam k_l and scattered beam k_s with polariton k_p.

2.6.2 Polariton wavevector from conservation argument

A vector diagram showing the conservation of energy and momentum in a Raman scattering process is shown in Figure 2.6. In a regular Stokes Raman

process, laser light of wavevector k_l is scattered into red-shifted beam of wavevector k_s. In an ISRS process, light in pump beam #1 of wavevector k_l (line segment $\overline{ad}$) interacts with light in pump beam #2 of wavevector k_s $\left(\overline{ab}\right)$, where k_l and k_s have two different frequencies within the bandwidth of the short pulse. For convenience we define $k_l = k_0 + \Delta k/2$ and $k_s = k_0 - \Delta k/2$ where k_0 is the wavevector of the central frequency in the short pump pulses. k_g $\left(\overline{ce}\right)$ is the excitation grating produced by the interference between the crossed pump beams of central wavevector k_0:

$$k_g = 2k_0 \sin(\theta/2) \tag{2.66}$$

k_p $\left(\overline{bd}\right)$ is the wavevector of the polariton, θ ($\angle bae$) is the angle between the two pump beams in the sample, and φ ($\angle fbd$) is the angle between the wavevectors of the polariton and the grating. By conservation of energy:

$$\omega_p + \omega_s = \omega_l \tag{2.67}$$

where ω_p is the frequency of the polariton, ω_s is the frequency of the scattered light, and ω_l is the frequency of the laser. Conservation of momentum also holds:

$$\vec{k}_s + \vec{k}_p = \vec{k}_l \tag{2.68}$$

So

$$\omega_p = c'\left(k_l - k_s\right) = c'\Delta k \tag{2.69}$$

where $c' = c/\sqrt{\varepsilon_\infty}$ is the speed of the laser light in the sample.

The relationship between k_p and k_g can be easily found with the help of a geometrical construct in Figure 2.6. Line segments $\overline{bf}$ and $\overline{ef}$ are created to form parallelogram *cbfe*. Line segments $\overline{de}$ and $\overline{ef}$ are $\Delta k/2$ in length, and angles $\angle edf$ and $\angle efd$ equal $\alpha/2$, so $\overline{df} = \Delta k \cos(\theta/2)$. From this information and Eq. (2.69) we get the relationship between k_p and k_g:

$$k_p^2 = k_g^2 + \left(\Delta k \cos(\theta/2)\right)^2 = k_g^2 + \left(\omega_p/c'\right)^2 \cos^2(\theta/2) \tag{2.70}$$

$$\varphi = \cos^{-1}\left(\frac{k_g}{k_p}\right) \tag{2.71}$$

The relationship between k_p and k_g is conventionally expressed in terms of k_s and k_l using the law of cosines:

$$k_p^2 = k_s^2 + k_l^2 - 2k_s k_l \cos(\theta) \tag{2.72}$$

Some authors describing transient grating experiments in phonon-polaritons have made use of Eq. (2.72) in interpreting the wavevector of the polariton[7, 16]. Eq. (2.70) can readily be derived from Eq. (2.72), which is a fundamental and well-known relationship in the literature on Raman spectroscopy of phonon-polariton modes [2, 26]. Equation (2.70) simply restates this relationship explicitly in terms of the wavevector of the transient grating.

For any experimentally determined grating wavevector k_g and polariton frequency ω_p the actual polariton wavevector magnitude k_p and direction φ can be determined from the above relations. Note that the polariton wavevector is always larger than the wavevector of the grating, and that the difference increases with larger polariton frequencies.

2.6.3 Polariton wavevector from phase matching condition

In this section we will see how the process of generating coherent plane-wave polaritons from a moving excitation grating imposes a phase-matching condition between the phase velocities of the grating and polariton. From this we derive exactly the same relationship between the wavevector of the grating and the polariton, showing that this relationship is not only required by conservation, but is also compatible with a transient grating experiment. (We must rule out the possibility that the polariton is allowed by conservation but is not phase matched to the grating. If this were true the polariton would not be generated coherently in a transient grating experiment.)

First we must consider the phase velocity of the grating, as represented in Figure 2.2. Line segments $\overline{bc}$ and $\overline{dc}$ represent the phase front of the two forward moving pump beams. The group velocity of the pump beams equals the speed of light in the sample c', as represented by vectors $\overline{ab}$ and $\overline{ad}$.

The grating formed from the intersection of these two phase fronts has phase velocity v_g given by vector $\overline{ac}$:

$$v_g = \frac{c'}{\cos(\theta/2)} \tag{2.73}$$

The phase velocity of the grating is always greater than the speed of light in the material.

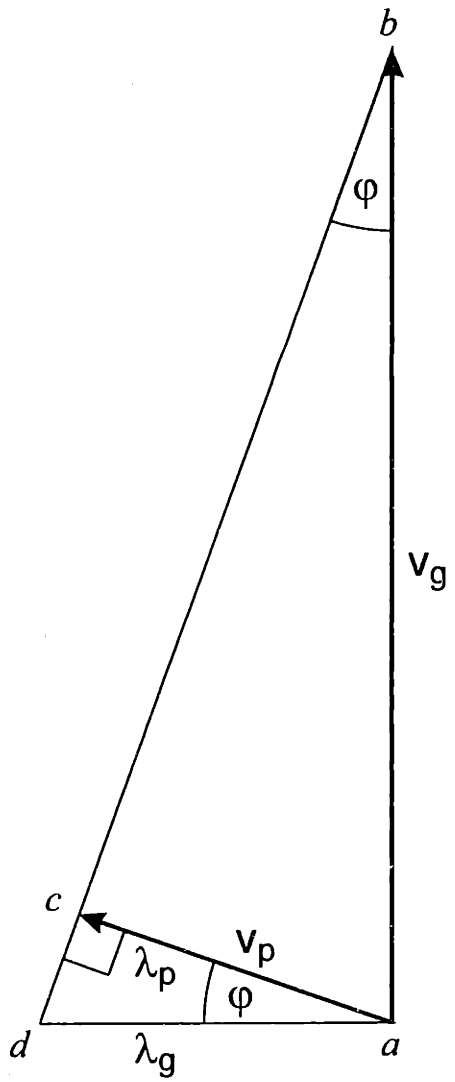

Figure 2.7 Vector diagram showing the phase matching between the polariton wavefront $\overline{bc}$ and the forward moving grating $\overline{ad}$.

The phase matching condition may be introduced by considering a single bright fringe of the grating. Each fringe considered independently is similar to a single tightly focused beam, which excites a range of wavevectors from zero to an upper bound determined by its spatial width. In a grating a narrow range of the polariton wavevectors will add together coherently to form a plane wave in each direction. The angle of the polariton wavefront is found by considering that as the grating moves from point *a* to point *b* in Figure 2.7 the polariton wave moves from point *a* to point *c*. The phase velocity of the grating v_g is represented by $\overline{ab}$ and the phase velocity of the polariton v_p is represented by $\overline{ac}$. The line segment $\overline{bc}$ represents the phase front of the polariton. The angle of the polariton wave can be found by the ratio of the phase velocities of the grating and the polariton[27]:

$$\sin(\varphi) = \frac{v_p}{v_g} = \frac{\omega_p}{k_p v_g} \tag{2.74}$$

To relate k_p and k_g we now let $\overline{ac}$ represent the wavelength of the polariton λ_p, while $\overline{ad}$ represents the wavelength of the grating λ_g.

$$\lambda_p = \lambda_g \cos(\varphi) \tag{2.75}$$

$$k_g = k_p \cos(\varphi) \tag{2.76}$$

By squaring Eq. (2.76) and using the phase matching condition from Eq. (2.74), we get:

$$k_g^2 = k_p^2\left(1-\sin^2(\varphi)\right) = k_p^2 - \left(\frac{\omega_p}{v_g}\right)^2 \tag{2.77}$$

Substituting for the phase velocity of the grating from Eq. (2.73) we have the relationship between k_p and k_g:

$$k_p^2 = k_g^2 + \left(\frac{\omega_p}{c'}\right)^2 \cos^2(\theta/2) \tag{2.78}$$

$$\varphi = \cos^{-1}\left(\frac{k_g}{k_p}\right) \tag{2.79}$$

Therefore we have shown that in a transient grating experiment the phase matching condition for the coherent generation of polaritons leads to the exact same relationship between k_p and k_g required by the conservation of energy and momentum (Equations (2.70) and (2.71)).

2.6.4 Discussion of the polariton wavevector

The equations and parameters for all the following dispersion curves for $LiTaO_3$ are from Wiederrecht et. al.[23].

2.6.4.1 Lower branch

The difference in the lower branch of the polariton dispersion curve introduced by the difference between the polariton and grating wavevector may be seen in Figure 2.8. Here the theoretical curve for the lower polariton branch of $LiTaO_3$ is first plotted as $\{k_p, \omega_p\}$, which is the true dispersion

relation. Then the grating wavevector k_g for each $\{k_p, \omega_p\}$ pair is calculated, and the dispersion curve is plotted vs. k_g. This indicates how the dispersion curve would appear in the raw transient grating experiment data. It can be seen that if the difference between k_p and k_g is not taken into account, errors of up to 8% will occur.

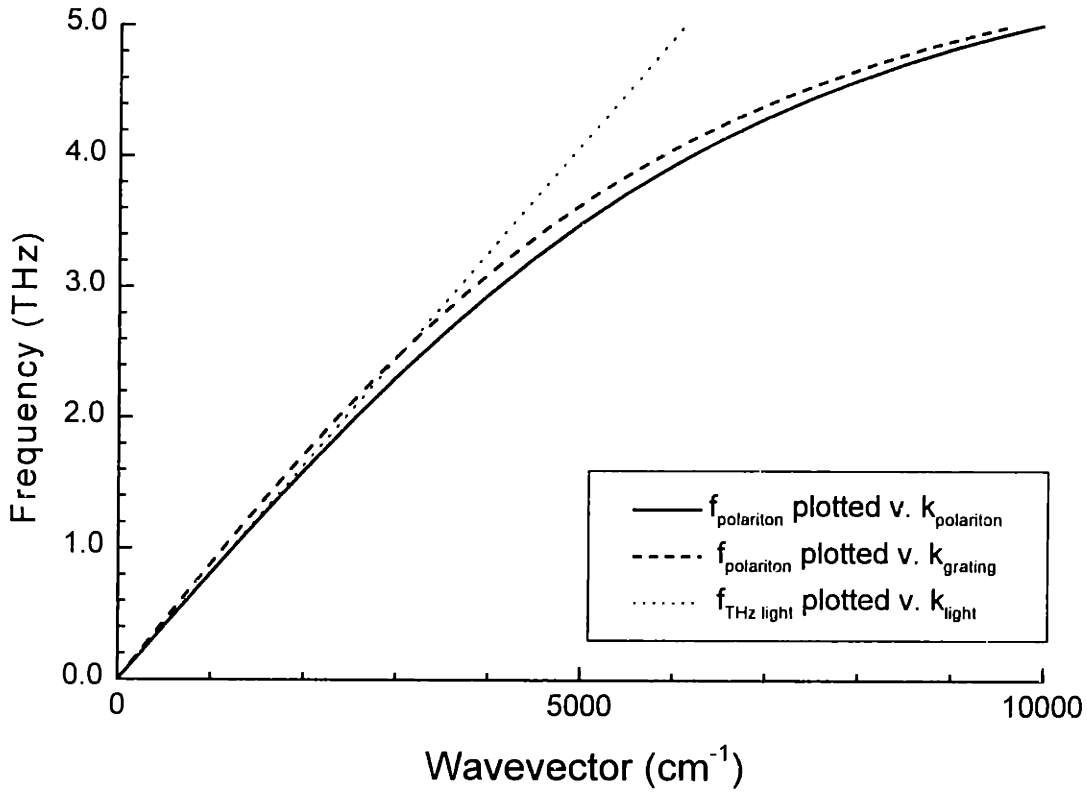

Figure 2.8 Plot showing the difference in the lower polariton branch between the measured relation between the polariton frequency and the *grating* wavevector compared to the true dispersion relation between the polariton frequency and the *polariton* wavevector.

2.6.4.2 Upper branch

There is a very large disparity in the upper polariton branch between the true polariton dispersion curve $\{k_p, \omega_p\}$ and the dispersion relation measured by a transient grating experiment $\{k_g, \omega_p\}$. First, there is a substantial range of the polariton curve at low polariton wavevectors that cannot be driven by a light scattering mechanism because energy and momentum cannot be conserved. Second, there can be a very large disparity between k_g and k_p in the regions where polariton generation is allowed by conservation considerations.

The fact that polaritons cannot be generated by a light scattering process at the low-k portion of the upper branch can be understood by recalling that the polariton frequency ω_p is determined by the difference Δk between excitation wavevectors k_i and k_s, while Δk determines only the minimum value of the polariton wavevector k_p:

$$\omega_p = \omega_i - \omega_s = \Delta\omega = c'\Delta k = c'(k_i - k_s) \tag{2.80}$$

$$k_p \geq \Delta k \tag{2.81}$$

The minimum value for k_p is obtained for forward scattering, where k_i, k_s and k_p are parallel. At low values of Δk, the associated frequency $\Delta\omega$ is below the frequency of the upper polariton branch. Hence this scattering

mechanism cannot provide the energy to drive the upper polariton branch at low wavevectors.

The minimum upper branch polariton wavevector that can be driven by the light scattering process can be determined graphically by plotting the dispersion relation of the excitation beams $\Delta\omega = c'\Delta k$ on the same plot as the dispersion curve of the upper branch as in Figure 2.9. The portion of the upper branch to the right of the intersection of the two curves satisfies $k_p \geq \Delta k$ and is allowed by energy considerations. The portion of the upper branch that is to the left of the intersection does not satisfy this relation and cannot be generated by light scattering.

The relationship between k_p and k_g for the upper branch follows the expression derived above. In the case of the upper branch, there is a very large disparity between the experimental dispersion curve that relates ω_p to the grating wavevector k_g and the actual polariton dispersion curve that relates ω_p to the polariton wavevector k_p, as can be seen in Figure 2.9. The difference is much more pronounced than in the lower branch because the polariton frequencies are much higher. It is imperative for the interpretation of any transient grating experiment of the upper polariton branch to calculate the actual polariton wavevector k_p from the experimentally determined k_g and ω_p.

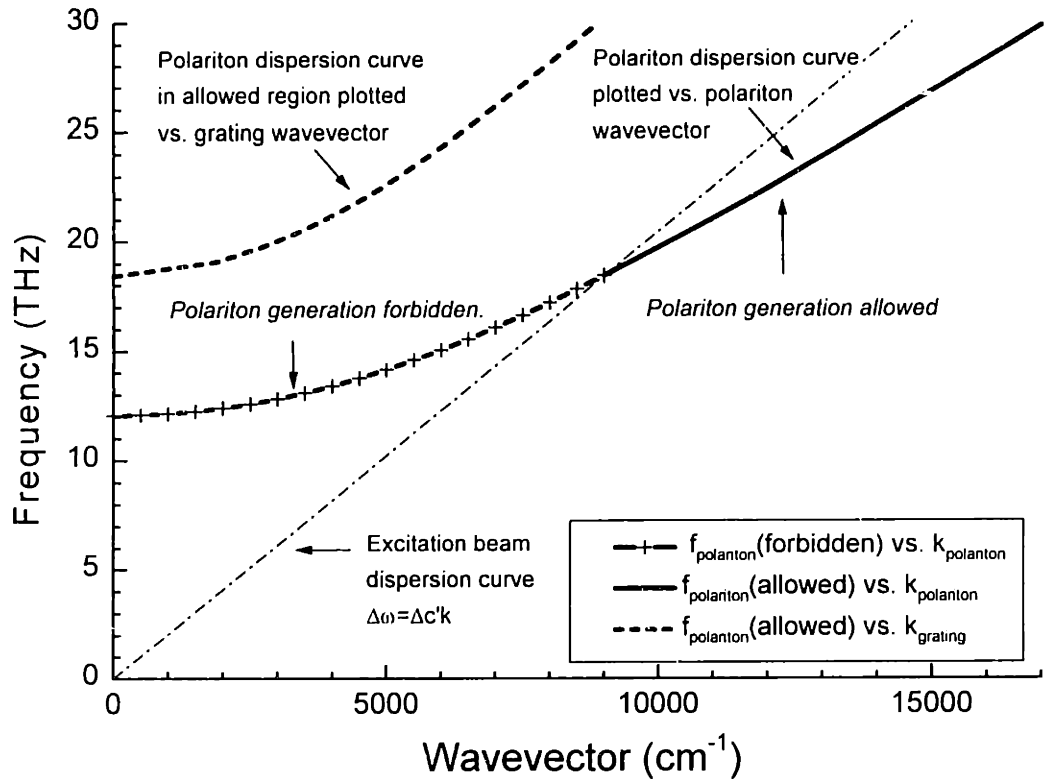

Figure 2.9 Plot showing the difference in the upper polariton branch between the measured relation between the polariton frequency and the *grating* wavevector compared to the true dispersion relation between the polariton frequency and the *polariton* wavevector. A large portion of the upper polariton branch at low wavevectors cannot be coherently generated by light scattering. The portion of the branch that can be generated exhibits a very large disparity between the wavevectors of the grating vs. the polariton.

2.6.4.3 The angle between polariton and grating

The polariton field generated by a moving interference grating consists of two plane waves moving with angles of $\pm\varphi$ to the grating. The two plane waves have opposite sideways component and equal forward components. The size of the angle with respect to the grating is determined by the phase

velocities of the grating and the polariton. At small wavevectors the lower branch of the polariton becomes light-like, and the phase velocity of the polariton becomes $v_p \approx c/\sqrt{\varepsilon_0}$. The phase velocity of the grating is essentially the speed of light in the material because for small wavevectors the angle between the beams approaches zero, so $v_g \approx c/\sqrt{\varepsilon_\infty}$. Therefore at small wavevectors the angle of propagation of the polariton from Eq. (2.74) becomes:

$$\varphi_{lower\ branch} = \sin^{-1}\left(\frac{v_p}{v_g}\right) \xrightarrow[k\to 0]{} \sin^{-1}\left(\sqrt{\frac{\varepsilon_\infty}{\varepsilon_0}}\right) \tag{2.82}$$

In some materials the polariton velocity is a significant fraction of the speed of light in the material. In these materials the angle between polariton and grating is substantial. For example, in $LiTaO_3$, φ approaches 24° as $\omega_p \to 0$. The angle diminishes with increasing wavevector in the lower polariton branch because the dispersion curve flattens out and the phase velocity of the polariton becomes small.

The polariton plane waves in the lower branch may be visualized by examining Figure 2.10, which shows a plot of a numerical simulation of phonon-polaritons in two dimensions[28]. The response clearly consists of two sets of plane waves propagating away from each other at a forward angle. The constructive and destructive interference between the angled plane waves forms a diamond shaped pattern in the region of overlap. Diffraction

of the probe beam from this interference pattern generates the signal in a time-resolved transient grating experiment.

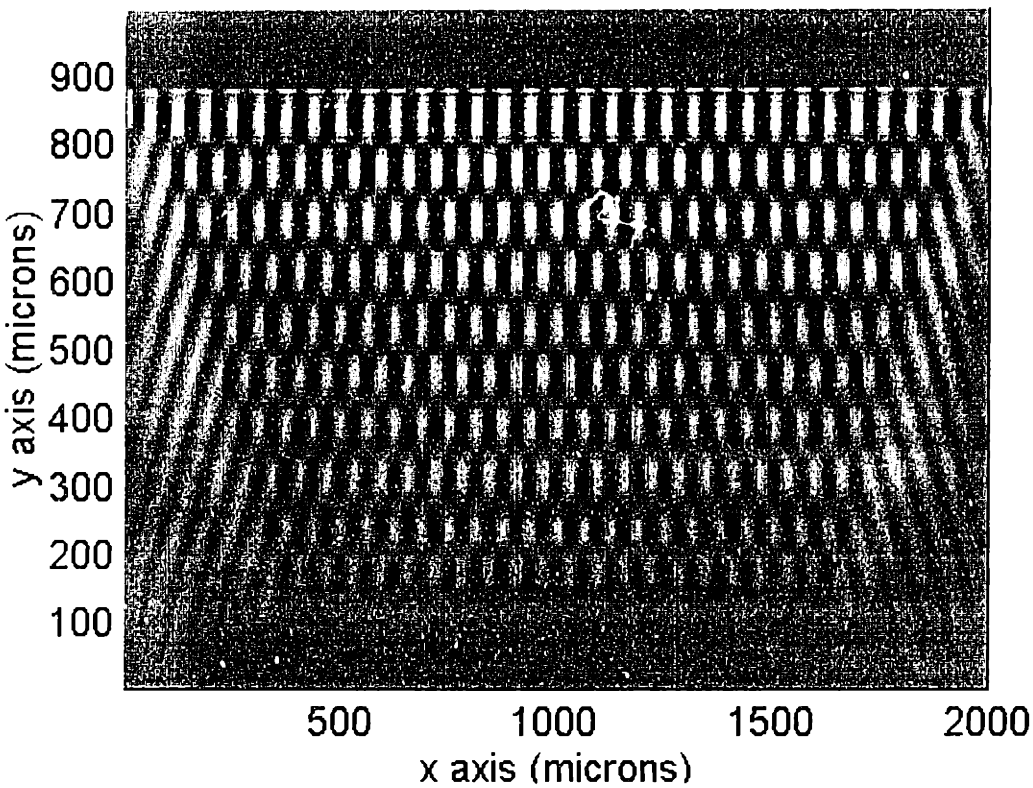

Figure 2.10 Gray-scale plot of coherent phonon displacements Q(x,y,t). The excitation pulses form an interference pattern which is moving in the +y direction (vertical). Q displacement direction is along the z axis (out of the page). Grating wavevector k_g = 1000 cm^{-1}, polariton k_p = 1153 cm^{-1}, polariton wavelength = 63 microns.

The polaritons of the upper branch have wavevectors directed parallel to the excitation beams for $k_g = 0$, so $\varphi = 90^\circ$ and the scattering is completely in the forward direction. In this case the polariton is a single forward moving plane wave that is phase matched to the traveling excitation pulse. As k_g increases, the upper branch polariton takes on the characteristic of two plane waves, each propagating close to the forward direction, with one having a

small component to the left and the other an equal component to the right. As k_g increases φ decreases, until the polariton waves become light-like with a phase velocity approaching that of IR light in the sample. The limiting polariton angle at large wavevectors is given by the following expression:

$$\varphi_{upper\ branch} = \sin^{-1}\left(\frac{v_p}{v_g}\right) \xrightarrow[k\to\infty]{} \sin^{-1}\left(\sqrt{\frac{\varepsilon_\infty}{\varepsilon'_\infty}}\right) \tag{2.83}$$

where ε'_∞ is the permittivity at frequencies above the transverse optic phonon frequency. This is generally greater than the permittivity at optical frequencies ε_∞ due to higher frequency polar phonon modes. In $LiTaO_3$, φ approaches 53° in the upper branch at large wavevectors.

2.6.4.4 Significance to experiments

A number of published measurements of phonon-polaritons using transient grating experiments were fit to the theoretical dispersion curves, which consists of pairs of grating wavevectors and polariton frequencies $\{k_g, \omega_p\}$. This is incorrect, as the theory describes the function connecting the polariton wavevector with the polariton frequency $\{k_p, \omega_p\}$, and as we have seen the polariton wavevector differs in magnitude from the grating wavevector. Therefore the polariton wavevector must first be calculated from the experimental grating wavevector and the polariton frequency. Only then should the theoretical expression be fit to the data.

One way the theoretical dispersion curve may be fit to the experimental data is by using the permittivity values as parameters. Ignoring the difference between the wavevectors will lead to errors in the permittivity values obtained from the fit. The percentage error in the extracted permittivity values is approximately $\varepsilon_\infty/\varepsilon_0$ when the fit is made to only the lower branch. This can be derived by examining the low frequency limit of the lower branch of the dispersion curve. For small ω_p and k_p the dispersion relation simply reduces to:

$$\frac{\omega_p^2}{k_p^2} = \frac{c^2}{\varepsilon_0} \tag{2.84}$$

If we suppose that kg = kp, and fit the experimental dispersion data to this formula, we can extract an erroneous value for ε_0, which we will call ε_0':

$$\varepsilon_0' = \frac{c^2 k_g^2}{\omega_p^2} \tag{2.85}$$

The correct value for ε_0 can be found by substituting the relationship between k_p and k_g from Eq. (2.70):

$$\varepsilon_0 = \frac{c^2}{\omega_p^2}\left(k_g^2 + \frac{\omega_p^2 \varepsilon_\infty}{c^2}\cos^2\left(\frac{\alpha}{2}\right)\right) \approx \varepsilon_0' + \varepsilon_\infty \tag{2.86}$$

For $LiTaO_3$ the error is about 16%, using the values from Wiederrecht et. al.[23]. For $\varepsilon_0' = 34$ and $\varepsilon_\infty = 5.5$, this gives $\varepsilon_0 = 39.5$. For comparison, a numerical re-fitting of the experimental dispersion curve using Eq. (2.70) to

map the grating wavevector to the polariton wavevector yields $\varepsilon_0 = 38.4$ and $\varepsilon'_\infty = 9.6$.

For other ferroelectrics such as $KNbO_3$ and $BaTiO_3$, however, the error will be less than 1% because ε_0 is very large compared to ε_∞ in these materials [6]. In these materials the polariton propagates nearly perpendicular to the pump axis, and the difference between k_p and k_g is small.

2.6.5 Conclusions on polariton generation

We have shown that the two-dimensional propagation of polaritons is important in interpreting the experimental data from transient grating experiments in ferroelectrics. The failure to account for the forward component of the polariton wavevector leads to the erroneous identity between the grating wavevector and that of the polariton. This will cause substantial errors in the interpretation of polariton dispersion data in materials such as $LiTaO_3$ where the polariton velocity is high. The disparity between the polariton and grating wavevectors is especially severe in the upper polariton branch, where in addition a large portion of the polariton dispersion curve cannot be accessed by light scattering experiments.

2.7. Diffraction of light from transient polariton gratings

The polariton field generated by the pump grating in an ISRS experiment consists of two plane waves, moving away from each other in the horizontal

direction with a smaller forward component. The interference between these two polariton waves creates a periodic grating because the displacement of the ions modulates the electronic polarizability through the differential polarizability $\partial\alpha/\partial x$. This is the same term that plays a key role in the ISRS force. The interfering plane waves create a index of refraction or phase grating that is stationary in the horizontal direction but moves forward with a phase velocity equal to the pump grating. Therefore a probe beam at the Bragg angle will be perfectly phase matched to this moving grating, and coherent diffraction of the probe beam will occur. This diffracted light is the signal beam in an ISRS experiment.

2.7.1 Diffraction from a phase grating

The diffraction efficiency η for a thick*, unslanted index of refraction grating is given by Eichler et. al., Eq. (4.32)[31]:

$$\eta = \frac{I_1}{I_i} = \exp\left(\frac{-Kz}{\cos\alpha}\right)\left(\sin^2\frac{\pi\Delta nz}{\lambda\cos\alpha} + \sinh^2\frac{\Delta Kz}{4\cos\alpha}\right) \qquad (2.87)$$

---

* In L.R. Williams' thesis[29] it is asserted that the short spatial extent of the ultrashort pulses makes the grating act like a thin grating (p28). This is not actually the case. The grating produces a phase-matched excitation with a forward velocity equal to the forward velocity of the grating. Since the probe is also perfectly phase matched to the excitation at Bragg angle, the probe sees a constant phase grating throughout the sample[30]. In other words, in the reference frame of the probe pulse, the grating is not moving and appears exactly the same as an unslanted grating that extends throughout the sample. Therefore the thick grating condition applies. Williams also refers to the appearance of multiple orders of self-diffraction of the pump beams as further evidence of a thin grating. However, this effect can be explained by other electronic nonlinearities at high pump intensities, and will be treated in another section of this thesis.

where I_1 is the diffracted light, I_i is the incident light, α is the angle of incidence inside the sample, K is the complex part of the part of the index of refraction, z is the thickness of the grating, Δn is the change in index of refraction between peak and null in the grating, and λ is the wavelength of the light in vacuum. If the absorption in the sample is negligible, we can set $K = 0$. In addition, for small angles we can set $\cos\alpha = 0$. Eq. (2.87) then simplifies to

$$\eta \approx \sin^2\left(\frac{\pi \Delta n z}{\lambda}\right) \tag{2.88}$$

We need to relate the change in index of refraction Δn to the relative permittivity ε, which is given by:

$$\varepsilon = \varepsilon_1 + \Delta\varepsilon = \varepsilon_1 + N\frac{\partial\alpha}{\partial x}x_m \tag{2.89}$$

N is the number of oscillators per unit volume, and x_m is the maximum ionic displacement. We want to relate the following relationship to Eq. (2.89):

$$n = n_1 + \Delta n \qquad n_1 = \sqrt{\varepsilon_1} \tag{2.90}$$

We take the square root of the permittivity to get index of refraction, and take a first order power expansion of the square root about $\Delta\varepsilon = 0$ to get an expression for Δn.

$$n = \sqrt{\varepsilon_1 + \Delta\varepsilon} \approx \sqrt{\varepsilon_1} + \frac{\Delta\varepsilon}{2\sqrt{\varepsilon_1}} = n_1 + \frac{\Delta\varepsilon}{2n_1} \tag{2.91}$$

$$\Delta n = \frac{\Delta \varepsilon}{2n_1} = \frac{1}{2n_1} N \frac{\partial \alpha}{\partial x} x_m \quad * \tag{2.92}$$

We can now plug this result into the expression for the diffraction efficiency Eq. (2.88):

$$\eta \approx \sin^2\left(\frac{\partial \alpha}{\partial x} \frac{\pi N x_m z}{2n_1 \lambda} \right) \tag{2.93}$$

We can see from this result that the diffraction efficiency is related to the differential polarizability $\partial\alpha/\partial x$ and the ionic displacement x_m. Note that the diffracted light goes as the sine squared of the actual lattice oscillations. Since $\sin^2\theta = 1/2 \cdot (\cos 2\theta + 1)$, the observed signal in the time-delayed probe beam will appear at twice its true frequency.

2.7.2 Calculating WOS signal using coupled-wave theory

To properly calculate higher order diffraction and multiple diffraction processes we need to use coupled-wave theory. This is essential in the wavevector overtone spectroscopy (WOS) experiments, where we are looking for diffraction from an integer multiple of the fundamental wavevector.

---

* Note that this equation differs by a factor of n^4 from the equation for Δn given in previous theses from this research group (L.R. Williams, [29] Eq. (2.33)),G.P. Wiederrecht, [32] Eq. (2.7)). I believe these previous equations to be in error. The expression derived here can also be found in Eichler et. al., Eq. (4.30)[31].

The following derivation of the coupled-wave equations follows Eichler et. al. with the addition that I introduce the harmonics of the fundamental grating wavevector into the equations. We start by assuming that we can express the relevant modulations of the permittivity in terms of multiples of a fundamental grating wavevector q:

$$\varepsilon(x,z) = \varepsilon + \sum_{l=1}^{\infty} \Delta\varepsilon_l \cos(lqx) \tag{2.94}$$

ε is the unperturbed permittivity, $\Delta\varepsilon_l$ is the modulation of the permittivity associated with the wavevector harmonic l. This expression also assumes that the gratings are not slanted. We proceed by expressing the incident probe wave in terms of its wavevector $\vec{k}_i$ inside the sample:

$$A_i = \frac{A_i}{2}\exp\left[i\vec{k}_i \cdot \vec{r}\right] + \text{c.c.} = \frac{A_i}{2}\exp\left[ik_i(x\sin\alpha_i + z\cos\alpha_i)\right] \tag{2.95}$$

where α_i is the angle of incidence inside the sample. The diffracted waves are treated as plane waves that satisfy the Helmholtz wave equation:

$$\nabla^2 E + k^2\varepsilon(x,z)E = 0 \tag{2.96}$$

The electric field throughout the sample is treated as a superposition of the diffracted waves of all orders:

$$E(x,z) = \sum_{m=-\infty}^{m=\infty} S_m(z)\exp\left[i\vec{\sigma}_m \cdot \vec{r}\right] + \text{c.c.} \tag{2.97}$$

$S_m(z)$ are the amplitudes of the individual diffracted waves with index number m as a function of the distance into the sample z, $\vec{\sigma}_m$ is the

wavevector of diffracted wave m and is defined by $\vec{\sigma}_m = \vec{k}_i - m\vec{q}$.

Substituting the expression for the spatial modulation of the permittivity in Eq. (2.94) and the expression for the electric field in Eq. (2.97) into the wave equation Eq. (2.96) we get

$$\sum_m \left[\frac{\partial^2 S_m}{\partial z^2} + 2ik_i \cos\alpha \frac{\partial S_m}{\partial z} - \vec{\sigma}_m \cdot \vec{\sigma}_m S_m + k^2 \varepsilon S_m + \frac{k^2 \varepsilon_l}{2}\left(S_{m-l} + S_{m+l}\right) \right] \exp\left(i\vec{\sigma}_m \cdot \vec{r}\right) = 0 \tag{2.98}$$

$k = 2\pi/\lambda$ is the wavevector magnitude of light in air, so $k_i = \sqrt{\varepsilon_\infty}\, k$. Setting each exponent equal to zero and substituting for k and k_i in terms of λ, we get:

$$\frac{\partial^2 S_m}{\partial z^2} + 4\pi i \frac{\sqrt{\varepsilon_\infty}\cos\alpha}{\lambda} \frac{\partial S_m}{\partial z} + q^2 m\left[\frac{4\pi\sqrt{\varepsilon_\infty}}{q\lambda} \sin\alpha - m \right] S_m + \sum_{l=1}^{\infty} \frac{2\pi^2}{\lambda^2} \varepsilon_l \left(S_{m+l} + S_{m-l}\right) = 0 \tag{2.99}$$

I assume that the sample is non-absorbing so I omit the complex part of the permittivity. In addition, if the diffracted wave intensities vary slowly with distance compared to the wavelength, then we can ignore the second derivative without significantly impairing the accuracy.

The last term in Eq. (2.99) specifies the coupling between diffracted waves based on the grating harmonics ε_l. For the fundamental wavevector, l=1 and the coupling is only between adjacent waves. The 0th order may couple

to the ±1st orders, the 1st order may couple to the 0th and 2nd orders, etc. Higher order diffraction is calculated by multiple diffraction steps. To get third order diffraction, for example, the 0th order must diffract to the 1st order, the 1st to the 2nd, and the 2nd to the 3rd.

Overtones of the fundamental wavevector can directly couple waves that are not adjacent. For example, the 2nd overtone can couple the 0th wave to the 2nd, and the 2nd to the 4th. The 3rd overtone can couple the 0th to the 3rd wave, etc.

In a thick grating, higher order diffraction is strongly suppressed. Waves diffracted after the first order are not properly phase matched because the diffraction is not at Bragg angle. Therefore phase cancellation occurs over the distance the beams travel through the grating. Eq. (2.99) is a complex equation so the S_m contain phase information. This phase information ensures that the phase cancellation effects are computed properly.

2.8. Relating the mechanical and electrical energy in polaritons

In this section I will derive the relative phase and magnitude between the electric field and the lattice displacements. Then I will derive expressions for the peak mechanical and electrical energy in the polariton, and the proportion of the mechanical energy to the total energy. We will have to use these expressions to calculate the displacement produced by the impulsive

driving force, because the energy is divided between the electric field and the harmonic oscillator. Therefore the peak displacement of the oscillator is less than if the oscillator were not coupled to the electric field.

2.8.1 Magnitude and phase between E and Q:

Starting with the equation of motion for the polariton (Eq. (2.45)), we assume a solution of the form $Q = Q_0 e^{i(kx-\omega t)}$ and $E = E_0 e^{i(kx-\omega t-\phi)}$, where ϕ is the phase between E and Q. This gives us:

$$e^{-i\phi}E_0 = \frac{\left(-\omega^2 - b_{11} - i\omega\Gamma\right)}{b_{12}}Q_0 \tag{2.100}$$

Substituting for b_{12} and b_{11} from Eqs. (2.42) and (2.43) and taking the magnitude we get:

$$\frac{E_0}{Q_0} = \left[\frac{\left(\omega_T^2 - \omega^2\right)^2 + \left(\omega\Gamma\right)^2}{\epsilon_0\left(\varepsilon_0 - \varepsilon'_\infty\right)\omega_T^2}\right]^{1/2} \tag{2.101}$$

If damping is negligible, we can simplify:

$$\frac{E_0}{Q_0} \approx \frac{\omega_T^2 - \omega^2}{b_{12}} \tag{2.102}$$

The phase can be found by taking the arctan of the imaginary divided by real components:

$$\phi = \tan^{-1}\left(\frac{\omega\Gamma}{\omega_T^2 - \omega^2}\right) \tag{2.103}$$

For small damping and a frequency not too close to the resonant frequency $(\omega = \omega_T)$ the phase angle will be negligible.

2.8.2 Energy in mechanical oscillator

The peak energy density (energy per volume) in the mechanical oscillator is simply:

$$U_m = Q_0^2 \omega_T^2 \tag{2.104}$$

Note that this does not depend on the polariton frequency, just the peak displacement Q_0. This is because the spring constant contained in ω_T^2 does not change with the polariton frequency. The polariton frequency is determined by the wavelength of the electric wave, not by the local mechanical oscillators. The wave equation for the polariton is entirely in the electric field equation of motion (Eq. (2.60)).

2.8.3 Energy in electro-magnetic field

The energy density in the electro-magnetic field is twice the electric field energy density of $1/2\, D \cdot E$, since the magnetic energy density is equal to the electric energy density.

$$U_{EM} = D \cdot E = \left(b_{21} Q_0 E_0 + \epsilon_0 \varepsilon'_\infty E_0^2\right) \tag{2.105}$$

where I have substituted from Eqs. (2.47), (2.40), (2.43) and (2.44). Using Eq. (2.102) with the assumption that the damping is negligible, we get:

$$U_{EM} \approx Q_0^2 \left[\left(\omega_T^2 - \omega^2 \right) + \frac{\varepsilon'_\infty}{\varepsilon_0 - \varepsilon'_\infty} \frac{\left(\omega_T^2 - \omega^2 \right)^2}{\omega_T^2} \right] \tag{2.106}$$

The electro-magnetic field energy is greatest for small frequencies.

2.8.4 Ratio of mechanical to total energy

We figure the ratio of energy densities using Eqs. (2.104) and (2.106)*:

$$\frac{U_M}{U_{tot}} \approx \frac{\omega_T^2}{\left(2\omega_T^2 - \omega^2 \right) + \frac{\varepsilon'_\infty}{\varepsilon_0 - \varepsilon'_\infty} \frac{\left(\omega_T^2 - \omega^2 \right)^2}{\omega_T^2}} \tag{2.107}$$

Assuming zero damping, the energy becomes completely mechanical at resonance. This is not true with a nonzero damping. If the damping is significant, then Eq. (2.106) will have to be re-derived with the damping included.

2.9. Calculating the differential polarizability and lattice displacement

2.9.1 Introduction

The differential polarizability $\partial\alpha/\partial x$ can be calculated from an experimental

---

* This equation differs from the one presented in L. Dhar's thesis (ref. [33], Ch. 5, Eq. 20). I believe the error in this thesis is at Eq. 19, where the mechanical energy terms are expressed as the sum of the instantaneous kinetic and potential terms. Dhar apparently taken the sum of the two maximum values instead taking either the maximum kinetic or the maximum potential as the energy of the mechanical oscillator.

measurement of the diffraction efficiency. The diffraction efficiency given by Eq. (2.93) is repeated here for convenience.

$$\eta \approx \sin^2\left(\frac{\partial\alpha}{\partial x}\frac{\pi N x_m z}{2n_1\lambda}\right) \tag{2.108}$$

We can see that we can extract the differential polarizability from the diffraction efficiency measurement if we know the maximum ionic displacement x_m.

2.9.2 Maximum ionic displacement

The maximum displacement of the ions can be estimated from the equation of motion of the harmonic oscillator. We will ignore damping for this estimate. The following derivation assumes a perfect delta function driving force. We will consider the effect of a driving impulse with a finite Gaussian pulse shape in the next section.

The equation of motion for a harmonic oscillator driven by the ISRS force is

$$m\ddot{x} + kx = \frac{\epsilon_0}{2}\frac{\partial\alpha}{\partial x}E^2(t) \tag{2.109}$$

where ϵ_0 is the permittivity of free space. We use a Gaussian time profile for the electric field. The width is set to 2τ so the intensity profile has width $= \tau$.

$$E(t) = E_0 \exp\left(\frac{-t^2}{2\tau^2}\right) \tag{2.110}$$

Assuming the system is starting at $x = 0$, $\dot{x} = 0$, the momentum after the impulse p_i can be found from the time integral of the impulse force:

$$p_i = \int F \cdot dt = \frac{\epsilon_0}{2}\frac{\partial \alpha}{\partial x} E_0^2 \int \exp\left(\frac{-t^2}{\tau^2}\right) = \frac{\epsilon_0}{2}\frac{\partial \alpha}{\partial x} E_0^2 \sqrt{\pi}\tau \qquad (2.111)$$

From the definition of the average Poynting vector, the electric field amplitude can be related to the pulse intensity in the dielectric medium (Lorrain and Corson, Eq. (11-64)[13]):

$$E_0^2 = \frac{I_0}{n\epsilon_0 c} \qquad (2.112)$$

Since we have taken the time integral of the intensity, it makes sense to express the impulse as a function of the energy density per pulse ΔU:

$$\Delta U = \int I \cdot dt = \sqrt{\pi}\tau I_0 \qquad (2.113)$$

Substituting Eq. (2.112) and (2.113) into Eq. (2.111),

$$p_i = \frac{\partial \alpha}{\partial x}\frac{\Delta U}{2nc} \qquad (2.114)$$

The initial momentum can be related to the maximum displacement by the conservation of energy. Immediately after the impulse, the all of the oscillator's energy is kinetic. However, this energy gets divided between the energy of the mechanical oscillator and the energy of the electric field, as we saw in the previous section. One quarter cycle later, the kinetic energy is zero, the mechanical energy is all potential energy, and the electric field

energy is at its maximum. At this point the oscillator is at its maximum displacement. We equate these two energies and solve for the displacement.

$$\frac{k_i x_m^2}{2} = \frac{U_M}{U_{tot}} \frac{p_i^2}{2m} =; \quad x_m = \sqrt{\frac{U_M}{U_{tot}}} \frac{p_i}{\sqrt{mk_i}} = \sqrt{\frac{U_M}{U_{tot}}} \frac{p_i}{m\omega_T} \tag{2.115}$$

Note that the spring constant for the ions is related to the resonant frequency ω_T, not the polariton frequency ω. Substituting from Eq. (2.114), we get the desired expression for the maximum displacement x_m:

$$x_m = \frac{\partial \alpha}{\partial x} \sqrt{\frac{U_M}{U_{tot}}} \frac{\Delta U}{m\omega_T 2nc} \tag{2.116}$$

There is one factor missing from the derivation so far: the efficiency of the ISRS driving mechanism, which decreases towards zero at small wavevectors. The ISRS efficiency was derived by Tom Dougherty and is presented in Section 5.6 in his thesis[34]. The efficiency is related to the amplitude factor K_1 given in the following equation:

$$\begin{aligned} K_1 &= \frac{2\sqrt{(AC+BD)^2 + (AD-BC)^2}}{C^2 + D^2} \\ A &= c^2k^2 - \varepsilon_\infty\left(\omega_1^2 - \gamma_1^2\right) \\ B &= 2\varepsilon_\infty \omega_1 \gamma_1 \\ C &= 2\omega_1\left(\omega_1^2 - \omega_2^2 - (\gamma_1 - \gamma_2)^2\right) \\ D &= -4\omega_1^2(\gamma_1 - \gamma_2) \end{aligned} \tag{2.117}$$

ω_1 and ω_2 are the lower and upper branch frequencies, γ_1 and γ_2 are the damping factors of the lower and upper branches, and k is the wavevector of the polariton. The ISRS efficiency can be found by taking the ratio of K_1 at the wavevector k to K_1 at $k=\infty$ ($K_1(k)/K_1(\infty)$). This factor is now inserted into the previous expression for x_m to get the correct maximum displacement with the ISRS efficiency included:

$$x_m = \frac{\partial\alpha}{\partial x}\frac{K_1(k)}{K_1(\infty)}\sqrt{\frac{U_M}{U_{tot}}}\frac{\Delta U}{m\omega_T 2nc} \tag{2.118}$$

This derivation presumes a delta function for the impulsive driving force. Real pulses have a nonzero duration, of course. When the duration of the driving pulse becomes a significant fraction of the period of oscillation, the pulse will start to become less effective in driving the oscillator. To calculate the efficiency of a pulse of nonzero duration, we must calculate the convolution of the pulse and the oscillator's impulse response. This is done in the next section.

2.9.3 Finite pump pulse duration

We write the convolution of a force with Gaussian time profile with the impulse response of the oscillator:

$$F(t) = \frac{1}{\tau\sqrt{\pi}}\int_{-\infty}^{t}\exp\left(\frac{-t'^2}{\tau^2}\right)\exp(i\omega(t-t'))dt' \tag{2.119}$$

The first term in the integrand is the driving force, while the second is the sinusoidal response of the harmonic oscillator. We solve the integral by completing the squares:

$$-\frac{t'^2}{\tau^2}+i\omega(t-t')=-\left(-\frac{t'}{\tau}-\frac{i\tau\omega}{2}\right)^2+\left(i\omega t-\frac{\tau^2\omega^2}{4}\right)=A^2+B \quad (2.120)$$

We solve Eq. (2.119) by substituting this expression for the exponents.

$$F(t)=\frac{1}{\sqrt{\pi}}e^{B}\int_{-\infty}^{t}e^{-A^2}dA\xrightarrow[t\to\infty]{}e^{B}=\exp(i\omega t)\exp\left(-\frac{\tau^2\omega^2}{4}\right) \quad (2.121)$$

The first exponent is just the solution to the harmonic oscillator. The second exponent is the amplitude factor that gives the effect of the convolution on the amplitude of the oscillator. This factor ranges from 1 for a delta function to 0 for an infinitely long pulse.

We can write the final expression for the maximum displacement by multiplying the response for the delta function impulse in Eq. (2.118) by the convolution term from Eq. (2.121).

$$x_m=\frac{\partial\alpha}{\partial x}\frac{K_1(k)}{K_1(\infty)}\sqrt{\frac{U_M}{U_{tot}}}\frac{\Delta U}{m\omega_T 2nc}\exp\left(-\frac{\tau^2\omega^2}{4}\right) \quad (2.122)$$

2.9.4 Calculating differential polarizability

We can now put the results from the last three sections together to derive the differential polarizability from the measured diffraction efficiency. We

substitute the expression for the maximum displacement from Eq. (2.122) into the equation for diffraction efficiency Eq. (2.108).

$$\eta \approx \sin^2\left(\left(\frac{\partial\alpha}{\partial x}\right)^2 \frac{\pi N z \Delta U}{4\lambda\varepsilon_\infty m\omega_T c}\frac{K_1(k)}{K_1(\infty)}\sqrt{\frac{U_M}{U_{tot}}}\exp\left(-\frac{\tau^2\omega^2}{4}\right)\right) \quad (2.123)$$

For small values of the diffraction efficiency, we can ignore the sin function. Then we notice that the diffraction efficiency should increase as the square of the pump intensity ΔU.

Now we solve for the differential polarizability:

$$\frac{\partial\alpha}{\partial x} = 2\sqrt{\frac{\lambda\varepsilon_\infty m\omega_T c\cdot\sin^{-1}\left(\sqrt{\eta}\right)}{\pi N z\Delta U}\frac{K_1(\infty)}{K_1(k)}\sqrt{\frac{U_{tot}}{U_M}}\exp\left(\frac{\tau^2\omega^2}{4}\right)} \quad (2.124)$$

The differential polarizability can be found from a simple diffraction efficiency measurement if the appropriate material parameters are known.

This expression has been derived for the phonon-polariton response. It is valid for a pure phonon response if U_M/U_{tot} is set to one.

2.9.5 Calculating miscellaneous properties

The equations for calculating the grating phase modulation, the phase shift between diffracted beams from the front and back of the sample, and the electric field produced by the ionic displacement.

The grating phase modulation is given by:

$$\phi = \frac{2\pi\Delta n d}{\lambda} \tag{2.125}$$

The phase difference between beams diffracted between front and back of the sample is

$$Q = \frac{2\pi d\lambda}{\Lambda^2 n} \tag{2.126}$$

The value of this parameter indicates whether the thick or thin grating equations apply. The thin grating condition applies when $Q << 1$. The thick grating condition applies when $Q >> 1$. As indicated in the footnote above, the thick grating condition applies to this experiment.

The electric field E_m generated by the displacement of the polar mode can be found as follows:

$$E_m = \frac{P}{\epsilon_0 \varepsilon'_\infty} = \frac{q_{eff} x_m N}{\epsilon_0 \varepsilon'_\infty} \tag{2.127}$$

where q_{eff} is the effective ionic charge per unit cell as defined in Eq. (2.38), and ε'_∞ is the permittivity for frequencies above the lowest transverse optic mode. This is the field of the THz polariton response, not the field associated with pump or probe laser beams.

2.10. References

1. Born, M. and H. Kun, *Dynamical Theory of Crystal Lattices*. 1954, Oxford: Oxford University Press.

2. Barker, A.S. and R. Loudon, *Response Functions in the Theory of Raman Scattering by Vibrational and Polariton Modes in Dielectric Crystals.* Reviews of Modern Physics, 1972. **44**(1): p. 18-46.
3. Albert, O., *et al.*, *Time-resolved nonlinearities from nonsymmetric polar phonons in PbTiO3 and KNbO3 perovskites.* J. Opt. Soc. Am. B, 1996. **13**(1): p. 29-33.
4. Bakker, H.J., S. Hunsche, and H. Kurz, *Time-resolved study of phonon polaritons in LiTaO3.* Phys. Rev. B, 1993. **48**(18): p. 13524-13537.
5. Dhar, L. and K.A. Nelson, *Single-pulse and multiple-pulse femtosecond spectroscopy of ferroelectric materials.* Ferroelectrics, 1995. **164**: p. 1-13.
6. Dougherty, T.P., G.P. Wiederrecht, and K.A. Nelson, *Impulsive stimulated Raman scattering experiments in the polariton regime.* Journal of the Optical Society of America B, 1992. **9**(12): p. 2179-2189.
7. Etchepare, J., *et al.*, *Third-order nonlinear susceptibilities and polariton modes in PbTiO3 obtained by temporal measurements.* Phys. Rev. B, 1990. **41**(17): p. 12362-12365.
8. Grenier, P., *et al.*, *Soft-mode studies in KTa0.93Nb0.07O3 with use of the time-resolved third-order optical susceptibility chi3.* Phys. Rev. B, 1993. **47**(1): p. 1-4.
9. Kien, D.P., J.C. Loulergue, and J. Etchepare, *Nonlinear response to polariton waves driven in perovskites by femtosecond pulses.* Opt. Commun., 1993. **101**: p. 53-59.
10. Loulergue, J.C. and J. Etchepare, *E-symmetry phonon polaritons in PbTiO3.* Phys. Rev. B, 1995. **52**(21): p. 15160-15165.
11. Planken, P.C.M., *et al.*, *Femtosecond time-resolved studt of the generation and propagation of phonon polaritons in Li NbO3.* Phys. Rev. B, 1992. **45**: p. 7106-7114.
12. Wiederrecht, G.P., *et al.*, *Anomalous Polariton Dynamics in LiTaO3.* Ferroelectrics, 1993. **150**: p. 103-118.
13. Lorrain, P. and D. Corson, *Electromagnetic Fields and Waves.* Second ed. 1970, San Francisco: W. H. Freeman and Company.
14. Auston, D.H. and M.C. Nuss, *Electrooptic Generation and Detection of Femtosecond Electrical Transients.* IEEE Journal of Quantum Electronics, 1988. **24**(2): p. 184-196.
15. Auston, D.H., *et al.*, *Cherenkov Radiation from Femtosecond Optical Pulses in Electro-Optic Media.* Phys. Rev. Lett., 1984. **53**(16): p. 1555-1558.
16. Grenier, P., *et al.*, *Measurement of the soft polariton in KTa0.93Nb0.07O3 by time-resolved four-wave mixing.* Physical Review B, 1994. **50**(22): p. 16295-16308.
17. Kaminow, I.P. and J. W. D. Johnston, *Quantitative Determination of Sources of the Electro-Optic Effect in $LiNbO_3$ and $LiTaO_3$.* Physical Review, 1967. **160**(3): p. 519-522.
18. Steinfeld, J.I., *Molecules and Radiation.* 1989, Cambridge, Massachusetts: The MIT Press.

19. Zhang, X.-C., *et al.*, *Terahertz optical rectification from a nonlinear organic crystal.* Appl. Phys. Lett., 1992. **61**(26): p. 3080-3082.
20. Bakker, H.J., S. Hunsche, and H. Kurz, *Observation of THz Phonon-Polariton Beats in LiTaO3.* Phys. Rev. Lett., 1992. **69**(19): p. 2823-2826.
21. Böer, K.W., *Survey of Semiconductor Physics.* 1990, New York: Van Nostrand Reinhold.
22. Loulergue, J.C. and J. Etchepare, *Two-photon absorption in PbTiO3 with subpicosecond pulses at 620nm.* Ferroelectrics, 1992. **125**: p. 505-510.
23. Wiederrecht, G.P., *et al.*, *Explanation of anomalous polariton dynamics in LiTaO3.* Phys. Rev. B, 1995. **51**(2): p. 916-932.
24. Bakker, H.J., S. Hunsche, and H. Kurz, *Investigation of anharmonic lattice vibrations with coherent phonon polaritons.* Phys. Rev. B, 1994. **50**(2): p. 914-917.
25. Kien, D.P., J.C. Loulergue, and J. Etchepare, *Phase-transition analysis through soft-phonon-polariton behavior in the temporal domain: A/sub 1/ symmetry investigation of the PbTiO/sub 3/ perovskite.* Phys. Rev. B, 1993. **47**(17): p. 11027.
26. Shen, Y.R. and N. Bloembergen, *Theory of Stimulated Brillouin and Raman Scattering.* Phy. Rev., 1965. **137**(6A): p. 1787-1805.
27. Auston, D.H., *Subpicosecond electro-optic shock waves.* Appl. Phys. Lett., 1983. **43**(8): p. 713-715.
28. Brennan, C.J. and K.A. Nelson, *Simulation of time-resolved wavevector overtone spectroscopy of anharmonic phonon-polaritons in ferroelectrics.* Ferroelectrics, 1997. **in print**.
29. Williams, L.R., *Femtosecond Time-Resolved Spectroscopy of Organic Molecular Crystals*, in *Chemistry.* 1988, Massachusetts Institute of Technology: Cambridge, MA. p. 139.
30. Yan, Y.-x. and K.A. Nelson, *Impulsive stimulated light scattering. I. General theory.* J. Chem. Phys., 1987. **87**(11): p. 6240-6256.
31. Eichler, H.J., P. Günter, and D.W. Pohl, *Laser-Induced Dynamic Gratings.* 1986, Berlin: Springer-Verlag.
32. Wiederrecht, G.P., *Femtosecond Time-Resolved Spectroscopy of Phonon Dynamics in Organic Molecular and Ferroelectric Crystals*, in *Chemistry.* 1992, Massachusetts Institute of Technology: Cambridge. p. 243.
33. Dhar, L., *Impulsive Stimulated Scattering Spectroscopy of Thin Film and Bulk Ferroelectric Systems*, in *Chemistry.* 1994, Massachusetts Institute of Technology: Cambridge, MA. p. 135.
34. Dougherty, T.P., *Femtosecond Through Nanosecond Time Resolved Spectroscopy of Structural Phase Transitions*, in *Chemistry.* 1991, Massachusetts Institute of Technology: Cambridge, MA. p. 177.

Chapter 3:
Theory of Anharmonic Phonon-Polaritons

3.1. Introduction

In this chapter we will examine the two most significant sources of possible lattice anharmonicity that will alter the phonon-polariton response. The two factors that we will examine are nonlinearity in the ionic restoring force and nonlinearity in the lattice polarization. These nonlinearities can modify the polariton oscillations in a manner that are potentially observable in a transient grating experiment.

3.2. Anharmonic equations of motion

3.2.1 Linear equations of motion

The equations of motion for the polariton are reproduced here from Chapter 2:

$$\ddot{Q} = b_{11}Q - \Gamma\dot{Q} + b_{12}E + F' \tag{3.1}$$

$$\nabla^2\mathbf{E} = \frac{\varepsilon'_\infty}{c^2}\ddot{E} + \mu_0 b_{21}\ddot{Q} \tag{3.2}$$

$$P = b_{21}Q + b_{22}E \tag{3.3}$$

$$b_{11} = -\omega_T^2 \tag{3.4}$$

$$b_{12} = b_{21} = \omega_T \sqrt{\epsilon_0 (\varepsilon_0 - \varepsilon'_\infty)} \tag{3.5}$$

$$b_{22} = \epsilon_0 (\varepsilon'_\infty - 1) \tag{3.6}$$

3.2.2 Nonlinear coefficients

First we will examine nonlinearity in the restoring force, which occurs when the potential energy surface that governs the ionic motions is anharmonic. We can express a nonlinear force in terms of an expansion of the effective spring constant b_{11} as a power series in Q:

$$\begin{aligned} b_{11}(Q) &= -\omega_T^2 + \left.\frac{\partial b_{11}}{\partial Q}\right|_{Q=0} Q + \frac{1}{2}\left.\frac{\partial^2 b_{11}}{\partial Q^2}\right|_{Q=0} Q^2 + \ldots \\ &\equiv b^{(0)} + b^{(1)} Q + b^{(2)} Q^2 + \ldots \end{aligned} \tag{3.7}$$

Next we can consider nonlinearity in the polarization. α is the macroscopic polarizability that relates polarization to the macroscopic field; $P = \epsilon_0 N \alpha E$. (It is not the microscopic or molecular polarizability that relates the polarization to the local electric field.) In general the polarizability α would include all contributions to the polarization. However, since we deal with the polarization associated with Q explicitly in Eq. (3.3), α refers to all the other components of the polarizability. We expand α in a power series:

$$\alpha(Q) = \alpha_0 + \left.\frac{\partial \alpha}{\partial Q}\right|_{Q=0} Q + \frac{1}{2}\left.\frac{\partial^2 \alpha}{\partial Q^2}\right|_{Q=0} Q^2 + \ldots \tag{3.8}$$

The derivatives in α are primarily due to changes in the electronic polarizability with ionic displacement. Eq. (3.8) is an expression of the

adiabatic approximation, where the electronic wavefunctions are parameterized in terms of the nuclear positions. The electronic polarizability is a function of the electronic wavefunctions, and is therefore parameterized in the same manner. The derivatives in α may also have contributions stemming from anharmonic coupling between the lowest frequency TO mode that is involved in the polariton response and higher frequency polar optic modes.

We can relate α to the permittivity ε'_∞, and expand the permittivity as a nonlinear function of Q:

$$\varepsilon'_\infty(Q) = N\alpha(Q) \equiv \varepsilon^{(0)} + \varepsilon^{(1)}Q + \varepsilon^{(2)}Q^2 + \ldots \tag{3.9}$$

Therefore b_{22} becomes a function of Q as well:

$$b_{22}(Q) = \epsilon_0\left(\varepsilon'_\infty(Q) - 1\right) \tag{3.10}$$

We will not include any Q dependence of b_{12}. b_{12} is an expression of the amount of polarization produced by the ionic displacement, and is therefore an indication of the effective charge on the ion (Böer[1], section 11.2.1). Of course, the effective charge on the ion may change with the electronic wavefunctions. However, this may be treated as an electronic polarization so is adequately described in $\alpha(Q)$.

3.2.3 Anharmonic equations of motion

The equations of motion may be rewritten to show all the terms that vary with the lattice displacement Q. These are the anharmonic equations of motion for the polariton:

$$\ddot{Q} = b_{11}(Q)Q - \Gamma\dot{Q} + b_{12}E + F' \tag{3.11}$$

$$\nabla^2 E = \frac{1}{c^2}\varepsilon'_\infty(Q)\ddot{E} + \mu_0 b_{21}\ddot{Q} \tag{3.12}$$

The nonlinear restoring force affects the phonon part of the polariton through the $b_{11}(Q)$ in Eq. (3.11), while the nonlinear polarization affects the electromagnetic wave through the $\varepsilon'_\infty(Q)$ term in Eq. (3.12).

It should be pointed out that even the linear component of the polarizability $\partial\alpha/\partial Q$ will cause the polariton to become anharmonic. This is because the permittivity $\varepsilon'_\infty(Q)$ will contain a first order term in Q: $N\,\partial\alpha/\partial Q \cdot Q$. This introduced a second order term in Eq. (3.12) when it is multiplied by $\ddot{E}$, which is proportional to Q for any given polariton frequency. Therefore, the polariton equation of motion is intrinsically anharmonic in any ISRS experiment, where $\partial\alpha/\partial Q$ must be nonzero. The magnitude of the anharmonicity arising from $\partial\alpha/\partial Q$ will be discussed in Chapter 8.

In the polariton regime (frequencies well below ω_T), the phonon and the electromagnetic wave are strongly coupled, and Q and E are nearly in phase

(they will be exactly in phase if the damping term Γ=0). The polariton may be thought of as a long-wavelength electromagnetic wave in a highly polarizable medium. The nonlinear restoring force ($b_{11}(Q)$) appears as a nonlinear susceptibility and is indistinguishable from the nonlinear permittivity $\varepsilon'_{\infty}(Q)$. At frequencies approaching ω_T, the phonon becomes decoupled from the electric field. Then Eq. (3.11) becomes the only relevant equation of motion, and $b_{11}(Q)$ will be the only nonlinear term to influence the phonon. This suggests that $b_{11}(Q)$ should be characterized by conducting the experiment at large wavevectors (large angles between pump beams) in order to reach the portion of the dispersion curve that approaches ω_T.

3.2.4 Solutions to the nonlinear equations

The solutions to the linear equations can be written as:

$$\begin{aligned} Q_l(t) &= Q_0 \exp\left[i(kx-\omega t)\right] \\ E_l(t) &= E_0 \exp\left[i(kx-\omega t)\right] \end{aligned} \tag{3.13}$$

The periodic solutions to the nonlinear equations will contain integer multiples of k and ω as follows:

$$\begin{aligned} Q_{nl}(t) &= \sum_n Q_n \exp\left[in(kx-\omega t)\right] = \sum_n q_n Q_l^n(t) \\ E_{nl}(t) &= \sum_n E_n \exp\left[in(kx-\omega t)\right] = \sum_n e_n E_l^n(t) \end{aligned} \tag{3.14}$$

This describes the nonlinear response as a power series in the linear solutions. The higher order terms are introduced in the multiplication of the power series $b_{11}(Q)$ and $\varepsilon'_{\infty}(Q)$ with the linear solution.

3.3. Wavevector Overtone Spectroscopy

3.3.1 Observing frequency harmonics

It is seen here that the nonlinear polarization $N\alpha(Q)E$ can introduce harmonics of the wavevector and frequency into the nonlinear polariton response. If the frequency harmonics are of sufficient amplitude, one would expect to observe them in a standard ISRS experiment, where the diffracted light is proportional to $\left(Q_{nl}(t)\cdot\partial\alpha/\partial Q\right)^2$. However, if the harmonics are small in amplitude compared to the fundamental frequency, they may not be observable in the signal due to the limited dynamic range and signal-to-noise ratio of the experiment. The limited frequency response of the experiment could also preclude the observation of the harmonics. The signal is squared in the diffraction process, which means all frequencies are doubled. (However, one may sometimes observe the true frequencies in the $LiTaO_3$ data due to heterodyning with a relaxational mode.) The convolution with the Gaussian temporal profile of the probe pulse yields a frequency response proportional to $\exp\left(\omega^2\tau^2/4\right)$, where τ is the 1/e half-width pulse duration. The roll-off of sensitivity at higher frequencies could make the harmonics unobservable, especially in the presence of strong fundamental frequency.

3.3.2 *Observing wavevector harmonics*

Instead of looking for harmonics of the frequency, however, one can look instead for the harmonics, or overtones, of the wavevector. This can be done by introducing the probe at the Bragg angle for the grating component at nk instead of the fundamental grating at k. For small wavevectors, this means that the probe angle is approximately a multiple of the pump angle $\theta/2$. To observe the 2nd harmonic (n=2) you would set the probe angle to approximately θ. To observe the 3rd harmonic, the probe angle would be approximately $3\theta/2$. The diffracted signal from the wavevector overtone would be observed at an equal and opposite angle on the other side of the sample.

The key to this idea is that the larger probe angles are not phase matched for coherent diffraction from the fundamental grating. The probe light can be diffracted from the fundamental grating through an angle of $n\theta$ only through higher-order diffraction mechanism, which are highly suppressed in thick gratings such as the interference pattern produced by the coherent polaritons. This provides a much more sensitive method to observe the anharmonic components of the polaritons.

3.3.3 *A problem with nonlinearity in the diffraction grating*

The signal is generated by the diffraction of the probe pulse from a grating consisting of the modulation of the index of refraction by the lattice displacement Q times the differential polarizability $\partial\alpha/\partial Q$. The problem is

that either or both Q and $\partial\alpha/\partial Q$ may be nonlinear, and as we will see below, the results are indistinguishable. In both cases we may observe harmonics of the frequency and wavevector in the diffracted signal.

In the first case the displacement Q_{nl} is nonlinear, while the differential polarizability $(\partial\alpha/\partial Q)_l$ is linear. This can occur if the nonlinearity in the polariton is due to $b_{11}(Q)$. Using the expression for Q_{nl} from Eq. (3.14), we get this expression for the product:

$$\left(\frac{\partial\alpha}{\partial Q}\right)_l Q_{nl}(t) = \frac{\partial\alpha}{\partial Q}\sum_n q_n Q_l^n(t) = \sum_n q_n' Q_l^n(t) \tag{3.15}$$

This gives us the signal which contains frequency and wavevector harmonics.

In the second case the displacement Q_l is linear, while the differential polarizability $(\partial\alpha/\partial Q)_{nl}$ is nonlinear. This is not strictly possible since the nonlinear polarizability will introduce anharmonicity to the polariton response as discussed above. However, if the nonlinearity is small, it will have little effect on the polariton. It may still have a substantial effect on the diffracted signal, which is sensitive to very small modulations in the index of refraction, especially when the path length through the crystal is long. Taking the derivative of Eq. (3.8), we get:

$$\left(\frac{\partial\alpha}{\partial Q}\right)_{nl} Q_l(t) = \left.\frac{\partial\alpha}{\partial Q}\right|_{Q=0} Q_l + \frac{1}{2}\left.\frac{\partial^2\alpha}{\partial Q^2}\right|_{Q=0} Q_l^2 + \ldots = \sum_n a_n Q_l^n(t) \qquad (3.16)$$

This has exactly the same form as the previous equation.

As a result of this problem, we do not know if the observation of frequency and wavevector harmonics is an indication of anharmonicity of the polariton or just nonlinearity in the differential polarizability.

3.3.4 A solution for the problem: the ω(nk) response

There is another solution for the anharmonic polariton equations of motion in Eqs. (3.11) and (3.12) that only applies to damped systems. It is possible to generate polaritons which have a wavevector nk equal to an overtone of the fundamental wavevector and a frequency of $\omega(nk)$. That is, the frequency of the new polariton is not a harmonic of the fundamental frequency, but has the frequency given by the dispersion relation $\omega(k)$ for the wavevector nk. The numerical simulations I performed have verified the possibility of the $\omega(nk)$ signals.

The polaritons generated in this manner will propagate according to the equations of motion. In addition, they can propagate independently of the fundamental polariton. This is not the case for the harmonics discussed above that go as $\exp[in(kx-\omega t)]$, which exist only in conjunction with the fundamental response.

I have not yet worked out a complete analytical treatment for the $\omega(nk)$ response, but a qualitative description will suffice to convey the principle points. The $\omega(nk)$ response will occur only in a damped system. Let us consider the anharmonic polariton at its peak displacement at one-quarter cycle. Ignoring the temporal component for now, the spatial response will go as $\sum \exp[inkx]$. This is true whether the nonlinearities are in the polarizability or the ionic restoring force or a combination of both. The nonlinearities will cause the distortion of the sinusoidal spatial response and thereby create the spatial harmonics.

Now let us turn off all the nonlinearities just past the first half cycle. The spatial profile of the polariton will still contain the harmonics of the wavevector. These will now propagate according to the linear polariton equations of motion, and their frequency will be $\omega(nk)$. In effect, the nonlinearities encountered in the maximum amplitude during the first half cycle act as a pump grating or a source to generate the $\omega(nk)$ components.

The $\omega(nk)$ components will be generated during each maximum excursion. If the system is not damped, the $\omega(nk)$ components from each cycle will not add up in phase, as their frequency is incommensurate with the fundamental. However, if the system is strongly damped, the largest nonlinearities encountered will be during the first half cycle. Any $\omega(nk)$ responses

generated during later cycles will be much weaker and will not cancel the response from the first cycle. I imagine the first half cycle of a damped nonlinear polariton as an impulsive grating, generating signals at the harmonics of the wavevector. These subsequently propagate in a linear manner as the amplitude of the fundamental polariton diminishes.

The $\omega(nk)$ signals are generated by nonlinearity in the polariton response, but not by the combination of a nonlinear differential polarizability and a linear polariton response. Therefore the existence of these signals will be useful for distinguishing the nonlinearity in the diffraction process from nonlinearity in the polariton response.

3.3.5 Nonlinearities in the pump grating

The above discussion assumes that the impulsive driving force from the transient pump grating is entirely sinusoidal. The nonlinearity of $(\partial\alpha/\partial Q)_{nl}$ should not affect the ISRS driving mechanism, since Q=0 for an impulsive force. Therefore all the higher order terms go to zero, leaving only the linear $\partial\alpha/\partial Q$ term. However, other sorts of optical nonlinearities may distort or alter the pump grating in such a way to introduce spatial harmonics into the pump grating. These spatial harmonics can produce the $\omega(nk)$ response even if the entire polariton and diffraction systems are completely linear. Chapter 8 discusses the possible influence of self-diffraction in the pump grating on the experimentally observed $\omega(nk)$ signals.

3.4. Extracting nonlinear coefficients from WOS data

3.4.1 Perturbation expansion

We may extract the nonlinear coefficients in both the ionic restoring force and the polarization from the WOS experimental data. We can do this by first expanding Q and E in harmonics of ω and k, and expressing the nonlinear terms in power series of Q.

$$Q(x,t) = Q_1 e^{i(kx-\omega t)} + Q_2 e^{2i(kx-\omega t)} + \ldots \quad = \quad Q^{(1)} + Q^{(2)} + \ldots \tag{3.17}$$

$$E(x,t) = E_1 e^{i(kx-\omega t)} + E_2 e^{2i(kx-\omega t)} + \ldots \quad = \quad E^{(1)} + E^{(2)} + \ldots \tag{3.18}$$

$$\begin{aligned} b_{11}(Q) &= b^{(0)} + b^{(1)}Q + b^{(2)}Q^2 + \ldots \\ &= b^{(0)} + b^{(1)}\left(Q^{(1)} + Q^{(2)} + \ldots\right) + b^{(2)}\left(Q^{(1)} + Q^{(2)} + \ldots\right) + \ldots \end{aligned} \tag{3.19}$$

$$\begin{aligned} \varepsilon'_{\infty}(Q) &= \varepsilon^{(0)} + \varepsilon^{(1)}Q + \varepsilon^{(2)}Q^2 + \ldots \\ &= \varepsilon^{(0)} + \varepsilon^{(1)}\left(Q^{(1)} + Q^{(2)} + \ldots\right) + \varepsilon^{(2)}\left(Q^{(1)} + Q^{(2)} + \ldots\right) + \ldots \end{aligned} \tag{3.20}$$

The perturbation expansion is straightforward but a lot of algebra is required. I will derive the 2nd order equations to illustrate the process. The first step is to plug the above expressions into the equation of motion of the ionic oscillator Eq. (3.11). We will neglect the damping term for algebraic simplicity. The first order terms give us this relation:

$$-\omega^2 Q_1 = b^{(0)} Q_1 + b_{12} E_1 \tag{3.21}$$

From this we can relate the magnitude of the 1st order electric field to the 1st order displacement.

$$E_1 = \frac{-\left(\omega^2 + b^{(0)}\right)}{b_{12}} Q_1 \equiv \gamma_1^{(1)} Q_1 \tag{3.22}$$

The superscript of $\gamma_1^{(1)}$ is the index of the order, while the subscript indicates the index of the harmonic with which it is associated. We now equate all the 2nd order terms resulting from inserting the above expansions into Eq. (3.11) . We get the following expression:

$$-4\omega^2 Q_2 = b^{(0)} Q_2 + b^{(1)} Q_1^2 + b_{12} E_2 \tag{3.23}$$

From this we can relate the magnitude of the 2nd order electric field to the 2nd order displacement.

$$E_2 = \frac{\left(-4\omega^2 - b^{(0)}\right) Q_2 - b^{(1)} Q_1^2}{b_{12}} \equiv \gamma_2^{(2)} Q_2 + \gamma_1^{(2)} Q_1^2 \tag{3.24}$$

The superscript of $\gamma_j^{(i)}$ is the index of the order, while the subscript indicates the index of the harmonic with which it is associated. For example, $\gamma_1^{(2)}$ is the coefficient of the second order term involving the first harmonic, which is a second order term because it is squared.

The third and higher order relationships between Q_j and E_j are found in the same manner.

The nonlinear coefficients $b^{(i)}$ and $\varepsilon^{(i)}$ are now found by substituting the above expansions in the electro-magnetic wave equation Eq. (3.12). The first order equation simply recovers the dispersion relation. The second order equation is:

$$4k^2E_2 = \frac{1}{c^2}\left(\omega^2\varepsilon^{(1)}Q_1E_1 + 4\omega^2\varepsilon^{(0)}E_2\right) + 4\omega^2\mu_0 b_{21}Q_2 \qquad (3.25)$$

After substituting for the E_j terms, we get an expression in terms of Q. We can then solve for Q_2 in terms of Q_1:

$$\frac{Q_2}{Q_1^2} = \frac{4k^2\gamma_1^{(2)} - \frac{1}{c^2}\left(\gamma_1^{(1)}\omega^2\varepsilon^{(1)} - 4\omega^2\varepsilon^{(0)}\gamma_1^{(2)}\right)}{-4k^2\gamma_2^{(2)} + \frac{1}{c^2}4\omega^2\varepsilon^{(0)}\gamma_2^{(2)} + 4\omega^2\mu_0 b_{21}} \qquad (3.26)$$

3.4.2 Extracting the nonlinear coefficients from the data

The second order expression in Eq. (3.26) contains the first order terms in both the ionic restoring force $b^{(1)}$, which is a component of $\gamma_1^{(2)}$, and the permittivity $\varepsilon^{(1)}$. Each additional power that we solve for will give the next higher order of coefficients in $b^{(i)}$ and $\varepsilon^{(i)}$. For example, we can now solve for the third order equation which will give the amplitude of Q_3 relative to Q_2 and Q_1 in an expression involving $b^{(2)}$ and $\varepsilon^{(2)}$.

It is important to note that anharmonicity in Q and E are produced by the *linear* terms in the expansions of the restoring force coefficient b_{11} and the permittivity ε'_∞ as given in Eqs. (3.19) and (3.20). Since $\varepsilon^{(1)} = N\,\partial\alpha/\partial Q \cdot Q$,

and we must have a nonzero differential polarizability $\partial\alpha/\partial Q$ in an ISRS experiment, the polariton response is inherently anharmonic. The differential polarizability must produce some component at the second harmonic of k and ω in Q and E even if the restoring force coefficient b_{11} is not a function of Q.

The coefficients of the expansions of b_{11} and ε'_∞ may be found from the WOS data using Eq. (3.26) and higher order relationships in the following manner. First, the data must be relatively free of nonlinear contributions from the pump grating caused by self-diffraction or other effects. Second, the data must show that nonlinearity in the polariton response, rather than nonlinearity in the diffraction of the probe beam, is the primary source of the wavevector overtone signals. This is confirmed by the presence of strong $\omega(nk)$ signals. Then the amplitudes of the harmonics in the displacement Q_j are simply found from the peak diffraction efficiency η_j at each of the wavevector overtones, using the equations derived in Chapter 2.

$$\eta_j \approx \sin^2\left(\frac{\partial\alpha}{\partial x}\frac{\pi z}{n\lambda}\sqrt{\frac{N}{2\mu}}Q_j\right) \tag{3.27}$$

The peak diffracted signal usually occurs at the first ionic maximum after the transient T=0 response. (Care must be taken in the experiment to ensure that the experimental conditions are as identical as possible for the various wavevector overtone measurements to ensure accurate comparisons of the overtone diffraction efficiencies.)

The coefficients of the expansions of b_{11} and ε'_∞ are then found by fitting Eq. (3.26) and higher order relationships to the experimental Q_j. Since each power in the expansion yields a single equation involving an unknown coefficient of both b_{11} and ε'_∞, two WOS measurements at different wavevectors k must be performed to solve for both coefficients.

In summary, an expansion of the anharmonic components of the polariton equations of motion yield equations relating the coefficients of the expansions of b_{11} and ε'_∞ to the amplitudes of the WOS data. The *ith* overtone yields information about the *(i-1)* coefficients of the expansions. WOS data from at least two different wavevectors is needed to solve for the coefficients of the two expansions.

3.5. References

1. Böer, K.W., *Survey of Semiconductor Physics*. 1990, New York: Van Nostrand Reinhold.

Chapter 4:
Numerical Simulation of Anharmonic Phonon-Polaritons

4.1. Introduction

I developed a numerical program to simulate phonon-polaritons in ferroelectrics in two dimensions. The starting point for this work was a program written by my predecessor, Lisa Dhar[1]. The purpose of this program is to simulate ultrafast optical experiments in ferroelectrics to better understand the physics of the complex interactions that occur. The program can handle many experimental configurations and details, including grating or pump-probe experiments, coupling of the polaritons to other material modes, anharmonic lattice and dielectric responses, higher order and higher wavevector diffraction of the probe beam, and sequences of multiple pump pulses.

4.2. Polariton equations of motion

In the computer program, the equations of motion derived in Chapter 2 are translated to discrete time and space difference equations. The relationships between the continuous partial derivatives and the finite difference equivalents for any function $F(x,t)$ are given by:

$$\frac{\partial F(x,t)}{\partial t} \rightarrow \frac{F_{i,j}^{n+1} - F_{i,j}^{n}}{\Delta t}; \quad \frac{\partial^2 F(x,t)}{\partial^2 t} \rightarrow \frac{F_{i,j}^{n+1} - 2F_{i,j}^{n} + F_{i,j}^{n-1}}{\Delta t^2} \qquad (4.1)$$

$$\frac{\partial F(x,t)}{\partial x} \rightarrow \frac{F^n_{i+1,j} - F^n_{i,j}}{\Delta x}; \quad \frac{\partial^2 F(x,t)}{\partial^2 x} \rightarrow \frac{F^n_{i+1,j} - 2F^n_{i,j} + F^n_{i-1,j}}{\Delta x^2} \tag{4.2}$$

The superscripts denote the time index of the values, while the subscripts *i,j* give the x and y indexes of the values. The values of Q and E at time step *n+1* are found using the values from the present time step *n* and the previous time step *n-1* using implicit formulas [2]:

$$Q^{n+1}_{i,j} = \frac{1}{1+\Gamma\Delta t}\left[\Delta t^2\left(b_{11}Q^n_{i,j} + b_{12}E^n_{i,j} + F^n_{i,j}\right) + \left(2+\Gamma\Delta t\right)Q^n_{i,j} - Q^{n-1}_{i,j}\right] \tag{4.3}$$

$$E^{n+1}_{i,j} = \frac{1}{\frac{\varepsilon'_\infty}{c^2} + \mu_0\sigma\Delta t}\left[\begin{array}{l} \Delta t^2\left(\frac{E^n_{i+1,j} - 2E^n_{i,j} + E^n_{i-1,j}}{\Delta x^2} + \frac{E^n_{i,j+1} - 2E^n_{i,j} + E^n_{i,j-1}}{\Delta y^2}\right) \\ +\left(\frac{2\varepsilon'_\infty}{c^2} + \mu_0\sigma\Delta t\right)E^n_{i,j} - \frac{\varepsilon'_\infty}{c^2}E^{n-1}_{i,j} \\ -\mu_0 b_{21}\left(Q^{n+1}_{i,j} - 2Q^n_{i,j} + Q^{n-1}_{i,j}\right) \end{array}\right] \tag{4.4}$$

The new value of Q at time *n+1* is found using Eq. (4.3), and this value is then used in Eq. (4.4) to find the new value of E. The forcing function $F^n_{i,j}$ is the spatially periodic impulse force generated by the crossed excitation pulses through the ISRS mechanism[3]:

$$F^n_{i,j} = \frac{1}{2}\epsilon_0\left(\frac{\partial\alpha_{k,l}}{\partial x}\right)E^n_k(i,j)E^n_l(i,j) \tag{4.5}$$

E_k and E_l represent the electric field polarization components and $\partial\alpha_{k,l}/\partial x$ is the differential polarizability of the phonon mode. Since the optic field in

the pump pulses is very much larger than the induced far-IR radiation in the crystal we can let E_k and E_l represent only the optic field. In experiments on uniaxial ferroelectrics, the excitation pulses are often polarized parallel to each other and to the polar axis of the crystal. The program in its current form is limited to this scalar case. All the electric field components as well as Q are polarized along the polar axis of the crystal.

Substituting Q for x we get the force in normal mode units:

$$F_{i,j}^{n} = \frac{N\epsilon_0}{4}\left(\frac{\partial \alpha_{k,l}}{\partial Q}\right)E_k^n(i,j)E_l^n(i,j) \tag{4.6}$$

Note that this formulation varies by a factor of 1/2 from the ISRS force in the theses of previous Nelson group graduate students[4, 5]. I believe that an error was introduced into the previous works in the change of the force to normal mode units.

4.2.1 Equations for coupling a relaxational mode to the polariton

The analytical expression for coupling of the polariton mode to a relaxational mode was given in Chapter 2. After making the substitution $B^{r1}Q_r = Q_r'$ and the finite difference equivalent of the time derivative we solve for the latest value of Q_r:

$$Q_r^n = \frac{\Delta t Q^n + \tau Q_r^{n-1}}{\Delta t + \tau} \tag{4.7}$$

In the program Q_r^n is updated using Eq. (4.7) then the term $B^{1r}B^{r1}Q_r^n$ is added to the force function $F_{i,j}^n$ in Eq. (4.3) and used to calculate Q^{n+1}. In practice we can assume that $B^{1r} = B^{r1}$. Since Q_r^n is in general a very slowly changing quantity there is no need to solve self-consistently for Q_r^n and Q^n. If these two interacting quantities were changing on approximately the same time scale then a self-consistent solution would have to be used instead of the simple iterative solution used here.

4.3. Simulating pump and probe pulses

4.3.1 Propagation of pump pulses

The equations for calculation of the position of the pump pulses, their spatial profiles, and the resulting interference grating are given in Chapter 2.

4.3.2 Propagation of probe pulse

The position of the center of the probe pulse is calculated using simple trigonometry. The probe is assumed to travel left to right. The position of the probe pulse at the first Bragg angle is:

$$\begin{aligned} x(t) &= x_0 + c' \sin(\theta/2) \cdot (t - t_0) \\ y(t) &= c' \cos(\theta/2) \cdot (t - t_0) \end{aligned} \tag{4.8}$$

The pump pulse is rotated with respect to the axes in the simulation coordinates because the pump beam is incident at an angle $\theta/2$. x', y' are the coordinates in which the pump profile is not rotated. The intensity profile is

calculated in these coordinates then transferred back to the simulation coordinates.

$$\begin{bmatrix} x'(t) \\ y'(t) \end{bmatrix} = \begin{bmatrix} \cos(\theta/2) & -\sin(\theta/2) \\ \sin(\theta/2) & \cos(\theta/2) \end{bmatrix} \begin{bmatrix} x(t) \\ y(t) \end{bmatrix} \tag{4.9}$$

$$I(x,y) = I(x',y') = I_0 \pi^{-1} \frac{1}{\sigma_x \sigma_y} e^{-\left(\frac{x'}{\sigma_x}\right)^2} e^{-\left(-\frac{y'}{\sigma_y}\right)^2} \tag{4.10}$$

However, rather than calculating the intensity at each point, a pre-calculated rectangular array of numbers representing the two-dimensional intensity profile is used instead. This intensity array is called the "probe mask". Eq.(4.8) is used to calculate the position of the center of the probe mask array, and then the pre-computed values in the array are used to determine the probe intensity at each point.

One major simplification concerning the propagation of the probe pulse is that the probe at the fundamental Bragg angle is the only one for which the position and orientation is calculated. The diffraction and coupled wave equations for probe beams at the Bragg angles for the spatial harmonics of the excitation grating are calculated from the region in the grid that is sampled by the probe at the first Bragg angle. The inaccuracies introduced by this simplification deal primarily with the phase matching of the probe with the polariton field. At larger probe angles there will be a loss of high-frequency information in the actual experiment if the sample is too thick.

The possible loss of phase matching in the probe at the higher Bragg angles will not be accurately simulated by this program.

4.4. Calculation of diffracted probe by coupled-wave algorithm

The ISRS signal consists of light diffracted by the phonon displacements Q, which induce changes in the refractive index through the linear electro-optic effect. If the spatial modulation of Q has a period d, then a transient diffraction grating with wavevector magnitude $k_d = 2\pi/d$ is formed. The intensity of light diffracted by grating wavevector k_d is proportional to the square of the Fourier transform of the displacements along the x axis, summed over the y axis and weighted by the probe intensity profile $P_{i,j}^n$.

$$\Delta\varepsilon_l^n = N\frac{\partial\alpha}{\partial Q}\mathrm{FFT}_{l,i}\left(\sum_j P_{i,j}^n Q_{i,j}^n\right) \tag{4.11}$$

where $\mathrm{FFT}_{k_d,i}$ is the fast Fourier transform over index spatial index i and returning results in terms of wavevector index l. The diffraction grating with wavevector k_d may be monitored by a variably delayed probe pulse which is incident on the sample at the Bragg angle α for that wavevector, given by

$$\sin(\alpha) = m\cdot\left(\frac{k_d\lambda_p}{4\pi}\right) \qquad m = \pm1, \pm2, \pm3, \ldots \tag{4.12}$$

where α is the angle of incidence with respect to the bisector of the excitation beams, m is the order of the diffraction, and λ_p is the wavelength of the probe beam.

In the wavevector overtone spectroscopy experiment we are interested at looking for spatial components of the grating that are harmonics of the fundamental wavevector $k_d = m \cdot k_g$. If these spatial components exist then there will be diffracted signal when the probe is at the first Bragg angle for k_d. The diffracted light will not consist entirely of signal diffracted from k_d, however. At each probe angle there will also be contributions due to higher-order diffraction from the fundamental wavevector and possibly from lower-order harmonics. In fact, light from any order can diffract into the adjacent order, whether higher or lower.

To properly calculate higher order diffraction and multiple diffraction processes we need to use coupled-wave theory. An extension of this theory suitable for the wavevector overtone experiments was developed in Chapter 2. The resulting equation was:

$$\frac{\partial^2 S_m}{\partial z^2} + 4\pi i \frac{\sqrt{\varepsilon_\infty}\cos\alpha}{\lambda}\frac{\partial S_m}{\partial z} + q^2 m\left[\frac{4\pi\sqrt{\varepsilon_\infty}}{q\lambda}\sin\alpha - m\right]S_m + \sum_{l=1}^{\infty}\frac{2\pi^2}{\lambda^2}\varepsilon_l\left(S_{m+l} + S_{m-l}\right) = 0 \tag{4.13}$$

4.4.1 Numerical simulation of coupled-wave equations

The coupled-wave equations with the approximations mentioned above can be put into the following form:

$$\frac{dS_m}{dz} = C_1 m[C_2 - m]S_m + C_3 \sum_{l=1}^{\infty} \varepsilon_l (S_{m+l} + S_{m-l})$$
$$C_1 = \frac{iq^2\lambda}{4\pi\sqrt{\varepsilon_\infty}\cos\alpha} \quad C_2 = \frac{4\pi\sqrt{\varepsilon_\infty}}{q\lambda} \quad C_3 = \frac{i\pi}{2\lambda\sqrt{\varepsilon_\infty}\cos\alpha} \tag{4.14}$$

This describes a set of coupled first order differential equations. This type of problem can be easily integrated using a 4th order Runge-Kutta algorithm. Defining $f(S_m) \equiv dS_m/dz$ and $f(\mathbf{S}) \equiv d\mathbf{S}/dz$, where $\mathbf{S}$ is a vector consisting of all S_m, we can write a vector version of the 4th order Runge-Kutta integration algorithm:

$$\begin{aligned}
d\mathbf{S}_1 &= f(\mathbf{S}^n) \\
d\mathbf{S}_2 &= f\left(\mathbf{S}^n + \frac{\Delta z}{2} d\mathbf{S}_1\right) \\
d\mathbf{S}_3 &= f\left(\mathbf{S}^n + \frac{\Delta z}{2} d\mathbf{S}_2\right) \\
d\mathbf{S}_4 &= f(\mathbf{S}^n + \Delta z\, d\mathbf{S}_3) \\
\mathbf{S}^{n+1} &= \mathbf{S}^n + \frac{\Delta z}{6}(d\mathbf{S}_1 + 2d\mathbf{S}_2 + 2d\mathbf{S}_3 + d\mathbf{S}_4)
\end{aligned} \tag{4.15}$$

The wave strengths S_m^n are updated at each time step by propagating the pulses forward by a distance $\Delta z = c\Delta t/\sqrt{\varepsilon_\infty}$, which is the distance light travels during one time step. At each time step the program calculates the

diffracted waves for a number of different probe angles, and for each probe angle the diffracted waves are calculated for the whole range of probe delay times. Therefore the actual S values are stored in a three dimensional array $S^n_{i,j,m}$, where i is the index for the probe angle, j is the index for the probe delay, and m is the index for the diffracted wave. So unlike the experiment, where the signal for various values of probe delay are found over many excitation pulses, and the data for various probe angles are found over several experiments, the program acquires all this information from one simulated pump pulse.

The initial condition for the simulation is $S^0_{i,j,0} = 1$, that is, for each probe angle i and probe delay j all the probe intensity is initially in m=0 (the non-diffracted wave). We are interested in the Bragg angle diffraction from the wavevector harmonics $l \cdot q$, where q is the fundamental wavevector and $l = 1,2,3\ldots$. The first probe angle should yield signal at the first diffracted wave, the second probe angle at the second diffracted wave, etc. Therefore the program records the final wave $S^N_{l,j,l}$ when n equals the total number of steps N. The wave that is diffracted at the same angle number l as the probe angle is recorded for each value of the probe delay time, as this is the Bragg diffracted signal for the wavevector harmonic $l \cdot q$.

4.5. Setting up the finite difference grid

The program is based on a finite difference grid that is separated into three distinct regions. The first region represents a dielectric region in front of the ferroelectric crystal; the second region represents the crystal; and the third region represents a dielectric region behind the crystal. The regions in front and in back of the crystal are necessary to accurately simulate the reflection and transmission of the THz polariton field. In the second region the equations of motion for both the lattice displacement Q and the electric field E are solved using Eqns. (4.3) and (4.4). In the first and third regions only the electric field is solved for using Eq. (4.4). The index of refraction is assumed to be linear in regions 1 and 3, and different indexes of refraction can be assigned to the two regions.

An artificial damping term (a conductivity) is introduced into regions 1 and 3 to absorb electromagnetic waves that propagate away from the surface of the crystal. This damping term increases linearly from 0 to a maximum value specified by the user at the edge of the simulation grid. Damping terms are also added to region 2 at the right and left sides of the grid. At each side there is a damping region of user specified extent in which the electrical damping term increases from 0 to the maximum specified value at the grid boundary. In this region the mechanical damping term Γ increases linearly from its normal value to a larger value specified by the operator. These additional terms in the left and right damping zones in region 2 help prevent the polariton waves from reflecting back in from the grid boundaries and

interfering with the outgoing waves, which would confuse the simulation results. The driving forces are also set to zero in the damping regions to prevent numerical artifacts arising from driving overdamped and therefore slowly relaxing dipole modes. These create undesired low-frequency components that propagate into the simulation grid, which can also interfere with the simulations.

All three regions have the same user-specified grid spacing in the x-direction, which is perpendicular to the pump axis. Each region can have a different grid spacing in the y-direction, parallel to the pump axis. This is to allow a larger grid spacing in the dielectric regions where the wavelengths may be longer for a given frequency due to lower index of refraction. The dielectric regions 1 and 3 are not allowed to have different grid spacing in the x-direction because this would make it difficult to ensure continuity of the wave equations at the boundary with region 2. In addition, the wavelength of the excitation in the x-direction is established by the grating wavevector. Since the wave equations are continuous at the boundaries, the grids in regions 1 and 3 need the same spacing in the x-direction as region 2 to accurately simulate the horizontal component of the wave.

The grid size must be chosen so there are at least 5 or 6 grid points per wavelength for the shortest wavelength of interest in the simulation. The program can automatically set the grid size if the user requires. The user must specify how many points are to be used for the fundamental

wavelength as specified by the excitation wavevector k_g. For wavevector overtone simulations it is necessary to specify a number appropriate for the highest wavevector harmonic that one hopes to observe in the simulation. For instance, if you specify 25 points per wavelength, you can accurately simulate up to the 5th wavevector overtone.

The time step must be chosen for both good accuracy and stability. If the time step is too large the simulation will become unstable. The condition for stability is:

$$\frac{1}{\varepsilon}\left(\frac{c\cdot\Delta t}{\Delta x}\right)<1 \qquad (4.16)$$

where Δx is the grid spacing in either the x or y direction, Δt is the time step, and ε is the permittivity in the region of interest. To ensure an additional margin of stability the program will give an error message if the left hand term in Eq. (4.16) is greater than 0.5.

4.6. Overall program operation

The first step of the program is to read in the parameters that specify the simulation to be performed. The simulation parameters are specified in a text file called "params.txt". This file contains all the simulation parameters for a single pump pulse experiment, including simulation control parameters, material properties, and the configuration of the experiment to be simulated. An example of the input file "params.txt" is shown in Appendix C. Multiple

pump pulse experiments, such as experiments using shaped pulse trains, may be simulated using an additional input file to specify the pump pulse sequence. This file is called "pump_pulses.txt".

After the parameter files have been read in and parsed, the parameters are converted to program units. The units used in the program are femtoseconds, microns, microcoulombs, and femtograms. These units were chosen to avoid very large exponents in the floating point calculations, although since all the calculations are double precision I am not certain that this is necessary. Some program constants such as grid sizes and array sizes are also set during this phase.

The next step in the program execution is to allocate memory for the arrays. All arrays are dynamically allocated, which means that the memory is obtained from the operating system after the program has started to run. This allows the simulation grids and the arrays containing the time-resolved probe signals to be any size up to the limit of memory in the computer. Some of the subroutines need additional storage arrays to perform their calculations. These routines allocate their own memory for these arrays the first time that they are called.

At this point, the simulation is ready to run. At each time step, the program sweeps through the grid, performing computations of the equations of motion. Within region 2, the force from the pump beams at each point is

calculated using Eq. (4.6); the relaxational mode is updated using Eq. (4.7) and the resulting force from the relaxational mode is added to the pump force; forces from anharmonic terms in the lattice restoring force are computed and added to the total force; the lattice displacements are updated using Eqn. (4.3) ; and the electric field is updated in all three regions using Eq. (4.4).

After the equations of motion are calculated at the current time step, the diffraction grating sampled by the probe pulses is computed. The coupled-wave equations are integrated by one time step to calculate the diffracted probe light for each value of the probe angle and probe delay.

At intervals specified by the user, files containing any or all of the following quantities are printed out: the current lattice displacement; the current electric field; the Fourier transform of the current diffraction grating sampled by the probe pulse; and the time-integrated coupled wave magnitudes for the Bragg diffraction from the spatial harmonics of the grating. The final output of the simulation is in the last printout of the coupled-wave magnitudes.

The program is also capable of simulating pump-probe type experiments, where the observed signal is due to a change in the polarization angle of the probe beam. The modulation of the probe is due to a change in birefringence produced by the polariton displacement. In this case there is no coupled wave output file. The output files that normally contains the transform of the

diffraction grating sampled by the probe are used instead to hold the birefringence sampled by the probe instead.

The total simulation time and the range and increment of the probe delay times are specified by the user. The program will give a warning if the simulation will end before the probe pulse with the biggest delay can traverse the sample. This will cause the signal to show anomalous damping for the largest values of the probe delay. The program can automatically set the maximum probe delay time so all the probe pulses pass completely through the sample before the simulation ends.

4.7. References

1. Dhar, L., *Impulsive Stimulated Scattering Spectroscopy of Thin Film and Bulk Ferroelectric Systems*, in *Chemistry*. 1994, Massachusetts Institute of Technology: Cambridge, MA. p. 135.
2. Cheney, W. and D. Kincaid, *Numerical Mathematics and Computing*. 1980, Monterey, CA: Brooks/Cole Publishing Company.
3. Shen, Y.R. and N. Bloembergen, *Theory of Stimulated Brillouin and Raman Scattering*. Phy. Rev., 1965. **137**(6A): p. 1787-1805.
4. Wiederrecht, G.P., *Femtosecond Time-Resolved Spectroscopy of Phonon Dynamics in Organic Molecular and Ferroelectric Crystals*, in *Chemistry*. 1992, Massachusetts Institute of Technology: Cambridge. p. 243.
5. Williams, L.R., *Femtosecond Time-Resolved Spectroscopy of Organic Molecular Crystals*, in *Chemistry*. 1988, Massachusetts Institute of Technology: Cambridge, MA. p. 139.

Chapter 5:
Numerical Simulation Results

5.1. Introduction

In this chapter I will present some of the results from the phonon-polariton simulation program described in the previous chapter. This program has proven itself invaluable in this investigation.

5.2. Simulation of the polariton wavevector problem

In Chapter 2 it is explained how the wavevector of the polariton differs from the wavevector of the grating, because the wavevector of the polariton has a forward component. The relation between the wavevectors of the grating and the polariton is derived from conservation considerations, and it is also proven that the polariton wave that is allowed by conservation is properly phase matched to the moving grating. This insight was suggested by the 2-D simulation results, such as the one shown in Figure 2.10. It is clear from this picture that the polariton field consist of two plane waves moving with a substantial forward component. Because the analytical models previous researchers used were one-dimensional, the two-dimensional aspect of the polariton behavior in a transient grating experiment had been largely overlooked. The computer program, however, solved the 2-D problem correctly.

The relationship between the wavevector of the grating and the polariton is given by the following expression:

$$k_p^2 = k_g^2 + (\omega/c')^2 \cos^2(\theta/2) \qquad (5.1)$$

where k_p is the polariton wavevector, k_g is the grating wavevector, ω is the polariton frequency, c' is the speed of light in the sample, and θ is the angle between the two pump beams. The relationship between ω and k_p is given by the dispersion relationship for the polariton:

$$\omega^4 \varepsilon'_\infty + \omega^3 i\Gamma \varepsilon'_\infty - \omega^2\left(c^2 k_p^2 + \omega_T^2 \varepsilon_0\right) - \omega\, i\Gamma c^2 k_p^2 + \omega_T^2 c^2 k_p^2 = 0 \qquad (5.2)$$

The analytical relationship between the polariton and grating wavevector magnitudes given in Eq. (5.1) has been confirmed in simulations of grating experiments, using realistic parameters for $LiTaO_3$ obtained from previous experimental data [1]. Figure 5.1 depicts the theoretical dispersion relation Eq. (5.2) plotted as a solid curve, along with phonon-polariton frequencies determined from simulated grating experiments. The frequencies are plotted against the grating wavevector (open circles) and the polariton wavevector (crosses). There are significant deviations from the theoretical curve when the frequency is plotted against the grating wavevector, while there is a near-perfect fit to the theoretical curve when plotted against the polariton wavevector. This shows two things: the simulation program solves the linear polariton program accurately over a wide range of wavevectors; and it confirms the analytical relationship between grating and polariton wavevectors expressed in Eq. (5.1).

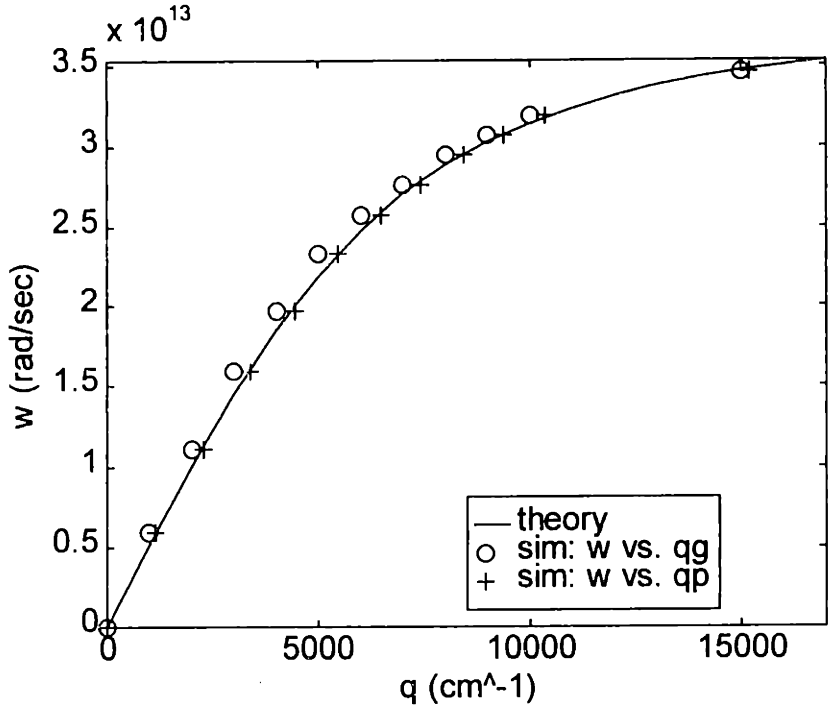

Figure 5.1 Plot of phonon-polariton frequency ω vs. wavevector q for $LiTaO_3$. The theoretical dispersion relation is shown by the solid curve. The frequency values derived from simulations fall along this curve when plotted vs. polariton wavevector, calculated with the polariton phase velocity taken into account, but not when plotted vs. the grating wavevector.

5.3. Anharmonic potentials

We now examine the effects of a nonlinear lattice restoring force (i.e. an anharmonic lattice potential) on the ISRS experiment by treating the coefficient b_{11} as a power series in Q:

$$b'_{11}(Q) = -\left(\omega_0^2 + a_1 Q + a_2 Q^2 + \ldots\right) \tag{3}$$

In the standard grating experiment, the probe beam is incident at the Bragg angle for diffraction by the excitation grating q_g, and the first-order diffracted beam is detected at the same angle on the other side of the sample. In order

to introduce substantial anharmonicity we choose a_1 and a_2 such that $\omega_0^2 \approx a_1 Q \approx a_2 Q^2$ at the largest value of Q encountered in the harmonic simulations. A comparison of the simulated ISRS signal for the harmonic and anharmonic potentials is shown in Figures 5.2a and 5.2b. The anharmonic simulation has a somewhat higher damping rate and its period of oscillation shows a slight amplitude dependence. However, the anharmonic simulation displays no frequency harmonics in the calculated diffracted signal, as the power spectrum in the inset of Figure 5.2b shows. (The power spectrum peaks at 2ω instead of ω in the linear and nonlinear response cases because the ISRS signal is proportional to the square of the response.)

These simulations demonstrate that lattice anharmonicity does not produce frequency harmonics in the first-order diffraction of the probe at Bragg angle. This is because the nth harmonic of the fundamental frequency is associated with nth harmonic of the wavevector in the expansion, which has terms that go as $\exp[ni(kx - \omega t)]$. If only first-order diffraction is considered, the nth harmonic will only appear in signal diffracted from the nth wavevector overtone. However, the frequency harmonics can be coupled into the diffracted signal at the first Bragg angle by higher-order diffraction. We will see in a later section that much more information about the effects of lattice anharmonicity is obtained when the full coupled-wave diffraction algorithm is used in the simulations.

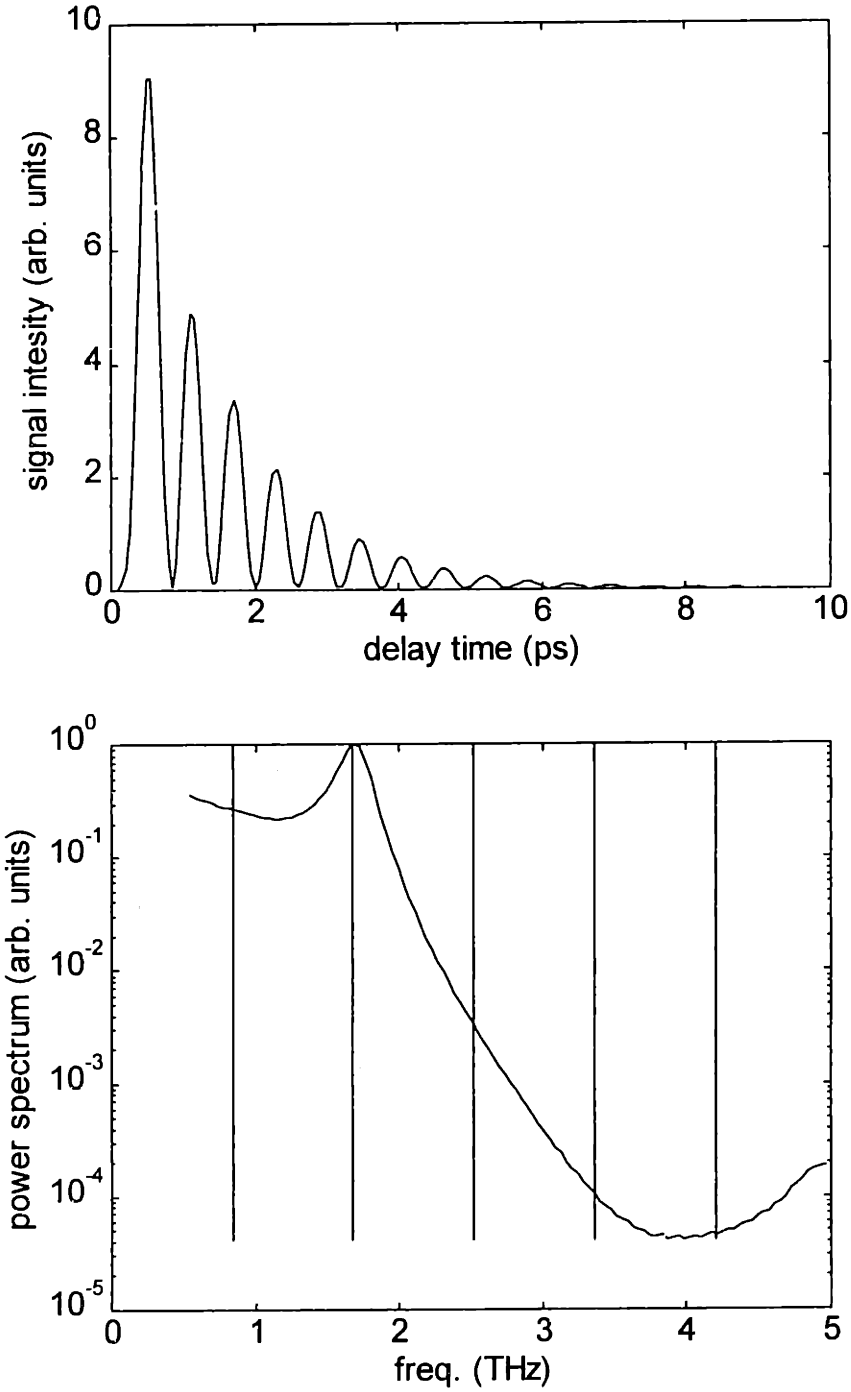

Figure 5.2a Top: simulated ISRS signal for harmonic lattice model. Bottom: the power spectrum with dashed vertical markers denoting the multiples of the phonon-polariton frequency ω.

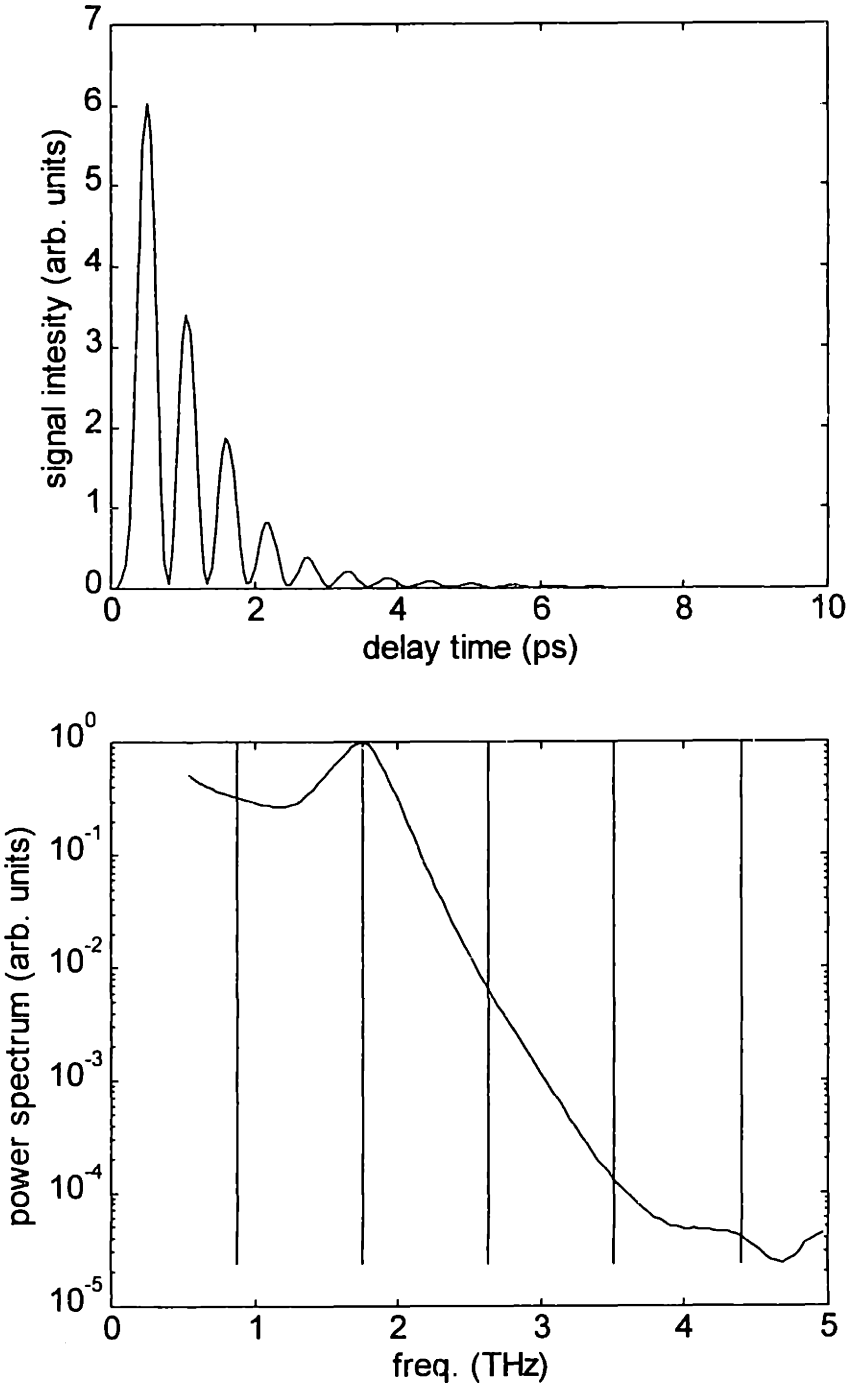

Figure 5.2b: Top: simulated ISRS signal for anharmonic lattice model. Bottom: the power spectrum with dashed vertical markers denoting the multiples of the phonon-polariton frequency ω. No harmonics of the fundamental show up in the first-order diffraction at the first Bragg angle.

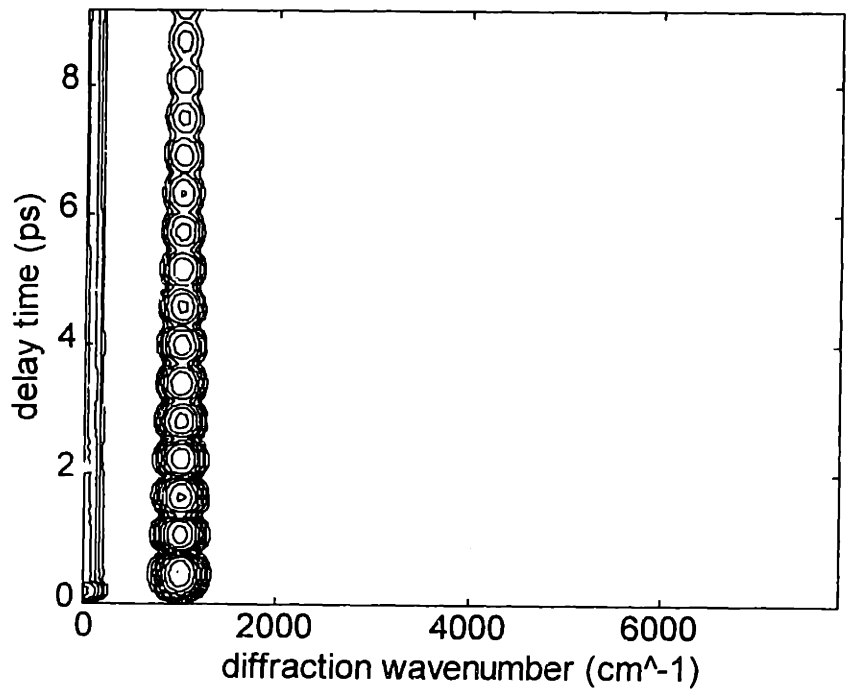

Figure 5.3a Contour plot of log of diffraction grating magnitude vs. time as a function of the diffraction grating wavevector (harmonic potential).

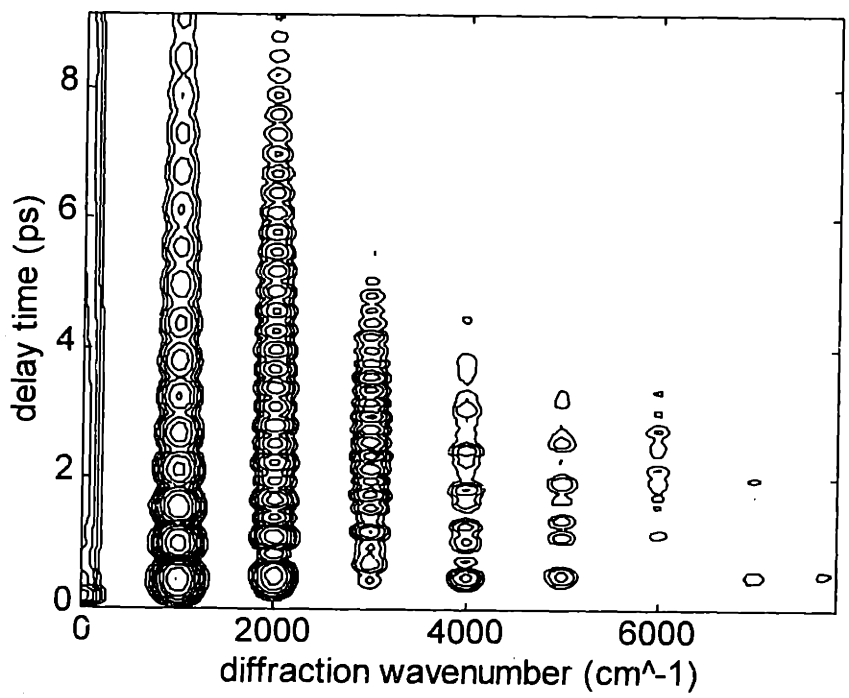

Figure 5.3b Contour plot of log of diffraction grating magnitude vs. time as a function of the diffraction grating wavevector (harmonic potential).

5.4. Wavevector overtone spectroscopy

We can simulate wavevector overtone spectroscopy results by calculating the diffraction grating magnitude as a function of the diffraction wavevector q_d. Figure 5.3 shows signals whose amplitudes cover a range of four decades, plotted logarithmically against probe delay time and diffraction wavevector. The results for the harmonic potential are shown in Figure 5.3a, which indicates signal only at the fundamental wavevector component. The results for the same anharmonic potential used above are shown in Figure 5.3b, which indicates substantial signal levels at the harmonics of the grating wavevector. The plots in Figures 5.3a and 5.3b depict the diffraction grating produced by the polariton displacement, calculated as the material response to an impulsive driving force, convoluted with the finite 80-fs probe pulse duration. The effect of this convolution is to filter out the high-frequency components in the response.

These simulation results clearly show the potential of the WOS technique. It is evident from these results that the lattice anharmonicity creates substantial spatial overtones in the diffraction grating associated with the polariton displacement. It appears obvious that a probe beam introduced at the Bragg angle for one of these grating overtones would be diffracted and could be used to measure the time response of the overtone signal. However, these simulations show only what the magnitude of the diffraction grating, not what the resulting diffracted signal will be. The next addition to the program

was the coupled-wave algorithm for computing the actual diffracted signal, including higher order diffraction, etc.

5.5. Coupled-wave simulations

I added the coupled-wave diffraction algorithm described in Chapter 2 to get more accurate simulations of the diffracted probe signal. The results from one such simulation with arbitrary 3rd and 4th coefficients in the ionic potential are shown in Figure 5.4a-5.4d. The damping is much too small in these simulations because $LiTaO_3$ exhibits coupling between the polariton mode and certain other phonon modes at particular wavevectors, which increases the damping[2]. I have not included this phenomenon in the polariton simulation program. This set of simulations was not intended to accurately model $LiTaO_3$, however. The purpose was to see what types of signals might be observed in a WOS measurement.

The four plots in Figure 5.4a-5.4d represent simulated signal for probe angles at the 1st through 4th Bragg angles. Harmonics of the fundamental are clearly seen at the 1st Bragg angle in Figure 5.4a, which differs from the result shown in Figure 5.2b. This shows that the detailed modeling of the diffraction process is essential to understanding the spectroscopic content of the anharmonic grating experiment. The frequency harmonics appear at the first Bragg angle because they are coupled from higher wavevectors by higher-order diffraction processes and the additional coupling between waves due to the wavevector overtones. The results of figure 5.2b differs

from those of Figure 5.4a because the latter include these effects whereas the former do not.

The simulations for the 2nd through 4th wavevector overtone (i.e. the 2nd to 4th Bragg angle) reveal complicated spectra marked by the appearance of the expected $\omega(nk)$ signal, that is, the frequency associated with the integer multiple of the grating wavelength in the linear polariton dispersion curve. We also see harmonics of the $\omega(nk)$ frequencies and harmonics of the fundamental frequency $\omega(k)$. Finally, there are a number of other peaks in the power spectra that appear to be sum and difference frequencies. The peaks that can be identified are labeled in the power spectra in the insert of each plot.

These simulations show that we may expect clear WOS signals if any appreciable amount of lattice anharmonicity is influencing the polaritons. In particular, these simulations made it clear that the $\omega(nk)$ signals are the distinctive signature of the lattice anharmonicity. Nonlinearity in the electro-optic coefficient may result in nonlinearity in the diffraction process. This can generate harmonics of the fundamental frequency, and can also create wavevector overtone signals which contain harmonics of the fundamental. It does not produce the $\omega(nk)$ signals, however. Therefore, the $\omega(nk)$ frequencies are what we would hope to find in a WOS experiment.

Chapter 8 presents the results of WOS experiments in $LiTaO_3$ where the $\omega(nk)$ signals were indeed observed. The data from the experiment differs substantially from the simulation results presented here, which may be expected because arbitrary anharmonic coefficients were used. However, the qualitative agreement between the simulation results and experiment is quite good. All of the types of frequencies discussed above are clearly present in both the simulated and experimental WOS results.

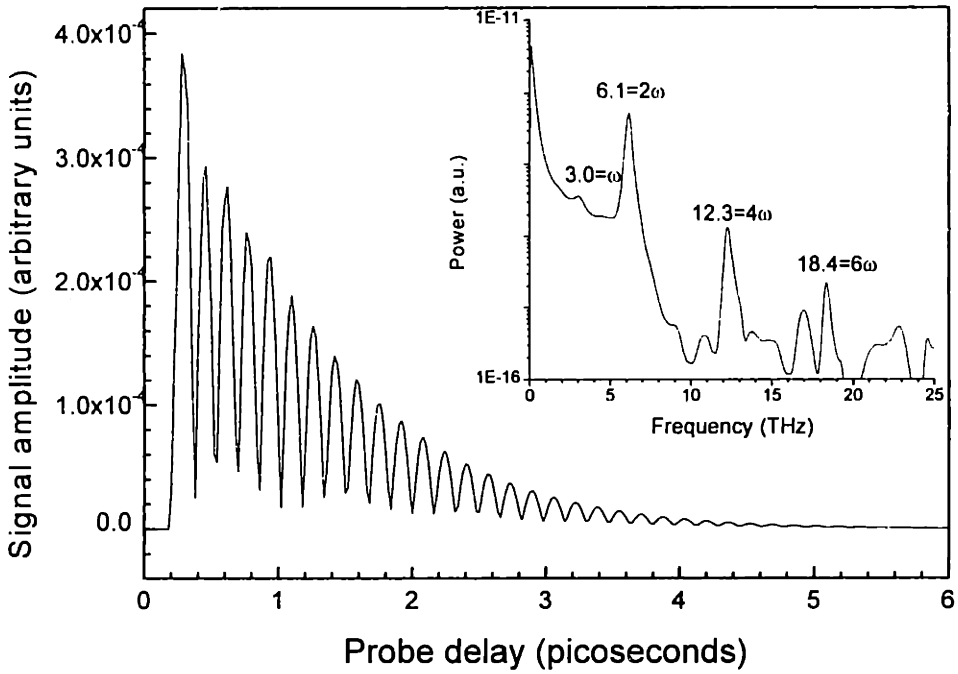

Figure 5.4a Simulation of arbitrary anharmonic potential in $LiTaO_3$ at 1st Bragg angle with coupled-wave algorithm. Note the harmonics of the fundamental.

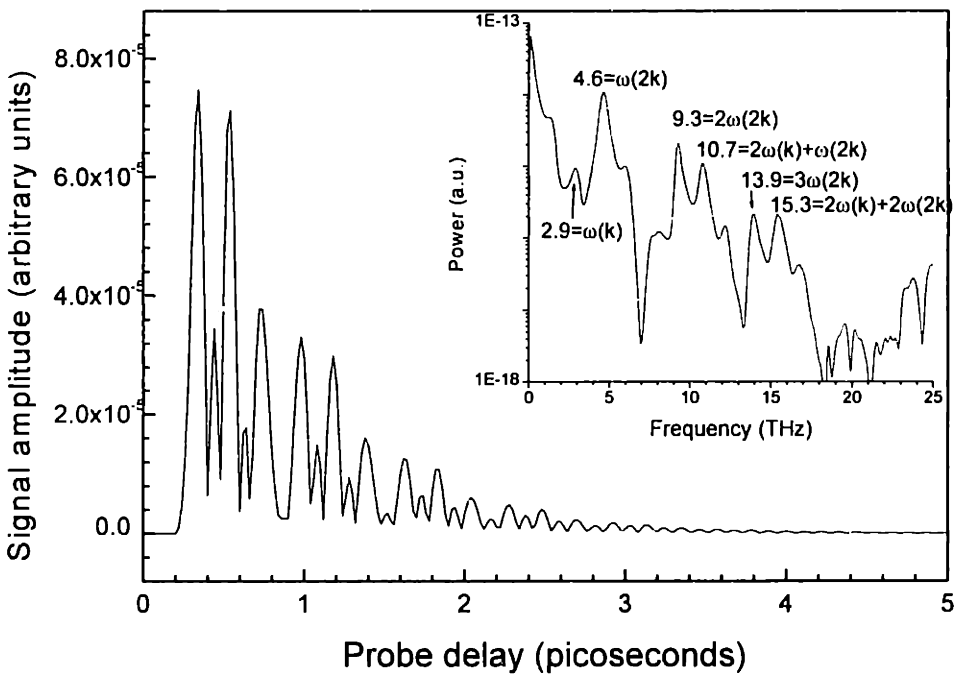

Figure 5.4b Simulation of arbitrary anharmonic potential in $LiTaO_3$ at 2nd Bragg angle (2nd wavevector overtone). Note the ω(2k) signals and sum and difference frequencies.

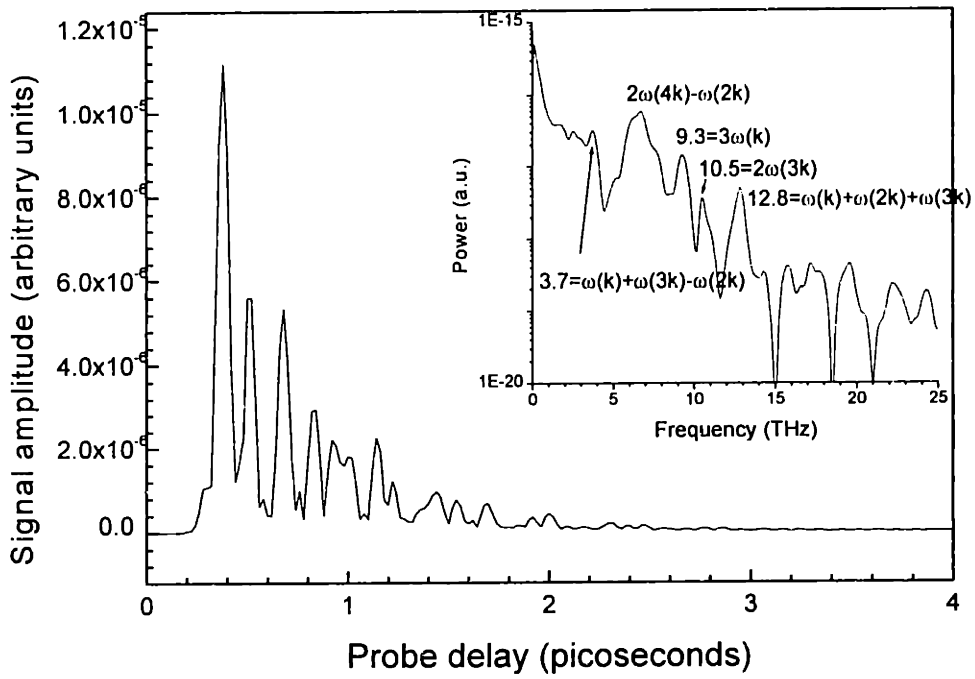

Figure 5.4c Simulation of arbitrary anharmonic potential in $LiTaO_3$ at 3rd Bragg angle (3rd wavevector overtone). Note the ω(3k) signals and sum and difference frequencies.

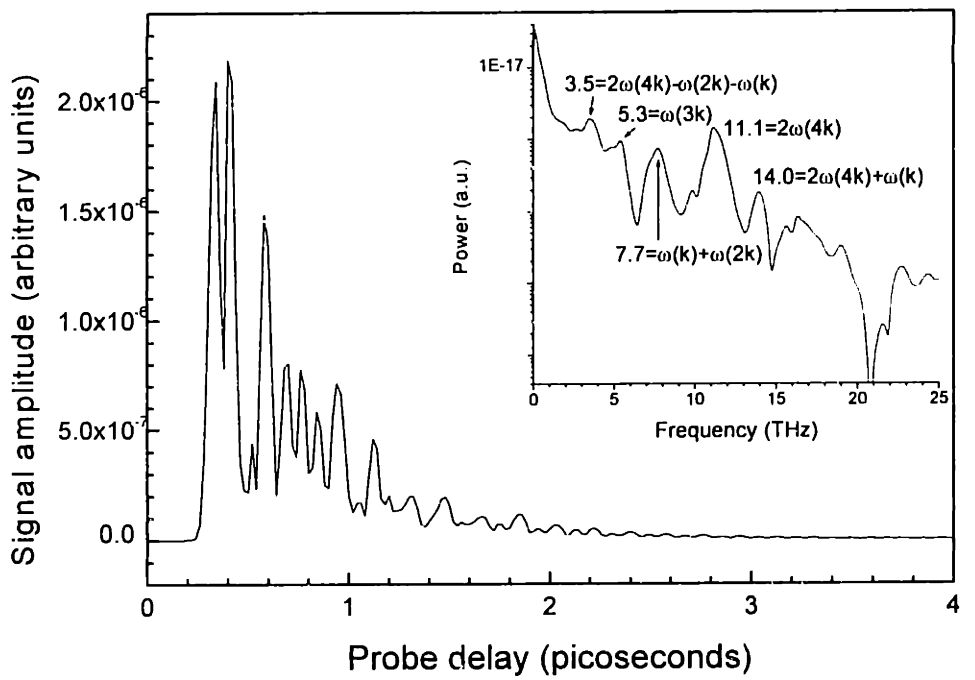

Figure 5.4d Simulation of arbitrary anharmonic potential in $LiTaO_3$ at 4th Bragg angle (4th wavevector overtone). Note the ω(4k) signals and sum and difference frequencies.

5.6. References

1. Wiederrecht, G.P., *et al.*, *Explanation of anomalous polariton dynamics in LiTaO3.* Phys. Rev. B, 1995. **51**(2): p. 916-932.
2. Wiederrecht, G.P., *et al.*, *Anomalous Polariton Dynamics in LiTaO3.* Ferroelectrics, 1993. **150**: p. 103-118.

Chapter 6:
The ISRS-WOS Experimental Apparatus

6.1. Introduction

The wavevector overtone experiment is a modification of the standard transient grating ISRS experiment. The major addition is the means to easily change the angle of the probe beam so it can be introduced at the Bragg angle for the spatial overtones. In addition the experimental apparatus contains several refinements to improve the signal quality and to reduce signal noise due to fluctuations in the pump beam. These refinements include active servos to stabilize the pointing of the beams, a servo to regulate the average power level of the incoming beam, and the means to sort and select the data by pulse intensity. These techniques improve the data quality for the anharmonic measurements which are intrinsically noisy in nature.

6.2. The laser system

The laser system used for these experiments is a multipass amplified Ti:sapphire system built by Dr. Jianping Zhou[1]. Operating at peak performance this system can produce 1.45 millijoule, 22 fs pulses at a repetition rate of 1KHz. The system consists of a self-modelocked Ti:sapphire oscillator, a reflective pulse stretcher, a two-crystal multipass Ti:sapphire amplifier, and a reflective pulse compressor. The short pulse from the oscillator is stretched to approximately 70 ps to provide a much

lower peak power inside the amplifier crystals. After amplification, the pulse is re-compressed to achieve the shortest possible pulse duration.

A preprint of a paper describing this laser system is included in Appendix A.

6.3. The optics

6.3.1 The configuration of the optics

A schematic of the experiment is shown in Figure 4.1. The experiment is a transient grating experiment with adjustable probe angle.

The pulse proceeds through the experiment as follows. The pulse passes through aperture A1 and reflects from piezo mirror PM1. Scattered light from PM1 is focused onto the 4-quadrant photodiode QD1, which is used with a servo controller to keep the beam centered on PM1 by adjusting a piezo mirror at the output of the amplifier. The beam pointing servo system is documented in Appendix B. (Aperture A1 and the subsequent apertures except A8 are placed to assist the alignment of the experiment. They are fully open during the operation of the experiment.)

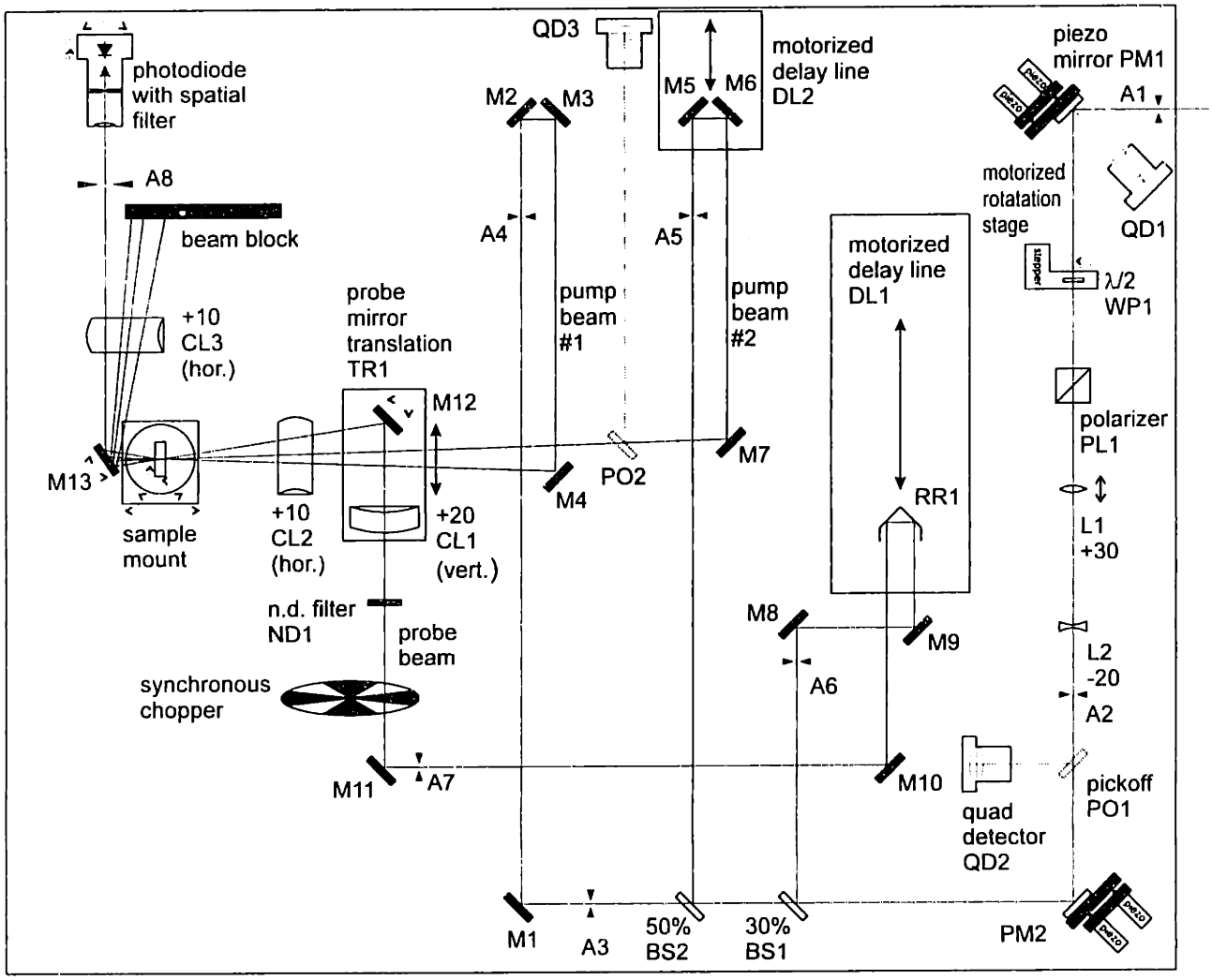

Figure 6.1 Schematic of WOS experiment optics.

The pulse then passes through half-wave plate WP1 and polarizer PL1. WP1 is mounted in a stepper motor rotation stage that is controlled by the computer. The waveplate is used to in conjunction with PL1 to adjust the intensity of the input beam by variably rotating its polarization. Calcite cube polarizer PL1 rejects the horizontal component of the rotated beam and passes only the vertical component. The computer monitors the average

light intensity of the beam and adjusts the waveplate angle to maintain a constant light intensity. The pump intensity signal is derived from the sum of the signals from all four quadrants of QD2.

The pulse is collimated by a telescope formed from lenses L1 and L2. A combination of a convex and a concave lens is used instead of two convex lenses because the pulse is intense enough to produce white light in air if it is brought to a focus. This will stretch and distort the pulse shape as well as introducing undesired wavelengths into the pulse. L1 is on a translation stage to adjust its focus. I have found that it is not good to collimate the beam to a small diameter at the output of the telescope, as this results in a high peak intensity that can damage the optics in the experiment. Instead, it is better to create a larger diameter beam that is slightly converging as it travels to the sample, so that the desired spot size at the sample is obtained without damaging optical components.

A small fraction of the beam is reflected to QD2 from pickoff PO1. PO1 is a thin glass slide that is AR coated for 800nm on one side. It is mounted in a beam splitter mount. The position of the reflected beam is detected by QD2 and sent to the servo controller regulating the position of PM1. QD2 and PM2 are equidistant from PO1, so the servo ensures that the beam is stable at PM2.

The beam then proceeds to the beamsplitters BS1 and BS2. 30% of the beam is split off for the probe beam, while the rest is used for the two pump beams. BS2 is a 50% beam splitter that is used to produce two pump beams of equal intensities. BS1 and BS2 are antireflective (AR) coated for 800nm and produce their specified beam splitting proportions for S-polarized light (i.e. light is polarized orthogonal to the plane of reflection) at a 45° angle of incidence.

The first pump is directed to the sample by M1, M2, M3 and M4. The second pump beam is directed to the sample by M5, M6, and M7. M5 and M6 are mounted on an Oriel motorized translation stage DL2. The position of this stage is adjusted so the two pump beams are precisely coincident at the sample. An autocorrelation between the two pump beams can be performed by sweeping the delay of pump #2 with respect to pump #1 using DL2. The second pump beam passes through pickoff PO2 which reflects a small portion to quad detector QD3. The signal from QD3 is sent to the servo controller that regulates the position of piezo mirror PM2. QD3 and the sample are approximately equidistant from PO2, so the servo maintains a constant position of the beam at the sample.

The probe is directed to the sample by M8, M9, RR1, M10, M11 and M12. RR1 is mounted on a Klinger translation stage DL1 to provide the delay for the probe pulse. The probe also passes through a chopper that is synchronized with the pump beam, so it blocks every other pulse. I found

that chopping the probe yields better results than chopping one of the pump beams. The biggest source of noise and background is light scattered from the coincident pump beams by self-diffraction and other non-linear effects. The purpose of chopping a beam is to modulate the signal so it can be detected using a demodulator that will filter out the noise and background. In this case most of the noise and background comes from the pump, while the signal comes from the probe. Therefore the best application of the chopper is to modulate the signal directly by chopping the probe beam. After the signal is detected using a demodulator the noise and background from the pumps will be averaged out. The demodulator can either be implemented in hardware in the form of a lock-in amplifier, or in software as described in a later section.

The probe beam then passes through an optional neutral density filter ND1 to reduce its intensity if needed. In low-power experiments (<10 mw) no ND filter was used. At higher powers (>50mw) I generally used an OD 1.0 filter to reduce the probe intensity by a factor of 10. Excessive probe intensity causes excessive light scattering from the probe pulse. At high enough intensities the probe pulse creates white light in the sample. The quality of the data decreases dramatically under these conditions.

The probe then passes through a +20 cm focal length cylindrical lens CL1. This lens is mounted with its cylindrical axis in the vertical direction, so it focuses light in the horizontal direction. Its purpose is to concentrate the

probe light to a region in the middle of the grating where the diffraction efficiency is highest. CL1 is mounted on translation stage TR1 along with M12 so it remains roughly the same distance from the sample as M12 is translated to change the probe beam angle.

The angle of the probe beam is set using the translation and rotation of M12. This mirror is mounted on a manual translation stage with 2" of travel. A micrometer adjuster is used to set its location. The horizontal adjuster in the mirror mount for M12 is also fitted with a micrometer. The angle and position of M12 are set manually by calculating the position and rotation and setting the micrometers accordingly.

All three beams pass through +10 cm focal length cylindrical lens CL2 on their way to the sample. CL2 is mounted horizontally to focus the light in the vertical direction. The two pump beams are focused to a horizontal line on the sample, while the pump beam is focused to an ellipse as it has been focused in both directions. The lens is mounted approximately 8.5 cm from the sample. I have found that the strongest signal at low wavevectors is not obtained when the pump beams are highly focused on the sample. Better results are obtained when the beams are about 150 microns in the vertical direction. The pump beams are usually about 1 to 2 mm full-width half-max (FWHM) at the sample in the horizontal direction.

The sample is mounted on a kinematic prism holder which is on a rotation stage mounted on a translation stage. The translation stage allows the sample to be moved forward and backwards along the pump axis to change the spot size at the sample. The calibrated rotation stage is used to measure the pump angle and to rotate the crystal so it is normal to the pump axis. The kinematic prism holder is used to ensure that the crystal is normal to the beam along the other axes.

After the beams have passed through the sample the diffracted signal is directed towards the detector by mirror M13. M13 is equipped with a micrometer on its horizontal axis so its angle can be set in accordance with the angle of M12. The diffracted light is re-collimated in the vertical direction with cylindrical lens CL3. In general it is not necessary to collimate the signal in the horizontal direction because the diffraction in the sample selects a narrow range of horizontal wavevectors. Aperture A8 is used to select the signal light and block the other beams and as much scattered light as possible.

The detector consists of an unamplified photodiode with an integral spatial filter mounted on a kinematic mount and an X-Y translation stage. The optics are mounted in 1" diameter lens tube which screws into the front of the Thor labs photodiode unit*. This shields the detector from ambient light

* The detector is assembled from the following Thor Labs components: A DET100 detector is mounted to a KM1-T 1" thin optic kinematic mount using a SM1T2 lens tube

very well. A 1" focal length lens focuses the signal light onto a pinhole, which may be 25-100 microns in diameter, depending on the amount of spatial filtering desired. The pinhole rejects most of the light that does not arrive exactly on center with the lens, that is, it selects a narrow range of wavevectors in the horizontal and vertical directions. This system is effective in blocking scattered from the detector. A 1" optical lowpass filter is also inserted in the lens tube to attenuate any doubled light coming from the sample. The photodiode is mounted directly behind the pinhole. Its surface area is large enough so all the light passing through the pinhole will strike the detector.

The spatial filter selects only a narrow range of wavevectors in the incoming light and filters out the rest. The wavevector selectivity of this system is as good or better than the conventional technique of sending the signal a long distance and selecting the signal with an aperture. In addition this system is much better shielded from ambient and scattered laser light than a conventional photodetector. It also has the additional benefit of being very compact and not requiring a long, convoluted path for the signal.

---

coupler. A SM1L10 1" beam tube containing a pinhole with a 1" outside diameter is screwed into the other side of the mount. The pinhole is 25 microns in diameter, although larger pinholes can be used to make the initial alignment easier. A 1/2" diameter 1" focal length lens is mounted in a AD1T adapter in a SM1V05 adjustable focus lens tube which is screwed into the end of the 1" lens tube. Additional 1" elements such as lowpass filters or neutral density filters are mounted in SM1L05 1/2" lens tubes and screwed into the front of this assembly.

6.3.2 Alignment of the optics

The beam is introduced to the experiment through A1. When the beam is centered on A1 it should be near center on PM1. The kinematic mount holding QD1 is adjusted so the servo system is properly centered, and then the servo is engaged. This fixes the beam position on PM1.

PM1 is then adjusted manually to align the beam through A2. The beam should now be well centered on WP1, PL1, L1, and L2. If not, these optics should be moved until they are centered on the beam. The spot size at the sample should be checked. Roughly align one pump until it reaches the sample. The spot size may be changed by translating L1. Pickoff PO1 is then adjusted to center the servo attached to QD2, and then this servo is engaged. This fixes the beam on PM2.

PM2 is adjusted to center the beam on A3. The beam should be centered on BS1 and BS2. M1 is adjusted to center the beam on A4, while BS2 is adjusted to center the beam on A5. The beams going to A4 and A5 should be checked to ensure that they are level to the table. M6 should be adjusted to make the reflected beam is parallel to the incoming beam. This can be done by completely retracting the stepper motor positioner that moves DL2 and sweeping DL2 through its 1" travel by hand. The beam reflected from M7 should not move as DL2 is moved from one end to the other. If the beam moves M6 should be adjusted until the beam movement is eliminated.

Be careful to exert force only on the moving plate of DL2 and apply the force only in the direction of motion.

6.3.2.1 Adjusting the pump angle

The positions of M4 and M7 determine the angle between the pump beams. In the present setup we do not change the pump angles often, so no convenient method has been provided to change the angles. The mirror mounts for M4 and M7 must be unscrewed and moved about on the table by hand. When the mirrors are in their proper places, M4 and M7 are adjusted to overlap the pump beams on the sample. The two pump beams should be at the same height as each other and level to the table; this should be checked with a ruler. The sample should be translated up or down to place it in the beams, rather than moving the beams up and down. Once the beams are at the right height and level, the horizontal controls on M4 and M7 can be adjusted to overlap the beams on the sample. Once the two pump beams have been adjusted, the third beam servo may be centered and engaged. PO2 is adjusted to center the beam on QD3, and the servo controlling PM2 is then engaged. This keeps the beam fixed at the sample.

The pump angle can be measured using the vernier scale on the rotation stage for the sample mount. Insert a white card with a small hole in the path of pump beam #2 between M6 and M7 so pump #2 goes through the hole. Rotate the sample so that the reflection from pump #2 falls back on itself, adjusting the vertical tilt of the sample if necessary. Record the angle on the rotation stage. Now rotate the stage clockwise until the reflection of pump

#1 is centered on the hole in the card. Pump beam #1 can be reduced in size using A4 to make its center position easier to see. Record the angle on the rotation stage. The pump angle is twice the difference of the two recorded angles.

If the angle is not correct then M4 should be moved, pump #1 realigned, and the angle measured again. M7 should not be moved since the servo attached to QD3 and PM2 is already engaged.

6.3.2.2 Aligning the probe

BS1 is adjusted to center the probe beam on A6. M8 and M9 must be adjusted so the beam traveling to RR1 is parallel to the axis of travel of delay line DL1. First adjust M8 and M9 so the beam is parallel to the table, roughly parallel to DL1 and entering RR1 on its right side. Tape a white card over the front of RR1 and make a spot with a felt-tip pen where the beam hits it. Translate DL1 completely forward, and adjust M8 to put the beam on the spot. Translate DL1 all the way back, and adjust M9 to put the beam on the spot. Iterate this procedure until the beam stays on the spot throughout the range of motion of DL1.

After DL1 is aligned, use M10 to center the beam on A7. M11 should be adjusted so the probe beam is level to the table and is parallel to the translation stage TR1. The height of the probe beam should be about 2mm less than the height of the pump beams. If this is not the case M10 and M11 should be adjusted to lower or raise the probe beam. M12 should be

positioned so the probe is centered in the horizontal direction but at its upper edge in the vertical direction. M12 should be unscrewed and moved into position if necessary. Do not steer the beam with M11 to center it on M12, as the beam must be parallel to TR1. M12 should not be raised high enough to clip the two pump beams.

The chopper should be checked to make sure that the probe beam passes through it without clipping. The chopper should be run to make sure that the chopped pulse is blocked completely while the unchopped pulse passes completely. If this is not the case, rotate the chopper about its axis if possible or raise or lower it to bring it in phase with the probe pulses.

To align for Bragg angle, TR1 is moved so the point where the probe hits M12 is directly below pump beam #2. M12 is adjusted so the probe pulse is centered on the pump pulses at the sample. The alignment can be checked by looking at the transmitted beams, where the probe should be directly above pump #2. The reflection of the probe from the front face of the sample can also be observed along pump #1 between M3 and M4. The reflection of the probe should be directly above pump #1.

6.3.2.3 Aligning the detector

Because of the good wavevector selectivity the detector must be pointing exactly at the source of the signal light. The detector is moved in the horizontal and vertical directions to center the signal beam on the lens. The tilt of the detector unit in the horizontal and vertical planes is then adjusted to

maximize the electrical signal from the detector. When performing the initial alignment it may be difficult to get the signal through the pinhole. A lens tube with no pinhole may be used to find the initial alignment. Then a lens tube with a big pinhole can be substituted, and finally the smallest pinhole (25 microns diameter) can be installed. Once the experiment has been aligned the detector generally just needs some fine adjustments to optimize the signal.

6.4. Electronics

The electronics for this experiment consist of the amplifiers for the probe and pump photodetectors, the timing circuit, and the data acquisition board.

6.4.1 The signal photodetector circuit

The scattered probe signal is detected by a commercial photodetector from Thor Labs, part number DET100. This photodetector contains a silicon PIN photodiode, which has a 20 ns rise time, a 13.7 mm active area, and a spectral range of 350-1100 nm. The detector contains a 12 volt battery to bias the photodiode. The photodetector is connected to the input of a Stanford Research Systems (SRS) SR560 preamp by 8" of RG-58 coax cable. The preamp has a very high input impedance (100 MOhm, 25 pF). If the photodetector were to operate into this impedance, it would charge up the cable capacitance and the input capacitance to nearly 12 volts. Then there would be very little bias voltage across the detector, resulting in a loss of signal and linearity.

It is essential in this type of circuit to provide a DC resistance from the signal line to ground of the appropriate value. A certain amount of charge ΔQ is conducted by the photodiode during a pulse. This charge creates a voltage in the total circuit capacitance which is given by $\Delta V = \Delta Q / C_{tot}$, where C_{tot} is the total circuit capacitance consisting of the sum of the photodiode capacitance, the cable capacitance and the input capacitance of the amplifier. It is clear that we want to minimize C_{tot} to maximize the voltage we get for a given amount of charge, and therefore for a given amount of light. We also want the voltage to be nearly gone by the following pulse, as substantial overlapping of successive pulses may introduce errors into the data. A resistor from the signal line to the signal ground will discharge the capacitance with a time constant equal to *RC*. The original voltage will be decayed to less than 1% of its original amplitude after 5 time constants. The resistance that should be used to get five time constants between pulses is given by the following formula:

$$R \approx \frac{\Delta T}{5\left(C_{diode} + C_{cable} + C_{preamp}\right)} \qquad (6.1)$$

ΔT is the time between the pulses. In this experiment, $C_{diode} \approx 40$ pF, C_{cable} = 28.5 pF/ft * 0.7 ft = 20 pF, C_{preamp}=25 pF. For a pulse interval of one millisecond this gives R = 2.4 MOhm. The exact value of this resistance is not very critical. It is, however, important that some resistance be used. This is true in general for all unamplified photodiodes used with high

impedance amplifiers. It is true in particular for the SRS SR510 lock-in amplifiers which are AC coupled and provide no DC path to ground.

Since the electrical pulse from the photodiode is in essence integrated by the circuit capacitance, the response time of the photodiode is of little importance in this configuration. Therefore it is better to choose a diode with a larger active area and a lower noise figure than one with high speed.

6.4.2 The pump photodetector circuit

The data analysis program sorts each signal pulse according to the amplitude of the incoming pulse. Only pulses that fall within a specified window are averaged into the data. The pulse amplitude signal is obtained indirectly from quad detector QD2. Inside the servo controller that QD2 is attached to the amplitudes of all four quadrants are summed to get a total amplitude signal. This sum signal is stretched by the circuit shown in Figure 4.2. This circuit catches the peak amplitude of each input pulse and provides an output pulse with a one millisecond time constant. This output pulse is easy for the data acquisition board to digitize. This circuit is used instead of a more complicated sample and hold circuit with good results.

The 0.01 uF capacitor is charge through the 1N914 diode. The op-amp keeps the voltage on the capacitor equal to the input voltage as long as the voltage is increasing. When the input voltage falls below the voltage on the capacitor, the diode becomes reverse biased and no longer conducts.

Therefore the voltage on the capacitor remains constant except for the discharge current through the 100K resistor. The net effect is to follow the input to its peak and then slowly decline in voltage until the next input pulse. The second op-amp buffers the voltage on the capacitor and drives external circuits with a low impedance.

This small circuit is mounted inside one of the servo control boxes. Its input is the SUM signal from Pin 6 of U12. See Appendix B for details of the servo controllers.

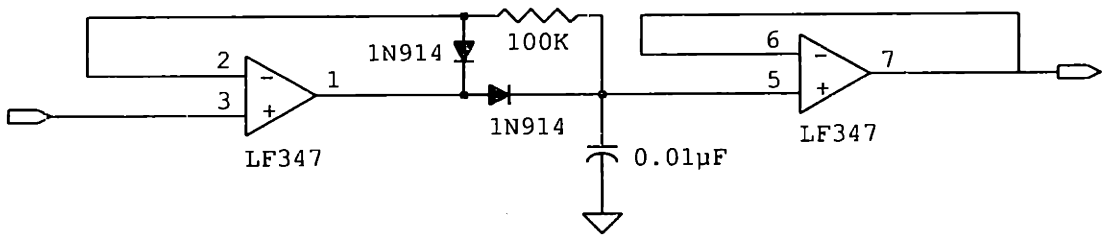

Figure 6.2 Peak hold circuit for pump intensity circuit.

6.4.3 The timing circuit

The timing circuit consists merely of a SRS DG535 delay generator and a divide-by-two circuit. The DG535 is used to generate timing signals for the 1KHz amplifier. The DG535 is programmed to generate a trigger pulse 40 microseconds after the amplified laser pulse. 40 microseconds was chosen to allow enough time for the photodiode circuits to stabilize. This trigger pulse is sent to the data acquisition board, where it is used to clock the data acquisition as described below. The output of the DG535 is set to drive a 50

ohm load, so a 50 terminator is needed at the input to the data acquisition connector box.

The trigger pulse is also sent to a small divide-by-two circuit mounted inside the external connector box for the data acquisition board, which is simply a TTL flip-flop which toggles output state on every input pulse. This circuit generates a 500 Hz square-wave output. This signal is sent to the clock input for the chopper control unit. The chopper then synchronizes itself to the 500 Hz signal and chops every other probe pulse. The output of the divide-by-two is also sent to the third analog input line for the A-D converter on the data acquisition board. The A-D measures this line on each pulse along with the signal and pump amplitudes so the program can determine whether the probe beam was chopped or not.

6.4.4 The data acquisition board

The data acquisition (DAQ) board is a Lab-PC+ from National Instruments. This is a fairly low-cost board with 12-bit resolution and an 83 KHz maximum acquisition rate. The board is configured to scan in three analog channels each millisecond. The three channels are the signal voltage, the pump amplitude voltage, and the chopper state signal, which is the output of the divide-by-two circuit mentioned above. Each time it is triggered, the DAQ board performs one conversion of each of the three channels in rapid succession and writes the data to a memory buffer.

The DAQ board has several limitations that influence its configuration in this experiment. Although the DAQ board has both analog and digital inputs, it cannot switch between analog and digital input operation within a millisecond. This is why the chopper state signal, a TTL digital signal, is read in as a analog voltage. The Lab-PC+ cannot switch between different gain settings for different channels during a single scan. Therefore all the signals must be in the same voltage range. In this experiment the Lab-PC+ is set for an input range of 0 to 10 volts. This requires the use of an external preamplifier for the signal photodetector. The DAQ board is connected to the external junction box by a flat unshielded ribbon cable. The analog lines are on adjacent wires, and there is capacitive coupling from one wire to the next. This means that there is interference between the analog signal lines if the signal sources have a high impedance. For this reason an unamplified photodetector should not be connected directly to the DAQ board; the signal should go through a low-impedance preamplifier or buffer circuit first.

The data acquisition technique that is used in this experiment is called "multiple channel interval scanning with an external scan clock"*. Each conversion of all three channels in succession is called a scan. The DAQ board is configured in software to read in a specified number of scans. The first time the trigger pulse is received the conversion process starts. Upon each subsequent trigger one scan is performed, and the data is added to a

* This technique is described on pages E-17 to E-18 in the Lab-PC+ manual and on pages 9-5 to 9-8 in the LabVIEW Data Acquisition Basics Manual for LabVIEW version 4.0.

memory buffer. The board continues to perform one scan per trigger pulse until the specified number of scans have been made. In this manner the DAQ board digitizes every pulse until the specified number of pulses have been read.

This technique requires the timing signal from the DG535 delay generator to be applied to two inputs of the DAQ board. First is the hardware trigger input (EXTTRIG, pin 38). The first pulse received on this line after the DAQ board has been activated by the software will start the acquisition process. The second is the external scan clock input (COUTB1, pin 43). This input triggers each scan.

There is another clock involved; the channel clock. This determines how fast the board switches from one channel to the next when performing a single scan. This clock should be set to the internal clock on the DAQ board, and its speed should be as high as possible.

The data acquisition is configured for buffered I/O. The data from the scans are fed into a memory buffer. The control software can read the data from the buffer in large chunks at much longer intervals than the 1 millisecond acquisition interval. This is important because it is not practical to have the computer try to read each data point at each millisecond. While the computer hardware is certainly fast enough to accomplish this task, multitasking operating systems and data acquisition software (Windows 95

and LabVIEW 4.0) are not designed to be responsive on this time scale. The buffered I/O technique allows the data acquisition to be timed completely in hardware, while the software is allowed to respond at longer time intervals.

In summary, there are five inputs from the experiment to the data acquisition board. There are three analog inputs; the signal voltage, the pump amplitude voltage, and the chopper state signal. The two digital inputs are the hardware trigger input and the external scan clock input. Both of these are attached to the output of the DG535 delay generator.

6.5. Data acquisition and control software

The experiment is run by custom software written using LabVIEW 4.0. The software runs the experiment, acquires the data, plots the data while the experiment is progressing, and saves the data to a file when the experiment is complete. The name of the experimental code is "Grating experiment with Klinger.vi". The control panel of this program is shown in Figure 4.3.

The software controls the following hardware: the DAQ board in the computer, the Klinger CC-1.2 stepper motor controller for the probe pulse delay, the Oriel 20010 stepper motor controller for the pump #2 delay and the waveplate rotator, and the Stanford Research Systems SR-560 preamplifier for the signal photodetector. The DAQ board is controlled directly through the computer's ISA bus. The Oriel controller and the SRS

preamplifier are controlled by serial port interfaces. The Klinger controller is controlled by a GPIB interface.

6.5.1 Data acquisition and processing

This section describes how the data from the DAQ board is processed. The acquisition software performs the function of a lock-in amplifier with the added ability to discriminate the data by pulse intensity.

The data acquisition board is configured to digitize a set of consecutive pulses and store the data in a memory buffer. 500 is a typical value for the number of pulses to be digitized at one time. For each pulse there are three numbers stored: the signal amplitude, the pump amplitude, and the chopper state. After the set of points have been acquired, the each signal amplitude datum is sorted according to the value of the corresponding pump amplitude. The user specifies a maximum and a minimum value of the pump amplitude and a number of intervals or bins to divide the range into. For each bin, two numbers are stored: the total sum of all the signal amplitude data, and the number of points added together. In addition, two sets of data are maintained: those pulses where the probe was chopped, and those pulses where the probe was not chopped.

For each data point, the program examines the value of the pump amplitude and the chopper state and selects the appropriate bin. The signal amplitude for that data point is added to the sum, and the number of points for that bin

is incremented by one. After all the data has been sorted, the average unchopped signal can be computed by dividing the sum of the unchopped signal amplitudes by the number of points, and the average chopped signal can be computed the same way. The average chopped signal is the component of the signal due to scattered light, electrical offsets, and other contributions to the background. The true signal is then the difference between the average unchopped and chopped signal amplitudes.

The technical name for this procedure is synchronous demodulation. The probe signal is amplitude modulated in the experiment by chopping every other pulse. The signal strength is demodulated in the software by taking the difference between the amplitudes of adjacent pulses. The time average of the demodulated signal is found by summing the differences in amplitude over a sequence of pulses, or alternatively by taking the difference in the sums as described above. This time averaging is equivalent to passing the data through a low-pass filter to remove high-frequency components.

In effect, this data processing is the equivalent of a lock-in amplifier implemented in software. The lock-in provides the same function: synchronous demodulation followed by low-pass filtering. The advantage of the software method is that we can first sort the data by pump pulse intensity. The data in each bin will have been generated by an arbitrarily small range of pump intensity. This allows us to minimize the effect of shot-to-shot fluctuations on the data. This is particularly important for the anharmonic

measurements; because the anharmonic phenomena are high-order processes, they are extremely sensitive to the pump intensity. By sorting the data before demodulating it we reduce the sensitivity to intensity fluctuations.

It was my original intention to save and analyze the data in all the intensity bins. In the early version of the experiment the laser suffered large shot-to-shot fluctuations and also showed long-term fluctuations in average power. These two effects made the distribution in pulse intensity over the course of an experiment quite large. Therefore it made some sense to try to make use of the entire distribution of the intensity-sorted data. However, improvements in the laser amplifier reduced the pulse-to-pulse fluctuations, and the use of the power control servo described below eliminated the long-term fluctuations. These improvements narrowed the distribution of the pump intensity values so much that most of the data fell into a narrow range of pulse intensities. As it was no longer useful to analyze the data for the entire range of the intensity bins, the data acquisition program was modified to only store the data for the bin with the greatest number of counts.

The net result for the data acquisition is that the data is windowed by pulse intensity. Data points with a pulse intensity below the lower threshold or above the upper threshold are discarded, while those within the limits are averaged into the data. However, the multiple-bin structure is retained in the program, as it is used in the power control servo routine.

6.5.2 Power control servo

The data acquisition program contains code to regulate the average pulse intensity by controlling the rotation of a half-wave plate. There is a waveplate and polarizer near the input to the experiment as described in the section on the optical configuration. The angle of the waveplate sets the angle of the polarization of the transmitted light. Since the horizontally polarized light is rejected by the polarizer, the intensity of the pulse decreases as the angle of the polarization moves away from the vertical. The pulse intensity can be regulated by adjusting the angle of the waveplate until the desired amount of light passes through the polarizer.

The operation of the servo routine is simple; the program attempts to ensure that the center bin contains the greatest number of data points. After each set of points is acquired, the program sorts the data according to pulse intensity. It also determines the index number of the bin that the greatest number of the new points were put in. The difference in the index number of this bin and the index of the center bin is taken. The waveplate is then moved a number of steps given by an integer scaling factor times the difference in index numbers. For example, suppose there are 7 bins, that the greatest number of points in the last set of data were in the second bin, and that the scaling factor is -2. The center bin has an index number of 4. The waveplate will be rotated by (2-4)*(-2) = 4 steps clockwise. (A negative number of steps implies a counterclockwise rotation).

The magnitude of the scaling factor for the servo should be found by trial and error. A value of 2 seems to work fine. The sign of the scaling factor depends on the initial orientation of the waveplate. If the sign of the feedback is wrong, the servo will keep rotating the waveplate constantly in one direction. If this occurs, change the sign of the scaling factor.

6.5.3 Experiment program outline

1. Initialize GPIB and Klinger controller; initialize preamp; set preamp gain.
2. Initialize DAQ; measure initial average pulse intensity for 5 seconds; set the max and min bin values based on initial average pulse intensity or a user defined value (the program will attempt to maintain the pulse intensity constant throughout the experiment).
3. Initialize the data array; begin experiment loop in which the probe delay sequence is swept through one or more times and data is taken at each delay value:
    - 3.1. Position Klinger (probe delay line) at first data point.
    - 3.2. Run through scan of delay line. At each delay value:
        - 3.2.1. Read specified number of pulses.
        - 3.2.2. Advance the Klinger.
        - 3.2.3. Calculate signal; add to data array.
        - 3.2.4. Plot the signal for bin with the most counts.
        - 3.2.5. Plot the histogram of number of counts per bin.
        - 3.2.6. Adjust the waveplate angle.

3.3. Return Klinger to zero position.

3.4. Save data if the experiment is done or aborted.

3.5. Loop to 3.1.

4. Clear the DAQ.

5. Loop to beginning of experiment.

6.5.4 Autocorrelation program

There is a second version of the experiment program that is modified for autocorrelation. Its name is "Auto-correlate with Oriel.vi". The autocorrelation is a three beam measurement where the signal is the T=0 probe beam diffracted at the first Bragg angle. In other words, the probe delay is adjusted for maximum signal at T=0. The autocorrelation is found by sweeping the delay of pump #1 using the Oriel stepper motor delay line DL2. This delay line is attached to the same controller that drives the waveplate rotator, as this controller can drive two stepper motors. The signal is acquired and analyzed in the same manner as above, except the data is recorded and plotted vs. the pump #1 delay instead of the probe delay. After each sweep the three-beam autocorrelation is calculated and a FWHM value for the pulse is obtained. The calculations assume a Gaussian pulse.

The autocorrelation factor for the convolution of a Gaussian pulse with a Gaussian pulse squared is 0.816. The single Gaussian is the variably delayed pump #2. The Gaussian squared is the overlap of the pump #1 with the

probe. The measured FWHM value obtained from the data is multiplied by 0.816 to obtain the FWHM of the input pulse.

Note that since this is a three-beam autocorrelation, the data is not necessary symmetrical with respect to the delay.

6.6. Electromechanical components

The electromechanical components consist of a Klinger stepper motor translation stage with 6" of travel and one micron step size, a Klinger CC-1.2 stepper motor controller, an Oriel 18512 stepper motor translation stage with 1" of travel and 2 micron step size, an Oriel 13049 stepper motor rotation stage with 360° of travel and 0.02° step size, an Oriel 20010 stepper motor controller capable of controlling two stepper motors, and three laser pointing servo units.

The Klinger translation stage and controller are used for the probe delay line, while the Oriel translation stage and controller are used for the pump beam #2 delay line, which is used for autocorrelation. The Oriel rotation stage is used to regulate the pulse intensity by rotating a waveplate.

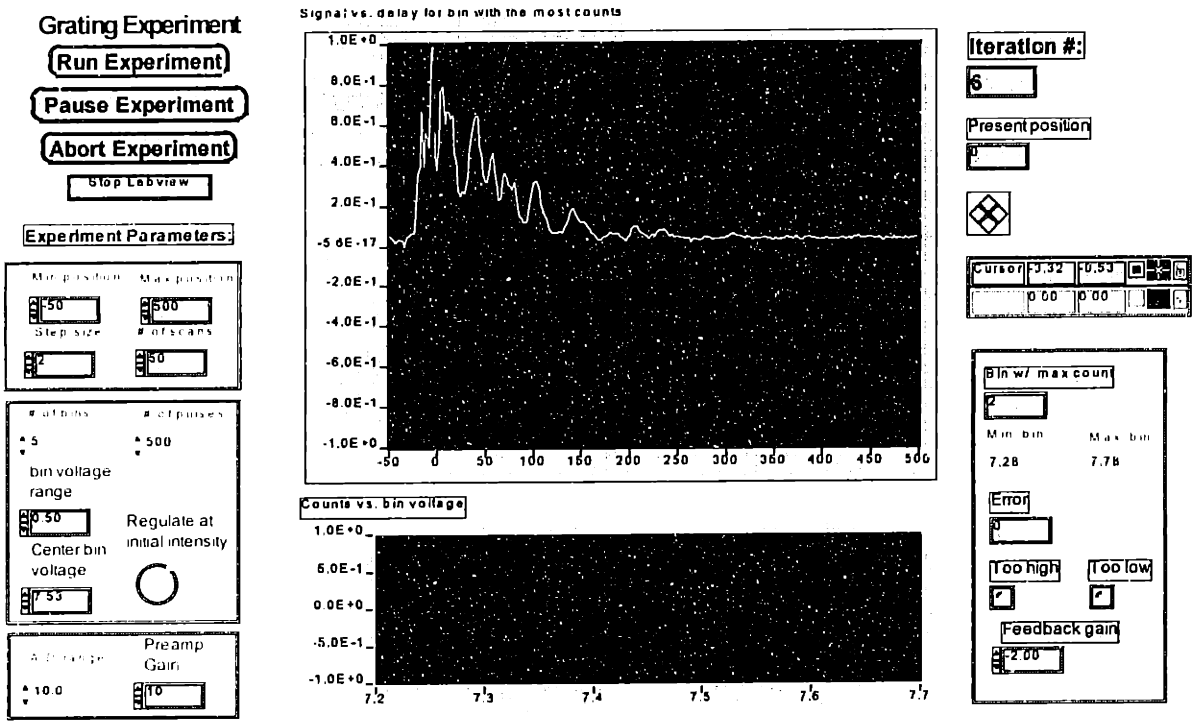

Figure 6.3 Control panel of the LabVIEW data acquisition and control program.

6.7. References

1. Zhou, J. and K.A. Nelson. High efficiency, multipass Ti:sapphire amplifier producing 1.45 millijoule, 22 fs pulses at 1KHz. in Optical Society Annual Meeting (OSA). 1996. Rochester, NY.

Chapter 7:
ISRS-WOS Experimental Technique

7.1. Introduction

This chapter summarizes the method for performing the WOS experiment and the three-beam autocorrelation measurement. I first discuss the procedure for performing an ISRS experiment with the probe at the first Bragg angle. Next I describe how to perform the three-beam autocorrelation experiment, which is an essential tool for day-to-day characterizing and optimizing of both the laser system and the experimental apparatus. Finally I talk about how to perform the overtone measurements with the probe at higher Bragg angles.

7.2. ISRS experiment at first Bragg angle

The experiment can be broken down into the following steps. This assumes that the experiment has already been aligned as discussed in a previous chapter.

1. Set the pulse power.
2. Set the pump angle.
3. Set the probe angle.
4. Overlap the beams.
5. Get timing.
6. Get signal.

7. Align the detector.
8. Autocorrelate; adjust the pulse compressor.
9. Run initial sweep.
10. Optimize the alignment for the oscillatory component.
11. Check the pulse power.
12. Run the experiment.

These steps are discussed in more detail below.

7.2.1 Set the pulse power

The power is set by monitoring the pulse intensity with a power meter inserted between the second piezo mirror PM2 and the first beam splitter BS1 and then rotating the control knob of the motorized waveplate rotation stage by hand. This will be hard to do if the motor windings are enabled, as the current in the windings prevents the motor from turning easily. If this is the case, make sure the control program is not running, and reset the Oriel controller by pushing the reset button on the back or turning off the power.

20 to 50 milliwatts is a good power level for the alignment and autocorrelation that follows.

7.2.2 Set the pump angle

The beam angle is set by unscrewing and moving one of the final mirrors for the pump beams. Since pump #2 goes through the servo, its steering mirror (M7) should not be moved if possible. This means that the steering mirror for pump #1 (M4) should be moved. This requires a bit of trial and error to

achieve a particular angle, but the following steps help minimize the number of trials.

1. Calculate the angle you want. $\theta/2$ is the angle of one pump beam with respect to the bisector.

$$\left(\frac{\theta}{2}\right) = \sin^{-1}\left(\frac{k\lambda}{4\pi}\right) \tag{7.1}$$

2. Set pump #2 so it is centered on the sample and level to the table. Move the sample up or down instead of moving the beam in the vertical direction.
3. Turn the sample rotation stage to reflect pump #2 back on itself. Closing the aperture for pump #2 (A5) partially will reduce the beam size and make the overlap easier to determine. Change the tilt of the sample to adjust the vertical angle of the reflection.
4. Record the angle of the probe θ_i.
5. Rotate the sample to $\theta_f = \theta_i + \theta/2$.
6. Place a card to the left of M4. On the right side you should see pump #1. On the left you should see the reflection of pump #2 from the sample. Translate M4 towards or away from M3 until pump #1 is coincident with pump #2.
7. Overlap pump #1 with pump #2 on the sample.
8. See if the reflection of pump #1 is collinear with pump #2.
9. If necessary, repeat steps 6 to 8 until the correct angle is achieved.

7.2.3 Set the probe angle

The translation stage TR1 for the probe steering mirror M12 should be moved until the point at which the probe beam hits M12 is directly below pump #2. Adjust M12 until the probe is centered on the pump beams at the sample.

7.2.4 Overlap the beams

The beams should already be overlapped on the sample. Normally I conducted the experiments with the sample about 1" to 1.5" in front of the focal point of the cylindrical lens where the vertical size of the beam was about 150 microns. Beams of this size can be overlapped reasonably well by eye. However, you should be wearing your safety glasses, so you can't see the beams. The IR viewers I've used don't have the clarity or resolution to be useful in this type of alignment. You can overlap the beams by mounting a pinhole in a sample holder, inserting it in place of the sample, and adjusting all three beams for maximum transmission through the hole. Tweak the beams using M4, M7, and M12. When this is done, the sample can be re-installed, and the beams should overlap in the sample.

7.2.5 Get timing

The ferroelectric crystals that we've experimented with emit frequency doubled light at high intensities. This can be used to get timing between the beams, i.e. adjusting the path length of the beams so they are coincident at the sample. If you are unsure whether the timing is close to perfect, you

should get a piece of string and measure the path length of all three beams, starting at BS1. The path lengths should be nearly equal when DL2 is near the middle of it's travel, and DL1 is near the front of its travel.

Timing between the two pulses is found by looking for the appearance of violet doubled light between the two red Ti:sapphire pump beams when the beams are viewed on a card after the sample. A fluorescent card is useful to highlight the doubled light. Move DL2 back and forth until you observe the doubled light. This translation stage can be moved forward against the restoring spring by hand, making quick sweeps simple. When DL2 is set to maximize the doubled light, tweak up only the vertical position of pump #1.

Timing of the probe is found in the same way: looking for doubled light between the transmitted probe and pump #2. Move the Klinger until the doubled light is found and maximized. Tweak up the vertical overlap of the probe using M12. Do not use M11, as this will make the probe beam not parallel to translation stage TR1.

7.2.6 Get signal

If you are lucky, you should now see a spot of light above the transmitted pump #1. If not, look for it using the IR viewer and a white card placed so that pump #1 passes just underneath. This will allow you to see a faint signal beam without the pump saturating the IR viewer. Make sure it is signal by checking to see that it disappears if you block either pump beam. Make fine

adjustments to the horizontal and vertical controls of M12 the position of TR1 to optimize the signal. Also tweak the vertical position of pump #1.

If you can't find signal, go back to checking the timing. You should see doubled light between all three pulses at once. Also check to make sure that the polarization and crystal orientation are correct. For many of the ferroelectric experiments, all three beams are vertically polarized, and the polar axis (c-axis) of the crystal is vertically oriented.

If you still can't find signal, try finding it with the detector. Remove the pinhole from the detector. Center pump #1 on A8 using the signal steering mirror (M13), and close A8 until it just passes the center of the beam. Translate the photodetector until pump #1 is centered on the lens of the detector. Now use M13 to lower pump #1 until it strikes the iris of A8 just below the hole. Make sure the chopper is on. Observe the signal from the preamp on an oscilloscope. Look for a signal with alternating peaks or with a large peak every 2 ms. Move M13 around a bit to optimize it. Make sure it is signal by checking to see that it disappears if you block either pump beam. Once you find signal, maximize it as described above.

7.2.7 Autocorrelate and adjust compressor

Autocorrelate the signal using the 3-beam technique described below. The pulse duration can change substantially from day to day, and obtaining a short pulse is essential for good data. The pulse compressor should be

adjusted for the shortest pulse length. The only adjustment that should be made to the compressor is the translation of the grating.

7.2.8 Run initial sweep

Run an initial sweep of the data acquisition program. You should see reasonable looking ISRS data. However, the electronic peak may be very large compared to the oscillations that follow. Find the delay value of the first oscillatory maximum (in microns) after the electronic using the cursor controls on the control program's data graph.

7.2.9 Optimize alignment for signal

We want the alignment to be optimized to generate the greatest signal for the oscillatory Raman phonon signal, not for the electronic peak. Due to self-focusing of the beams in the sample or some other optical effect, the angle of the probe that produces the best phonon oscillation signal is slightly different than that which produces the best T=0 electronic signal.

Move the Klinger delay line to the delay setting found in the previous step. (There is a sign difference between the control program display and the Klinger due to the orientation of the Klinger delay line. A positive motion of the Klinger moves the retroreflector RR1 towards M9, shortening the delay. Therefore, move the Klinger in the negative direction for a positive delay.) Now optimize the probe using small tweaks of M12 and TR1.

Don't forget to return the Klinger to the zero position once you are done tweaking.

7.2.10 Check the pulse power

Check the pulse power as described above and adjust if necessary.

The LabView program is called "Grating experiment with Klinger.vi". On the front panel of the program there is a button marked "Regulate at initial intensity". Click on this to turn it on. When the experiment is run, the present power level will be measured, and this level will be maintained for all successive runs or until the power level is reset.

7.2.11 Run the experiment

Run the experiment. Monitor the overload light on the preamp to make sure that the gain isn't too high. The gain on the preamp should be set as high as possible without overloading. Change the gain using the LabView program controls rather than those on the preamp front panel. The SRS preamp can listen but cannot talk to the computer, so the LabView program has no way of knowing what the gain is if it has been set outside of the program.

The experiment can be aborted at any time. The data collected from all the fully completed sweeps of the probe delay can then be saved. The data from partially completed sweeps are discarded.

7.3. Three-beam autocorrelation

The three-beam autocorrelation is a technique to measure the pulse width using the T=0 diffracted probe light from the actual sample. (T=0 indicates that the probe beam is perfectly coincident with pump #1). The autocorrelation is performed by sweeping the delay of pump #2 using delay line DL2, which is the Oriel stepper motor translation stage with a corner reflector. The great advantage of this technique is that it gives the pulse width in the exact same configuration as the experiment. Therefore the autocorrelation can be taken immediately before the experiment so the pulse duration can be known with good certainty. This is important as we need to know the pulse duration to properly calculate the peak pump intensities in the anharmonic experiments.

Autocorrelating in the experiment itself gives the very important advantage that the pulse compressor can be adjusted to give the shortest pulse duration *at the sample*. The pulse travels through a considerable amount of material in the experiment: waveplates, polarizers, beam splitters, and lenses. Each of these components add a certain amount of dispersion to the pulse. By adjusting the compressor to give the shortest pulse at the sample, the compressor is set to pre-compensate for all the dispersion of these components. If the pulse were optimized with an external autocorrelator, then the pulse duration at the sample would probably be longer due to the added dispersion introduced by the optics in the experiment.

7.3.1 Adjusting the autocorrelation measurement

The pulse width measured in the three-beam autocorrelation is sensitive to the alignment of all three beams and the timing between pump #1 and the probe beam. The signal at T=0 should be carefully maximized. The actual signal from the SRS preamp should be observed on an oscilloscope, and the following controls adjusted to maximize the signal amplitude. The most important parameters are the vertical overlap of the two pumps (adjust the vertical control on M1), the horizontal and vertical angles of the probe (adjust M12) and the probe timing. The probe translation stage TR1 may be used to make fine adjustments in the probe timing. One should ensure that the probe beam is well centered in the pump beams after adjusting M12 and TR1. If it is not centered, it should be re-centered using TR1 and the probe delay DL1 readjusted to give good T=0 overlap. Also make sure that the alignment of the signal going to the photodiode is optimized using M13 and the tilt controls on the photodiode kinematic mount. The final tweaks should be made with M12 and TR1 to optimize the signal.

The probe beam should be reasonably well focused in the horizontal direction, particularly when the pump beams intersect at large angles. Because the pump beams are cylindrically focused and propagate at an angle, the two beams will intersect for a range of delay times longer than the true autocorrelation (Figure 1). As the delay on pump #2 is swept from a negative to positive delay, the point of intersection of the two pulses sweeps from right to left in the sample. The resultant autocorrelation in a

convolution of the horizontal spatial shape of the pulses with the temporal profile of the pulses. If the pump is well focused in the horizontal direction, the T=0 signal will be generated only for a small region of the spatial overlap of the two pump pulses. This will give an accurate autocorrelation.

7.4. Wavevector Overtone Measurements

Before searching for the wavevector overtone signals, the experiment should be well-aligned at the first Bragg angle and T=0. The second wavevector signal can be found using this method:

1. Calculate relative displacement and rotation of pump steering mirror M12 for a relative angle increase of $\theta/2$.
2. Calculate the new settings for M12 and TR1. Move them. Move the probe delay line forward by 1/2 the amount TR1 was moved.
3. Scan probe delay DL1 and look for doubled light between the probe and pump pulses. Optimize the probe delay for the doubled light.
4. Place a card after the signal steering mirror M13 so the pump beams pass underneath. Look for the first order diffracted light using an IR viewer. This signal should be centered between the pump beams. Tweak M12 and TR1 to optimize.
5. Make sure the probe is centered in the pump beams. If not, center it with probe translation stage TR1 and compensate by moving probe delay DL1 half the distance in the opposite direction. Fine tune the delay for best T=0 signal.

6. Now look for the second Bragg angle signal using an IR viewer. It should be the same distance from the first order light as the transmitted probe. It should be to the left of the transmitted probe #2. Manually chop pumps 1 and 2 and look for a spot that changes as you chop the pumps.
7. Steer this signal through A8 to the photodetector using M13. The angular change for M13 should be nearly the same as for M12. (It will be slightly different because M13 does not trar.slate.)
8. Observe the signal on the scope. The signal will be a pulse train with a bigger pulse every 2ms. Block the pumps to make sure that it's signal and not just scattered pump light.
9. Adjust the pointing of the photodetector and M13 to optimize the signal. Then tweak M12 and TR1 to optimize further. (It may take several iterations of this step to get the best signal.)

This procedure is repeated to go from each higher wavevector signal to the next higher one.

Higher wavevector signals may be too faint to see with the IR viewer. These may still be found by the photodetector. If TR1, DL1, M12 and M13 are set carefully you should be able to see the signal. Increasing the size of the pinhole in the photodetector will help find signal at the expense of more noise and scatter.

It may also help to find higher order signals by stepping over one diffraction order at a time from the probe spot. Start with the transmitted probe directed

to the photodetector using M13. At each spot, optimize the signal using signal steering mirror M13 and the photodetector angle controls. Then rotate M13 in the horizontal direction to find the next spot while observing the signal on the scope. The angular change and the corresponding micrometer settings required to move M13 from one angle to the next should already be known. While the micrometer readings will not be exact, they will help prevent becoming confused over which diffraction spot is which.

The data should be taken with a sufficiently small step size in the probe delay sequence to resolve higher frequency components. A step size of 3 microns gives a Δt of 20 fs and a signal bandwidth of 25 THz, which is high enough for all the signals encountered so far. Using a smaller step size may make the data look smoother, but by the Nyquist sampling theorem it will not provide any more information for frequency components within this bandwidth.

Chapter 8:
Experimental Results in Lithium Tantalate

8.1. Introduction

I have performed a series of experiments on ferroelectric lithium tantalate crystals to attempt to produce and observe large amplitude ionic motion and to observe signatures of anharmonicity in the subsequent oscillations. The results show that the polariton amplitudes are not very large compared to thermal displacements, but show marked anharmonicity nevertheless. The evidence for lattice anharmonicity is the following: the maximum lattice displacement calculated from the diffraction efficiency; frequency harmonics observed in the ISRS data at the first Bragg angle; and spatial harmonics of the wavevector in the WOS experiments. The results are consistent with the theoretical expectations and provide strong evidence for lattice anharmonicity in the phonon-polariton modes in lithium tantalate.

8.2. Differential polarizability and maximum displacement

8.2.1 Description of diffraction efficiency measurements

The differential polarizability can be calculated from a measurement of the diffraction efficiency, as described in Chapter 2. The diffraction efficiency measurement is simple in concept but it is not easy to do repeatably in practice. The measurement is started by setting up the ISRS grating

experiment and observing the time-delayed probe signal. The diffraction is measured at the first oscillatory maximum after the T=0 electronic response. The probe delay corresponding to the first maximum of the polariton response is determined, and then the probe delay is left on that value. The alignments of all three input beams as well as the diffracted beam and the detector are then fine adjusted to give the maximum signal diffraction as measured by a photodetector. The diffraction efficiency is very sensitive to the experimental alignment, and this sensitivity is probably the main source of the experimental uncertainty. The diffraction efficiency is also dependent on the intensity of the pump beams. In the linear theory the diffraction efficiency is not dependent on probe beam intensity, but in practical experiments it is, due to nonlinearities which influence the diffraction at higher power levels. The efficiency is also critically dependent on the temporal overlap between the two pumps, and this is another parameter that must be adjusted carefully.

The intensity of the transmitted probe light with the pumps blocked is first measured. Then the intensity of the diffracted probe beam is measured, first with all three incident beams unblocked, then with the pumps blocked, and then with the probe blocked. These two latter measurements record the amount of scattered background light. Their values are subtracted from the total diffracted light with no beams blocked. The ratio of the diffracted intensity minus background to the transmitted probe intensity is taken.

I performed a large number of measurements over a wide range of power measurements. The best diffraction efficiency I recorded occurred at a pump beam intensity of 50 microjoules per pulse, with a full-width half-max (FWHM) spot size of 160 microns by 2000 microns. The measured diffraction efficiency was 38%. With no beams blocked, 51% of the beam was transmitted, 38% diffracted to first order, and 11% scattered elsewhere.

I do not consider these measurements to be extremely accurate or repeatable due to the sensitivity to alignment. Nevertheless, on this instance a diffraction efficiency of close to 1/2 was clearly obtained. The diffracted beam looked nearly as bright as the transmitted beam, and the transmitted probe beam brightened noticeably when either pump beam was blocked.

Diffraction efficiencies decreased at higher power levels. This is due to the onset of strong nonlinear optic effects on the probe pulses. The first is self-focusing. The index of refraction is reduced in the regions where the light is brightest. This causes a lensing effect which focuses the beam as it travels through the sample. This lowers the diffraction efficiency in two ways. First, the distance in the vertical direction covered by the pump beams becomes smaller than the probe beam, which does not experience as much self-focusing due to lower intensity. The grating then covers only a fraction of the probe beam, so the less probe light is diffracted. Second, when the beam contracts in the vertical dimension to a size on the order of the polariton wavelength, the grating becomes inefficient at generating the

polaritons because of diffraction in the vertical direction. The result is that the grating becomes less effective the further the light travels into the sample.

At higher intensities, white light generation starts to occur. When the light is highly focused, self-phase modulation becomes so strong that a large range of new light frequencies are generated. The efficiency of the grating is completely destroyed under these conditions. Even when the sample is producing white light, the region in the front of the sample where the beam has not yet become very focused may still be acting as an effective grating. As a result, the effective depth of the grating diminishes as the power level is increased past the point where strong self-focusing occurs.

8.2.2 Differential polarizability calculations

8.2.2.1 Differential polarizability from diffraction measurement

The following parameters apply to the diffraction efficiency measurements in $LiTaO_3$.

Parameter:	**Value:**	**Description:**
η	0.38	diffraction efficiency
n	2.34	index of refraction for visible light
ε_∞	5.46	permittivity at optical frequencies
ε'_∞	8.5	permittivity at near IR frequencies
ε_0	34	permittivity at far IR frequencies

λ	8×10^{-7} m	wavelength of laser light in vacuum
m	1.95×10^{-26} kg	reduced mass of mode for 10 atom unit cell, $LiTaO_3$ (11.7 au)
τ	20×10^{-15} s	pulse duration, 1/e half width
ω	1.25×10^{13} rad/sec	frequency of polariton at k=2700 cm^{-1}
c	3×10^{8} m/s	speed of light in vacuum
N	2.73×10^{27} /m^3	number of oscillators per volume, unit cell size: a=b=5.15Å, c=13.8Å
z	2×10^{-3} m	depth of sample
h (FWHM)	160×10^{-6} m	beam height
w (FWHM)	0.002 m	beam width
ΔJ	50×10^{-6} J	pulse energy
ΔU	98 J/m^2	average peak energy density in pulse

Calculated Parameters:

$\sqrt{U_{tot}/U_M}$	0.46	calculated fraction of energy in mech. oscillator
$\partial\alpha/\partial x$	2.8×10^{-18} m^2	calculated differential polarizability
x_m	3.7×10^{-3} Å	maximum displacement at maximum power

Table 8.1

The intensity profile can be expressed as:

$$I(x,y,t)=\frac{\Delta J}{\pi^{3/2}\sigma_x\sigma_y\sigma_t}e^{-\left(\frac{x}{\sigma_x}\right)^2}e^{-\left(\frac{y}{\sigma_y}\right)^2}e^{-\left(\frac{t}{\sigma_t}\right)^2} \tag{8.1}$$

The integral over the intensity gives the pulse energy ΔJ. The average energy density ΔU in Joules/m^2 is calculated as follows:

$$\Delta U=\frac{1}{\sqrt{2}}\frac{\Delta J}{\pi(0.6\cdot h)(0.6\cdot w)} \tag{8.2}$$

The factors of 0.6 convert the FWHM height and width to 1/e half width values to normalize the power distribution for the Gaussian profiles in both dimensions. The $1/\sqrt{2}$ factor gives the RMS intensity along the height dimension. Since the probe is focused at the center of the grating, the intensity along the horizontal direction is not averaged but is assumed to be at the peak value. The intensity is integrated over time to get the total impulse.

The proportion of the impulse energy delivered to the mechanical oscillator is given by:

$$\frac{U_M}{U_{tot}}\approx\frac{\omega_T^2}{\left(2\omega_T^2-\omega^2\right)+\frac{\varepsilon'_\infty}{\varepsilon_0-\varepsilon'_\infty}\frac{\left(\omega_T^2-\omega^2\right)^2}{\omega_T^2}} \tag{8.3}$$

This gives 46% of the energy in the mechanical oscillator at this frequency. This is plausible since we are in the crossover region of the dispersion curve where the polariton has nearly equal light-like and phonon-like properties.

The differential polarizability is calculated using the following expression:

$$\frac{\partial\alpha}{\partial x} = 2\sqrt{\frac{\lambda\varepsilon_\infty m\omega_T c\cdot\sin^{-1}\left(\sqrt{\eta}\right)}{\pi N z\Delta U}}\frac{K_1(\infty)}{K_1(k)}\sqrt{\frac{U_{tot}}{U_M}}\exp\left(\frac{\tau^2\omega^2}{4}\right) \qquad (8.4)$$

The values in Table 8.1 produce a value of $2.8\mathbf{x10^{-18}}$ $\mathbf{m^2}$ for the differential polarizability (the ISRS efficiency $K_1(k)/K_1(\infty)$ is 0.29 at this wavevector). This is very large compared to the typical value of 10^{-16} cm^2 (10^{-20} m^2) cited in previous works[1]. (The typical differential polarizability value is not for $LiTaO_3$, which has an unusually large value).

8.2.2.2 Differential polarizability from electro-optic coefficient

It is interesting to compare this experimentally derived value to the theoretical expression relating the differential polarizability to the electro-optic coefficient that was derived in Chapter 2. The expression is:

$$\frac{\partial\alpha}{\partial x_i} = \frac{m\omega_T^2\varepsilon_\infty^2}{2Nq_i}r_{33} \qquad (8.5)$$

Given an r_{33} value of $2.5x10^{-11}$, we get a value of $3.6x10^{-18}$, which is about 29% bigger than the value from the diffraction measurement.

8.2.2.3 Discussion of results

The reason for the discrepancy between the two calculated values for $\partial\alpha/\partial x$ is probably within experimental error. It might be expected that the diffraction efficiency measurement would yield a lower number. Any misalignment can cause the diffracted light to drop dramatically in intensity,

and there are many mechanical degrees of freedom in the apparatus that require very fine adjustment. It is probable that I did not obtain the optimum diffraction efficiency. There are also possible problems with measuring the power level accurately. The power level tends to fluctuate a fair amount, and these measurements were taken before I developed the servo system to regulate the laser power in the experiment. Another possible source of error is the assumption that the beam profile is Gaussian, which is not exactly true. This could lead to errors in the power density term ΔU.

The model from which Eq. (8.5) is derived is very simplistic and may overestimate the differential polarizability. It assumes that $\partial\alpha/\partial x$ for this particular mode is the only contribution to r_{33}. This is not true; though the differential polarizability for this mode dominates the contributions from other optic modes and the electronic contribution, those other terms are not zero. This simplification inflates the value for $\partial\alpha/\partial x$. The model also relies on an estimation for the effective charge q_i for the mode, which may be in error.

I have examined the possibility that the electro-optic model in Chapter 2 neglects the difference between local and macroscopic electric fields. The fields that produce a force on the ions and the fields in the energy calculations should be treated as local fields, while the fields in the definitions of the susceptibilities are treated as macroscopic fields. The local and macroscopic fields are linearly related. Likewise, the polarizability α

may be treated as the local polarizability or macroscopic polarizability depending on the context. The local and macroscopic polarizabilities are related by a simple expression. I have chosen not to introduce these distinctions into the model in Chapter 2 in order not to confuse the main issue, which is that the Raman driving force is the same as the electro-optic force for polariton generation in $LiTaO_3$ and similar materials. However, it makes no difference in the final expression of Eq. (8.5), as all the terms relating macroscopic to local variables cancel in the end. (The polarizability in (8.5) is the macroscopic polarizability, which is related to the polarization by the expression $P = \epsilon_0 N\alpha E$, where E is the macroscopic field.)

8.2.3 Calculation of maximum displacement and energy in the mode

The maximum displacement can be calculated using the following formula derived in Chapter 2:

$$x_m = \frac{\partial\alpha}{\partial x}\frac{K_1(k)}{K_1(\infty)}\sqrt{\frac{U_M}{U_{tot}}}\frac{\Delta U}{m\omega_T 2nc}\exp\left(-\frac{\tau^2\omega^2}{4}\right) \qquad (8.6)$$

We have all the parameters in Table 8.1 except for the maximum impulse energy ΔU. As explained above, the maximum energy that was used in the grating experiment was considerably more than the value that gave the best efficiency in the diffraction measurements. At high power levels, the transient grating drops in effectiveness as it travels into the crystal, but the impulsive force is still effective in the front of the crystal. The maximum power that was used in the experiments was 5 times the power used for the

diffraction measurements. Also, we are calculating the peak displacement in the center of the pump beam where the intensity is greatest, not the RMS value over the vertical direction so we remove the factor of $1/\sqrt{2}$ from Eq. (8.2). This gives $\Delta U = 693$ J/m^2.

This pulse energy produces a displacement of $x_m = 3.7\text{x}10^{-13}$ m = $3.7\mathbf{x10^{-3}}$ Å. This is about 0.8% of the normal mode static displacement of 0.49 Å. This is large compared to previously reported typical values[2] of 10^{-4}. However, it does not seem large enough to qualify for the term "large amplitude displacement", which suggests displacements comparable to static ferroelectric displacement. Another order of magnitude in amplitude at least is required.

It is instructive to compare the energy and displacement produced in the mode via ISRS with the thermal energy and displacement at room temperature. The thermal energy E_T for a distributed mode is found from the Planck distribution[3]:

$$\langle E_T \rangle = \frac{h\upsilon}{\exp\left(\frac{h\upsilon}{T}\right) - 1} \tag{8.7}$$

For a 2 THz polariton at 300°K, this gives $\langle E_T \rangle = 3.5 \times 10^{-21}$ J. In a classical model, the maximum thermal displacement for the polariton is:

$$x_T = \sqrt{\frac{2\langle E\rangle(U_M/U_{tot})}{m\omega_T^2}} \tag{8.8}$$

This gives $x_T = 0.11$ Å.

The energy associated with the polariton displacement can be calculated as:

$$E_m = \frac{1}{2} m\omega_T^2 x_m^2 \left(\frac{U_{tot}}{U_M}\right) \tag{8.9}$$

This gives $E_m = 4.2\text{x}10^{-24}$ J, which is about 0.12% of the thermal energy in the mode.

These results are summarized in Table 8.2.

Parameter	**Value**	**Description**
x_m	$3.7\text{x}10^{-3}$ Å	maximum mode displacement
E_m	$4.2\text{x}10^{-24}$ J	ISRS energy in mode
x_T	0.11 Å	maximum thermal displacement
$\langle E_T\rangle$	$3.5\text{x}10^{-21}$ J	thermal energy in mode
x_0	0.49 Å	static normal mode displacement

Table 8.2

It is clear from these results that we must increase the energy delivered to the mode by two orders of magnitude before the ISRS energy becomes comparable to the thermal energy at room temperature.

8.2.3.1 Contribution of differential polarizability to polariton anharmonicity

At this point we can calculate the contribution of the nonlinearity in the polarization to the anharmonicity in the polariton response. We know the value of $\partial\alpha/\partial Q$, which produces a change in the polarizability of $N\,\partial\alpha/\partial Q \cdot Q$. The resultant change of the polarization is $N\,\partial\alpha/\partial Q \cdot QE$, and the change in energy is $N\,\partial\alpha/\partial Q \cdot QE^2$. Since E is proportional to Q in the linear polariton solution, the differential polarizability dα/dQ introduces a cubic term in the energy, and is therefore the lowest order anharmonic term. We can estimate that $\Delta\varepsilon_\infty = N\,\partial\alpha/\partial Q \cdot Q \sim 2.8\text{x}10^{-3}$ from the values in Table 8.1, or about 0.05% of the permittivity.

8.3. Overtones in ISRS data at first Bragg angle

In Chapter 3 I discussed the expected signature of nonlinearity in both the polarization and the ionic restoring force. By nonlinearity I mean that the parameter in question varies as a nonlinear function of the displacement Q. Nonlinearity in either term is expected to result in harmonics of the fundamental polariton frequency in the diffracted signal in the standard ISRS configuration, where the probe is at the 1st Bragg angle. Since the diffracted signal is derived from the square of the displacement, the fundamental frequency ω will appear as 2ω in the data. The second harmonic will appear as 4ω, etc. $LiTaO_3$ also has an exponentially decaying relaxational mode

that can heterodyne with the signal. Due to the heterodyning it is also possible to observe signals at 1ω, 3ω, etc.

Figures 8.1 to 8.4 display the results of ISRS experiments in $LiTaO_3$ at four different power levels. (The frequencies ω are given in units of 1/ps rather than rad/ps.) The anharmonicity in the observed signal is evident in both the time data and the power spectrum. The data taken at the lowest pump energy level (28 μJ) looks nearly sinusoidal. There are possible peaks in the power spectrum at 4ω and 6ω, but these are really in the noise. At a pulse energy of 56 μJ, a distinct 4ω peak starts to appear. At 84 μJ, clear peaks at 4ω and 6ω emerge in the power spectrum, with a possible peak at 8ω. The time signal is starting to deviate noticeably from a sinusoidal response. At 128 μJ, there are peaks at 2ω, 3ω, 4ω, 5ω, 6ω, 7ω, 8ω. At this power level the time signal looks markedly non-sinusoidal, particularly in the first 5 or 6 oscillations.

The data contains a lot of unusual features near T=0. This portion of the signals can be attributed to nonlinear interactions between the pump and the probe beams. The effects that we observe in this region are varied and interesting. Due to the focusing effect of the pump beams, the probe may be deflected away from the detector, causing a drop in signal. Depending on the relative delay between the pump and probe, the probe may actually extract energy from the pump beams, so the transmitted probe exits with

more energy when the pump beams are present than when they are blocked. I have also observed a dip in the signal below zero immediately preceding T=0. This means that there is less scattered light in the direction of the detector when the probe is not chopped than when it is. (Recall that the probe beam is chopped in these experiments, and the signal consists of the signal with the probe unblocked minus the signal with the probe blocked.) The negative diffracted signal occurs at the same point at which the transmitted probe beam is gaining energy from the pumps as it passes through the sample. In general, the responses near T=0 are very sensitive to alignment and are not very repeatable. I chose to ignore the response about T=0, and focused my efforts on obtaining the best signal in the subsequent oscillations well after T=0.

I have selected a starting point in each data set for the Fast Fourier Transform (FFT) for the power spectrum to avoid anomalous features at T=0. The start and end points in the time data for the FFT are marked with arrows in the plot.

8.3.1 Discussion of ISRS results

Despite the 5-fold range of pump energy in this set of data, the polariton frequency does not change between data sets (within experimental error). This can be explained in two ways. First, we can suppose that the polariton oscillation is linear and the observed anharmonicity is due to nonlinearity of the differential polarizability influencing the diffraction of the pump beam.

In this context, the frequency does not change because there is no change in the polariton other than amplitude. This possibility is discussed in Chapter 3, where the possibility that harmonics of the fundamental frequency and wavevector might be produced by nonlinearity in the diffraction process is examined.

The second explanation is that the polariton is indeed anharmonic, but the dominant nonlinearity anti-symmetric, so its effect is opposite when Q is positive than when Q is negative. Such a term may be a 2nd order term in the force (a cubic term in the potential), or a second order term in the permittivity. The effect of such a nonlinearity tends to cancel when integrated over a full cycle, as it tends to speed up one half cycle but slow down the other.

A point in favor of the anharmonic polariton interpretation is that the data appears too irregular to be explained as a power series acting on a sinusoidal response, which is what the first postulate supposes. However, if anharmonicity of the polariton is involved, there will be a greater range of frequencies and wavevectors generated in the polariton response. There may be polaritons that have a frequency unrelated to the fundamental frequency as well. The interference and mixing among these various components of the response as they propagate at different group velocities and directions may be responsible for the complexity of the data.

Note the apparent decrease in the damping of the time signal as the power increases. This is difficult to explain in terms of the nonlinear model as it is presented in Chapter 3. One possibility is that this is due to saturation effect in the diffraction of the probe signal. The hypothesis is that due to saturation of the diffraction of the probe beam caused by large displacements, the initial part of the data is reduced in amplitude relative to the rest of the data. This would reduce the relative decrease in the signal amplitude compared to the decrease in the polariton amplitude with time, which would look like decreased damping. Possible causes for saturation of the diffraction are nonlinearities in the differential polarizability, or the diffraction equation itself, which goes as $\sin^2(Q)$. I think this last explanation is very likely, because we observe diffraction efficiencies of nearly 50% in experiments under these conditions. Under these conditions the intensity of the diffracted signal does not increase linearly with the polariton amplitude due to significant depletion of the probe beam.

Another fact to remember when considering the damping is that there are only about 20 fringes in the grating between the half-max points, as explained in Chapter 2. This translates into about 20 oscillations in the data before the signal drops off dramatically. (There will be 10 full wavelengths of the polariton propagating in each direction through the probe beam, which translates into 20 oscillations because the diffracted signal is squared.)

Figure 8.4 shows a rapid drop-off in signal after about 20 cycles, which is consistent with this argument.

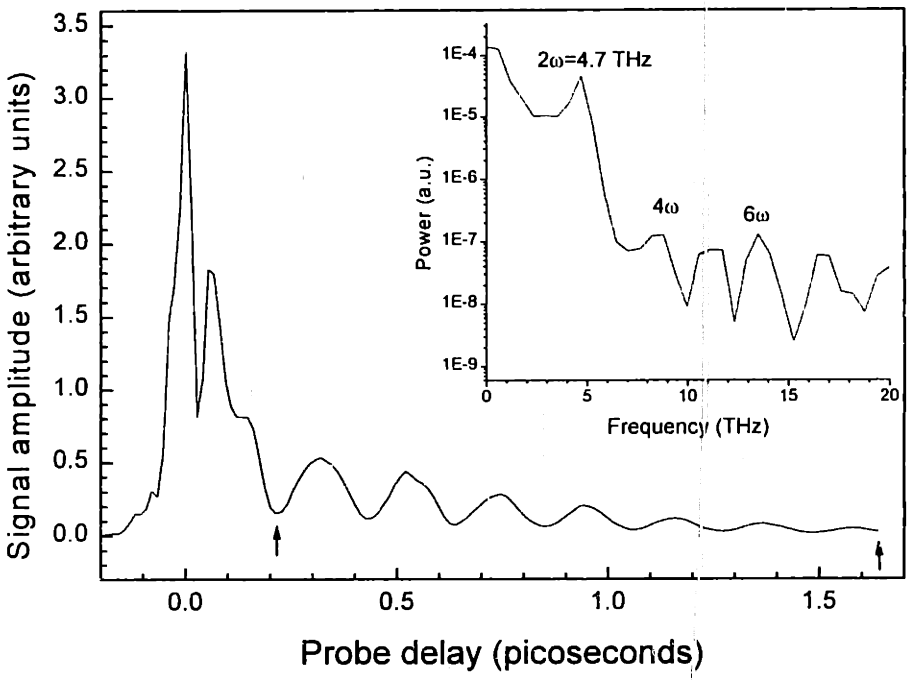

Figure 8.1 ISRS data on $LiTaO_3$ with k_g=3000 cm^{-1}, ΔJ=28 μJ

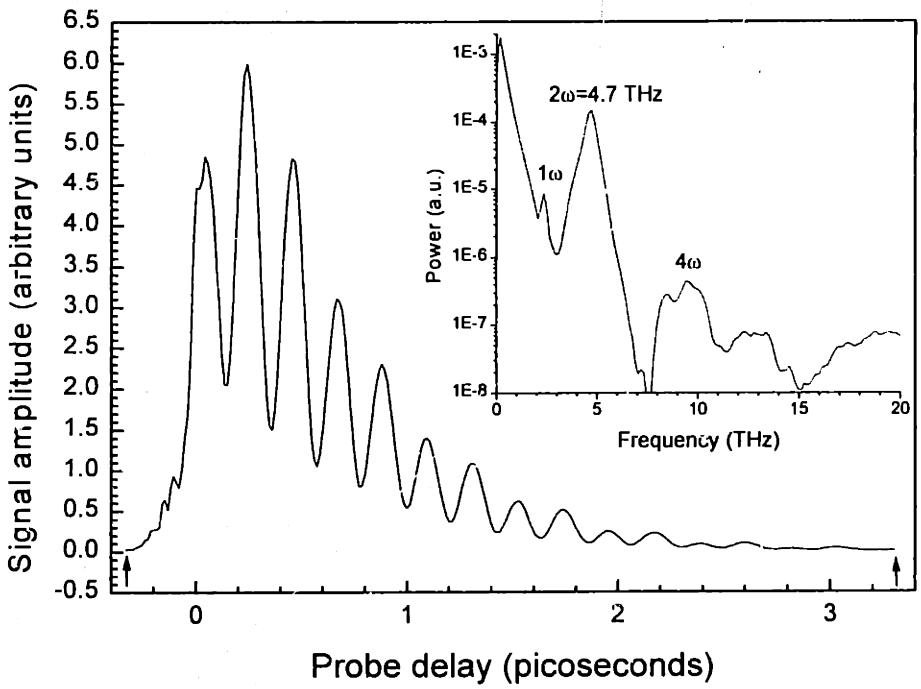

Figure 8.2 ISRS data on $LiTaO_3$ with k_g=3000 cm^{-1}, ΔJ=56 μJ

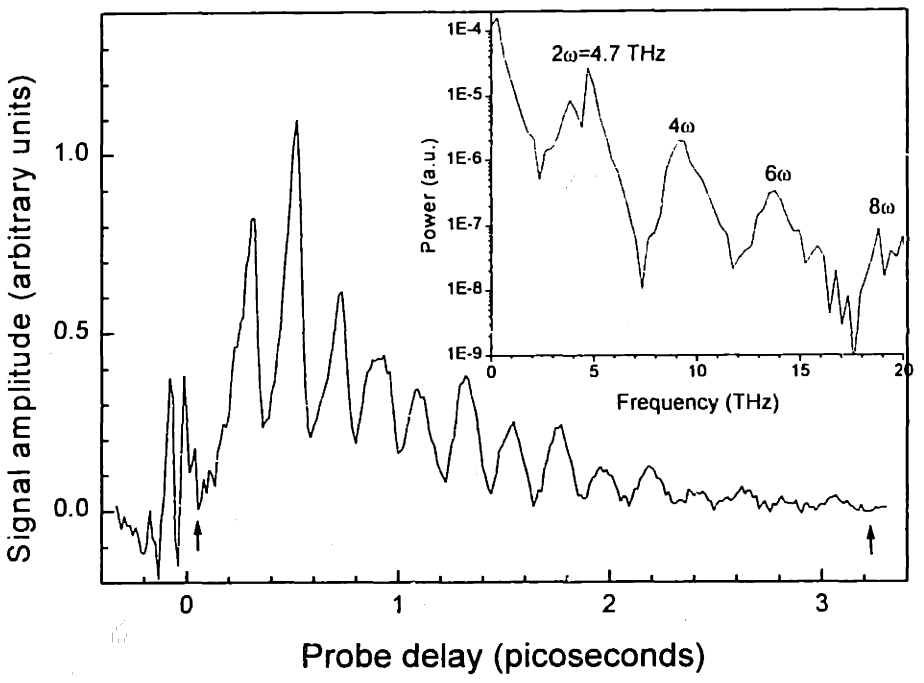

Figure 8.3 ISRS data on $LiTaO_3$ with k_g=3000 cm^{-1}, ΔJ=84 μJ

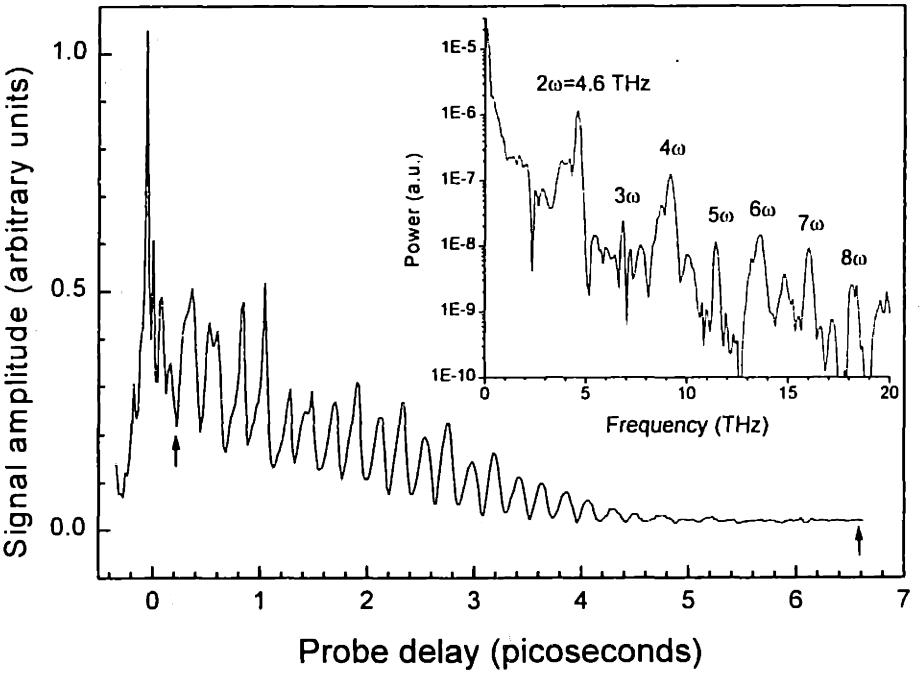

Figure 8.4 ISRS data on $LiTaO_3$ with k_g=3000 cm^{-1}, ΔJ=128 μJ

8.4. Wavevector Overtone Spectroscopy results

I performed wavevector overtone spectroscopy measurements on $LiTaO_3$ at four different pump levels: 28, 55, 110, and 220 μJ/pulse. The best results were obtained at 110 μJ, as 220 μJ was near the onset of white light generation and the signal-to-noise ratio was substantially worse. (Some of the data was taken at 140 μJ instead of 110 μJ. The pulse energy is noted in the captions of the figures.) No overtone signals were observed at 28 μJ , and the signals at 55 μJ were very faint and noisy. The results from the 2nd through 5th overtones, measured at the 2nd through 5th Bragg angles at 110 μJ/pulse are shown in Figures 8.5 to 8.8. Note that the frequencies ω are given in units of 1/ps rather than rad/ps.

8.4.1 Discussion of WOS results

The temporal responses of these measurements are complex, as are the power spectra. Several features stand out in the data. In each power spectrum there is a peak corresponding to ω(nk) or 2ω(nk) or both, where n is the index of the Bragg angle. These signals were anticipated in the theory in Chapter 3 and in the simulation results in Chapter 5. In the model systems they can be produced when the nonlinear terms distort the polariton response at large displacements. The distortion along the horizontal direction creates harmonics or overtones in the polariton grating, which act as sources of new polaritons with wavevectors equal to the spatial overtones. These solutions

are viable in a damped system, where phase cancellation over many cycles is incomplete because of the decreasing amplitude of the polariton response.

Peaks corresponding to the fundamental frequency ω or its harmonics can also be found in the power spectra. This is due to diffraction processes of 2nd or higher order, as discussed in Chapter 3 in the coupled wave diffraction theory section. In effect, the probe can diffract once into a first order beam, and from there it can diffract into a second order beam, etc. As each diffraction step goes as the square of the grating intensity, which is proportional to the polariton displacement in the linear model, the higher-order diffraction will introduce even harmonics of ω into the WOS signal. In addition, there can be heterodyning with non-oscillating grating components produced by relaxational modes or from DC gratings caused by photo-refractive damage or other effects. These can introduce odd harmonics of ω into the WOS signal.

Weak cross-talk between orders of the WOS signal is possible. In particular, there might be some $\omega((n-1)k)$ or $\omega((n+1)k)$ signal in the nth Bragg angle measurement. Signal from $\omega(nk)$ might also diffract to $\omega(2nk)$ by second-order diffraction. For example, there is a $2\omega(2k)$ peak in the 4th wavevector overtone data. This is signal from the second wavevector overtone diffracting at second order. Nonlinear mixing between frequencies to produce sums and difference frequencies is also possible. In fact, the diffraction process will produce sums and differences of all the frequencies

in the polariton response due to the fact that the diffracted light goes as the grating amplitude squared. The diffraction grating of the response goes as $d\alpha/dQ*Q$, which may or may not be linear in Q.

I have annotated the power spectra in the cases that the peaks can be clearly attributed. Not all the peaks in the power spectra can be accounted for as $\omega(k)$, $\omega(nk)$, or one of the harmonics of these frequencies. The nonlinear mixing inherent in the diffraction process makes distinguishing any but the strongest frequencies difficult. I have selected a subset of each data set for the FFT to avoid the anomalous T=0 features. The start and end points in the time data for the FFT are marked with arrows in the plot.

We can clarify the frequency domain response of the polariton by using a heterodyne detection system in the grating experiment, which will be discussed in a later section. The heterodyne signal is linear in the amplitude of the diffraction grating, and therefore does not produce the sum and difference frequencies.

Figure 8.9 shows all the identified frequency peaks in the W[illegible]a superimposed on the dispersion curve of $LiTaO_3$. These frequencies provide convincing evidence of nonlinearity in the polariton response.

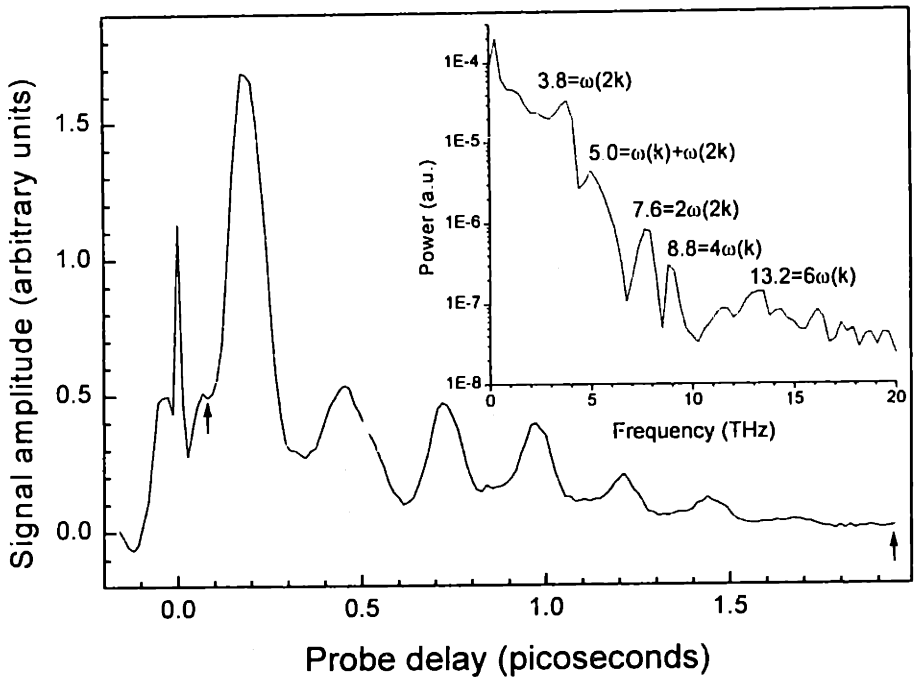

Figure 8.5 WOS data for $LiTaO_3$ at $2k_g$ with k_g=2700 cm^{-1}, ΔJ=140 μJ

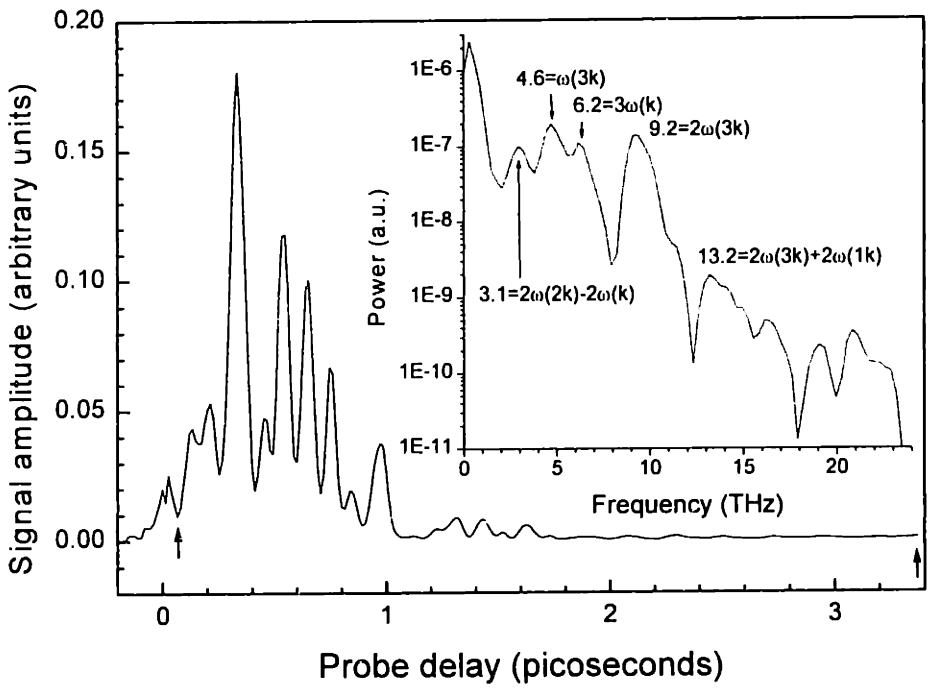

Figure 8.6 WOS data for $LiTaO_3$ at $3k_g$ with k_g=2700 cm^{-1}, ΔJ=110 μJ

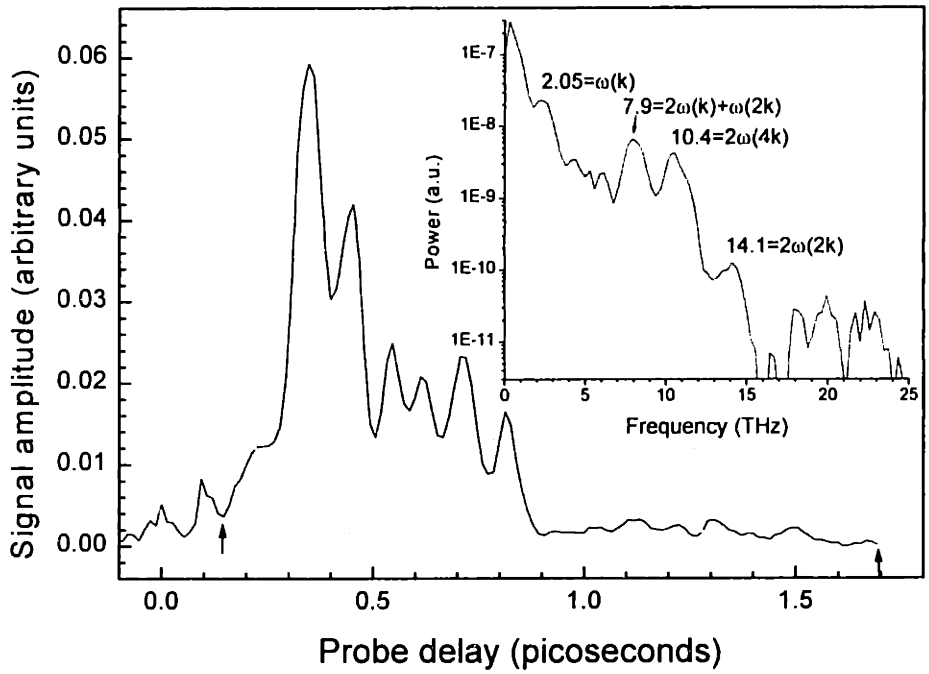

Figure 8.7 WOS data for $LiTaO_3$ at $4k_g$ with k_g=2700 cm^{-1}, ΔJ=110 μJ

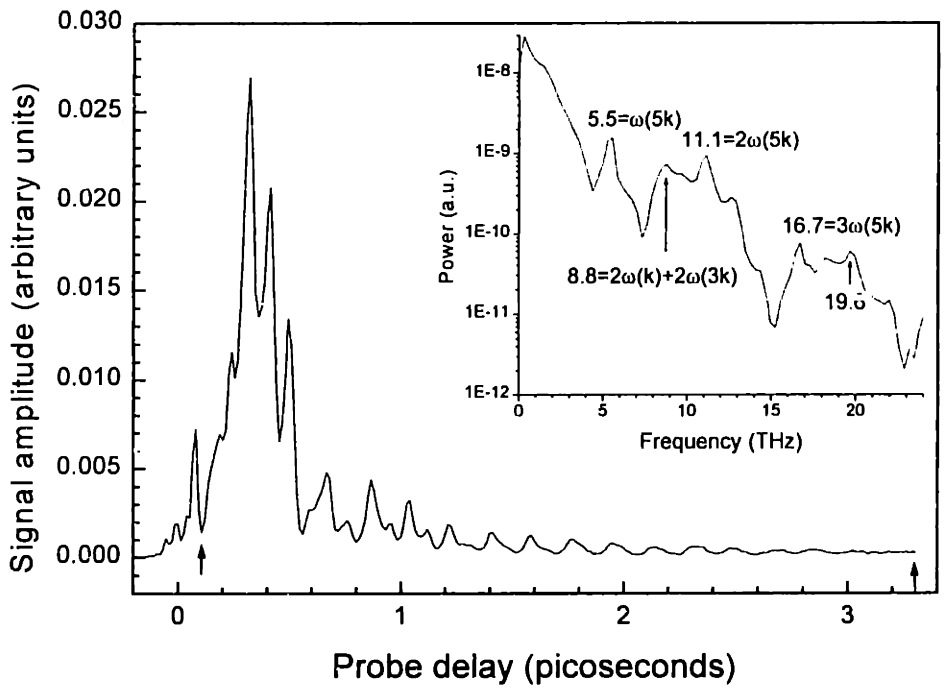

Figure 8.8 WOS data for $LiTaO_3$ at $5k_g$ with k_g=2700 cm^{-1}, ΔJ=110 μJ

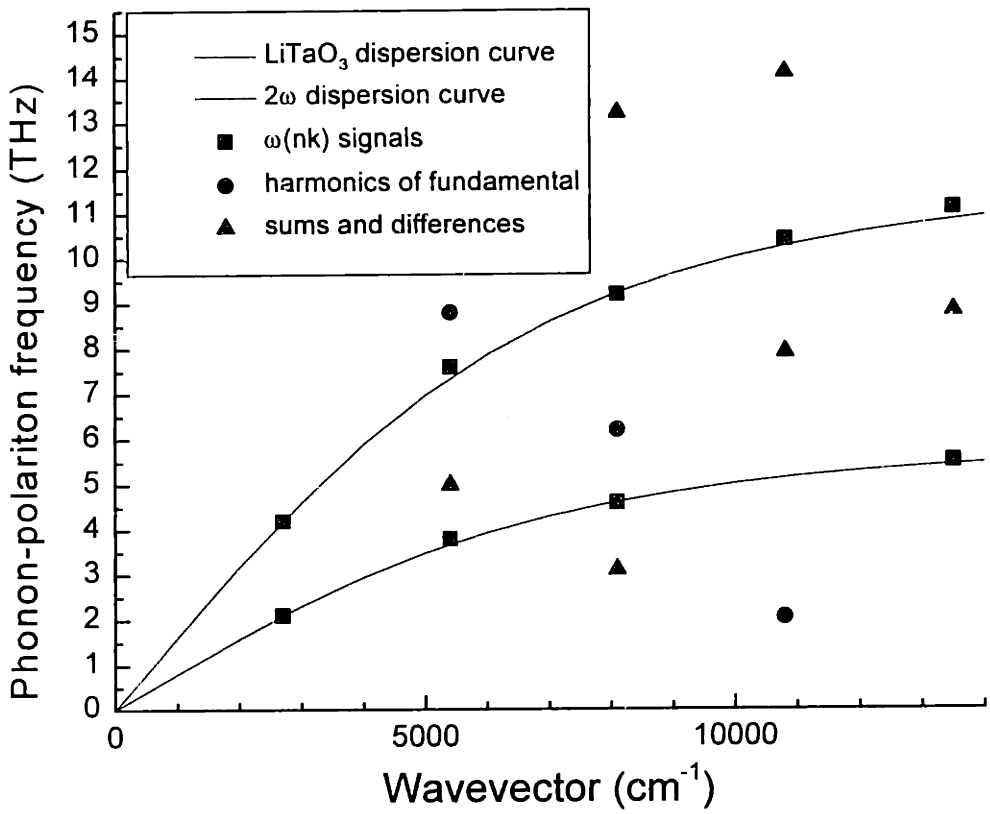

Figure 8.9 A plot of the identified frequency peaks in the WOS data. As expected, we have harmonics of the fundamental, the frequencies associated with the wavevector overtone by the linear dispersion relation ω(nk) and its harmonics, and sum and difference frequencies which may involve signals from lower overtones of the wavevector. The dispersion curve for $LiTaO_3$ and its second harmonic are plotted for reference.

8.4.2 Experimental artifacts in WOS

8.4.2.1 Nonlinear optical effects in the probe

One type of experimental artifact could produce spurious results in these experiments: nonlinearity in the pump grating. All the theory, discussion and simulations presented to this point have assumed that the grating is a sinusoidal function with a Gaussian temporal profile, and a Gaussian spatial

profile in the direction of the grating that is wide compared to the grating fringe spacing. However, there are purely optical nonlinearities that are not associated with the polariton response that can modify the experimental results.

8.4.2.2 Self focusing

The first phenomenon is self-focusing. We discussed how self-focusing can limit how far into the crystal the grating will be effective in producing an excitation grating. One point to add to that discussion is that as the light focuses, its effectiveness as a grating may increase as the light intensity increases before becoming worse as the light becomes over-focused and white light generation starts. The issue of self-focusing makes it difficult to estimate the peak optical field in the sample based on the pulse energy and the spatial and temporal dimensions at the face of the crystal, because the beam could be focused to a much smaller size, particularly in the vertical direction.

8.4.2.3 Self diffraction

Another troublesome nonlinear optic effect is self-diffraction, illustrated in Figure 8.10. The index of refraction within the pump grating is modulated by the electronic electro-optic effect. This produces an index of refraction grating that can diffract the pump beams. It is possible to create many orders of self-diffracted light, with each higher-order diffracted beam separated by a wavevector k_g in the horizontal direction from the previous one. The diffracted beams can interact with each other and with the pump beams to

create grating components that are multiples of the grating wavevector k_g. These interactions are depicted as dotted lines connecting the tips of the diffracted beams in Figure 8.10.

This presents a potentially serious difficulty to the WOS experiment because it means that the pump grating will not be sinusoidal, but can contain spatial components of wavevector nk_g. Therefore polaritons with frequency $\omega(nk)$ can be produced directly from the pump grating, without requiring any nonlinearity in the polariton response. Therefore, the wavevector overtone signals with frequency $\omega(nk)$ may be derived from optical nonlinearity in the optical pump grating, rather than nonlinearity in the polariton response.

8.4.3 Evidence for the authenticity of the WOS data

There is strong evidence that self-diffraction was not an important factor in the WOS experiment, particularly for the overtones 3 to 5. The first point is that if strong wavevector overtones were present in the pump grating, a large peak at T=0 should be evident in the data, as it is in the ISRS data at the first Bragg angle*. This T=0 peak is due to the electronic component of the electro-optic coefficient interacting with the very intense field of the pump

---

* The location of T=0 is found by adjusting the delay of the probe beam until frequency doubled light between pump and probe beams is observed. (The detector contains an optical filter to reject the doubled light during the actual data collection.) The position of the zero in the data is fairly certain despite the fact that there may be little or no diffracted light in the wavevector overtones at this time. However, the exact location of the T=0 may change by ±100 fs or so as the operator makes fine adjustments in the angle and position of the probe beam to optimize the Bragg angle.

grating to modulate the index of refraction. However, the T=0 peaks in the WOS data are very small, much smaller in fact than the subsequent oscillations. Second, if there were significant wavevector harmonics in the pump grating, the WOS data should appear as an impulsive oscillation with a maximum shortly after T=0 and declining in amplitude afterwards. In fact, the WOS data shows only a small signal after T=0, with most of the amplitude developing significantly after T=0.

The relationship between the WOS data and the fundamental polariton oscillation can be observed in Figures 8.11 to 8.14. In each the fundamental signal at the first Bragg angle is plotted with the WOS data. With the exception of the second overtone (k=2) data, the electronic peaks are very small at τ=0, indicating minimal diffraction into the selected wavevector due to self-diffraction or other optical nonlinearity in the pump grating. The peaks in the WOS data are also clearly coincident with peaks in the first few oscillations of the fundamental polariton. At maximum displacement the spatial distortion of the polariton waveforms is greatest, and the WOS signals are generated. This supports the theoretical expectation that the fundamental polariton will act as a pump grating for the generation of new frequencies at higher wavevectors.

I think that the data shown in Figures 8.12 to 8.14 is very strong evidence that the WOS signals are a manifestation of anharmonicity in the polariton, and that there are no significant artifacts from the pump grating. The case

for the k=2 data shown in Figure 8.11 is not so clear. There is an appreciable electronic response at T=0, and the first peak of the WOS signal is the biggest. However, the oscillations are not in proper phase with the electronic response. They are not in proper phase with the fundamental polariton either. I conclude that the response at k=2 is due to a combination of the polariton anharmonicity and the self-diffraction in the pump beams.

The possibility that the self-diffraction of the pump beams could create the $\omega(nk)$ signals occurred to me only after I performed these experiments, so I did not have a chance to measure the intensity of the self-diffracted light. However, at least 2 to 3 diffracted beams on either side of the pump beams were clearly visible in some of the experiments. (I did not record more information about this phenomenon because I did not realize that it might be significant at the time). A later section in this chapter discusses improvements in the experiment that could substantially reduce the higher-order self-diffraction in the pump beams, and thereby eliminate this source of potential ambiguity in the experiment.

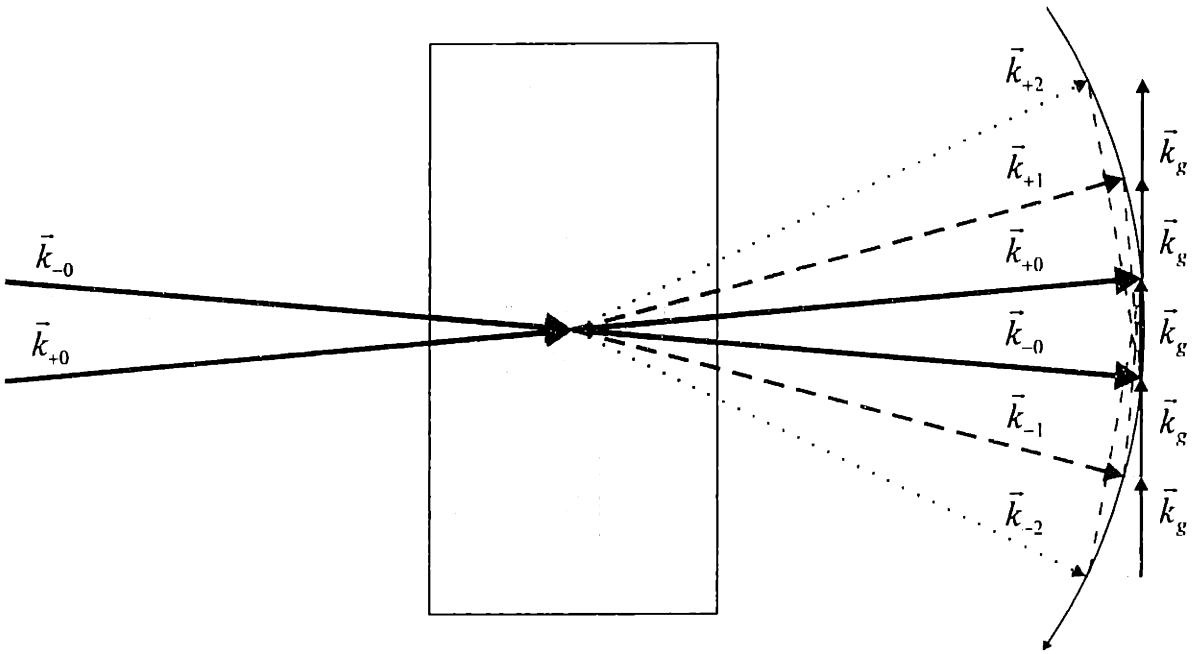

Figure 8.10 Self-diffraction of the two pump beams via nonlinear electronic interactions may create higher order pump gratings that can generate false W.O.S. signals.

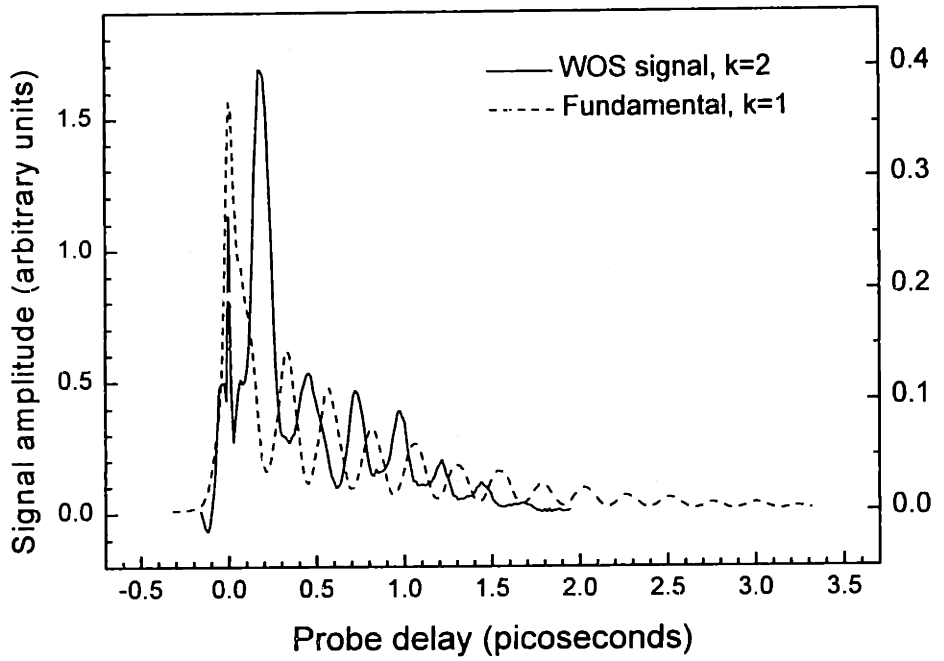

Figure 8.11 Fundamental ISRS data superimposed on 2k WOS signal.

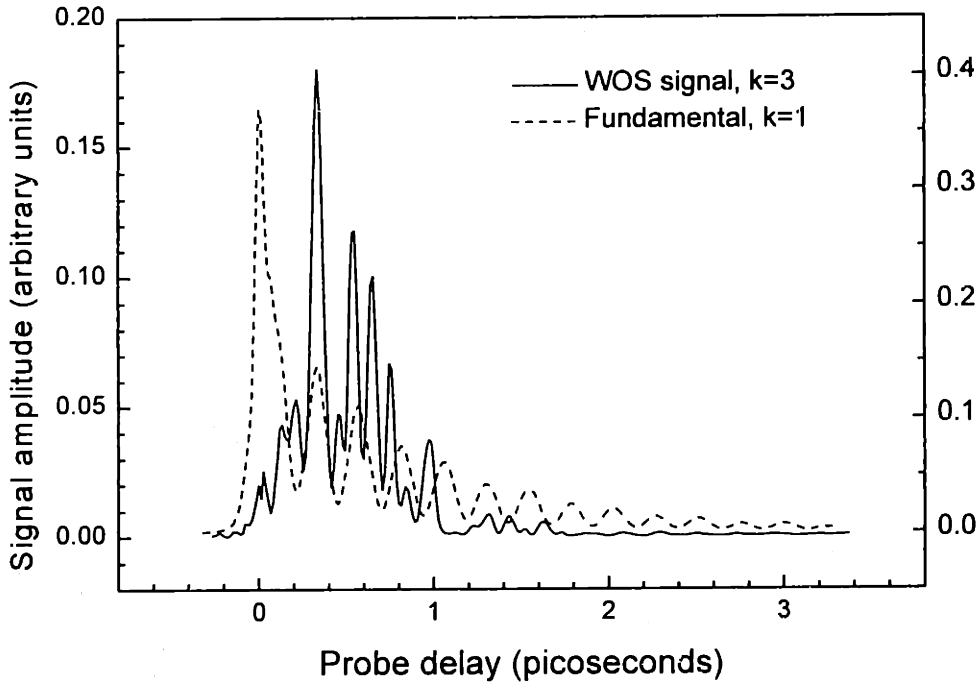

Figure 8.12 Fundamental ISRS data superimposed on 3k WOS signal.

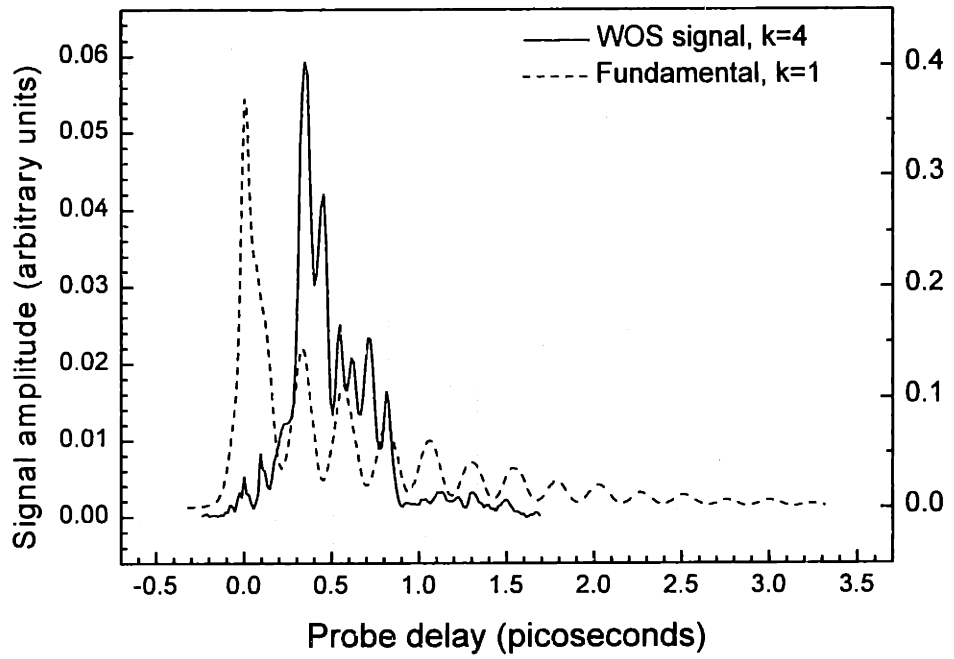

Figure 8.13 Fundamental ISRS data superimposed on 4k WOS signal.

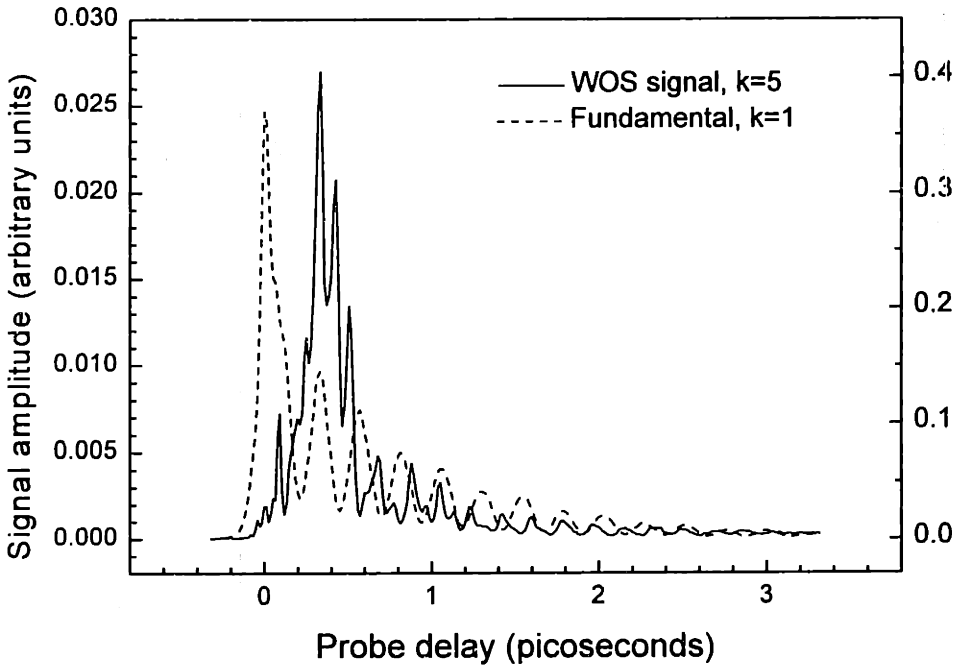

Figure 8.14 Fundamental ISRS data superimposed on 5k WOS signal.

8.5. Conclusions about the data

The data presented above provides strong evidence of anharmonicity in the polariton response. We observed the harmonics in both frequency and wavevector as predicted from the theory. In addition, we observed the $\omega(nk)$ signals that we expected would arise from polariton anharmonicity but not from nonlinearities in the diffraction process.

In general this is a difficult nonlinear problem to decipher. Optical nonlinearity in the pump can create harmonics of the grating wavevector which can produce the $\omega(nk)$ signals. Nonlinearity in either the differential polarizability or the potential energy surface can create harmonics of the frequency $n\omega$, harmonics of the wavevector nk, and new polariton frequencies $\omega(nk)$. Finally, nonlinearity in the differential polarizability acting in the diffraction grating can produce harmonics of the frequency $n\omega$, harmonics of the wavevector nk, but not new polariton frequencies $\omega(nk)$.

In order to conclude decisively that we are observing anharmonicity in the polariton, we have to rule out the possibility of optical nonlinearity in the pump grating. I think we can rule out self-diffraction in the 3rd, 4th and 5th wavevector overtones, but not in the 2nd overtone.

This leads us to the conclusion that the data provides a clear signature of lattice anharmonicity. The next step is to determine if the primary nonlinearity is in the polarization, the ionic restoring force, or both. We

have seen above that even the linear differential polarizability creates nonlinearity in the polarization in the electric wave equation. In Chapter 3 I derived perturbation expansions of the nonlinear terms. These could potentially be used to fit the simultaneous harmonics of the frequency and wavevector (the exp(ni(kx-ωt)) terms). However, data will have to be taken at two different wavevectors in order to extract the nonlinear coefficients in both the restoring force and the permittivity.

8.6. Improvements in future WOS experiments

8.6.1 Pump beam optical nonlinearities

The first thing that should be addressed in the WOS experiment is the nonlinear effects in the pump beam, particularly self-diffraction. If nothing else were done, the intensity of the diffracted pump light should be measured in order to calculate the pump grating that would form at *nk*. This would allow the calculation of the maximum ω(nk) signal that could be anticipated from pump nonlinearities. These measurements might confirm my conclusion that self-diffraction is not a significant effect in the WOS experiment.

The self-diffraction problem can be addressed experimentally by lengthening the pump pulse, while keeping the probe pulse as short as possible. This will have two benefits. First, the peak intensity will be reduced which will reduce the nonlinear pump effects. Second, the bandwidth of the pump pulse

will be reduced so that even if the pump does produce *nk* grating components, these components will be ineffective in driving the high frequency ω(nk) signals because the pulse duration is too long. For example, if a 30 fs FWHM pulse were stretched to 160 fs, the peak intensity would be reduced by more than 5. The efficiency of driving the fundamental polariton of 2 THz as in the WOS experiments above will be reduced by 30%, but the efficiency of driving the ω(5k) WOS signal will be reduced by 93%.

A simple way to stretch the pulse is to insert a piece of dispersive glass in the beam path after the probe pulse has been split off. This will stretch the pulse by chirping it, that is, spreading the frequency components in time with the redder components leading the bluer components. This will take about 1cm of a dispersive glass such as SF10[4]. This means that the pump grating changes wavevector with time. However, I calculate that this will introduce no more uncertainty in the wavevector than is present in the short pulse due to limited overlap of the pump beams, as discussed in Chapter 2.

Other problems to be addressed are self focusing and white light generation in the sample, which interfere with the diffracted signal. Lengthening the pump beam will alleviate these problems as well. In addition, using a very thin sample will allow much larger pump amplitudes, as it will eliminate most of the self-focusing effects which accelerate white light generation.

8.6.2 Pulse shaping

Stretching the pump pulse will permit more intense pump beams, which will increase polariton amplitudes. When the single-pump configuration is optimized, further gains can come from multiple pulse sequences. This was demonstrated in lithium tantalate by this research group several years ago[5]. A series of pulses are timed to be one cycle of the polariton frequency apart. Each pulse adds more energy to the polariton field. The amount of increase in the polariton amplitude depends on the damping rate, which establishes how much energy is retained from one cycle to the next. An increase in the maximum polariton amplitude of about a factor of 10 can be expected. If the pulse shaper is used for the pump beams, no other means is necessary to stretch the pump pulses, as this can be done with the pulse shaper.

Multiple pulse sequences can also be used to test various elements of the model of the WOS process. For instance, I postulate that the $\omega(nk)$ signals are generated primarily in the first half cycle when the polariton displacement is largest. This idea can be tested with a two-pulse sequence for the pump. The two pump beams should be separated by one half cycle of the polariton. The first pulse will drive the polariton as normal. The second should be π out of phase with the polariton and should stop the polariton response completely. (The relative amplitudes of the two pulses can be adjusted to accommodate the damping loss). If my idea is correct, the $\omega(nk)$ signals will be observed as before, but most of the $n\omega$ harmonics should be eliminated, as these are generated by the oscillations of the fundamental

polariton. This should greatly clarify the data and allow a more certain estimation of the polariton anharmonicity.

8.6.3 Heterodyne detection

A heterodyne detection system for ISRS has recently been reported[6]. A heterodyne detection system mixes the diffracted light with a reference beam derived from the same probe pulse of greater or equal intensity as the diffracted beam. Care must be taken to ensure that there is a constant phase relationship between the two pulses. In other words, the path length from the point where the two beams are split to where they mix at the detector must be stable to a fraction of the optical wavelength.

The diffracted beam interferes with the reference beam at the detector. Because of the phase interference between the two beams, the phase information from the diffraction grating is recovered. The light diffracted from the grating maxima is π out of phase with the light diffracted from the minima. The light diffracted from the maxima will constructively interfere with the reference, while the light from the minima will destructively interfere. The resulting signal is linear in the diffraction grating modulation, instead of going as the square as in the non-heterodyned case. This means that the signal is observed at the true frequency instead of at twice the frequency, and there will be no sum and difference frequencies generated between two different signal frequencies.

Prof. Keith Nelson has proposed a much simpler heterodyne method than the one used in the cited paper. A phase grating is to be used to split a probe and a reference beam into the ±1 diffraction maxima. The two beams are focused onto the sample by a lens. The reference beam will automatically be collinear with the diffracted pump beam as they emerge from the sample. The rest of the detection and signal processing system is the same as it is now. The probe angle will be selected by choosing one of many phase patterns all formed on one mask. To chose a probe angle, the mask is simply translated until the correct pattern is in the beam.

8.7. References

1. Yan, Y.-X., J. Edward B. Gamble, and K.A. Nelson, Impulsive stimulated scattering: General importance in femtosecond laser pulse interactions with matter, and spectroscopic applications. J. Chem. Phys., 1985. **83**(11): p. 5391-5399.
2. Wiederrecht, G.P., Femtosecond Time-Resolved Spectroscopy of Phonon Dynamics in Organic Molecular and Ferroelectric Crystals, in Chemistry. 1992, Massachusetts Institute of Technology: Cambridge. p. 243.
3. Kittel, C. and H. Kroemer, Thermal Physics. 1980, San Francisco: W.H. Freeman and Company.
4. Adachi, S., Calculation of dispersion on fs pulsewidth, . 1997.
5. Wiederrecht, G.P., et al., Anomalous Polariton Dynamics in LiTaO3. Ferroelectrics, 1993. **150**: p. 103-118.
6. Matsuo, S. and T. Tahara, Phase-stabilized optical heterodyne detection of impulsive stimulated Raman scattering. Chemical Physics Letters, 1997. **264**: p. 636-642.

Appendix A:
The amplified Ti:sapphire laser system

The following appendix is a preprint of a paper describing the laser system that was developed by Dr. Jianping Zhou. It is reproduced here with the permission of the authors.

High efficiency, multipass Ti:sapphire amplifier producing 1.45 millijoule, 22 fs pulses at 1 kHz

Jianping Zhou and Keith A. Nelson

Department of Chemistry, Massachusetts Institute of Technology, Cambridge, MA 02139

Phone: (617) 253-6295/1423 FAX: (617)253-7030

E-mail: jzhou@mit.edu and kanelson@mit.edu

Abstract

We have developed a high efficiency, multipass Ti:s amplifier which generates 1.45mJ, 22 fs pulses at 1 kHz repetition rate, based on the chirped pulse amplification technique. This novel design increases by 50% the pulse energy and extraction efficiency over previously reported high repetition rate multipass amplifiers while maintaining short pulse duration. We used two Ti:s crystals as gain media in one multipass configuration so that the thermal effect in each Ti:s crystal is reduced. By passing through both crystals a total of 13 passes, the amplified beam is deeply saturated, the stability and contrast ratio were improved.

In the past few years Kerr-lens mode locked Ti:sapphire oscillators have been built to produce pulses with sub-10 fs duration.[1-4] Typical output energies from these oscillators range from 1-10 nJ with repetition rate around 100 MHz. Using cavity-dumping technique sub-20 fs pulses with energy of 50-200 nJ were generated by several groups.[5-7] For many applications more energetic ultrashort femtosecond pulses are desirable. Chirped-pulse amplification (CPA)[8] skill has become a unique means for damage-free amplification of sub-30 fs pulses to gigawatt at kHz repetition rate[9-11] or to terawatt at 10 Hz.[12,13] These terawatt laser systems have been powerful tools to study high-field interactions, high-harmonic generation to soft x-ray regime[14] and x-ray lasers.[15] However, these systems typically occupy more than one optical tables. KHz repetition rate, femtosecond mJ level laser systems have shown to be very useful for ultrafast spectroscopy, micro-machining, and also fs coherent ultraviolet pulse generation. These kHz systems use less table space and generate more stable pulse train, which help on reducing the noise level and allows to see small signal features in very fine time windows. Recently, several groups have been using these mJ pulses to generate 10 fs or shorter energetic pulses through self-phase modulation technique in gas-filled hollow fibers.[16] This promising route toward generation of sub-5 fs pulses with higher intensities lays in mJ energy pulses with good stability due to the requirement of the high order nonlinear processes. Stable, efficient, high repetition rate, mJ amplifier systems become more and more important fs sources for a variety of researches

In this Letter we report a high efficiency, multipass Ti:s amplifier design which employed two Ti:s crystals as gain media in one amplifier configuration. This novel design resulted in the generation of 1.45mJ, 22 fs pulses at 1 kHz repetition rate with peak-to-peak energy stability better than 2.5%. This development extended past work on high-repetition rate CPA systems reported and combined the advantages of both multipass and regenerative amplifier configurations. To amplify ultrashort pulses with Ti:sapphire medium, the main

limits on the pulse duration are (a) the spectral narrowing due to the gain spectral shape and finite spectral bandwidth of optics and (b) the phase distortion of the amplifier system which limits one compresses the final pulse to transform-limited pulse shape.[12,17,18] Regenerative amplification is a well-established technique for the efficient generation of mJ energy ultrashort pulses from solid-state lasers with excellent beam quality. It employs a resonator cavity as the amplifier. However, in order to seed the amplifier and extract the amplified beam out, one polarizer (thin film or prism type) and a Pockels cell must be used inside the cavity. The efficient energy conversion requires the seeded pulse travels through them 12 to 18 times. Since the polarizer and Pockels cell have finite spectral bandwidth and certain amount of dispersion, the accumulated effects reduce the final bandwidth and add more phase distortion to the pulse. To date regenerative amplifiers showed the capability of generation of 350 μJ with 55 fs[19] and < 100 μJ with 30 fs at kHz[9] repetition rate and most of the commercial systems deliver about 1 mJ pulses with > 70 fs duration. To avoid a large ASE background this resonator configuration does not allow strong pump pulses. Multipass amplifier configuration has several advantages over the regenerative type. Since it is seeded directly with preselected pulses and there are no extra bandwidth limited devices needed inside the amplifier, the spectral bandwidth is preserved and the total phase dispersion is reduced. With multipass amplifiers, Lenzer *et al.*[10] produced 18 fs pulses with 100 μJ and Backus *et al.*[11] generated 21 fs with 1 mJ pumping with 6-7 mJ and 15 mJ of 527 nm, frequency doubled Nd:YLF laser pulses respectively. The final conversion efficiency with these previous multipass amplifier designs was limited to less than 7%, smaller than 10% of regenerative amplifiers. This was due to the high gain requirement with previous multipass design and the limited total number of passes without compromising the contrast ratio and beam quality. In our design, by using two gain media, we could propagate the seed pulse through them with 10 to 18 total passes and saturate both amplifier crystals completely for higher conversion efficiency and higher output pulse energy and still preserve short pulse duration.

Figure 1 shows the schematic of our amplifier design. The input to the amplifier is from a self mode-locked Ti:sapphire oscillator (Kapteyn-Murnane Labs, LLC, with 5 mm long Ti:s) that produces transform-limited <13 fs duration pulses, with a repetition rate of 82 MHz, at center wavelength of 775 nm, and a FWHM bandwidth of > 50 nm. The initial pulse energy is 6 nJ. The output beam passes through a folded double-path pulse stretcher, which uses one 600 groove/mm gold coated grating, blazed for 800 nm wavelength with diffraction efficiency > 90%, (Spectronic Instr., Inc.) and all-reflective optics to minimize material path length and chromatic aberration.[17] The total bandwidth acceptance of this stretcher is measured > 120 nm, and pulses are stretched to approximately 70 ps. Single pulses are selected from the modelocked train at 1 kHz by a KD*P Pockels cell (Quantum Tech., Inc.) and crossed calcite polarizers. This Pockels cell is driven by a home-built driver with < 10 ns opening window and switches between 0 and 5.8 kVolts synchronized with the Ti:s oscillator through a down counter and a time delayer (SRS, DG 535). It is placed between stretcher and amplifier to prevent amplified stimulated emission (ASE) in the amplifier from feeding back to the oscillator. An identical set of gratings is used in a standard, double-pass compressor design. The single-grating Littrow stretcher design maintains alignment while the separation and/or angle of the grating are adjusted. When combined with the relatively modest stretching factor (~6000), optimization of the pulse duration is straightforward and repeatable.

The amplifier itself consists of two Brewster-cut Ti:sapphire crystals and four 1-meter-curvature dielectric mirrors (CVI, TLM1-800). These four mirrors were place at the four corners of a 100cm x 12cm rectangle. These two Ti:s crystals were placed in the middle positions of the two 100-cm sides; each of these two spots is a common focus of two mirrors. They can be aligned such that the signal beam passes both crystals successively with a total of 13 passes, each pass crosses the same pumped regions inside both crystals and focuses near the crystals. The first crystal (Ti:s 1) is 7-mm long (a=2.1/cm, Crystal

System) and absorbs a total of 91% of the pump after double passes. The other (Ti:s 2) is 8-mm long (a=2.9/cm, Union Carbide) and absorbs 94% of the green beam. They are pumped longitudinally with 8.8 and 6.3 mJ of 527 nm light respectively from one frequency-doubled A-O Q-switched Nd:YLF laser (*Excel/Quantronix*). The pump beam is focused into both crystals with two 40-cm focal-length lenses for the first pass and refocused back to them with two 50/40 cm curvature mirrors. Small signal gain per pass was measured to be 3-4. The last two passes amplified the signal by 2 and 1.4 times respectively.

The seed beam from the stretcher was collimated to about a 0.5-mm waist and injected by a properly positioned mirror (M_1) on one of the diagonal line of the four-curved mirror. It focused to about a 380-μm in waist inside the Ti:s crystals. The pump beam was focused at the crystals with beam size measured to be about 500-μm. The divergence between the first and last pass of the signal beam was about 2.4 degree and the incident angle to these curved mirrors was reduced to 7 degrees. To align the successive passes overlapping with each other in both crystals, one only needs to make sure the separations of the spots on each mirror are the same and leveled. Once the first two spots are separated equally on all four curved mirrors, all the passes automatically cross each other in both crystals simultaneously. With a pump pulse of 15.1 mJ energy (14 mJ absorbed by two crystals), the signal pulses were amplified by a factor of 5×10^6 to 2.4 mJ and well saturated before compression. This gives a conversion energy efficiency of the pump to the amplified pulse of 16%. The seed pulse spectrum was intentionally centered at 775 nm to balance the gain-narrowing due to the amplification and red-shift due to the gain depletion by the red spectral components in the leading front of the chirped pulse. After amplification the spectrum was slightly narrowed to 42 nm and red-shifted to 803 nm. To compress the amplified pulse to near the transform-limited duration, we compensated both second- and third-order dispersion simultaneously by setting the incident angle to the compression gratings to be 4.0 degrees greater than the Littrow angle (13.9 degrees for 600 g/mm

grating) and left with $3.7x10^4$ fs^4 fourth-order dispersion according to the numerical simulation. The separation of the gratings was adjusted so that the shortest pulse duration was achieved. The throughput of the compressor was about 63%. This resulted in a final output pulse energy measured of 1.45 mJ. Figure 2 (a) shows the typical spectra without amplification (dash line) and with amplification (solid line) after propagating through the compressor. We measured the pulse duration by using a calibrated single-shot autocorrelator with a 70-μm-thick KDP as the second harmonic crystal. A sliced cross-section (+ line) is shown in figure 2 (b). The corresponding pulse duration was determined to be 22 fs assuming a $sech^2$-pulse based on the least square fit as shown in Fig. 2 (b) (solid line). The pulse duration deviates ≤2 fs across the whole beam and over a time period of eight-hour. Because of the deep saturation, the amplifier shows pulse-to-pulse energy fluctuation of ≤ 2.5%.

To suppress the ASE and beam cross-talking between passes, the beam passed successively through an seven-2mm-hole-array placed in one of the diagonal line of the four mirrors in which the amplified beam is collimated and spatially shaped every round trip. This hole-array, combining with the use of two gain media to lower the single-pass gain, eliminates most of the ASE and reduces the cross-talking. This improved the contrast ratios of main-pulse to pre-pulse and post-pulse to be better than 250:1. We examined the amount of ASE by simply turning on and off the high voltage supplied to the Pockels cell without physically blocking any optic path. With no high voltage on the Pockels cell, the amplified spontaneous emission was measured to be less than 70% of the amplified pulse energy and about 60 ns retarded. In the seeded case, ASE was suppressed to be less than 1/1000 of the signal. This indicates that the ASE intensity is below the pre- and post-pulses. Both crystals were cooled to 8-9 C to remove the excess heat energy from the pump beam.

We examined the beam focusability by measuring the beam diameter, divergence and the focal spot size using a CCD at the focus of a 75 cm focal length mirror at near normal

incidence. The beam size at the focus was measured 100±10 μm in diameter which is about twice the theoretical focal beam size. Figure 3 (a) shows the image of the focal spot and Fig. (b) vertical and horizontal intensity profiles of the beam with gaussian fits (solid lines). Small astigmatism was carried from the seed beam. These results indicate that this amplifier can generate field intensity > $7x10^{16}$ W/cm^2 at 1 kHz assuming the beam is focused with a f/5 optic, which is comparable to the hydrogen atomic binding strength.

In conclusion, by using two gain media in one amplifier configuration we have developed a new type of multipass amplifier which is capable of generating pulses of 1.45 mJ energy, 22 fs pulse duration at the pump energy of 15.1 mJ. By extending this multi-gain media design to three or more gain crystals with more pump energy, we could conceivably achieve higher efficiency, higher energy pulses with sub-30 fs pulse duration at high repetition rate.

We would like to thank Greg Wakeham for invaluable help on setting up the single-shot autocorrelator and the LabView software and Dutch Chung for a variety of help in the lab. Zhou would like to thank Professors M.M. Murnane and H.C. Kapteyn for encouraging him to test this idea. The authors acknowledge funding for this project from Office of Naval Research and National Science Foundation.

References:

1 M. T. Asaki, C. P. Huang, D. Garvey, J. Zhou, H. C. Kapteyn, and M. M. Murnane, *Opt. Lett.* **18,** 977 (1993).

2 J. Zhou, G. Taft, C. P. Huang, H. C. Kapteyn, and M. M. Murnane, *Opt. Lett.* **19,** 1149 (1994).

3 A. Stingl, M. Lenzner, C. Spielmann, F. Krausz, and R. Szipocs, *Opt. Lett.* **20,** 602 (1995).

4 L. Xu, C. Spielmann, F. Krausz, and R. Szipocs, *Opt. Lett.* **21,** 1259 (1996).

5 M. Ramaswamy, M. Ulman, J. Paye, and J. G. Fujimoto, *Opt. Lett.* **18,** 1822 (1993).

6 M. S. Pshenichnikov, W. P. d. Boeij, and D. A. Wiersma, *Opt. Lett.* **19,** 572 (1994).

7 G. N. Gibson, R. Klank, F. Gibson, and B. E. Bouma, *Opt. Lett.* **21,** 1055 (1996).

8 D. Strickland and G. Mourou, *Opt. Commun.* **56,** 219 (1985).

9 K. Wynne, G. D. Reid, and R. M. Hochstrasser, *Opt. Lett.* **19,** 895 (1994).

10 M. Lenzner, C. Spielmann, E. Wintner, F. Krausz, and A. J. Schmidt, *Opt. Lett.* **20,** 1397 (1995).

11 S. Backus, J. Peatross, C. P. Huang, M. M. Murnane, and H. C. Kapteyn, *Opt. Lett.* **20,** 2000 (1995).

12 J. Zhou, C. P. Huang, M. M. Murnane, and H. C. Kapteyn, *Opt. Lett.* **20,** 64 (1995).

13 C. P. J. Barty, C. L. GordonIII, and B. E. Lemoff, *Opt. Lett.* **19,** 1442-1444 (1994).

14 J. Zhou, J. Peatross, M. M. Murnane, H. C. Kapteyn, and I. P. christov, *Phys. Rev. Lett.* **77,** 1743 (1996).

15 B. E. Lemoff, G. Y. Yin, C. L. G. III, C. P. J. Barty, and S. E. Harris, *Phys. Rev. Lett.* **74,** 1574 (1995).

16 M. Nisoli, S. D. Silvestri, and O. Svelto, *Appl. Phys. Lett* .**68,** 2793 (1996).

17 J. Zhou, C. P. Huang, C. Shi, M. M. Murnane, and H. C. Kapteyn, *Opt. Lett.* **19,** 126 (1994).

18 C. B. J. Barty, G. Korn, F. Raksi, C. Rose-Petruck, J. Squier, A.-C. tien, K. R. Wilson, V. V. yakovlev, and K. Yamakawa, *Opt. Lett.* **21,** 219 (1996).

19 J. V. Rudd, G. Korn, S. Kane, J. Squier, and G. Mourou, *Opt. Lett.* **18,** 2044 (1993).

Figures

Figure 1: The schematic of a two gain media, multipass amplifier system which produces 1.45 mJ, 22 fs pulses at 1 kHz repetition rate.

Figure 2: Spectrum of the output pulses after compression: dash line, without amplification; solid line with amplfication.

Figure 3: Single-shot autocorrelation trace of a sample of the 1.45 mJ amplified and recompressed pulse: ++ line is the measurement, solid line is the fitting curve. Assuming a $sech^2$ pulse shape, the pulse duration is 22 fs.

Figure 4: The image of the focal spot (a) and beam profiles (vertical and horizontal) of the compressed pulse (b). The beam size was measured to be 100±10 μm in diameter which is about twice of the diffraction limit.

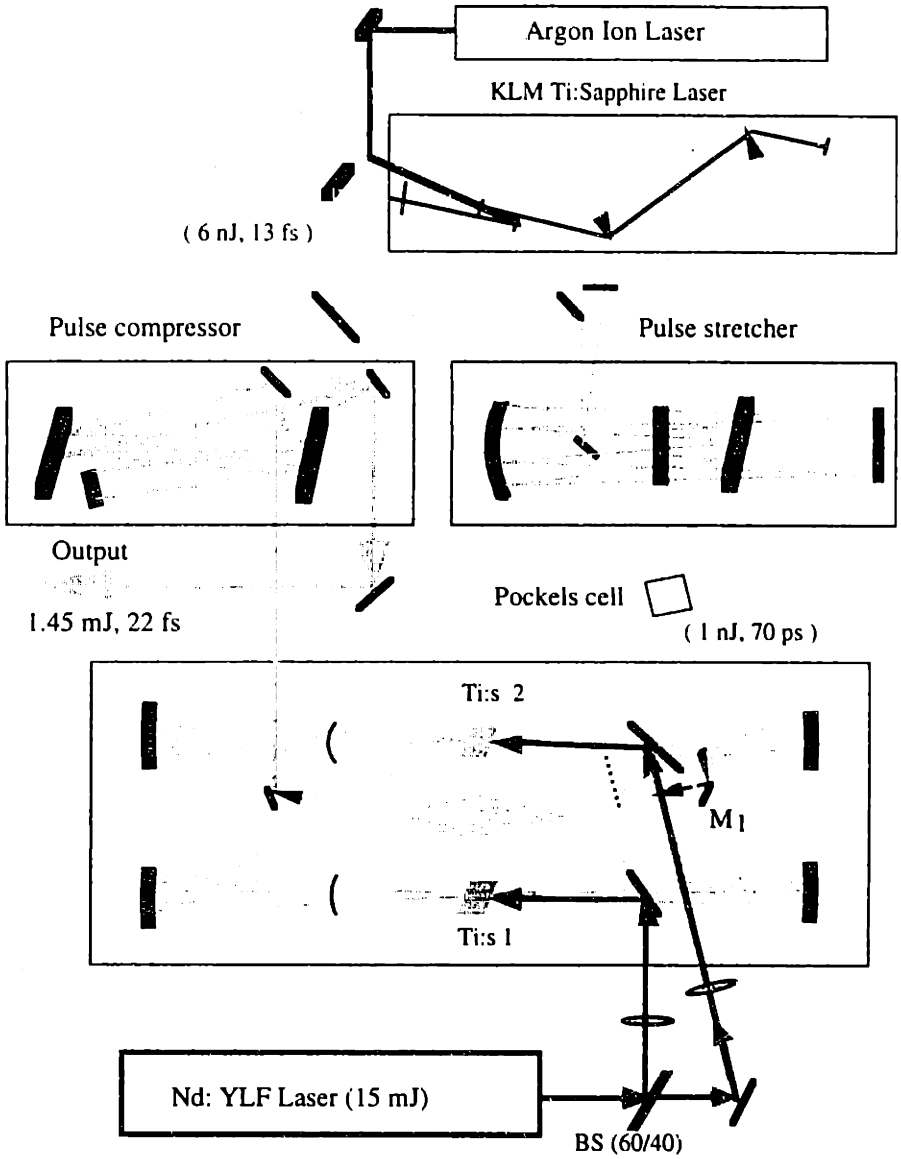
Argon Ion Laser
KLM Ti:Sapphire Laser
(6 nJ, 13 fs)
Pulse compressor
Pulse stretcher
Output
1.45 mJ, 22 fs
Pockels cell
(1 nJ, 70 ps)
Ti:s 2
M1
Ti:s 1
Nd: YLF Laser (15 mJ)
BS (60/40)

Figure 1

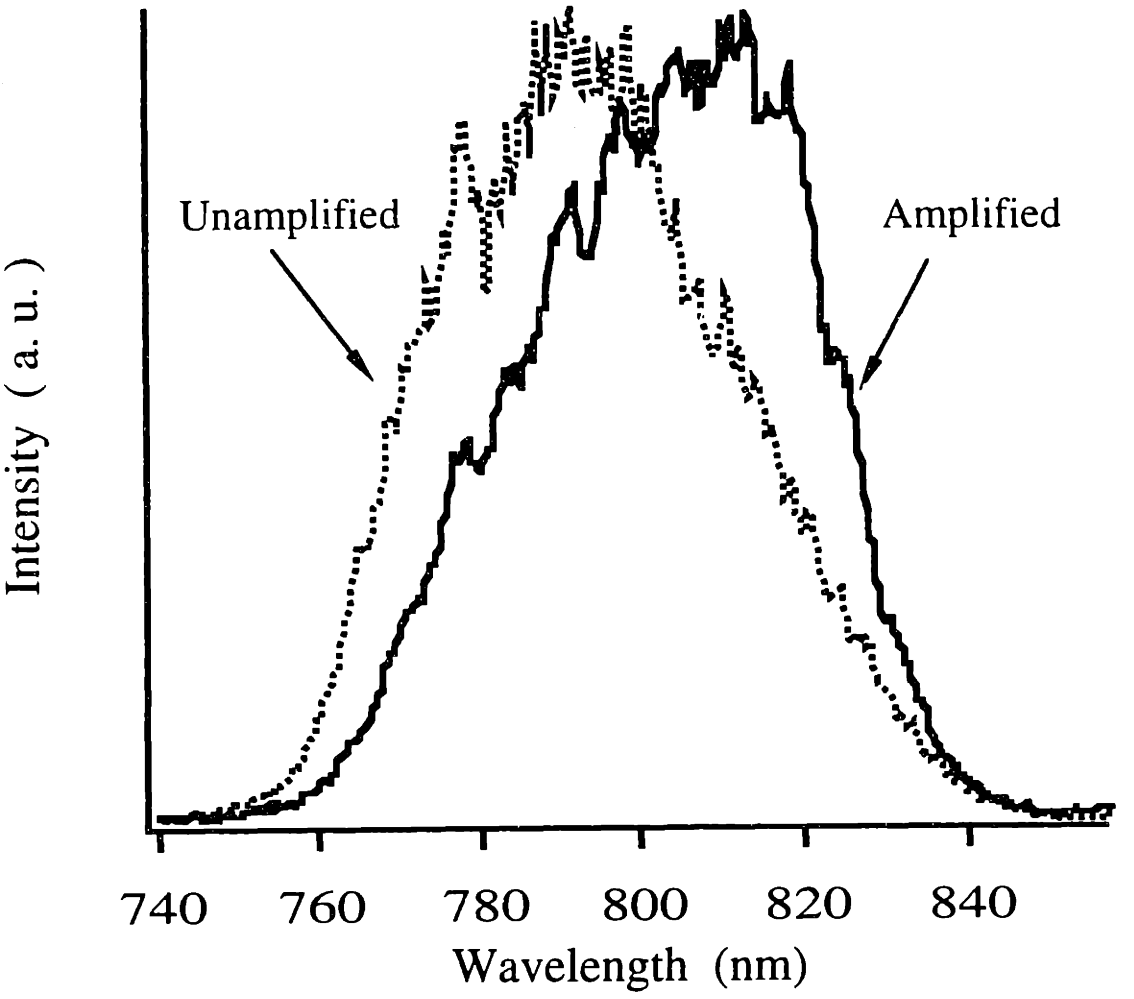
Unamplified
Amplified
Intensity (a. u.)
740
760
780
800
820
840
Wavelength (nm)

Figure 2

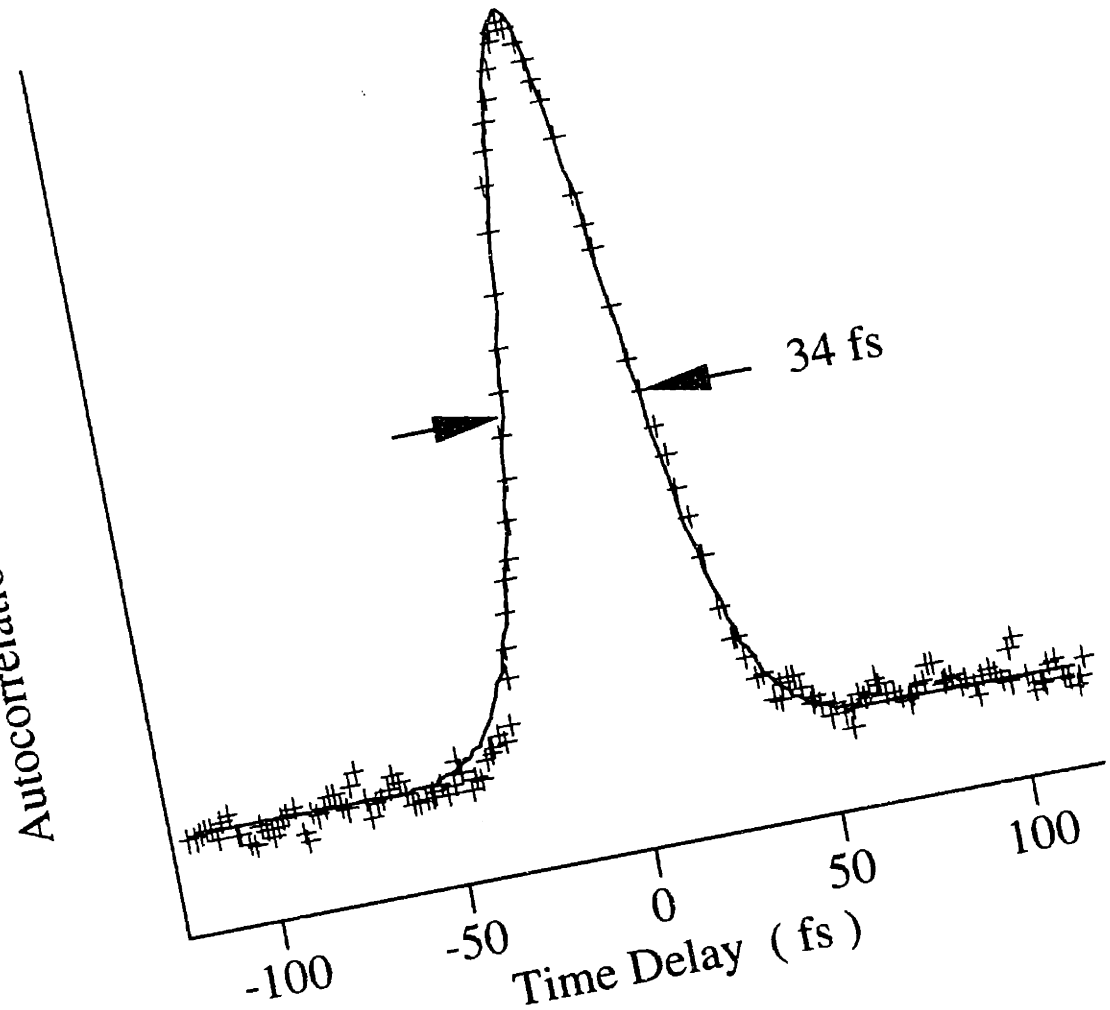
Autocorrelation Intensity (a. u.)
34 fs
-100
-50
0
50
100
Time Delay (fs)

Figure 3

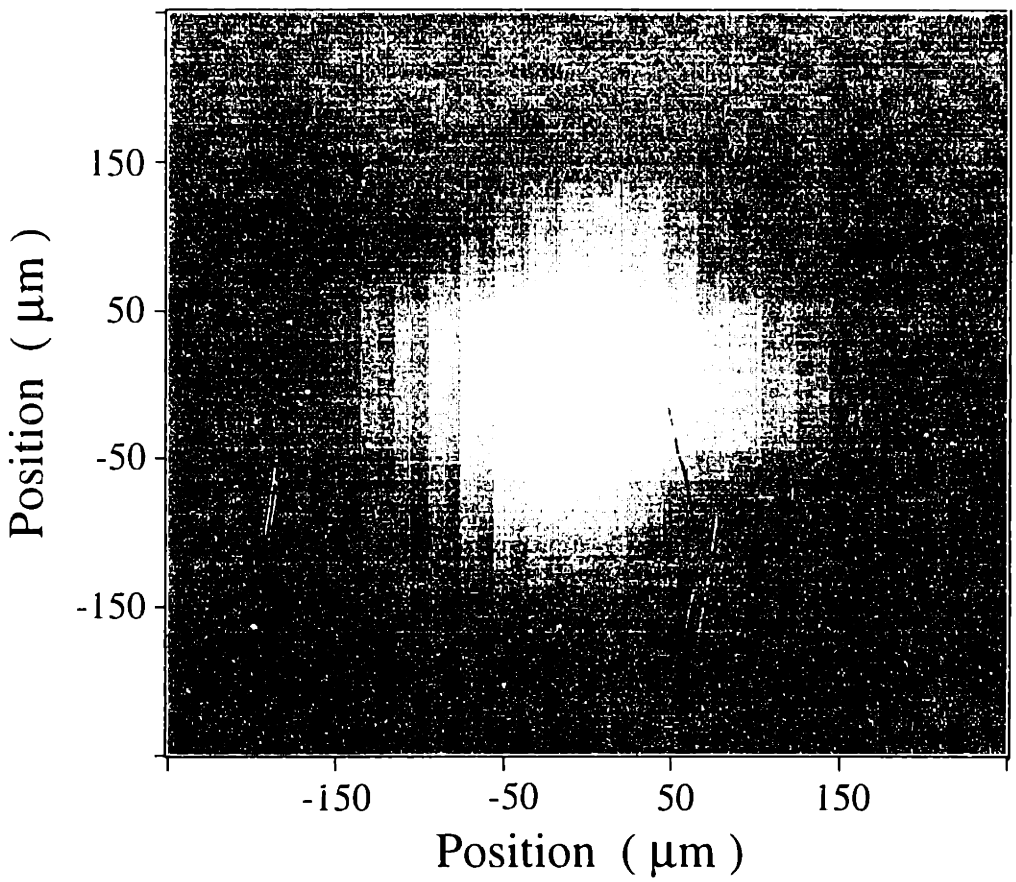

Figure 4 (a)

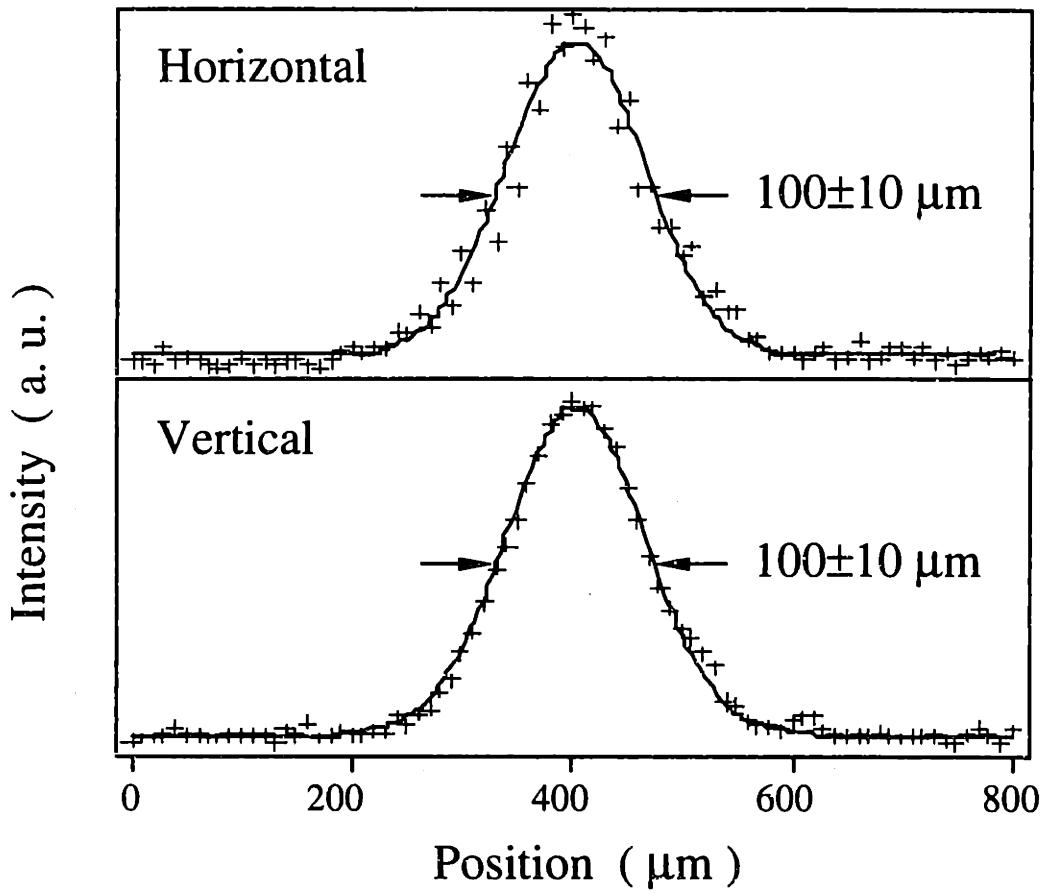
Horizontal
100±10 μm
Vertical
100±10 μm
Intensity (a. u.)
0
200
400
600
800
Position (μm)

Figure 4 (b)

Appendix B:
The Laser Pointing Servo System

B.1. Introduction

The laser pointing servo is a system to maintain precise alignment of laser experiments. It consists of a quad detector assembly to measure the deflection of the beam, a piezoelectric mirror mount to steer the beam, and the controller electronics. The controllers can be adjusted to accommodate most optics in the beam path between the piezo mirror and the quad detector. In addition, the controller automatically adapts to CW or pulsed lasers of any frequency greater than 1 Hz.

The concept of the pointing servo is very simple. The quad detector and associated circuitry provides an error signal which is proportional to the distance the beam is off target. This error signal is amplified by a large negative gain. The amplified signal is applied to the piezo mirror which moves in the direction to reduce the error signal. The final amount of error is inversely proportional to the amount of gain.

The practical servo is complicated by stability problems which are primarily caused by mechanical resonances. The servo will oscillate unless steps are taken to counteract these resonances. The primary criterion for stability is that the servo gain is less than unity at and above all the major resonance frequencies. The servo system provides an internal calibration device for

adjusting the servo gain in the actual optical system so this stability criterion is met.

B.2. Laser Pointing Servo Instructions

B.2.1 Setup Instructions:

The servo system consists of the controller unit, the piezo mirror, the optical pickoff, and the detector. The system is installed as follows:

1. Replace any turning mirror in the optical path with the piezo mirror.
2. Insert the optical pickoff in the beam path near the intended target of the beam. The thin glass slide in the pickoff should be at about 45 degrees to the beam. The amount of light reflected from the pickoff can be adjusted with this angle. As the angle approaches the Bragg angle (about 57 degrees) the amount of reflected light will decrease.
3. Position the detector so that the reflected beam from the pickoff is approximately centered in the detector. **BE CAREFUL OF REFLECTED LIGHT FROM THE SURFACE OF THE DETECTOR!** The detector is smooth and shiny and reflects laser light fairly well, so don't look at the face of the detector without appropriate eye protection.
4. Connect the piezo mirror to the controller, making sure that the horizontal and vertical channels are not mixed up. Plug in the detector. Turn on the controller. Switch the Servo Control switch to **Off**.

B.2.2 Alignment Instructions:

1. Make sure the power is **ON** and the Servo Control switch is set to **Off**. Turn both Gain controls to maximum (fully clockwise).
2. Align the beam using the manual adjustment knobs on the piezo mirror along with the other adjustable optic elements in the beam path.
3. When the beam is properly aligned, roughly center the reflected beam from the pickoff on the detector by using the adjusting knobs on the pickoff unit.
4. Adjust the Sensitivity rotary switch until the Amplitude meter is approximately centered. The meter should be above 2 and below 9. If you are on the lowest range and the meter is above 9 then too much light is hitting the detector. Adjust the incidence angle on the pickoff to be closer to the Bragg angle as discussed under step 2 in the Setup Instructions above. Alternatively, you may use a neutral density filter in front of the detector to reduce the light intensity. (The beam diameter should be about 4mm or larger on the lowest sensitivity setting to avoid exceeding the maximum power density of the detector.)
5. Adjust the horizontal control on the pickoff unit until the Horizontal meter on the controller swings from one side to the other. This indicates that the beam is near center on the horizontal axis. (You cannot really center the meter because the gain is too high, so it always will go to one side or the other.) If you tweak the knob back and forth, the meter should swing back and forth as you cross the center position. Ignore the Vertical meter.

6. Adjust the vertical control on the pickoff until the Vertical meter swings from one side to the other. Ignore the Horizontal meter.
7. Set the Servo Control Switch to **Calibrate**. If there is inverting optics in the beam path so that the direction of the beam displacement is reversed, switch the Horizontal Polarity switch to **Invert**. (Telescopes and spatial filters invert the beam.) Otherwise the Horizontal Polarity switch should be set to **Normal**. Turn the Horizontal Gain knob until the Horizontal meter is centered. (If the meter does not move from the -1 position try switching the Polarity switch to the opposite position). Repeat this process for the Vertical Gain and Vertical Polarity controls.
8. Switch the Servo Control switch to **Engage**. Both the Horizontal and Vertical meters should move near the center position and stay there. The servo is now adjusted and activated.

With pulsed lasers and under certain other conditions (short effective distance between piezo mirror and detector or large beam diameter) it will not be possible to center the meters because the servo gain is too low. The servo will still work under these conditions. Turn the gain knobs to their maximum position and switch the Servo Control switch to **Engage**. The meters should swing to a centered position. If they do not, try switching to the opposite polarity with the Polarity switches.

B.2.3 Pulsed lasers:

The best way to check the performance and gain of the servos using a pulsed laser is to put a BNC "T" on the coax cable going the piezo mirrors and monitor the output voltage on an oscilloscope. The correction voltage will have a step-wise appearance; the voltage will change in a step increment during the pulse and will be nearly constant between pulses. The step size should be an order of magnitude or more smaller than the overall fluctuations. In particular, large alternating steps are a sign of oscillation. However, very small step sizes will not be as effective in stabilizing the beam.

Note that the piezo mirrors will make a soft buzzing sound with a pulsed laser. This is due to the step-wise correction voltage, which introduces a lot of frequency components at the laser repetition frequency and its harmonics. This is normal. If the buzzing becomes very loud, check for oscillations with an oscilloscope.

B.2.4 Tweaking the beam alignment:

Once the servo is engaged, the beam positioning is set by the pickoff, not the piezo mirror.

To tweak the positioning of the beam, tweak the adjusting knobs on the pickoff. The piezo will automatically move the beam to re-center the reflection on the detector.

B.2.5 Re-centering the piezo mirror:

The piezo actuators can only move in and out a few microns. This is a very fine adjustment. If the beam alignment is moved very much by adjusting the pickoff, or if thermal drift is excessive, the piezo actuators may reach their maximum excursion. This can be monitored by looking at the Horizontal and Vertical meters. The actuators are in their active range if the meter reads between -1/2 and +1/2.

If the meters read more than +1/2 or less than -1/2, the piezo mirror should be re-centered. With the servo engaged, tweak the manual control knobs on the piezo mirror until the meters are at their center position. This will ensure that the actuators are active and that the beam is centered on the detector.

B.2.6 Deactivating the servo:

To deactivate the servo set the Servo Control switch to **Off**.

Do not turn off the servo power while the laser is running. The controller's output swings from 0 to 125 volts. The output is 62.5 volts when the servo is centered or when the Servo Control switch is set to **Off**. When the power is turned off the output is 0 volts, and the piezo actuators are fully retracted. This will misalign the beam.

B.2.7 Problems:

- If the servo does not stay centered or seems to jump between positions, make sure that the beam is not clipping and that the beam profile (spatial mode) is good. If the beam is clipped, the resulting reflections and diffracted light can confuse the servo and upset its stability.
- The servo cannot correct for poor mode quality. If the mode of the beam is fluctuating substantially, the servo may interpret this as positional fluctuations and try to compensate by moving the beam. This could make matters worse.
- High power lasers can suffer instabilities due to air currents which may be made worse by heating of the air in the beam by the laser. The servo will not help this. Use a beam tube.
- It is often not possible to use the servo when the beam is double-passed, especially when the return beam is much stronger such as the input to a regenerative amplifier.
- If it is not possible to calibrate the servo gain as described above, make sure that the beam diameter is not too big and that the spatial mode is good. A beam diameter of 2-3 mm seems to work well. The gain of the servo is inversely proportional to the beam diameter, so large beam diameters can cause the servo gain to fall below the level needed for calibration.
- If the piezo mirror makes loud buzzing or high pitched humming sounds, the servo is may be oscillating. (If the servo is used with a pulsed beam, the piezos will always buzz a little at the repetition rate of the laser. This

is normal.) Oscillation can occur when the gain is set too high. Recheck the servo calibration. Servo oscillations may also be caused by clipped beams or really bad spatial profiles. If re-calibration does not solve the problem, check the beam. The best way to check for oscillations is to monitor the output of the servo to the piezo mirror with an oscilloscope.

B.3. Servo circuit description

The schematics for the servo are shown in Figures B.1 to B.7.

Figure B.1 shows the input amplifier section for the servo. There are four independent amplifiers, one per quadrant of the quad photodiode. The quad photodiode (or quad detector) is a large photodiode with its anode divided into four equal quadrants. There is one common cathode which is connected to the +15v power supply. The four quadrants are reverse biased, and will conduct current proportional to the amount of light striking them. The single purpose of the servo system is to attempt to equalize the current in the four quadrants by steering the laser beam so it is centered on the quad detector. (Actually, we are attempting to center either an image or a small fraction of the beam.)

The signals from the quad detector are brought in on J2. The four amplifiers are precision JFET op-amps U1-U4. They are configured as transimpedance amplifiers; they produce an output voltage that is proportional to an input current. There are six CMOS analog switches U5-U10 that are used to

switch the gains of the op amps to one of six different gain settings. The analog switches are controlled by rotary switch J1 on the front panel. For each gain setting a different feedback resistor and capacitor is switched into the circuit.

The purpose of the feedback resistors is to set the transimpedance gain. The transimpedance gain is simply the value of the resistor in units of volts/amp. Therefore the transimpedance of this circuit ranges from 10^4 to $3x10^6$ volts/amp. The purpose of the capacitors is to set the impulse time constant of the amplifiers. The time constant of a resistor R in parallel with a capacitor C is simply the product RC. The time constant of the transimpedance amplifiers is 30 microseconds. This means that the response to a very short light pulse will be an electrical pulse with a rapid rise time, followed by an exponential decay with a 30 microsecond time constant. The purpose for this time constant is to stretch out the electrical pulse so that very short optical pulses produce a significant response from the servo. The servo response is determined by the electrical time constant and pulse amplitude, but is independent of the optical pulse duration if the optical pulse is much shorter than 30 microseconds.

Figure B.2 shows the arithmetic section of the servo. We want to derive two signals from the quad detector inputs proportional to the vertical and horizontal displacements. However, the signals from the quad detector are the amplitudes from the top right (TR), top left (TL), bottom left (BL), and

bottom right (BR) quadrants. The vertical signal V = (TR+TL) - (BR+BL), while the horizontal signal H = (TR+BR) - (TL+BL). The four sections of U11 perform the pair-wise sums, while the two sections of U13 perform the subtractions. U12 sums all four quadrants to generate the Sum signal. The H and V signals are sent to the gain control potentiometers on the front panel. The potentiometers are used to adjust the overall gain for each channel for stable feedback operation. The H and V signals are then applied to the divider circuits consisting of U14, U15, and U16. The divider circuits are made by connecting analog multipliers U15 and U16 in a negative feedback configuration. This circuit normalizes H and V by dividing them by the total pulse intensity. This ensures that amplitude fluctuations in the laser are not interpreted as fluctuations in the position.

Figure B.3 shows the filter section of the servo. U19 and U20 form the low-pass filters. Mechanical resonances in the piezo mirror unit cause large phase shifts to occur at frequencies above 1 KHz. If the servo system has a system gain of more than unity when these resonances create a phase shift of more than 180°, the servo will oscillate in an uncontrolled manner because the phase shift will have turned the negative feedback into positive feedback. The servo system must be compensated in some manner to prevent this from happening. The circuit shown here uses the simplest type of compensation: single-pole compensation. This means that a single stage in the system imposes a frequency response that reduces the gain as a 1/f function for frequencies above a given corner frequency. The gain and the value of the

corner frequency must be chosen so the gain is less than one at the resonant frequecies.

There are two sets of filters used in the circuit. The first consists of U19 and associated components. It gives the system a 1 KHz unity-gain frequency response; the frequency is reduced to unity at 1KHz. This outputs from this filter is used when the servo is engaged. The second filter consists of U20 and associated components. It gives the system a 25 Hz unity-gain frequency response. It is used during the calibration procedure to stabilize the servo against DC and low-frequency fluctuations.

Both filters are connected to analog switch U18. This switch disengages the servo when the Sum signal drops below one volt. This ensures that the servo will disengage when the beam is blocked. It also helps the servo respond correctly to pulsed lasers; the switch cuts off the exponential tail of the impulse response of the transimpedance amps, and the servo holds its state until the next pulse comes along. This allows the servo to respond in a pulse averaging mode. Only the active area of each impulse influences the servo, while the time in between the pulses is ignored. The response of the servo is given by a convolution over the last 10 pulses or so. This design allows the servo to respond correctly to any pulse repetition rate from 1 Hz to about 10 KHz. Above 10 KHz the impulses from the transimpedance amps will run together to form a continuous signal. Switch U18 will always be on, and the servo will switch to CW (continuous wave) mode.

The circuit that drives the Sum Meter is also shown on Figure 3. U17a is a peak hold circuit that catches the peak amplitudes and holds them with a time constant of 0.44 seconds. This allows an accurate measure of the amplitude of pulsed lasers, especially those with low repetition rates. The output of the peak hold circuit is buffered by U17b which drives the meter.

Figure B.4 shows the gain calibration circuit. The purpose of the gain calibration circuit is to achieve the proper level of gain for the whole servo system, including the uncharacterized beam path between the mirror and the detector. This is done by opening the servo feedback for all frequencies above 25 Hz, injecting a 300 Hz test signal into the amplifier circuit that drives the piezo mirrors, measuring the 300 Hz signal pickup up by the quad detector, and comparing it to a reference value. The gain of the circuit can then be adjusted until the detected level equals the reference value.

U21a and U21d form the oscillator circuit. Relay K1 turns on the oscillator when the control switch is in the Calibrate position. The 300 Hz signal is injected into the servo via relay K2, which is also engaged when the control switch is in the Calibration position. U22, U34, U23b and U23c form a simple lock-in amplifier. The lock in amplifier is triggered from the oscillator via U21b and locks into the 300 Hz feedback signal with a bandwidth of 1Hz. This filters out nearly all of the noise from the laser. The output from the lock-in is compared by U23a and U23d to a reference

voltage generated by U21c, which is simply the rectified and scaled output of the oscillator. The result of the comparisons is displayed by the H and V signal meters.

When the servo is engaged the feedback path from the filters to the output amplifier is closed by K3. When the control switch is in the Disengage position, neither the calibration nor the feedback signals are connected to the output amplifiers.

Figure B.5 shows the polarity and notch filter section. U24 and the polarity switches are used to select between an inverted and a noninverted signal. This allows the servo to accommodate inversion of the signal in the optical path from mirrors or lenses. U25 and associated components form a notch filter which provides strong attenuation in a frequency band centered on 4.8 KHz. This kills some very vigorous high frequency mechanical resonances that would destabilize the servo system if they were not attenuated. U31 generates a DC bias of 2.5 volts which establishes the DC output voltage of the power amps. U26 multiplies the 2.5 volts by 2 to give a 5 volt DC bias. The power amps have a gain of 12.5 which gives an output bias of 62.5 volts. This is 1/2 of their full range output voltage of 125 volts. The output voltage is set to this value because the piezo actuators require a unipolar driving voltage. This voltage is applied the piezos at all times that the power is on, even when the servos are disengaged. When the servos are engaged,

the correction signals to the servos are added to this bias voltage, and the total voltage to the servo can swing from about 2 to about 123 volts.

Figure B.6 shows the power amplifiers and their power supply. Let us consider just the H channel. U27 forms the differential stage of the amplifier, with the negative feedback provided by R152 and R154. This drives Q1, a class-A common-emitter voltage amplification stage. Q2 forms a constant-current load, and D14 and D15 are included to make the positive and negative slew rates of the amplifier approximately equal. D17-19 produce the bias voltage for the output stage. These diodes are epoxied to the heat sinks of Q3, Q4 and Q8 for thermal stabilization. The output stage consists of Q3 and Q8 in an NPN Darlington configuration, and Q4 and Q7 in a pseudo-PNP Darlington configuration. C72 provides the dominant pole for the amplifier compensation, and C73 is very important for stabilizing the local feedback in the output stage against high-frequency oscillations. Q5 and Q6 serve as current limiters for the output stage. D12 and D13 limit the output to 125 volts to protect the piezos from over-voltage. L1 and C74 form an RF filter for the output stage to help prevent RF interference. They also decouple the output from the load at high frequencies which improves high frequency stability. Full-wave rectifier U30 and associated capacitors provide the 150 volts to run the amplifiers. R180 bleeds the capacitors so they do not retain dangerous voltages for a long time after the power has been turned off.

Figure B.7 shows the wiring of the front and rear panels and the power connections. The high voltage transformer is a 1:1 isolation transformer. A commercial +/- 15v DC supply powers the rest of the circuit.

Figure B.1 Detector transimpedance amplifier circuit.

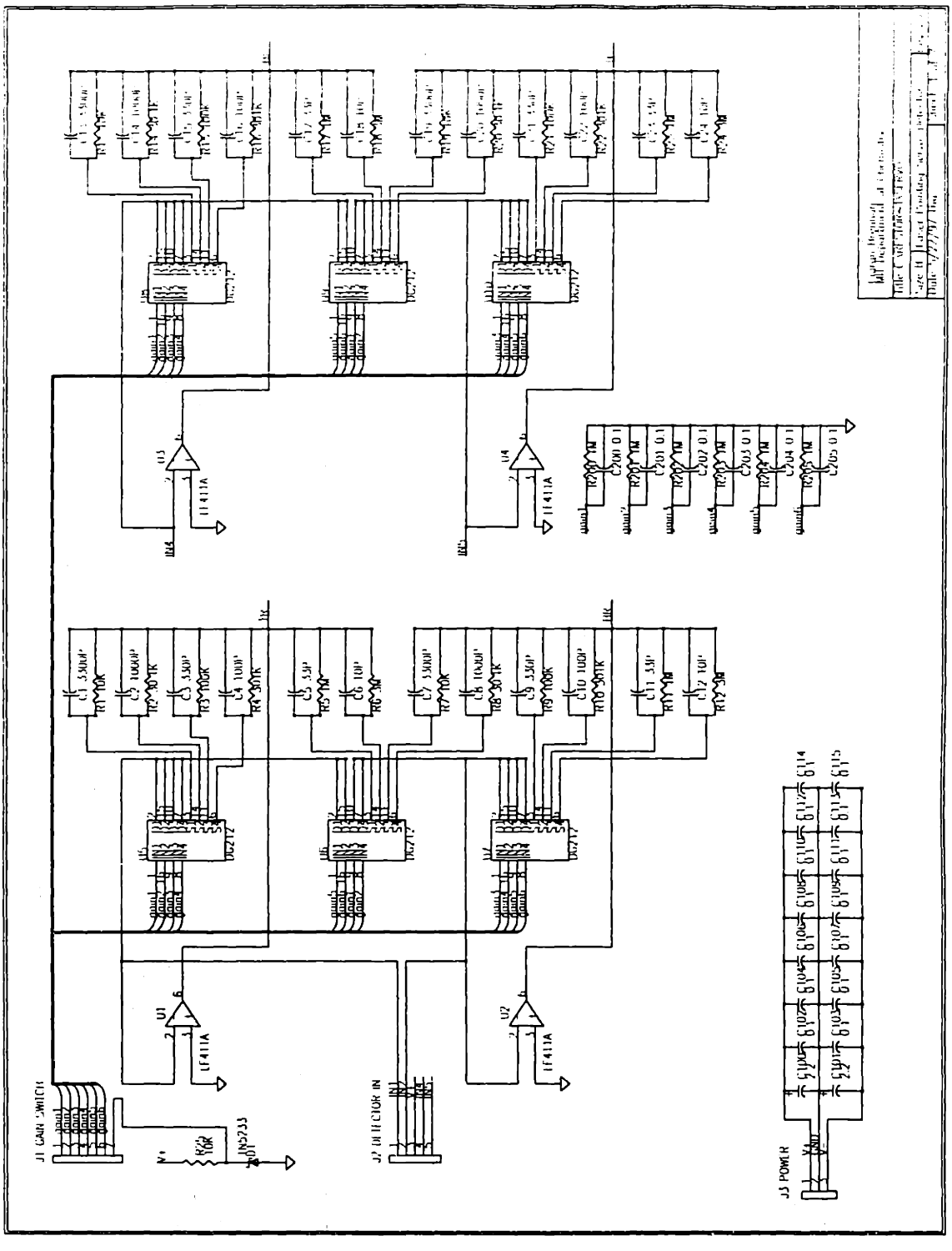

Figure B.2 Arithmetic circuit.

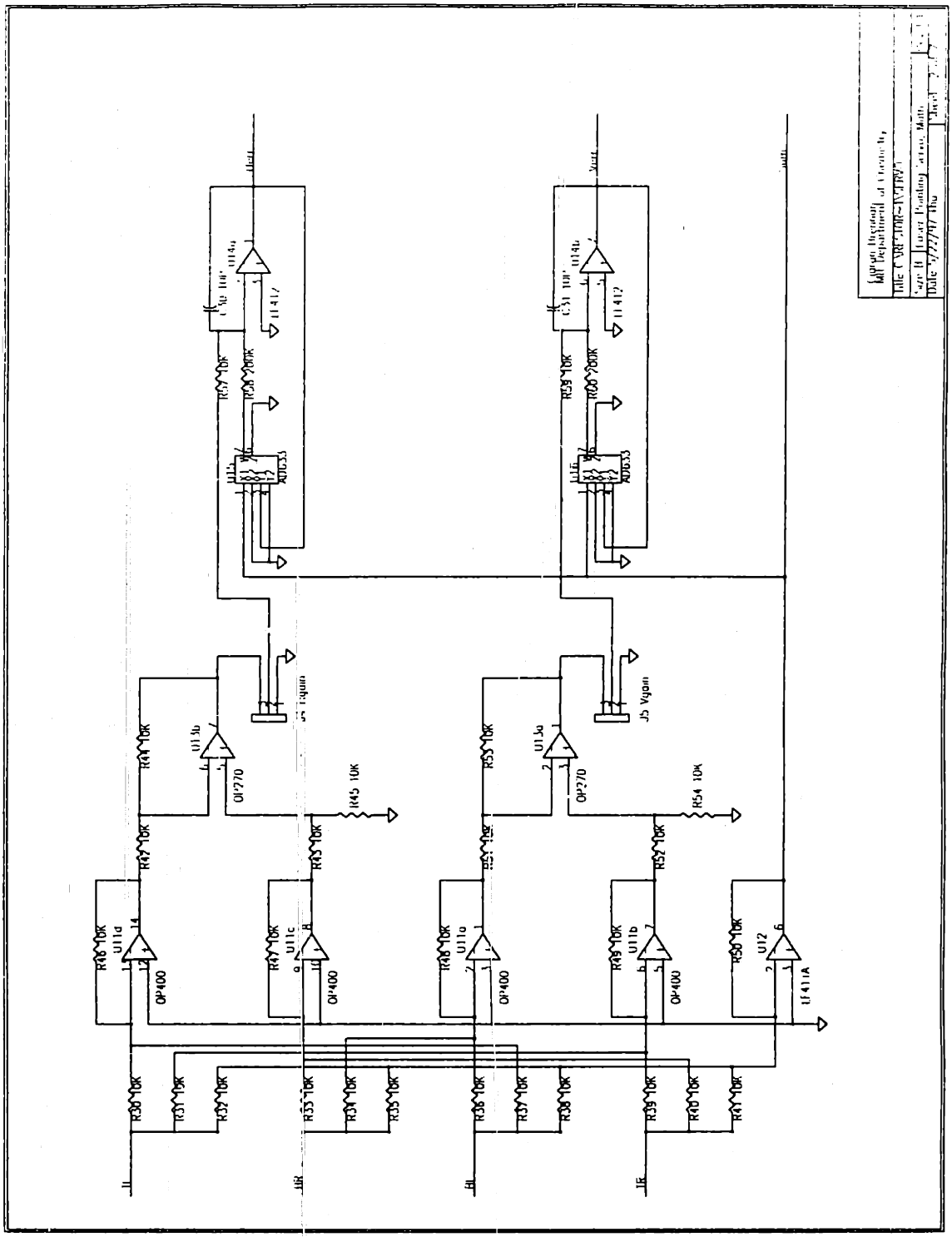

Figure B.3 Filter circuit and sum meter circuit.

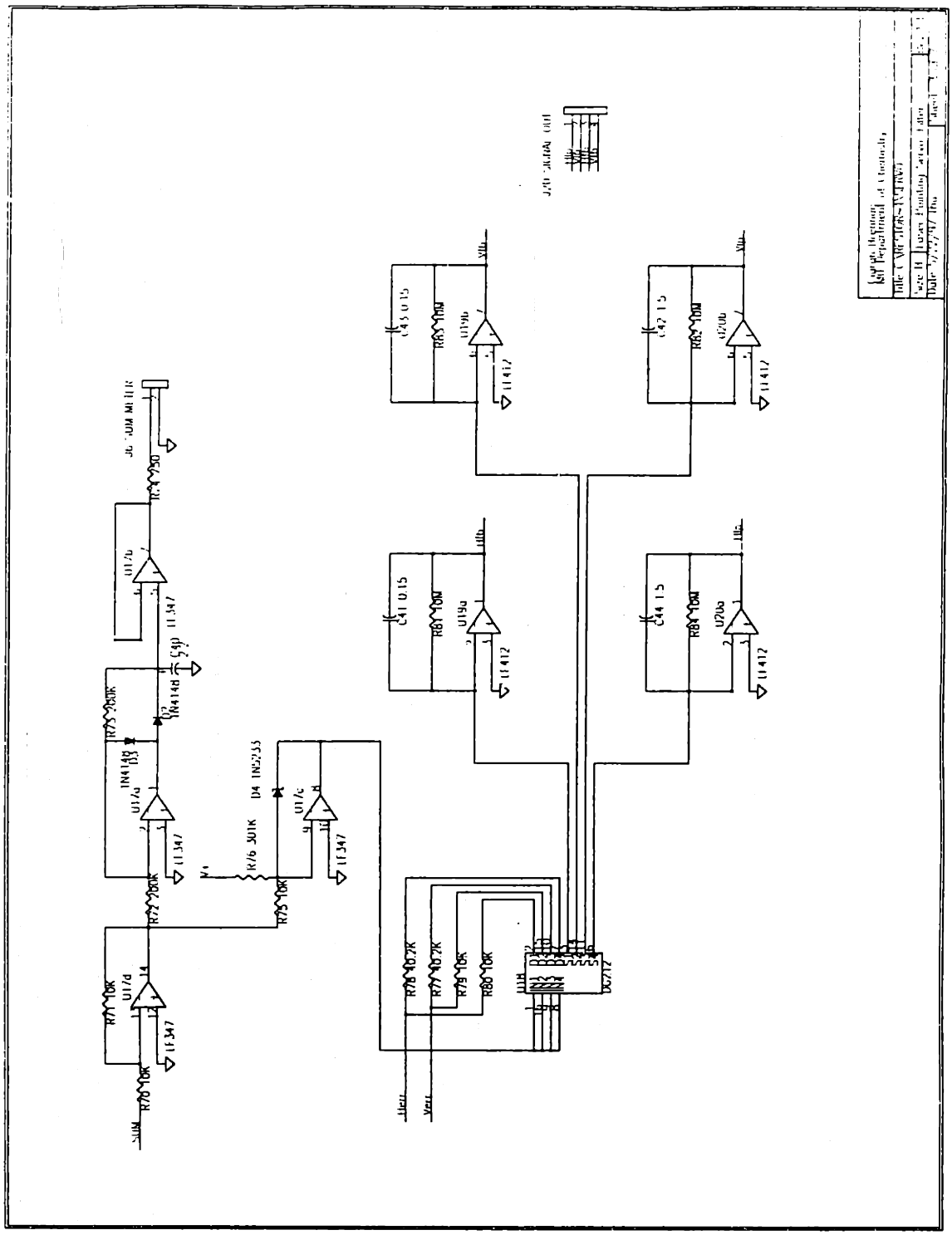

Figure B.4 Gain calibration circuit.

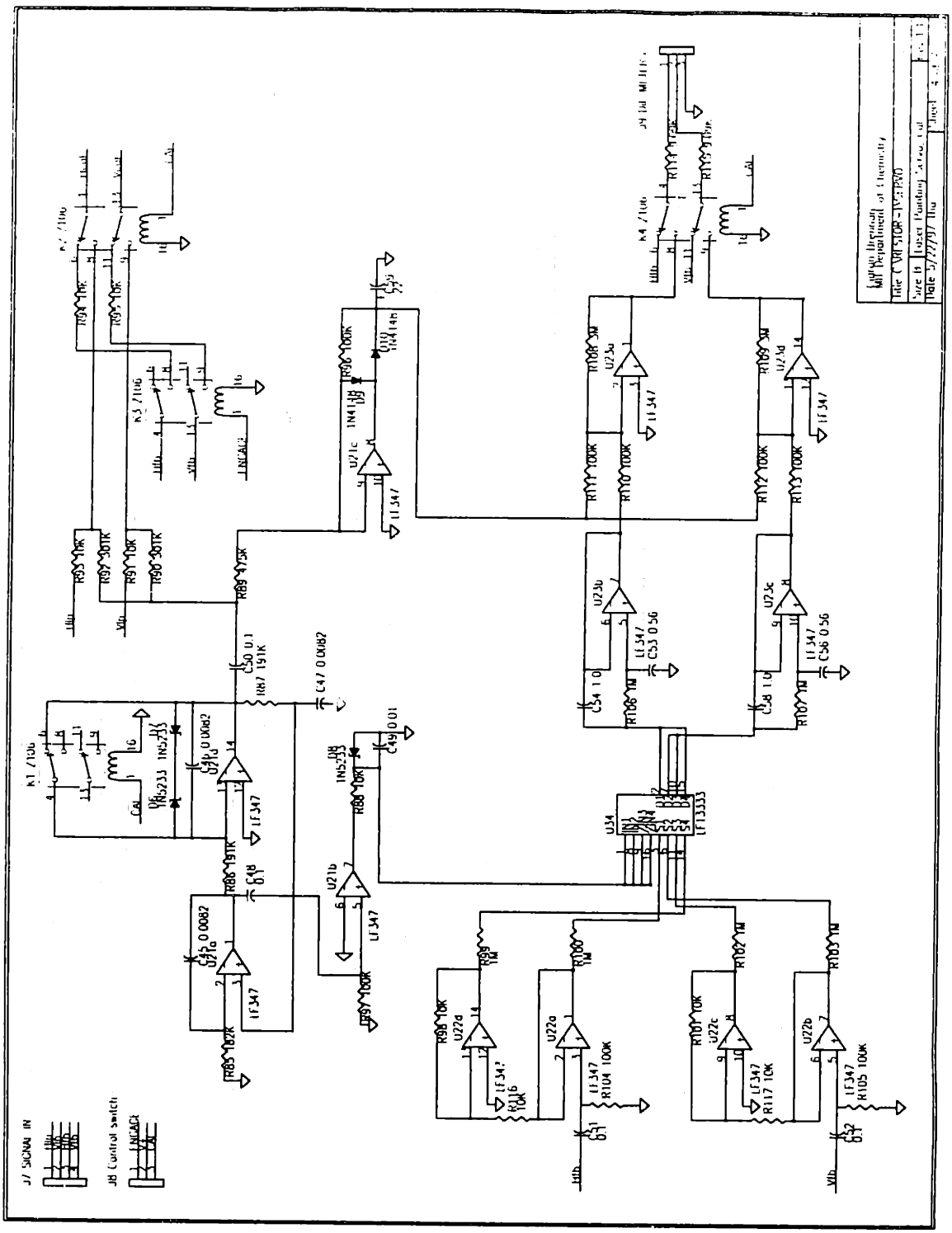

Figure B.5 Polarity, notch filter and bias circuits.

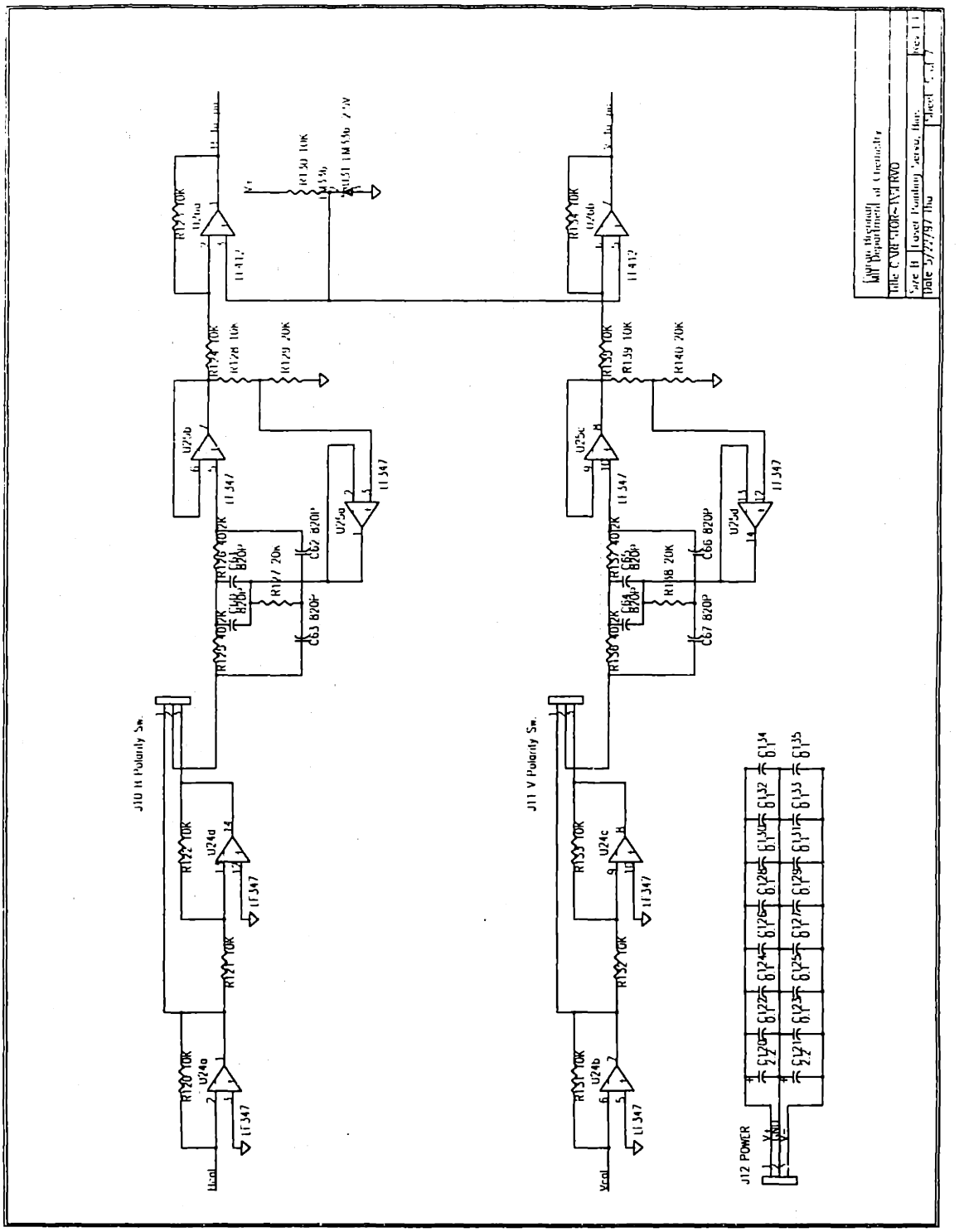

Figure B.6 Power amplifier circuit.

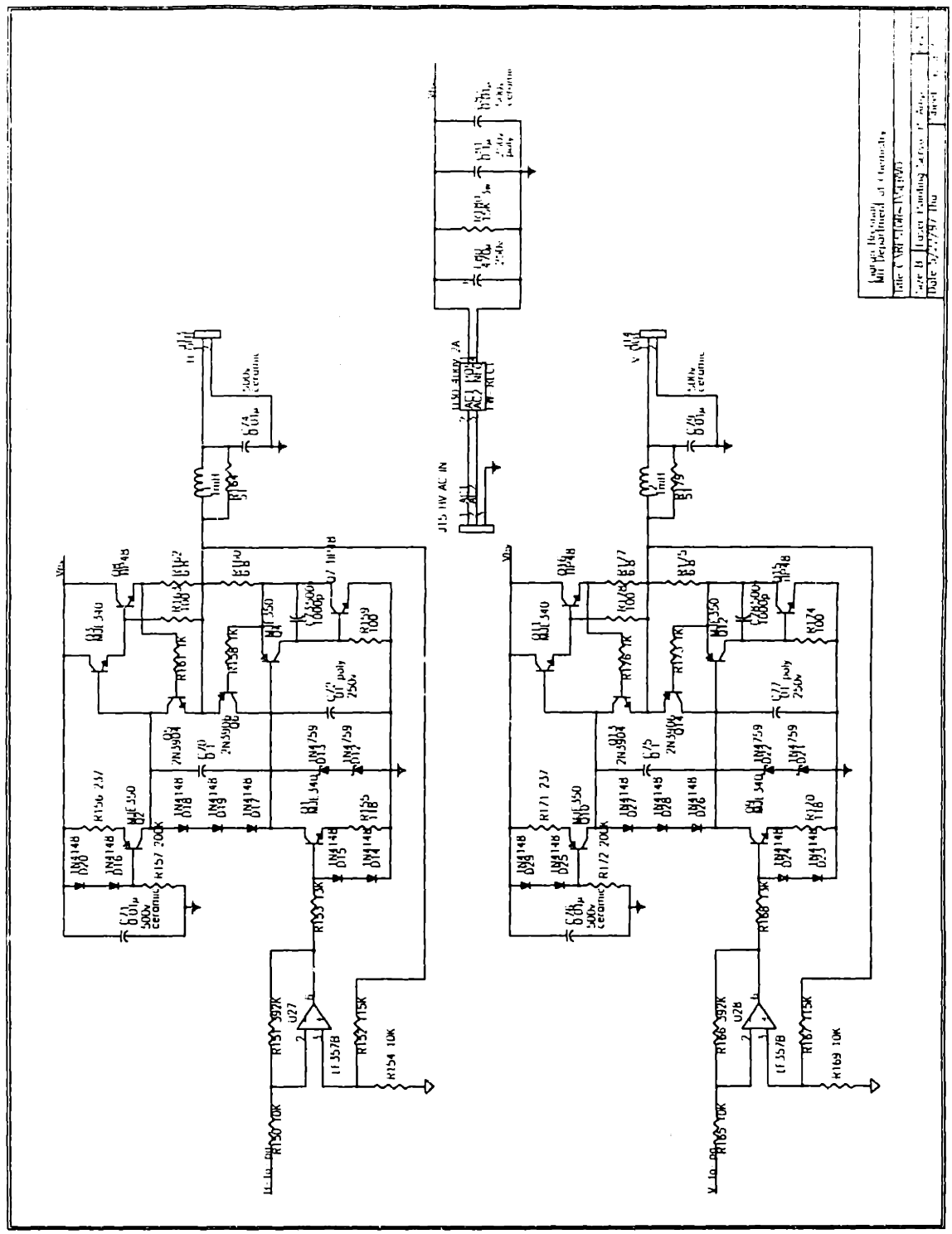

Figure B.7 Power supply and chassis wiring.

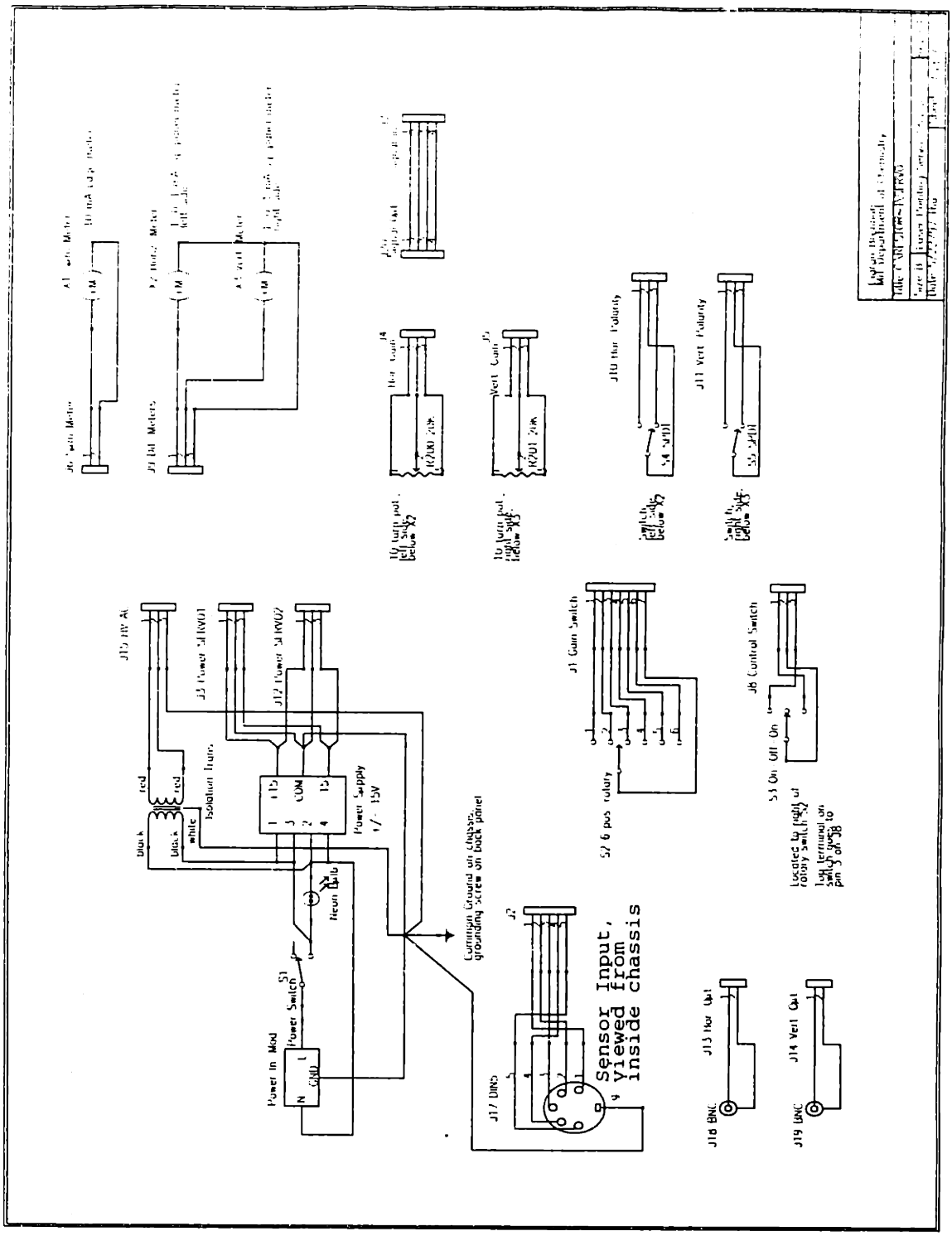

Appendix C:
The Polariton Simulation Program

C.1. The parameter file "params.txt"

```
; SIMULATION CONTROL PARAMETERS
;
; For good accuracy, use ~10 points per wavelength in space dimensions.
; DelayDT ~ 1/10 period for good-looking waveforms.
; The program will tell you if dT is too large.
;
;Starting State
StartState 0     0 = start with null state, 1 = start with stored state
SaveState 0      0 = don't save end state, 1 = save end state
;
;Time Parameters
Tstart 0       Starting time for simulation in femtoseconds
Tend 8000      End time for simulation in fs.
dT 1.5         Size of time steps
DelayDT 20       Time step for probe delay in femtoseconds
;
ProbeStart 0       Starting delay time for probe pulse in fs.
ProbeEnd 0     Ending delay time for probe pulse in fs. (-1=Tend, 0=auto)
;
;Space Parameters
dWL 20     Number of points per wavelength for auto grid
Xmax 600       Width of simulation area in microns
Xnum 600       Number of points in x direction (-1 = auto grid)
Ymax1 100      Thickness of front dielectric area in microns
Ynum1 50       Number of points in front dielectric (-1 = auto grid)
Ymax2 250      Thickness of ferroelectric area in microns
Ynum2 250      Number of points in ferroelectric area (-1 = auto grid)
Ymax3 100      Thickness of rear dielectric area in microns
Ynum3 50       Number of points in rear dielectric area (-1 = auto grid)
;
;Printing Controls
PrintQ 1       1 turns on printing of Q arrays, 0 turns off.
PrintE 1       1 turns on printing of E arrays, 0 turns off.
PrintV 1       1 turns on calculation and printing diffraction vector.
PrintW 1         1 turns on calculation and printing of coupled waves.
```

```
VecTs 0     Start time to print vectors and state arrays in fs.
VecTf -1        End time for printing vectors and state arrays in fs.  (-1 = Tend)
VecDT 490     Time step to print output vectors and state arrays (-1 = DelayDT)
;
;Boundary Conditions
BoundsX 1     0 = fixed bc's, 1 = fixed bc's with damping zones
DampZone 75     The width of the damping zones at both ends in microns
DampQMax 1e3  Max. additional damping for Q in damping zones (cm^-1)
DampEMax 0.02 The maximum damping rate for E at all boundaries
;
; EXPERIMENTAL CONFIGURATION PARAMETERS
;
;   Note: multiple pump pulses can be set in file pump_pulses.txt.
;   If the number of points is set to zero in pump_pulses.txt, or the
;   pump_pulses.txt file is missing, the default parameters below are used.
;
;
PumpPos -1        Default position of pump in microns (-1 = Xmax/2)
PumpTime 200    Default time of pump pulse
PumpLength 20   Default pulse length (1/e full width) in femtoseconds.
PumpWidth 4000 Default spatial width of pulses in microns (1/e full width)
PumpAmp 50      Default energy per pump pulse (microjoules)
Grating 1         1 = grating experiment, 0 = discrete pump beams
Kx 4          Grating wavevector in 10^3 cm^-1
Lamda 0.79     wavelength in microns
Temp 0      Sample temperature
;
ProbePos -1        Position of probe beam in microns (-1 = Xmax/2)
ProbeLength 20   Probe time duration (1/e full width), fs
ProbeAmp 1        Probe amplitude
ProbeWidth 200   Width of probe (1/e full width) in microns
ProbeAngle 1      Vertical angle in degrees
BeamHeight 100  Vertical size of probe and pump beam in microns
Intersect 0       Depth of pump/probe intersection (microns)
;
;
; MATERIAL PROPERTIES
; The following properties taken from Gary's Phys. Rev. B paper on LiTaO3.
;
; Phonon numbers
W_T 201         TO phonon freq. in cm^-1
W_L 402         LO phonon freq. in cm^-1
```

```
Gamma_1 14.9    Damping rate in cm^-1
Anharm3 1.23e6  Cubic anharmonicity factor
Anharm4 1.52e12    Quartic anharmonicity factor
;
; Electro-optic numbers
R33 2.5e-11        electro-optic coefficient (m/v)
ModeN 2.73e21  Number density of TO oscillators (1/cm^3)
ModeQ 12       Charge of single TO oscillator (electron units)
ModeM 11.73    Reduced mass of single TO oscillator (atomic units)
;
; Permittivity numbers
Eps_inf 5.46       High freq. permittivity
Eps_ip 8.5     Permitivity at LO frequency
Eps_front 1    Permittivity in front of sample
Eps_back 1     Permittivity in back of sample
;
; Relaxational mode numbers
Trelax 300     low freq relaxational mode in fsec
Brelax 1.1e4       relax. mode coupling factor B1rBr1 (cm^-2) (0 disables it)
```

C.2. The program source code

```
/* Program polariton.c */
/* Calculates 2-D time dependent propagation of polaritons using finite-difference technique */
/* Ciaran Brennan,  last revision 28 July 1996 */


/*  The major new feature of this version is to calculate the signal at the Bragg angles
    of the harmonics of the fundemental grating wavevector.  The output array becomes a
    matrix, with each column representing the signal at a wavevector harmonic.  The
    calculated signal combines the higher-order diffraction from lower wavevector
    harmonics with the 1st order diffraction from the higher order wavevector harmonic.
    Wave coupling theory is used to calculate the total diffracted signal.

    Anharmonic terms may be included in the potential.

   All the internal, input and output numbers are now scaled to real units.

    Output units are MV/um (1e12*V/m) for E, microns for displacement X, unitless
    relative permittivity changes for diffraction array V, and microjoules for signal
    array W.  If input parameter ProbeAmp is set to 1, then W may be interpreted as
    relative diffraction efficiency at the various probe angles.

    Internal units are in femtoseconds (fs), microns (um), microcoulombs (uC),
    and femtograms (fg).
```

```
Electric current -> microcoulombs/femtoseconds = giga-amps.
Electric potential -> (fg*um^2)/(uC*fs^2) = megavolts (MV).
Electric field -> MV/um.
Phonon freq. units -> 1/fs.
Normal mode displacement Q = sqrt(m*N/2)*X -> sqrt(fg/um).
Forcing function F, where F=(1/2)N(da/dQ)E^2, -> sqrt(fg/um)*(1/fs^2).
Permittivity of vacuum -> uC/(MV*um).
Energy -> fg*um^2/fs^2 = Kg*m^2/s^2 = Joule.

The phonon displacements, Q, are expressed as normal modes.  Q = X * sqrt(m*N/2),
where X = displacement, m = mass of mode, and N = density of oscillators.  While
this is inconvenient in terms of units, it makes the formulas identical to the
theoretical ones found in sources such as Born and Kun.

Input parameter units are different from the program units.  For example, the
frequencies in the params file are in cm^-1. The units for the input parameters
are indicated in the comments in the params file.

Program reads in parameters from 'params.txt'.  The parameters are identified by
a keyword followed by the numerical value for the parameter.  The simulated output is
light intensity scattered at the Bragg angle as a function of probe delay for a grating
experiment.  If it is not a grating experiment, the output is the birefringence
vs. delay time of the probe pulse .  This data is stored in a file called 'output'.
The output waveform is recorded at specified intervals in files called 'Vxxx', where
xxx is a number ranging from 000 to 999.

One or more pump pulses are entered in the file 'pump_pulses.txt'.  The first column is
the position in microns of the pulse center.  The next column is the time of the center
of the wavepacket.  Additional columns may be used to specify the amplitude, size, FWHM
duration, and shape of the pump pulses.  If one of these extra parameters is defined for
one pulse it must be defined for all the pulses.  Also, all the columns must be in the
right order, which is position, time, amplitude, size, duration, and shape.  The number
of columns (# of curves) and the number of pulses (# of points) must be specified in the
first line of the file 'pump_pulses.txt'.  If pump_pulses.txt does not exist or 'points'
is set to zero in pump_pulses.txt, a single pump pulse using the parameters from
'params.txt' is used.

Grating experiments may be calculated using the "Grating" option in the
params file.  This option uses two crossed beams to produce an interference grating.
The k vector for the interference pattern is specified in the params file, as are the
default pump beam widths and durations.  The center position of the two beams is
specified in the pump_pulses.txt file.  The default amplitude, size, and duration may
also be overridden by values specified in the pump_pulses.txt file.  For a grating
simulation, the simulated output represents scattering of the probe pulse at Bragg
angle.

Currently multiple pulses may be specified for a grating experiment, but they will
all have the same k vector.  An additional parameter may be added to the pump_pulses.txt
to allow a series of grating pulses with different wavevectors.
*/
```

```
#include <errno.h>
#include <stdlib.h>
#include <stdio.h>
#include <string.h>
#include <math.h>
/*  The math libraries are from C/Math Toolchest for Engineering and Scientific Applications
    by Charles P. Bernardin, ISBN 0-13-605866-3.  This is a book with a floppy disk containing
    the libraries.  The data types such as Real_Vector and Complex_Matrix are defined in the
    following header "mathlib.h". */
#include "mathlib.h"
/* #include <cmt.h> */ /* A header defining internal variables for mathlib. */

#define sqr(x) ((x)*(x))
/* The following are constants used for parsing the parameter file */
#define MAX_LEN 80
#define KeyLen 12
#define DBL_LEN 24
#define EndLEN 3
#define CTRL_Z 0x1a
#define MinExpon -7.0      /* The minimum exponent allowed for gaussian calculations (negative double)
*/
#define NumExpon 200       /* The number of pre-computed exponentials (positive int) */
#define maxWave 6          /* most pos. wave for diffraction calcs (must be pos.) */
#define minWave -maxWave   /* most neg. wave for diffraction calcs (must be neg.) */

/* Physical constants */
const double C = 0.3;     /* speed of light (um/fs) */
const double QE = 1.6e-13; /* charge of electron (uC) */
const double EPS0 = 8.854e-6; /* permittivity of vacuum, uC/(MV*um) */
const double MU0 = 1.255e6;   /* permeability of vacuum, fg*um/uC^2 */

/* Input parameters for simulation control */
    struct param1 {
        double dX;        /* X grid spacing */
        double dY1;       /* Y grid spacing in front dielectric region */
        double dY2;       /* Y grid spacing in ferroelectric sample */
        double dY3;       /* Y grid spacing in rear dielectric region */
        double Tstart; /* starting simulation time */
        double Tend;  /* ending simulation time */
        double dT;        /* time increment */
        double Xmax;/* size of sample in X direction */
        double Ymax;/* total size of simulation grid in Y direction */
        double DelayDT; /* probe delay step size */
        double DampZone;/* size of damping region at sides of array */
        double DampQMax;/* maximum mechanical damping of Q in DampZone */
        double dWL;       /* number of points per wavelength for auto grid  */
        double Ymax1;   /* size of front dielectric region in Y direction */
        double Ymax2;   /* size of sample in Y direction */
        double Ymax3;   /* size of rear dielectric region in Y direction */
        double DampEMax;/* max damping of E in DampZone = conductivity/EPS0 */
```

```
        double VecTs;    /* starting time for printing arrays */
        double VecTf;    /* end time for printing arrays */
        double VecDT;    /* time interval for printing arrays */
        int Xnum;        /* number of points in X direction */
        int Ynum;        /* total number of points in Y direction */
        int PrintV;      /* switch to turn on printing of diffraction vectors */
        int PrintQ;      /* switch to turn on printing of Q arrays */
        int PrintE;      /* switch to turn on printing of E arrays */
        int PrintW;      /* turns on calculation and printing of coupled waves */
        int BoundsX; /* governs fixed or damping boundaries */
        int Ynum1;       /* number of points in region 1 in Y direction */
        int Ynum2;       /* number of points in region 2 in Y direction */
        int Ynum3;       /* number of points in region 3 in Y direction */
        int StartState; /* start using saved arrays as initial condition */
        int SaveState; /* switch to enable saving of final state */
        int ProbeNum;    /* number of delay points in probe signal */
        int PrX;         /* X dimension of probe profile array */
        int PrY;         /* Y dimension of probe profile array */
    } SC = {1,1,1,1,0,0,0,0,0,0,0,0,0,0,0,0,
            0,0,0,0,0,0,0,0,0,0,0,0,0,0,0,1,1,1};
    /* SC <-> 'simulation control' */

/* Input parameters for material properties */
    struct param2 {
        double Omega;    /* internal number for phonon frequency */
       double EO1;       /* scaled electrooptic factor */
        double W_T;      /* TO phonon frequency in cm^-1 */
        double W_L;      /* LO phonon frequency in cm^-1 */
        double Gamma_1;   /* damping rate of phonon */
        double Anharm3;/* x^3 anharmonicity */
        double Anharm4;/* x^4 anharmonicity */
        double Eps_inf;  /* high freq. permittivity */
        double Eps_ip;   /* IR freq. > W_L permittivity */
        double Eps_0;    /* low frequency permittivity */
        double Eps_front;    /* permittivity in front region */
        double Eps_back;/* permittivty in back region */
        double Brelax;   /* coupling coefficient to relaxational mode */
        double Trelax;   /* time constant for relaxational mode */
        double ModeN;    /* number density for TO mode */
        double ModeQ;    /* charge for TO mode */
        double ModeM;    /* reduced mass for TO mode */
        double R33;      /* electrooptic coefficent */
    } MP = {1,0,1,1,0,0,0,1,1,1,1,1,0,0,1,1,0,0};
    /* MP <-> 'material properties' */

/* Input parameters for experimental configuration */
    struct param3 {
        double Theta;    /* angle of intersection between beams */
        double PumpTime;   /* default starting time of pump pulse */
        double PumpLength; /* default time duration of pump pulses */
        double PumpAmp;      /* default amplitude of pump pulses */
```

```
        double PumpWidth;  /* default size of pump pulses in X direction */
        double PumpPos;    /* default center position of pump pulses */
        double ProbePos;/* center position of probe pulses */
        double ProbeStart;   /* starting time for probe pulses */
        double ProbeEnd;   /* ending time for probe pulses */
        double ProbeLength;/* duration of probe pulses */
        double ProbeWidth;  /* X dimension of probe pulses */
        double ProbeAmp;   /* amplitude of probe pulses */
        double Kx;         /* wavevector of interference grating */
        double Lamda;      /* wavelength of pump and probe in vacuum */
        double ProbeAngle;  /* vertical angle of probe w.r.t pump */
        double BeamHeight; /* size of pump and probe in vertical dimension */
        double Intersect;  /* position of max overlap between pump and probe */
        double Temp;     /* temperature of sample */
        int Grating;       /* switch for grating experiment */
    } EC = {0,1,1,1,1,1,0,1,1,1,1,1,1,1,1,1,1,0,0};
    /* EC <-> 'experimental configuration' */

/* Global matrices and arrays */
    Real_Matrix Q[3];
    Real_Matrix Probe;
    Real_Matrix E[3];

/* Structure definitions */
    /* used for vectors that contain damping factors for both Q and E */
    struct sdamp {
        double Q;
        double E;
    };
    /* vectors that hold parameters for one or more pump pulses */
    struct pumpv {
        Real_Vector Pos;
        Real_Vector Tim;
        Real_Vector Len;
        Real_Vector Amp;
        Real_Vector Wid;
        Real_Vector Shp;
    };

/* Other global variables */

/* Subroutine declarations */
    void ConvertUnits(void);
     void ConvertUnits2(int, struct pumpv);
     Complex_Vector CVadd(Complex_Vector, Complex_Vector, Complex_Vector, int);
     Complex_Vector CVscalR(Complex_Vector, Complex_Vector, int, double);
     void Derivs(double, Real_Vector, Complex_Vector, Complex_Vector);
    void CWwrite(char *filename, Complex_Matrix * M, int rows, int columns);
    double ExpCalc(double);
    Real_Vector ExpInit(void);
    void Filenum(int, char[]);
```

```
  double Force(double, double, double, struct pumpv, int);
  struct sdamp * InitializeDamping(void);
  void InitializeMatrices(void);
  Real_Vector InitializeOverlap(void);
  Real_Matrix InitializeProbeMask(void);
 void ProbeSweep(int, double);
  int Qharmonics(Real_Vector, int);
 void ReadParams(void);
 struct pumpv ReadPump(int *, int *);
  void ReadState(double *, int *);
  void RK4(double, double, Real_Vector, Complex_Vector);
 int TimeStep(double, struct pumpv, int);
  void UnscaleQ(Real_Matrix, int, int, int);
  Complex_Matrix * WaveCouple(void);
 void WriteState(int, double, int);
 void XYread(char *filename, Real_Matrix M, int rows, int columns);
 void XYwrite(char *filename, Real_Matrix M, int rows, int columns);


/****************** MAIN ***********************************/
void main()
{
   char OutFileName[] = "output\\xxxx";
   char *WhichFile;
  char VecFile[] = "V000";
  char XStateFile[] = "X000";
  char EStateFile[] = "E000";
  char WStateFile[] = "W000";
  int i=0, j=0, VecNum=0;
  int Nparams, timeslice, Npulses;
  double pdt = 0, vct = 0, mxt = 0;
  double Time = 0;
   Real_Matrix Xq;
   Complex_Matrix * Smx;/* coupled wave intensities */
   struct pumpv PP;

   WhichFile = &OutFileName[7];

  /* Read in parameters from a file called "params" */
  ReadParams();

  /* Convert input params and calculate global constants */
  ConvertUnits();

   /* Read in the vectors of excitation pulse positions and times */
  PP = ReadPump(&Nparams, &Npulses);

  /* Convert pump pulse params */
  ConvertUnits2(Npulses, PP);

  /* Allocate memory for global arrays and initialize them to zero */
```

```
  InitializeMatrices();

   /* allocate array for unscaled output */
   Xq = mxalloc(NULL, SC.Ynum2, SC.Xnum);

 /* If dT is negative, then we start at Tend and go back to Tstart */
 if (SC.dT < 0) {
   Time = SC.Tend;
 } else {
   Time = SC.Tstart;
 } /* endif */

   /* Read in state arrays if called for */
  /* This changes Time and VecNum */
   if (SC.StartState) {
       ReadState(&Time, &VecNum);
    } /* endif */


/* ***** Main Loop ***** */
/*  Loop, increment time, propagate polaritons.  Exit inner loop to print and record matrices. */

   printf("Starting simulation. \n");
   for ( ; ; ) {
      do {
         Time = Time + SC.dT;   /* Increment simulation time. */
         pdt = pdt + SC.dT;    /* increment output counter */
         vct = vct + SC.dT;   /* increment vector */

         /* If Time exceeds Tend, save results and exit. */
         if ((Time > SC.Tend) || (Time < SC.Tstart)){
                XYwrite("output\\output", Probe, SC.ProbeNum, SC.PrX+1);

           /* If SaveState is set, then save all the matrixes before quitting */
           if (SC.SaveState) {
             WriteState(timeslice, Time, VecNum);
           } /* endif */

          exit(0);
         } /* endif */

         /*  Propagate the polaritons one time step. */
         timeslice = TimeStep(Time, PP, Npulses);   /* 'timeslice' tells which time slice is current in arrays */
            /* calculate probe diffraction when options are enabled */
            if (SC.PrintV||SC.PrintW){
                ProbeSweep(timeslice, Time);      /* Calculate effect of current displacement on probe pulse
*/
            }
            /* calculate coupled waves if option is turned on */
            if (SC.PrintW){
                Smx = WaveCouple();         /* calculate multiple wave diffraction */
```

```
    }

} while ( pdt < SC.DelayDT );    /* Repeat inner loop until time to compute output. */
pdt = 0;   /* reset output counter */

/* If time is in the right range and print counter is high enough,
print output vector and Q and E states. */

if ((Time>=SC.VecTs)&&(Time<=SC.VecTf)&&(SC.PrintV||SC.PrintQ||SC.PrintE||SC.PrintW)) {
 if (vct >= SC.VecDT ) {
  vct = 0;   /* reset vector counter */

   /* Print vector */
   if (SC.PrintV) {
    Filenum(VecNum, VecFile);
        /* copy V filename into filename string */
    strncpy(WhichFile, VecFile, 4);
    XYwrite(OutFileName, Probe, SC.ProbeNum, SC.PrX+1);
   } /* endif */

   /* Print Q */
   if (SC.PrintQ) {
        /* update the number for the Q file */
    Filenum(VecNum, XStateFile);
        /* copy Q filename into filename string */
    strncpy(WhichFile, XStateFile, 4);
        UnscaleQ(Xq, SC.Ynum2, SC.Xnum, timeslice);
    XYwrite(OutFileName, Xq, SC.Ynum2, SC.Xnum);
   } /* endif */

   /* Print E */
   if (SC.PrintE) {
        /* update the number for the E file */
    Filenum(VecNum, EStateFile);
        /* copy E filename into filename string */
    strncpy(WhichFile, EStateFile, 4);
    XYwrite(OutFileName, E[timeslice], SC.Ynum, SC.Xnum);
   } /* endif */

   /* Print coupled waves */
   if (SC.PrintW) {
        /* update the number for the W file */
    Filenum(VecNum, WStateFile);
        /* copy W filename into filename string */
    strncpy(WhichFile, WStateFile, 4);
    CWwrite(OutFileName, Smx, SC.ProbeNum, maxWave);
   } /* endif */

  VecNum++;
 } /* endif */
```

```
      } /* endif */
      printf("Time: %e\n", Time);

    } /* endfor */
}  /* End Main */

/* ConvertUnits ////////////////////////////////////////*/
/* Subroutine to convert input units and to calculate global constants
   based on the input parameters.
*/
void ConvertUnits(void)
{
   double cc, Tt;
    double cm_fs;
   cc = C*C;

   /* 0.001 converts THz to 1/fs; 0.03 converts cm^-1 to THz */
    /* 3e-5 converts cm^-1 to 1/fs */
    cm_fs = 3e-5;

   MP.Omega = 2 * pi_ * cm_fs * MP.W_T;  /* scales frequency to rad/fs */
   MP.Gamma_1 *= 2 * pi_ * cm_fs;        /* scales damping  */
   SC.DampQMax *= 2 * pi_ * cm_fs;       /* scales damping  */
    MP.Eps_0 = MP.Eps_ip * sqr(MP.W_L / MP.W_T); /* l.f. permittivity */
    MP.Brelax *= sqr(2 * pi_ *3.0e-5); /* convert cm^-2 to (rad/fs)^2 */

   EC.Kx *= 0.1;  /* Convert grating wavevector from 10^3 cm^-1 to micron^-1 */
   /* wavelength is reduced by the index of refraction */
    EC.Lamda /= sqrt(MP.Eps_inf);
    /* calculate the inclusive angle between the pump beams in the sample */
   EC.Theta = 2 * asin(EC.Kx * EC.Lamda / (4 * pi_));
    /* convert vertical angle to radians */
    EC.ProbeAngle *= pi_/180;

    /* Convert atomic mass units to femtograms */
    MP.ModeM *= 1.661e-9;
    /* Convert 1/cm^3 to 1/micron^3 */
    MP.ModeN *= 1.0e-12;
    /* convert electron units to microcoulombs */
    MP.ModeQ *= QE;
    /* convert m/V to micron/MV */
    MP.R33 *= 1.0e12;
    /* calculate the electro-optic factor used in the impulse force */
    MP.EO1 =
sqrt(MP.ModeM/(2*MP.ModeN))*sqr(cm_fs*MP.W_T*MP.Eps_inf)*EPS0*MP.R33/(4*MP.ModeQ);

    /* calculate auto grid sizes when dX, dY < 0 */
    if (SC.Xnum<0) { /* automatic dX is requested */
        SC.dX = 2.0*pi_/(SC.dWL*EC.Kx);   /* this will make dWL points per wavelength */
        SC.Xnum = (int)(SC.Xmax/SC.dX);
        printf("auto grid: Xnum = %d\n", SC.Xnum);
```

```
    } else {
      SC.dX = SC.Xmax / ((double) SC.Xnum);            /* x grid size */
    }
    if (SC.Ynum1<0) { /* automatic dY1 is requested */
        /* the wavelength in the vacuum is bigger by sqrt(MP.Eps_0) */
        SC.dY1 = sqrt(MP.Eps_0)*2.0*pi_/(SC.dWL*EC.Kx);  /* this will make dWL points per
wavelength */
        SC.Ynum1 = (int)(SC.Ymax1/SC.dY1);
        printf("auto grid: Ynum1 = %d\n", SC.Ynum1);
    } else {
      SC.dY1 = SC.Ymax1 / ((double) SC.Ynum1);          /* y grid size */
    }
    if (SC.Ynum2<0) { /* automatic dY2 is requested */
        SC.dY2 = 2.0*pi_/(SC.dWL*EC.Kx); /* this will make dWL points per wavelength */
        SC.Ynum2 = (int)(SC.Ymax2/SC.dY2);
        printf("auto grid: Ynum2 = %d\n", SC.Ynum2);
    } else {
      SC.dY2 = SC.Ymax2 / ((double) SC.Ynum2);          /* y grid size */
    }
    if (SC.Ynum3<0) { /* automatic dY3 is requested */
        /* the wavelength in the vacuum is bigger by sqrt(Eps_0) */
        SC.dY3 = sqrt(MP.Eps_0)*2.0*pi_/(SC.dWL*EC.Kx);  /* this will make dWL points per
wavelength */
        SC.Ynum3 = (int)(SC.Ymax3/SC.dY3);
        printf("auto grid: Ynum3 = %d\n", SC.Ynum3);
    } else {
      SC.dY3 = SC.Ymax3 / ((double) SC.Ynum3);          /* y grid size */
    }

  SC.Ymax = SC.Ymax1 + SC.Ymax2 + SC.Ymax3;
  SC.Ynum = SC.Ynum1 + SC.Ynum2 + SC.Ynum3;

    /* define auto probe and pump positions to be in center of array */
    if (EC.PumpPos < 0) {
        EC.PumpPos = SC.Xmax/2;
    }
    if (EC.ProbePos < 0) {
        EC.ProbePos = SC.Xmax/2;
    }

    /* Check all the stability conditions and report problems */
  if ( (SC.dT/SC.dX) * (SC.dT/SC.dX) * (cc)/MP.Eps_front > 0.5 ) {
    printf(" Time step too big for stability - decrease time step or increase dX.\n");
    exit(0);
  } /* endif */

  if ( (SC.dT/SC.dX) * (SC.dT/SC.dX) * (cc)/MP.Eps_inf > 0.5 ) {
    printf(" Time step too big for stability - decrease time step or increase dX.\n");
    exit(0);
  } /* endif */
```

```
  if ( (SC.dT/SC.dX) * (SC.dT/SC.dX) * (cc)/MP.Eps_back > 0.5 ) {
     printf(" Time step too big for stability - decrease time step or increase dX.\n");
     exit(0);
  } /* endif */

  if ( (SC.dT/SC.dY1) * (SC.dT/SC.dY1) * (cc)/MP.Eps_front > 0.5 ) {
     printf(" Time step too big for stability - decrease time step or increase dY1.\n");
     exit(0);
  } /* endif */

  if ( (SC.dT/SC.dY2) * (SC.dT/SC.dY2) * (cc)/MP.Eps_inf > 0.5 ) {
     printf(" Time step too big for stability - decrease time step or increase dY2.\n");
     exit(0);
  } /* endif */

  if ( (SC.dT/SC.dY3) * (SC.dT/SC.dY3) * (cc)/MP.Eps_back > 0.5 ) {
     printf(" Time step too big for stability - decrease time step or increase dY3.\n");
     exit(0);
  } /* endif */

   /* Set options for ProbeEnd */
  if (EC.ProbeEnd < 0) {
    EC.ProbeEnd = SC.Tend;

   } else if (EC.ProbeEnd == 0) {
       /* Set automatic length for probe delay and report any problems */
       /* Tt is the time it takes for light to traverse the sample */
       Tt = SC.Ymax2/C * sqrt(MP.Eps_inf);
       EC.ProbeEnd = SC.Tend - Tt;
       printf("\n");
       if (EC.ProbeEnd < 0) {
           printf("**** The automatic end probe delay is less than zero.\n");
           printf("**** Setting the end probe delay to Tend.\n");
           printf("**** The probe cannot fully cross the sample during the simulation.\n\n");
           EC.ProbeEnd = SC.Tend;
       } /* endif */
       printf("Tend is:                    %1.2e femtoseconds.\n", SC.Tend);
       printf("The time to cross the sample is:  %1.2e femtoseconds.\n", Tt);
       printf("The automatic end probe delay is: %1.2e femtoseconds.\n\n", EC.ProbeEnd);
   } /* endif */

  EC.ProbeStart = (floor(EC.ProbeStart / SC.DelayDT)) * SC.DelayDT;      /* Start at integer # times
DelayDT */
  SC.ProbeNum = (int) ((EC.ProbeEnd - EC.ProbeStart) / SC.DelayDT);

   if (EC.Intersect > SC.Ymax2){
       printf("The pump and probe overlap behind the rear of the sample.\n");
   }

}
/* ConvertUnits2 ////////////////////////////////////////*/
```

```
/* subroutine to make unit conversions and scale the pump
and probe pulse params.
*/
void ConvertUnits2(int Npulses, struct pumpv PP)
{
    int i;

    /* Calculate the Gaussian denominator coefficients from the
    FWHM values specified in the parameters.
    let a = (FWHM/2) / sqrt(-log(0.5)) ->
    then exp( -(x/a)^2) = 1/2 when x = half width.*/
    for (i=0; i<Npulses; i++){
        PP.Len[i] = (PP.Len[i]/2) / sqrt(-log(0.5));
        PP.Wid[i] = (PP.Wid[i]/2) / sqrt(-log(0.5));
    }
        EC.BeamHeight = (EC.BeamHeight/2) / sqrt(-log(0.5));
        EC.ProbeLength = (EC.ProbeLength/2) / sqrt(-log(0.5));
        EC.ProbeWidth = (EC.ProbeWidth/2) / sqrt(-log(0.5));

    for (i=0; i<Npulses; i++){
        /* Convert input power in microjoules to program units (MV/um)^2  */
        /* First, 1e6*uJ = 1J = 1 Kg*m^2/s^2 = 1 fg*um^2/fs^2 */
        PP.Amp[i] /= 1e6;
        /* Normalization for Gaussian profile, integrated over x, y, and t. */
        /* Units are now fg/fs^3. */
        PP.Amp[i] /= pow(pi_, 1.5)*PP.Wid[i]*PP.Len[i]*EC.BeamHeight;
        /* Power density I = (1/2)*EPS0*C*E^2, so E^2 = I*2/(EPS0*C). */
        /* Pump intensity units are now (MV/um)^2 = E field to second power. */
        PP.Amp[i] *= 2/(EPS0*C);
    }

}
/* CVadd ////////////////////////////////////////////*/
Complex_Vector CVadd(Complex_Vector v1, Complex_Vector v2, Complex_Vector v3, int n)
{
/*  add the two complex vectors:
       v1[n] =  v2[n] + v3[n]
    NOTE: this is a modified version of Cvadd from the mathlib.
*/
int i;

   for (i=0; i<n; i++) {
      v1[i].r = v2[i].r + v3[i].r;
      v1[i].i = v2[i].i + v3[i].i;
   }
return v1;
}
/* CVscalR ////////////////////////////////////////////*/
Complex_Vector CVscalR(Complex_Vector v1, Complex_Vector v, int n, double value)
{
 /*  multiply a complex vector by a real value: v1[] = value*(v[].r+i*v[].i)
```

```
   NOTE: this is a modified version of CvscalR from the mathlib. */
int j;

     for (j=0; j < n; j++) {
          v1[j].i = value*v[j].i;
          v1[j].r = value*v[j].r;
     }
return v1;
}
/* CWwrite ////////////////////////////////////////////*/
/* This writes the magnitude of the coupled wave matrix to a file. */
/* Only the wave with the same angle as the probe is printed. */
/* The order of indexes for M is [angle][time][wave]. */
/* The wave index = angle index - minWave+1 since the wave numbers are
    offset by minWave+1.
        M[][][0] -> wave specified by minWave.
        M[][][minWave+1] -> wave number 1 (signal at first Bragg angle).

        M[0][][] -> probe angle = first Bragg angle
    */
void CWwrite(char *filename, Complex_Matrix * M, int rows, int columns)
{
    int r=0, c=0;
    int mW = minWave;
    FILE *outf;

   outf = fopen( filename, "w" );

    for (r=0; r<rows; r++) {
        /* Print time in picoseconds in first output column */
        fprintf( outf, "%e", (EC.ProbeStart + r*SC.DelayDT)/1000);
        fprintf( outf, " ");
        for (c=0; c<columns; c++){
            fprintf( outf, "%e", Cmag(M[c][r][-mW+c+1]));
            fprintf( outf, " ");
        }
        fprintf(outf, "\n");
    }
    fclose(outf);
}
/* Derivs ////////////////////////////////////////////*/
/*  This subroutine calculates the derivatives of the wave coupling equation
    for the Runge-Kutta integration routine. */
void Derivs(double alpha, Real_Vector dEps, Complex_Vector S, Complex_Vector dS)
/* alpha is the probe angle, dEps is the permittivity modulation
array, S is vector of the coupled wave amplitudes,
dS is the derivatives of S calculated here.
*/
{
    int l, m, p;
    Complex C1;
```

```
    double C2b;
    static Complex czero;
    static double n, Dg, C2a, C3;
    static int pmax = (maxWave-minWave+1);
    static int firsttime=1;

    /* Initialize static variables */
    if (firsttime) {
        firsttime=0;

        /* make complex zero */
        czero.r = czero.i = 0;
        /* remember Lamda = wavelength in material */
        n=sqrt(MP.Eps_inf); /* index of refraction */
        Dg = 2*pi_/EC.Kx;   /* grating spacing in microns */
        /* constants for derivative calculations */
        C2a=sqr(EC.Kx);
        C3=2*sqr(pi_/(n*EC.Lamda));
    }
    C1=Complx(0, -4*pi_*cos(alpha)/EC.Lamda);
    C2b=(2*Dg/EC.Lamda)*sin(alpha);

    /*  Scan over all the waves and calculate
        the derivatives for the RK integration. */
    for (p=0; p<pmax; p++){
        /* Reset dS[p] */
        dS[p] = czero;
        /*  p is the index to the arrays.  m is the index of the
            diffracted waves. */
        m = p + minWave;
        /* Add the S coefficient */
        dS[p] = CscalR(S[p], C2a*m*(C2b-m) );
        /* Add up all the mixing with other waves */
        for (l=1; l<=maxWave; l++){
            if (p+l < pmax){
                dS[p] = Cadd(dS[p], CscalR(S[p+l], C3*dEps[l-1]));
            }
            if (p-l >= 0){
                dS[p] = Cadd(dS[p], CscalR(S[p-l], C3*dEps[l-1]));
            }
        } /* next l */
        /* Finally, scale by 1/C1 */
        dS[p] = Cdiv(dS[p], C1);
    }  /* next p */
}
/* ExpCalc ////////////////////////////////////////////*/
/* Interpolates exponential based on precalculated exponentials */
double ExpCalc(double N)
{
   double p, E1, E2, result;
   static Real_Vector ExpArray;
```

```
    static int firsttime=1;

    /* Initialize static variables */
    if (firsttime){
        firsttime=0;
       ExpArray=ExpInit();
    }

  if (N < MinExpon) {
    return 0;
  } else if (N > 0) {
    printf("Gaussian exponential greater than zero!\n");
    exit(0);
  } else {

     p = ((double)NumExpon - 1.0) - N * ((double)NumExpon - 1.0) / MinExpon;
     E1 = ExpArray[ (int) floor(p) ];
     if (p < NumExpon - 1) {
       E2 = ExpArray[ (int) ceil(p) ];
     } else {
       E2 = E1;
     }
     result = E1 + (p - floor(p)) * (E2-E1);
     return (result);

  } /* endif */
}
/* ExpInit ////////////////////////////////////////////*/
/*  Initializes array of exponentials for exponents between MinExpon and 0 */
Real_Vector ExpInit(void)
{
  int i;
  double di;
   Real_Vector ExpArray;

  ExpArray = valloc(NULL, NumExpon);
  for (i=0; i<NumExpon; i++) {
     di = (double) i;
     ExpArray[i] = exp(MinExpon - di * MinExpon / ((double)NumExpon - 1.0) );
  } /* endfor */

return ExpArray;
}
/* Filenum ////////////////////////////////////////////*/
/* subroutine to make character digits for vector filenumbers */
void Filenum(int number, char filename[])
{
  int hundreds, tens, ones;
  if (number > 999) {
    return;
  } /* endif */
```

```
    hundreds = number / 100;
    tens = (number - hundreds * 100)/10;
    ones = (number - hundreds * 100 - tens * 10);

    filename[1] = '0' + hundreds;
    filename[2] = '0' + tens;
    filename[3] = '0' + ones;
}
/* Force ////////////////////////////////////////////*/
/* This routine calculates the impulse force from the pump beam at a
given point (X,Y,T). It scans over the number of pulses given by
Npulses with properties specified in PP. */
double Force(double X, double Y, double T, struct pumpv PP, int Npulses)
{
    int p;
    double F, sx, SF, ty, TF;
    double sx1, sx2, SF1, SF2, ty1, ty2, TF1, TF2;
    double F1, F2;
    static double C1, tanTh, cosTh, sinTh;
    static int firsttime=1;

    /* Initialize static variables */
    if (firsttime){
        firsttime=0;
        C1 = C / sqrt(MP.Eps_inf);
       tanTh = tan(EC.Theta/2);
        cosTh = cos(EC.Theta/2);
        sinTh = sin(EC.Theta/2);

    }

    /* if X is in the damping zone, set F to zero and return */
/*  if ((X<SC.DampZone)||(X>SC.Xmax-SC.DampZone)){
        return 0.0;
    }
*/
     /* Sum at force at this point by adding up the effects of all the pump pulses. */
        F = 0;
     for (p=0; p<Npulses; p++) {

          if (!EC.Grating) {
         /* First, calculate spatial distribution */
         sx = X - PP.Pos[p];
         SF = ExpCalc( -1.0 * sx * sx / (PP.Wid[p] * PP.Wid[p]) );

         /* Now, calculate the time distribution of the current pulse, */
         /* taking into account time of pulse and propagation through sample for distance Y. */
         if (SF != 0) {
           ty = T - PP.Tim[p] - Y / C1;
           TF = ExpCalc( -1.0 * ty * ty / (PP.Len[p] * PP.Len[p]) );
```

```
            /* Sum up forces.  Each force contribution equals amplitude times space and time factors. */
            F = F + PP.Amp[p] * TF * SF;
          } /* endif */

          } else {   /* Calculate the effects of the grating */

              /* First, calculate spatial distribution */
          /* beam 1 is angled left to right */
           sx1 = (X - PP.Pos[p] - tanTh * Y) / PP.Wid[p];
           SF1 = ExpCalc( -1.0 * sx1 * sx1 );
          /* beam 2 is angled right to left */
           sx2 = (X - PP.Pos[p] + tanTh * Y) / PP.Wid[p];
           SF2 = ExpCalc( -1.0 * sx2 * sx2 );

          /* Now, calculate the time distribution of the current pulse, */
          /* taking into account time of pulse and propagation through sample for distance Y. */
          if (SF1 || SF2) { /* don't bother if forces are zero */
            sx = X - PP.Pos[p];    /*distance from center line */
           /* beam 1 is angled left to right */
            ty1 = T - PP.Tim[p] - (Y*cosTh + sx*sinTh)/C1;
            TF1 = ExpCalc( -1.0 * ty1 * ty1 / (PP.Len[p] * PP.Len[p]) );
           /* beam 2 is angled right to left */
            ty2 = T - PP.Tim[p] - (Y*cosTh - sx*sinTh)/C1;
            TF2 = ExpCalc( -1.0 * ty2 * ty2 / (PP.Len[p] * PP.Len[p]) );

           /* Calculate total force using the relative phase of two pulses. */
           /* The force equals product of time and space intensity profiles. */
            F1 = TF1*SF1 + TF2*SF2;
                if (F1){
                F2 = 2*cos(EC.Kx * sx) * sqrt(TF1*SF1 * TF2*SF2);
                   TF = F1 + F2;
                   /* Sum up forces. */
                   F = F + PP.Amp[p] * TF;
                }
          } /* endif */

          } /* endif - grating option */

      } /* endfor (pump pulses loop) */

return F;
}
/* InitializeDamping ////////////////////////////////*/
/* This routine initialized the damping array, which includes factors
for Q and E.  The damping zones at the sides of the array are calculated
here. */
struct sdamp * InitializeDamping(void)
{
    int dampz, i;
    struct sdamp * Damping;
```

```
  Damping = (struct sdamp *)calloc(SC.Xnum, sizeof(struct sdamp));
  dampz = (int)floor(SC.DampZone / SC.dX);

  if (SC.BoundsX == 1) {
    /* This is the case where damping zones are added to each end in the X direction to */
    /* damp out propagating waves */

    /* Damping for left damping zone */
    for (i=0; i<dampz; i++) {
      Damping[i].Q = (SC.DampQMax) * (1 - ((double) i)/((double) dampz) ) + MP.Gamma_1;
      Damping[i].E = SC.DampEMax * (1 - ((double) i)/((double) dampz) );
    } /* endfor */

    /* Damping for middle normal zone */
    for (i=dampz; i<SC.Xnum-dampz; i++) {
      Damping[i].Q = MP.Gamma_1;
      Damping[i].E = 0;
    } /* endfor */

    /* Damping for right damping zone */
    for (i=SC.Xnum-dampz; i<SC.Xnum; i++) {
      Damping[i].Q = (SC.DampQMax) * ((double) (i - SC.Xnum + dampz + 1))/((double) dampz) +
MP.Gamma_1;
      Damping[i].E = SC.DampEMax * ((double) (i - SC.Xnum + dampz + 1))/((double) dampz);
    } /* endfor */
  } else {
    /* otherwise damping is constant everywhere */
    for (i=0; i<SC.Xnum; i++) {
      Damping[i].Q = MP.Gamma_1;
    } /* endfor */
  } /* endif */

return Damping;
}
/* InitializeMatrices ////////////////////////////////*/
/* Subroutine to allocate memory for the global arrays and
initialize them to zero */
void InitializeMatrices(void)
{
  int i, m;
   double C1;

   C1 = C / sqrt(MP.Eps_inf);

  for (i=0; i<3; i++) {
    /* Allocate memory for matrices. */
    Q[i] = mxalloc(NULL, SC.Ynum2, SC.Xnum);
    E[i] = mxalloc(NULL, SC.Ynum, SC.Xnum);

    /* Initialize the matrices */
    mxinit(Q[i], SC.Ynum2, SC.Xnum, 0.0);
```

```
    mxinit(E[i], SC.Ynum, SC.Xnum, 0.0);

  } /* endfor */

  /* x size of probe array = 2*PrX */
  SC.PrX = (int) ceil(EC.ProbeWidth * sqrt(-MinExpon)/SC.dX);
   /* set PrX to next biggest power of 2 */
   frexp((double) (SC.PrX), &m);
   /* m is the binary exponent with a fractional (<1) mantissa */
   SC.PrX = (int)ldexp(1.0, m);     /* replaces fractional mantissa with 1 */

  /* y size of probe array = 2*PrY.  The array size is set so the
   Gaussian amplitude will be exp(MinExpon) at the ends of the array.
   The temporal Gaussian profile is set by ProbeLength, so the spatial
   Gaussian profile in the y direction is set by ProbeLength * C1. */
  SC.PrY = (int) ceil(EC.ProbeLength * C1 * sqrt(-MinExpon)/SC.dY2);

   /* Probe has ProbeNum rows (delay times) and
       PrX+1 wavevector components */
  Probe = mxalloc(NULL, SC.ProbeNum, SC.PrX+1);
  mxinit(Probe, SC.ProbeNum, SC.PrX+1, 0.0);

}

/* InitializeOverlap ////////////////////////////////////*/
/* Calculate the overlap between pump and probe vs. distance
    as a function of vertical angle of probe and the crossing
    point of the beams. */
Real_Vector InitializeOverlap(void)
{
    int i, j, znum;
    double dy, dz, dj, tanV, jsum, wz, norm;
    Real_Vector Overlap;

    /* allocate memory for probe overlap vector */
    Overlap = valloc(NULL, SC.Ynum2);

    znum = 25;    /* vertical grid */
    /* calculate the gaussian factor for j */
    wz = sqr(znum)/MinExpon;
    tanV = tan(EC.ProbeAngle);
    dz = EC.BeamHeight * sqrt(-MinExpon) / znum;

    norm = 0;
    for (j=-znum; j<=znum; j++){
        norm += ExpCalc(sqr(j)/wz) * ExpCalc(sqr(j)/wz);
    }
    for (i=0; i<SC.Ynum2; i++) {
        dy = i * SC.dY2 - EC.Intersect;
        /* dj = displacement of probe from pump in vert. direction */
        dj = fabs(dy * tanV)/dz;
```

```
        /* initialize integration */
        jsum = 0;
        for (j=-znum; j<=znum; j++){
            jsum += ExpCalc(sqr(j)/wz) * ExpCalc(sqr(j-dj)/wz);
        }
        jsum /= norm; /* normalize result */
        /* Overlap is the result of the integration */
        Overlap[i] = jsum;
    }

return Overlap;
}
/* InitializeProbeMask ////////////////////////////////*/
/* This routine allocates memory for the ProbeMask array,
and then initializes and normalizes its values. The ProbeMask
array is used to sample the diffraction components in the ProbeSweep
routine. */
Real_Matrix InitializeProbeMask(void)
{
  int i,j;
  double tanTh, sinTh, cosTh, x, xp, y, yp, C1;
   double scale=0;
   Real_Matrix ProbeMask;

  tanTh = tan(EC.Theta/2);
  sinTh = sin(EC.Theta/2);
  cosTh = cos(EC.Theta/2);
   C1 = C / sqrt(MP.Eps_inf);

  /* allocate storage for probe mask matrix and initialize */
  ProbeMask = mxalloc(NULL, 2*SC.PrY, 2*SC.PrX);
  for (i=0; i<2*SC.PrY; i++) {  /* scan over rows */
    y = (i - SC.PrY);
    for (j=0; j<2*SC.PrX; j++) {  /* scan over columns */
      x = j - SC.PrX;
      /* calculate coords rotated by -Theta/2 */
      /* x and y are coords for beam angled by Theta/2, going l to r */
      /* xp and yp are rotated coords for normal incidence */
      /* This rotates the pump profile by Theta/2 */
      xp = cosTh * x - sinTh * y;
      yp = sinTh * x + cosTh * y;
      /* scale xp and yp */
      xp *= SC.dX / EC.ProbeWidth;
      yp *= SC.dY2/(C1 * EC.ProbeLength);
      /* set weight of matrix element, which is proportional to E,
        not I, so the sqrt is taken */
      ProbeMask[i][j] = sqrt(ExpCalc(-xp * xp) * ExpCalc(-yp * yp));
        scale += ProbeMask[i][j];
    } /* endfor */
  } /* endfor */
   /* Calculate normalization factor for probemask. The sum is divided
```

```
    by PrX to get the average value along the x direction.  This is not
    necessary along the y direction because the rows are summed over in
    ProbeSweep, which ensures the normalization in the y direction. */
    scale /= 2*SC.PrX;
    /* apply normalization factor */
   for (i=0; i<2*SC.PrY; i++) {  /* scan over rows */
     for (j=0; j<2*SC.PrX; j++) {  /* scan over columns */
          ProbeMask[i][j] /= scale;
       }
    }

return ProbeMask;
}
/* ProbeSweep ////////////////////////////////////////*/
/* Subroutine to calculate the experimental waveform of birefringence
vs. probe delay. */
/* If Grating then this calculates the permittivity modulation across the
region sampled by the probe pulse, to be used to calculate the diffracted
signal strength later. */

void ProbeSweep(int TimeSlice, double T)
{
   int i, j, k, yj, xk;
    double ty, ty1, ty2, TF, PrbT;
   double Pscale;
   double Y=0, X=0;
    static Real_Matrix ProbeMask;
    static Real_Vector Overlap;
    static int Xprobe;
    static Real_Vector Ksample;
    static Complex_Vector Kdata;
   static double dEdQ, dPrb, Th3, C1, Cx, Cy;
    static int firsttime=1;

    /* Initialize static variables */
    if (firsttime){
        firsttime=0;

        /* initialize the ProbeMask arra */
        ProbeMask=InitializeProbeMask();
        /* initialize the overlap vector */
        Overlap = InitializeOverlap();
        /* 1st probe position in pixels */
       Xprobe = (int) (EC.ProbePos / SC.dX);
        /* allocate storage for probe FFT sample array */
        /* the size is 2*PrX + 2 because this will also store Kdata,
        a complex vector of size PrX + 1 */
        Ksample = valloc(NULL, 2*SC.PrX + 2);
        Kdata = (Complex_Vector) Ksample;
        /* the probe delay increment = DelayDT */
       dPrb = SC.DelayDT;
```

```
      /* Th3 = total angle between probe and center axis,
      including vert. and hor. angles */
      Th3 = atan(sqrt(sqr(tan(EC.Theta/2)) + sqr(tan(EC.ProbeAngle))));
      /* speed constants for x and y components of probe */
      C1 = C / sqrt(MP.Eps_inf);
      Cy = C1 * cos(Th3);
      Cx = Cy * tan(EC.Theta/2);
      /* dEdQ relates the displacement to a change of permittivity */
      dEdQ=(2*MP.EO1/EPS0);
  }


if (!EC.Grating) {
  /* if not grating experiment,
    calculate accumulated birefrigence on probe pulse */
 for (i=0; i<SC.ProbeNum; i++) {
   PrbT = EC.ProbeStart + dPrb * i;
   for (j=0; j < SC.Ynum2; j++) {
     Y = SC.dY2 * j;
     ty = T - PrbT  - Y/C1;
     TF = ExpCalc( -1.0 * ty * ty / (EC.ProbeLength * EC.ProbeLength) );
     Probe[i][0] = Probe[i][0] + TF * Q[TimeSlice][j][Xprobe] * EC.ProbeAmp * SC.dY2;
   } /* endfor */
 } /* endfor */

} else { /* if Grating */
   /* Calculate light scattered from grating pattern in direction of detector. */
  /* loop over probe time delays */
  for (i=0; i<SC.ProbeNum; i++) {
    /* For each probe delay, calculate contribution of displacements to scattering
      of probe, normalized by probe profile, length of timestep and size of grid.
      The probe is treated as 'ProbeNum' discrete probe pulses with
      uniform increments in delay. */
    /* First calculate whether the probe pulse is in active region */
    PrbT = EC.ProbeStart + dPrb * i;  /* delay for this probe pulse */
    ty1 = T - PrbT + SC.PrY*SC.dY2/(Cy);  /* beginning of probe pulse arriving */
    ty2 = T - PrbT - (SC.Ymax2+SC.PrY*SC.dY2)/(Cy);  /* end of probe pulse leaving */
      /* zero the sample array at each probe delay */
      vinit(Ksample, 2*SC.PrX+2, 0.0);

    /* See if the time exponentials are nonzero -> this probe pulse is in the
      ferroelectric region. If so, calculate the scattering of the probe pulse.
      Sweep over the rows and columns of the probe matrix, calculating the
      amplitude of Q in the region sampled by the probe, weighted by the cell size
      and the amplitude mask for the probe pulse.  The indexes
      yj and xk are used to find the entries in the Q matrix that overlap the
      probe pulse matrix.  Before calculating, make sure that only valid indexes
      for the Q array are used. The Q values are linearly related to scattering
      but they must be properly weighted by both the time and space gaussians for
      the probe pulse, as well as dT, dX, and dY */
```

```
if ((ty1 > 0) && (ty2 < 0)) {  /* pulse is in region, at least partly */

/* calculate the center position of probe pulse */
Y = (T-PrbT)*(Cy); /* valid only for pulse inside region */
/* calculate yj: starting y index to Q array - center position - 1/2 probe array. */
/* PrY is 1/2 the probe array size in y dimension */
yj = (int)(Y/SC.dY2+0.5) - SC.PrY;
/* calculate xk: the starting x index for Q array */
/* Xprobe is index for probe position, PrX is 1/2 probe array */
  /* Probe moves left to right */
  X = (T-PrbT)*(Cx);
xk = Xprobe + (int)(X/SC.dX + 0.5) - SC.PrX;

  /* calculate scattered light at each point */
  /* multiply the Cos and Sin arrays on each row and sum */
  /* this is the scattered light at Bragg angle */
  for (j=0; j<2*SC.PrY; j++) { /* scan over rows (y) */
       /* do only for valid row indexes */
       if ((j+yj >= 0) && (j+yj < SC.Ynum2)) {
        /* scaling is based on grid sizes and vertical overlap factor */
        Pscale = Overlap[j+yj];
    for (k=0; k<2*SC.PrX; k++) {  /* scan over columns (x) */
      /* do only for valid column indexes */
      if ((k+xk >= 0) && (k+xk < SC.Xnum)) {
       /* sample is weighted by probe intensity and size of cell */
            /* Ksample is summed over the rows (j) for each column (k) */
       Ksample[k] += ProbeMask[j][k] * Pscale * Q[TimeSlice][j+yj][k+xk];
      } /* endif */
    } /* endfor (k) */
      } /* endif */
  } /* endfor (j) */
  /* now take FFT to get k components of diffraction grating */
  /* the fftreal takes an real array of size 2*PrX, and returns a
    complex array of size PrX+1, which uses same memory as Ksample */
  Kdata = fftreal(Ksample, 2*SC.PrX);
} /* endif (probe in sample) */

  if (SC.PrintW){
      /*  probe array holds instantaneous value of diffraction grating
          when calculating wave coupling */
      for (k=0; k<SC.PrX+1; k++) {
          /* dEdQ is the electro-optic scaling factor for diffraction */
         /* the 1/PrX cancels the PrX amplitude factor from the FFT */
          Probe[i][k] = dEdQ * Cmag(Kdata[k]) / SC.PrX;
      }
  } else {
      /* If not using wavecoupling, the magnitude of the FFT is added
      to the probe array in an accumulated sum. */
      for (k=0; k<SC.PrX+1; k++) {
          /* 2*EO1 is the electro-optic scaling factor for diffraction */
          /* the 1/PrX cancels the PrX amplitude factor from the FFT */
```

```
                Probe[i][k] += dEdQ * Cmag(Kdata[k]) / SC.PrX;
            }
        }

    } /* endfor (i) */
  } /* endif */

}
/* Qharmonics ////////////////////////////////////////*/
/*  Subroutine to return array of the modulation of permittivity
    at integer multiples of grating wavevector Kx.  Returns 1 if
    Probe contains nonzero entries, 0 otherwise.  */
int Qharmonics(Real_Vector dEps, int j)
/* dEps is the fft of the permittivity array, j is the delay index */
{
    int l, pl, nz;
    static int firsttime=1;
    static double dq;

    /* Initialize static variables */
    if (firsttime){
        firsttime=0;
        dq = pi_/(SC.PrX*SC.dX);
    }

    nz = 0;

    /* assign values to dEps[] */
    for (l=0; l<maxWave; l++){
        /* pl is index of nonzero integer multiples of Kx in the fft array*/
        pl = (int)( (double)(l+1)*EC.Kx/dq);
        /* check to see if pl is a valid index */
        if (pl < SC.PrX+1){
            dEps[l] = Probe[j][pl];
            /* look for nonzero entries in dEps */
            if (dEps[l] && !nz) {
                nz=1;
            }
        } else {
            dEps[l]=0;
        }
    }

return nz;
}
/* ReadParams ////////////////////////////////////////*/
/* Subroutine to read parameter file called "params.txt". */
void ReadParams(void)
{
  /* Variables used to read in the parameters from the file "params" */
  FILE *params;
```

```
  char line[MAX_LEN], *line1;
  char value[DBL_LEN], keyword[KeyLen];
  char Comment[] = ";";


 /* These are variables used in parsing the parameter file. */
  int i = 0, relpos=0, cpos=0, test=0;

 /* Open parameter file, exit if not found. */
  if ( ( params = fopen("input\\params.txt", "r") ) == NULL ) {
    printf("Could not open data file input\\params.txt. \n");
     exit(0);
  } else {
    printf("Parsing the paramms file. \n");
  } /* endif */

/* loop and read in the parameter lines */
for ( ; ; ) {
cpos = 0;
test = 0;
relpos=0;

  /* read in a line: */
  if ( (line1 = fgets(line, MAX_LEN, params)) == NULL) {
     break;
  }

  /* parse the line to read the keyword. */
  for (i=0; i<KeyLen; i++ ) {    /* scan through characters */

    /* break if at EOL */
    if ((line[i] == '\0') || (line[i] == '\n')) {
       keyword[cpos] = '\0';
       relpos = i;
      break;
    }
    /* if char is a space or tab, check to see if info has already been read.  If so, break. */
    if ((line[i] == ' ') || (line[i] == '\t')) {
      if (test) {
         keyword[cpos] = '\0';
         relpos = i;
         break;
      } /* endif */
    /* if char is not space or tab, read char into keyword array.  Set flag to show info has been read. */
    } else {
       keyword[cpos] = line[i];
       cpos++;
       test = 1;
    } /* endif */
  } /* endfor (keyword loop) */
```

```
/* after keyword is read, the pointer relpos points to a space, tab, or endline */
/* reset test flag */
test = 0;
cpos = 0;

/* parse the line to read parameter. */
for (i=0; i<DBL_LEN; i++ ) {
/* scan through characters, starting at the last character read by the preceding section */

/* break if at EOL */
   if ((line[i + relpos] == '\0') || (line[i + relpos] == '\n')) {
      value[cpos] = '\0';
     break;
   }
/* if char is a space or tab, check to see if info has already been read.  If so, break. */
   if ((line[i + relpos] == ' ') || (line[i + relpos] == '\t')) {
     if (test) {
         value[cpos] = '\0';
         break;
     } /* endif */
/* if char is not space or tab, read char into value array.  Set flag to show info has been read. */
   } else {
      value[cpos] = line[i + relpos];
      cpos++;
      test = 1;
   } /* endif */
} /* endfor */

if (strncmp(line, Comment, 1) == 0) {
  /* if comment string do nothing, else read in parameters */
 } else if (relpos<2) {
     /* keyword should be at least 2 characters */

  /* SIMULATION CONTROL PARAMETERS */
} else if (strncmp(keyword, "Tstart", relpos) == 0) {
  SC.Tstart = atof(value);
} else if (strncmp(keyword, "Tend", relpos) == 0) {
  SC.Tend = atof(value);
} else if (strncmp(keyword, "dT", relpos) == 0) {
  SC.dT = atof(value);
} else if (strncmp(keyword, "dWL", relpos) == 0) {
  SC.dWL = atof(value);
} else if (strncmp(keyword, "Xmax", relpos) == 0) {
  SC.Xmax = atof(value);
} else if (strncmp(keyword, "Xnum", relpos) == 0) {
  SC.Xnum = atoi(value);
} else if (strncmp(keyword, "Ymax1", relpos) == 0) {
  SC.Ymax1 = atof(value);
} else if (strncmp(keyword, "Ynum1", relpos) == 0) {
  SC.Ynum1 = atoi(value);
} else if (strncmp(keyword, "Ymax2", relpos) == 0) {
```

```
  SC.Ymax2 = atof(value);
} else if (strncmp(keyword, "Ynum2", relpos) == 0) {
  SC.Ynum2 = atoi(value);
} else if (strncmp(keyword, "Ymax3", relpos) == 0) {
  SC.Ymax3 = atof(value);
} else if (strncmp(keyword, "Ynum3", relpos) == 0) {
  SC.Ynum3 = atoi(value);
} else if (strncmp(keyword, "DelayDT", relpos) == 0) {
  SC.DelayDT = atof(value);
} else if (strncmp(keyword, "PrintV", relpos) == 0) {
  SC.PrintV = atoi(value);
} else if (strncmp(keyword, "PrintQ", relpos) == 0) {
  SC.PrintQ = atoi(value);
} else if (strncmp(keyword, "PrintE", relpos) == 0) {
  SC.PrintE = atoi(value);
} else if (strncmp(keyword, "PrintW", relpos) == 0) {
  SC.PrintW = atoi(value);
} else if (strncmp(keyword, "VecTs", relpos) == 0) {
  SC.VecTs = atof(value);
} else if (strncmp(keyword, "VecTf", relpos) == 0) {
  SC.VecTf = atof(value);
} else if (strncmp(keyword, "VecDT", relpos) == 0) {
  SC.VecDT = atof(value);
} else if (strncmp(keyword, "BoundsX", relpos) == 0) {
  SC.BoundsX = atoi(value);
} else if (strncmp(keyword, "DampZone", relpos) == 0) {
  SC.DampZone = atof(value);
} else if (strncmp(keyword, "DampQMax", relpos) == 0) {
  SC.DampQMax = atof(value);
} else if (strncmp(keyword, "DampEMax", relpos) == 0) {
  SC.DampEMax = atof(value);
} else if (strncmp(keyword, "StartState", relpos) == 0) {
  SC.StartState = atoi(value);
} else if (strncmp(keyword, "SaveState", relpos) == 0) {
  SC.SaveState = atoi(value);

  /* MATERIAL PROPERTIES */
} else if (strncmp(keyword, "W_T", relpos) == 0){
  MP.W_T = atof(value);
} else if (strncmp(keyword, "W_L", relpos) == 0){
  MP.W_L = atof(value);
} else if (strncmp(keyword, "Gamma_1", relpos) == 0){
  MP.Gamma_1 = atof(value);
} else if (strncmp(keyword, "Anharm4", relpos) == 0){
  MP.Anharm4 = atof(value);
} else if (strncmp(keyword, "Anharm3", relpos) == 0){
  MP.Anharm3 = atof(value);
} else if (strncmp(keyword, "Eps_inf", relpos) == 0){
  MP.Eps_inf = atof(value);
} else if (strncmp(keyword, "Eps_ip", relpos) == 0){
  MP.Eps_ip = atof(value);
```

```
} else if (strncmp(keyword, "Trelax", relpos) == 0){
  MP.Trelax = atof(value);
} else if (strncmp(keyword, "Brelax", relpos) == 0){
  MP.Brelax = atof(value);
} else if (strncmp(keyword, "Eps_front", relpos) == 0){
  MP.Eps_front = atof(value);
} else if (strncmp(keyword, "Eps_back", relpos) == 0){
  MP.Eps_back = atof(value);
} else if (strncmp(keyword, "ModeN", relpos) == 0){
  MP.ModeN = atof(value);
} else if (strncmp(keyword, "ModeQ", relpos) == 0){
  MP.ModeQ = atof(value);
} else if (strncmp(keyword, "ModeM", relpos) == 0){
  MP.ModeM = atof(value);
} else if (strncmp(keyword, "R33", relpos) == 0){
  MP.R33 = atof(value);

  /* EXPERIMENTAL CONFIGURATION PARAMETERS */
} else if (strncmp(keyword, "PumpLength", relpos) == 0){
  EC.PumpLength = atof(value);
} else if (strncmp(keyword, "PumpAmp", relpos) == 0){
  EC.PumpAmp = atof(value);
} else if (strncmp(keyword, "PumpWidth", relpos) == 0){
  EC.PumpWidth = atof(value);
} else if (strncmp(keyword, "Grating", relpos) == 0){
  EC.Grating = atoi(value);
} else if (strncmp(keyword, "Kx", relpos) == 0){
  EC.Kx = atof(value);
} else if (strncmp(keyword, "Lamda", relpos) == 0){
  EC.Lamda = atof(value);
} else if (strncmp(keyword, "PumpPos",  relpos) == 0){
  EC.PumpPos = atof(value);
} else if (strncmp(keyword, "PumpTime",  relpos) == 0){
  EC.PumpTime = atof(value);
} else if (strncmp(keyword, "ProbePos",  relpos) == 0){
  EC.ProbePos = atof(value);
} else if (strncmp(keyword, "ProbeStart",  relpos) == 0){
  EC.ProbeStart = atof(value);
} else if (strncmp(keyword, "ProbeEnd",  relpos) == 0){
  EC.ProbeEnd = atof(value);
} else if (strncmp(keyword, "ProbeAmp",  relpos) == 0){
  EC.ProbeAmp = atof(value);
} else if (strncmp(keyword, "ProbeLength",  relpos) == 0){
  EC.ProbeLength = atof(value);
} else if (strncmp(keyword, "ProbeWidth",  relpos) == 0){
  EC.ProbeWidth = atof(value);
} else if (strncmp(keyword, "BeamHeight",  relpos) == 0){
  EC.BeamHeight = atof(value);
} else if (strncmp(keyword, "ProbeAngle",  relpos) == 0){
  EC.ProbeAngle = atof(value);
} else if (strncmp(keyword, "Intersect",  relpos) == 0){
```

```
    EC.Intersect = atof(value);
   } else if (strncmp(keyword, "Temp", relpos) == 0){
       EC.Temp = atof(value);
  } /* endif */

} /* endfor */

/* Apply defaults for undefined or improperly defined parameters here. */
  if (SC.VecTf <= 0) {
    SC.VecTf = SC.Tend;
  } /* endif */
  if (SC.VecDT <= 0) {
    SC.VecDT = SC.DelayDT;
  } /* endif */

  /* Close params file */
  fclose(params);
}
/* ReadPump ////////////////////////////////////////*/
/* Subroutine to read in the position and times of excitation pulses
from file "pump_pulses.txt." The data is stored in the data structure
of type 'pumpv'.  The subroutine returns a pointer to this array. */
struct pumpv ReadPump(int *Nparams, int *Npulses)
{
  Real_Vector x[1], y[5];
  int format, curves, i;
  unsigned points[1];
  Labels labels;
  char filename[] = "input\\pump_pulses.txt";
   struct pumpv PP;

  /* Read in the file using the function from math toolchest */
  math_abort = OFF;

  if ( xyread(filename, &format, &curves, points, &labels, x, y) == -1) {
    printf("Can't open input\\pump_pulses.txt file. \n");
    printf("Using pump pulse defaults from params.txt. \n");
     *Npulses=0;
     *Nparams=0;
     curves=0;
  } else {
       printf("Reading the pump_pulses.txt file. \n");
      /* Pass the number of parameters defined in the file and the number of pulses */
       *Npulses = points[0];
       if (curves > 4) {
           *Nparams = 4;
       } else {
           *Nparams = curves;
       } /* endif */
  }
   if (*Npulses==0){
```

```
        /* if "points" is set to zero in pump_pulses.txt, then ignore the
        parameters from the file and use the defaults from params.txt */
        curves=0;
        *Npulses=1;       /* need at least one default pump pulse */
    }

  /* Allocate memory space for arrays not defined by 'xyread' */
  switch (curves) {
  case 0:
    x[0] = valloc(NULL, *Npulses);
    y[0] = valloc(NULL, *Npulses);
  case 1:
    y[1] = valloc(NULL, *Npulses);
  case 2:
    y[2] = valloc(NULL, *Npulses);
  case 3:
    y[3] = valloc(NULL, *Npulses);
  } /* endswitch */

  /* If explicit parameters are not read in, set to default values defined in 'params' */
  for (i=0; i<*Npulses; i++) {
     switch (curves) {
     case 0:
       x[0][i] = EC.PumpPos;
       y[0][i] = EC.PumpTime;
     case 1:
       y[1][i] = EC.PumpAmp;
     case 2:
       y[2][i] = EC.PumpWidth;
     case 3:
       y[3][i] = EC.PumpLength;
     } /* endswitch */
  } /* endfor */

/* Assign arrays to named arrays */
     PP.Len = y[3];
     PP.Wid = y[2];
     PP.Amp = y[1];
     PP.Tim = y[0];
     PP.Pos = x[0];

return PP;
}
/* ReadState ////////////////////////////////////////*/
/* Subroutine to read in Q and E matrices at two saved time steps */
void ReadState(double *Time, int *VecNum)
    /* This reads the final state of the simulation, inputting matrices
    at two time steps.  It also reads in the last values for Time and
    VecNum, and returns these to the program.  */
{
    int rows, columns, t0, t1;
```

```
    FILE *status;
    t0 = 0;
    t1 = 1;

   /* Y = rows, X = columns  */
    /* read Q and E */
    columns = SC.Xnum;
   rows = SC.Ynum2;
    printf("Reading the stored Q matrices.\n");
   XYread("final\\Qfinal_0", Q[t0], rows, columns);
   XYread("final\\Qfinal_1", Q[t1], rows, columns);
   rows = SC.Ynum;
    printf("Reading the stored E matrices.\n");
   XYread("final\\Efinal_0", E[t0], rows, columns);
   XYread("final\\Efinal_1", E[t1], rows, columns);

    /* read Time, VecNum */
    status = fopen("final\\status", "r");
    fscanf(status, "%le\n", Time);
    fscanf(status, "%d\n", VecNum);
    fclose(status);

    /* read Probe array */
    printf("Reading the stored Probe matrix.\n");
   XYread("final\\probe", Probe, SC.ProbeNum, SC.PrX+1);

}
/* RK4 ////////////////////////////////////////////*/
/* Subroutine for integrating coupled wave equations by one step.
Uses a vectorized 4th order Runge-Kutta algorithm. */
void RK4(double h, double alpha, Real_Vector dEps, Complex_Vector S)
/* h is the step size, alpha is the probe angle, dEps is the permittivity modulation
array, S is vector of the coupled wave amplitudes.
*/
{
    int i;
    static Complex czero;
    static int pmax=maxWave-minWave+1;
    static Complex_Matrix dS;
    static Complex_Vector St;
    static double h2, h3, h6;
    static Real_Vector Ksample, Kdata;
    static int firsttime=1;

    /* Initialize static variables */
    if (firsttime){
        firsttime=0;

        /* make complex zero */
        czero.r = czero.i = 0;
```

```
        /* these arrays will hold the derivative values for the RK algorithm */
        dS = Cmxalloc(NULL, 4, pmax);   /* allocate mem */
        Cmxinit(dS, 4, pmax, czero);    /* zero mem */

        /* these vectors are used to hold temporary S values */
        St = Cvalloc(NULL, pmax);
        Cvinit(St, pmax, czero);

        /* Note: the following lines should be outside this initialization
        section if variable integration steps are used */
        h2 = h/2.0;
        h3 = h/3.0;
        h6 = h/6.0;
    }

    /* Calculate derives 1st time */
    Derivs(alpha, dEps, S, dS[0]);

    /* St = S + (h/2)*dS0 */
    CVadd(St, S, CVscalR(St, dS[0], pmax, h2), pmax);
    /* Calculate derives 2nd time */
    Derivs(alpha, dEps, St, dS[1]);

    /* St = S + (h/2)*dS1 */
    CVadd(St, S, CVscalR(St, dS[1], pmax, h2), pmax);
    /* Calculate derives 3rd time */
    Derivs(alpha, dEps, St, dS[2]);

    /* St = S + h*dS2 */
    CVadd(St, S, CVscalR(St, dS[2], pmax, h), pmax);
    /* Calculate derives 4th time */
    Derivs(alpha, dEps, St, dS[3]);

    /* S = S + (h/6)*(dS0 + 2*dS1 + 2*dS2 + dS3) */
    CVscalR(dS[0], dS[0], pmax, h6);
    CVscalR(dS[1], dS[1], pmax, h3);
    CVscalR(dS[2], dS[2], pmax, h3);
    CVscalR(dS[3], dS[3], pmax, h6);
    for (i=0; i<4; i++){
        CVadd(S, S, dS[i], pmax);
    }

}
/* TimeStep ////////////////////////////////////////////*/
/* Subroutine to increment the Q and E arrays.
   The routine returns an integer that tells which of the three
    time slices is current.  The current time slice is incremented
    in a rotating fashion, while the other two timeslices hold the
    previous states of Q and E.
*/
int TimeStep(double T, struct pumpv PP, int Npulses)
```

```
{
  int i, j, temp;
  double F, X, Y, dampQ, dampE;
  double AnQ3=0, AnQ2=0, Qrelax=0;
   static double Qmax=0;
   static Real_Matrix E1[3], E2[3], E3[3];
   static double b12;
   static struct sdamp * Damping;
   static Real_Matrix Qr;
  static double cc, Eps_ip, Eps_fc, Eps_bc, dXdX, dYdY, dTdT, OmOm, C1, C2;
   static Real_Vector Df, Db;
   static int t0 = 0, t1 = 1, t2 = 2;
  static int firsttime=1;

   /* Initialize static variables */
   if (firsttime) {
       firsttime = 0;

       /* Initialize the starting addresses of E1, E2, E3 */
       for (i=0; i<3; i++){
           E1[i] = &E[i][0];
         E2[i] = &E[i][SC.Ynum1];
          E3[i] = &E[i][SC.Ynum1+SC.Ynum2];
       }

       /* coupling factor between E and Q */
      b12 = MP.Omega * sqrt( (MP.Eps_0 - MP.Eps_ip) * EPS0 );

       Damping = InitializeDamping();
       /* Allocate memory for relaxational mode if it is enabled */
       if (MP.Brelax) {
           Qr = mxalloc(NULL, SC.Ynum2, SC.Xnum);
           mxinit(Qr, SC.Ynum2, SC.Xnum, 0.0);
       }
      cc = C * C;
       Eps_ip = MP.Eps_ip;
       Eps_fc = MP.Eps_front;
       Eps_bc = MP.Eps_back;
      dXdX = SC.dX * SC.dX;
       dTdT = SC.dT * SC.dT;
       OmOm = MP.Omega * MP.Omega;
       C1 = C / sqrt(MP.Eps_inf);
       C2 = b12/EPS0;

       /* Allocate memory for damping vectors */
       Df = valloc(NULL, SC.Ynum1);
        Db = valloc(NULL, SC.Ynum3);

       /* initialize values for damping vectors */
       /* Df is the damping for the front dielectric region */
       for (i=0; i<SC.Ynum1; i++) {
```

```
        Df[i] = SC.DampEMax * (SC.Ynum1-i)/SC.Ynum1;
      } /* endfor */

      /* Db is the damping for the back dielectric region */
      for (i=0; i<SC.Ynum3; i++) {
        Db[i] = SC.DampEMax * i/SC.Ynum3;
      } /* endfor */

    }

/*  The arrays have the origin in the top left corner, where i=0, j=0.
    The x index (i) progress from left to right.  The y index (j) progress
    from top to bottom.
*/

  for (j=0; j<SC.Ynum2; j++) {
    Y = SC.dY2 * j;

    for (i=1; i<SC.Xnum-1; i++) {
      X = SC.dX * i;
      dampQ = Damping[i].Q * SC.dT;
        dampE = Damping[i].E * SC.dT;
        /* Note:  dampE = conductivity/EPS0 * dT.  Units = (fs/um)^2.

          /* Get the force acting on this spot from the pump pulses */
          F = Force(X, Y, T, PP, Npulses);

          /* scale the force by electrooptic factor */
          F *= MP.EO1;
          /* calculate the thermal excitation */
          if (EC.Temp) {
            F += EC.Temp * normal(1,0);
          }

          /* Calculate anharmonic terms */
        if (MP.Anharm3) {
          AnQ2 = MP.Anharm3*(Q[t1][j][i]*Q[t1][j][i]);
        } /* endif */

        if (MP.Anharm4) {
          AnQ3 = MP.Anharm4*(Q[t1][j][i]*Q[t1][j][i]*Q[t1][j][i]);
        } /* endif */

          if (MP.Brelax) { /* if relaxational mode is enabled */
            /* update the relaxational mode at this point */
            Qr[j][i] = (SC.dT*Q[t1][j][i] + MP.Trelax*Qr[j][i]) / (SC.dT + MP.Trelax);
            Qrelax = MP.Brelax * Qr[j][i];
          }

        /* Calculate new Q */
        Q[t2][j][i] = ( 1.0 / (1.0 + dampQ) ) *
```

```
        (dTdT*(-OmOm*(Q[t1][j][i] + AnQ2 + AnQ3) + b12*E2[t1][j][i] + F + Qrelax) +
        dampQ*Q[t1][j][i] + 2.0*Q[t1][j][i] - Q[t0][j][i] );

      /* Calculate new E (with damping) */
        dYdY = SC.dY2 * SC.dY2;
        E2[t2][j][i] = 1/(Eps_ip + dampE) * (
            cc*dTdT*((E2[t1][j][i-1]-2.0*E2[t1][j][i]+E2[t1][j][i+1])/(dXdX) +
                (E2[t1][j-1][i]-2.0*E2[t1][j][i]+E2[t1][j+1][i])/(dYdY)) +
                (2.0*Eps_ip + dampE)*E2[t1][j][i] - Eps_ip*E2[t0][j][i]  -
                C2*(Q[t2][j][i] - 2.0*Q[t1][i][i] + Q[t0][j][i]) );

    } /* endfor */
  } /* endfor */

  /* Now update the E-field in dielectric region 1 using damping array Df */
  dYdY = SC.dY1 * SC.dY1;
  for (j=1; j<SC.Ynum1; j++) {  /* don't recalc first row */
     dampE = Df[j] * SC.dT;
    for (i=1; i<SC.Xnum-1; i++) {
        E1[t2][j][i] = 1/(Eps_fc+ dampE) * (
            cc*dTdT*((E1[t1][j][i-1]-2.0*E1[t1][j][i]+E1[t1][j][i+1])/(dXdX) +
                (E1[t1][j-1][i]-2.0*E1[t1][j][i]+E1[t1][j+1][i])/(dYdY)) +
                (2.0*Eps_fc + dampE)*E1[t1][j][i] - Eps_fc*E1[t0][j][i] );

    } /* endfor */
  } /* endfor */

  /* Now update the E-field in dielectric region 3 using damping array Db */
  dYdY = SC.dY3 * SC.dY3;
  for (j=0; j<SC.Ynum3-1; j++) {  /* don't recalc last row */
     dampE = Db[j] * SC.dT;
    for (i=1; i<SC.Xnum-1; i++) {
        E3[t2][j][i] = 1/(Eps_bc+ dampE) * (
            cc*dTdT*((E3[t1][j][i-1]-2.0*E3[t1][j][i]+E3[t1][j][i+1])/(dXdX) +
                (E3[t1][j-1][i]-2.0*E3[t1][j][i]+E3[t1][j+1][i])/(dYdY)) +
                (2.0*Eps_bc + dampE)*E3[t1][j][i] - Eps_bc*E3[t0][j][i] );

    } /* endfor */
  } /* endfor */

  /* Circularly permute times t0, t1, t2.  t1 will point to the new current time position. */
  /* t0 will be t-dt, t2 will be t + dt */
  temp = t0;
  t0 = t1;
  t1 = t2;
  t2 = temp;
  return t1;
}
/* UnscaleQ ////////////////////////////////////////////*/
void UnscaleQ(Real_Matrix Xq, int Ynum2, int Xnum, int timeslice)
/* This removes the sqrt(m*N/2) scaling factor from Q to
```

```
    get the real displacement.  The output units for displacement
    X are microns. */
{
    int i, j;
    double unscale;

    unscale = sqrt(2/(MP.ModeM*MP.ModeN));
    for (i=0; i<Ynum2; i++) {
        for (j=0; j<Xnum; j++) {
            Xq[i][j] = unscale * Q[timeslice][i][j];
        }
    }

}
/* WaveCouple ////////////////////////////////////////////*/
/* This subroutine calculates the total diffraction response
    using rigorous wave coupling theory.  It calculates the
    combination of higher-order diffraction plus diffraction
    from wavevector harmonics. It returns the coupled wave matrix. */
Complex_Matrix * WaveCouple(void)
{
    int i, j;
    double alpha;
    static Complex czero;
    static Complex_Matrix Smx[maxWave];
    static Real_Vector dEps;
    static double C1, h;
    static int pmax=maxWave-minWave+1;
    static int firsttime=1;

    /* Initialize static variables */
    if (firsttime){
        firsttime=0;

        /* make complex zero */
        czero.r = czero.i = 0;

        /* initialize the wave coupling variables and arrays */
        /* Smx and Tmx hold the couple wave state variables.
        The order of the indexes are [probe angle][time delay][wave number]
        Probe angle has maxWave entries, time delay has ProbeNum entries,
        and wavenumber has maxWave-minWave+1 entries. */
        for (i=0; i<maxWave; i++){
            Smx[i] = Cmxalloc(NULL, SC.ProbeNum, pmax);    /* allocate mem */
            Cmxinit(Smx[i], SC.ProbeNum, pmax, czero);    /* zero mem */
        }

        /* dEps holds the permittivity modulation array.  This is size maxWave
        because the highest order of q harmonics = highest wave calculated. */
        dEps = valloc(NULL, maxWave);  /* allocate mem */
        vinit(dEps, maxWave, 0);        /* clear mem */
```

```
    /* C1 is the speed of the probe pulses in the y direction */
    /* Note that I am ignoring the difference in forward speed as a function
    of the variable probe angle alpha.  At larger probe angles there may be
    a loss of phase matching that won't be calculated here. */
   C1 = C * cos(EC.Theta/2) / sqrt(MP.Eps_inf);
    /* h is the step size in the y direction per time step */
    h = C1 * SC.dT;

    /* Initialize the starting values of the coupled wave intensities */
    for (i=0; i<maxWave; i++){
        for (j=0; j<SC.ProbeNum; j++){
            /*  For a given angle i, the beam is initially in wave m=0.
                m=0 corresponds to an index of (-minWave), so this offset is
                included below.  This is the initial condition for all delay
                times j. Set this intensity to the scaled probe amplitude. */
            Smx[i][j][-minWave].r=EC.ProbeAmp;
        } /* end for */
    } /* end for */

} /* endif (firsttime) */

/* There is one major simplification in this routine - all the
permittivity information is obtained from the probe traveling at
the first Bragg angle as calculated in ProbeSweep.  However, the
difraction is calculated for probes at higher order Bragg angles, as
given by the index i below.  This will be inaccurate when the probe at
a higher angle samples the excitation differently from the probe at the
first angle.  One possibility is a loss of phase matching at higher
angles;  the probe travels forward at cos(alpha)*C/n, so at large
angles the probe will have a smaller forward velocity than the excitation.
This will cause a loss of signal due to poor phase matching, particularly
in thick samples.  This effect will not be correctly calculated here
because all the probe information is from the first angle only. In other
words, the information in dEps returned by Qharmonics is not dependent
on i, the index of the probe angle. */

/*  sweep through the different probe angles, where each probe
    angle is at the Bragg angle for a wavevector harmonic */
for (i=0; i<maxWave; i++){
   alpha = asin((i+1)*EC.Kx * EC.Lamda / (4 * pi_));

    /*  sweep through all the values of probe delay and recalculate
        the coupled wave intensities */
    for (j=0; j<SC.ProbeNum; j++){  /* j is the delay index */
        /* get the modulation array for this delay value */
        if (Qharmonics(dEps, j)){
            /*  Do a Runge-Kutta integration step if Qharmonics returns
                a one, indicating a nonzero modulation factor. */
            RK4(h, alpha, dEps, Smx[i][j]);
        }
```

```
        }
    }

return Smx;
}
/* WriteState ////////////////////////////////////////////*/
void WriteState(int timeslice, double Time, int VecNum)
/* This saves the final state of the simulation, saving matrices
    at two steps.  It also saves the time and vector number. */
{
    int rows, columns, t0, t1;
    FILE *status;

    /* figure out which time pointer is which */
    switch (timeslice) {
    case 2: t1 = 2; t0 = 1; break;
    case 1: t1 = 1; t0 = 0; break;
    case 0: t1 = 0; t0 = 2; break;
    default: {
        printf("Unexpected value for timeslice in WriteState.\n");
        exit(0);
            }
    }

   /* Y = rows, X = columns  */
    /* save Q and E matrices */
    columns = SC.Xnum;
   rows = SC.Ynum2;
    printf("Writing the stored Q matrices.\n");
   XYwrite("final\\Qfinal_0", Q[t0], rows, columns);
   XYwrite("final\\Qfinal_1", Q[t1], rows, columns);
   rows = SC.Ynum;
    printf("Writing the stored E matrices.\n");
   XYwrite("final\\Efinal_0", E[t0], rows, columns);
   XYwrite("final\\Efinal_1", E[t1], rows, columns);

    /* save Time and VecNum */
    status = fopen("final\\status", "w");
    fprintf(status, "%e\n", Time);
    fprintf(status, "%d\n", VecNum);
    fclose(status);

    /* save Probe array */
    printf("Writing the stored Probe matrix.\n");
   XYwrite("final\\probe", Probe, SC.ProbeNum, SC.PrX+1);

}

/* XYread ////////////////////////////////////////////*/
/* This routine reads in the ascii files.  This is different
from the routine called xyread in mathlib. */
```

```
void XYread(char *filename, Real_Matrix M, int rows, int columns)
{
    int r, c;
    FILE *inf;

   inf = fopen( filename, "r" );

    for (r=0; r<rows; r++) {
        for (c=0; c<columns; c++){
            fscanf( inf, "%le", &M[r][c]);
            fscanf( inf, " ");
        }
        fprintf(inf, "\n");
    }
    fclose(inf);
}
/* XYwrite ////////////////////////////////////////////*/
/* This routine writes the ascii files.  This is different
from the routine called xywrite in mathlib. */
void XYwrite(char *filename, Real_Matrix M, int rows, int columns)
{
    int r, c;
    FILE *outf;

   outf = fopen( filename, "w" );

    for (r=0; r<rows; r++) {
        for (c=0; c<columns; c++){
            fprintf( outf, "%e", M[r][c]);
            fprintf( outf, " ");
        }
        fprintf(outf, "\n");
    }
    fclose(outf);
}
```